Wide Bandgap Semiconductor Radiation Detectors for Extreme Environments

Thesis submitted for the degree of
Doctor of Philosophy

Grammatiki Lioliou
Department of Engineering and Design
University of Sussex

February 2017

Abstract

Wide bandgap semiconductor photodiodes were investigated for their suitability as radiation detectors for high temperature applications (≥ 20 °C), through measurements, calculations of key parameters of the devices, and relating the results back to the material, geometry of the detectors, environment under which the detectors were investigated, and previously published work. Three families of photodiodes were examined.

4H-SiC vertical Schottky UV photodiodes with Ni_2Si interdigitated contacts were characterised for their response under dark and UV illumination. Electrical characterisation up to 120 °C and room temperature responsivity measurements (210 nm to 380 nm) suggested that the devices could operate at low UV light intensities, even at high visible and IR backgrounds without the use of filters, and at high temperatures.

4H-SiC Schottky photodiode detector arrays with planar thin NiSi contacts were investigated for X-ray (≤ 35 keV) detection and photon counting spectroscopy at 33 °C. The electrical characterisation of the devices up to 140 °C and subsequent analysis suggested that the devices are likely to operate as high temperature X-ray spectrometers.

Results characterising GaAs p^+-i-n^+ mesa photodiode detectors for their room temperature visible and near infrared responsivity (580 nm to 870 nm), as well as their high temperature (≤ 60 °C) X-ray detection performance (at 5.9 keV) are presented. GaAs p^+-i-n^+ mesa photodiodes were also shown to be suitable for β^- particle (electron) spectroscopy and X-ray fluorescence spectroscopy (≤ 21 keV) at 33 °C.

The X-ray and electron spectroscopic measurements were supported by a comprehensive treatment of the noise components in charge sensitive preamplifiers. Calculations showed the potential benefits of using a SiC, rather than Si, JFET as the input transistor of such a preamplifier operating at high temperatures. The spectroscopic measurements, using both the 4H-SiC and GaAs photodiodes, are presented along with noise analysis to detangle the different noise components present in the reported spectrometers, identify the dominant source of noise, and suggest potential improvements for future spectrometers using the reported devices.

Acknowledgements

There are many people who helped me pursue a research degree and I am grateful to have met them.

Firstly, I wish to express my ineffable gratitude to my PhD supervisor Dr Anna Barnett. She welcomed me to the (new, back then) Semiconductor Materials and Devices Laboratory and believed in me from the very first moment. I wish to thank Dr Anna Barnett for sharing her knowledge and expertise with me, for her invaluable support, useful discussions and guidance over the course of my PhD. I would also like to thank Prof Robert Prance and Dr Helen Prance for proposing me to pursue a PhD in the Semiconductor Materials and Devices Laboratory, and their assistance thereinafter.

Special thanks goes to Massimo Mazzillo, Prof Jo Shien Ng, Xiao Meng, Dr Alton Horsfall, and Dr Hua Khee Chan for fabricating and providing the devices used in this thesis. I would like to gratefully acknowledge the financial support of School of Engineering and Informatics, University of Sussex, in the form of a PhD scholarship.

Thanks to my colleagues throughout the SMDL, Tina Gohil, Richard Parsons, Shifan Zhao, Michael Whitaker, and Dr Silvia Butera, for their friendship and all the fruitful discussions during our breaks. Their support and understanding on a daily basis has been determinant for the successful completion of my PhD. A particular thanks goes to Dr Elizabeth Rendon for reminding me the importance of being grateful for small things. Thanks also go to Martin Nock for technical support and patient guidance with the experimental work performed in this thesis.

I would specially like to thank each and every teacher of mine, for inspiring me and motivating me since I was a child. They have taught me the beauty of learning and being curious about the world around me. Thanks to my beloved people, Dimitris, Christina, and Natassa for their support, company, and for always being there for me.

Last and most importantly, my gratitude goes to my mum, my dad, and my sister for their unconditional love and support. I wish to thank them for caring for me so much and always putting my happiness before their own. They are the reason I strive to be a better person every day.

Contents

Publications

Barnett, A.M., **Lioliou, G.**, and Ng, J.S., 2015, *Characterization of Room Temperature AlGaAs Soft X-ray Mesa Photodiodes*, Nuclear Instruments and Methods in Physics Research A, Vol. 774, pp. 29-33.

Lioliou, G., Mazzillo, M.C., Sciuto, A., and Barnett, A.M., 2015, *Electrical and Ultraviolet Characterization of 4H-SiC Schottky Photodiodes*, Optics Express, Vol. 23, pp. 21657-21670.

Lioliou, G., and Barnett, A.M, 2015, *Electronic Noise in Charge Sensitive Preamplifiers for X-ray Spectroscopy and the Benefits of a SiC Input JFET*, Nuclear Instruments and Methods in Physics Research A, Vol. 801, pp. 63-72.

Butera, S., **Lioliou, G.**, and Barnett, A.M., 2016, *Gallium Arsenide ^{55}Fe X-ray-Photovoltaic Battery*, Journal of Applied Physics, Vol. 119, Art. No. 064504.

Lioliou, G., Meng, X., Ng, J.S., and Barnett, A.M., 2016, *Characterization of Gallium Arsenide X-ray Mesa p-i-n Photodiodes at Room Temperature*, Nuclear Instruments and Methods in Physics Research A, Vol. 813, pp. 1-9.

Lioliou, G., Meng, X., Ng, J.S., and Barnett, A.M., 2016, *Temperature Dependent Characterization of Gallium Arsenide X-ray Mesa p-i-n Photodiodes* Journal of Applied Physics, Vol. 119, Art. No. 124507.

Zhao, S., Gohil, T., **Lioliou, G.**, and Barnett, A.M, 2016, *Soft X-ray Detection and Photon Counting Spectroscopy with Commercial 4H-SiC Schottky Photodiodes*. Nuclear Instruments and Methods in Physics Research A, Vol. 830, pp. 1-5.

Butera, S., **Lioliou, G.**, Krysa, A.B., and Barnett, A.M., 2016, *Characterization of $Al_{0.52}In_{0.48}P$ Mesa p-i-n Photodiodes for X-ray Photon Counting Spectroscopy*, Journal of Applied Physics, Vol. 120, Art. No. 024502.

Gohil, T., Whale, J., **Lioliou, G.**, Novikov, S.V., Foxon, C.T., Kent, A.J., and Barnett, A.M., 2016, *X-ray Detection with Zinc-Blende (Cubic) GaN Schottky Diodes*, Scientific Reports, Vol. 6, Art. No. 29535.

Butera, S., **Lioliou, G.**, Krysa, A., and Barnett, A.M., 2016, *$Al_{0.52}In_{0.48}P$ ^{55}Fe X-ray-photovoltaic Battery*, Journal of Physics D: Applied Physics, Vol. 49, Art. No. 355601.

Lioliou, G., and Barnett, A.M., 2016, *Gallium Arsenide Detectors for X-ray and Electron (Beta Particle) Spectroscopy*, Nuclear Instruments and Methods in Physics Research A, Vol. 836, pp. 37-45.

Lioliou, G., Chan, H.K., Gohil, T., Vassilevski, K.V., Wright, N.G., Horsfall, A.B., and Barnett, A.M., 2016, *4H-SiC Schottky Diode Arrays for X-ray Detection*, Nuclear Instruments and Methods in Physics Research A, Vol. 840, pp. 145-152.

Whitaker, M.D.C., **Lioliou, G.**, Butera, S., and Barnett, A.M., 2016, *$Al_{0.2}Ga_{0.8}As$ X-ray Photodiodes for X-ray Spectroscopy*, Nuclear Instruments and Methods in Physics Research A, Vol. 840, pp. 168-173.

Butera, S., **Lioliou, G.**, Krysa, A.B., and Barnett, A.M., 2016, *Temperature Dependence of an AlInP ^{63}Ni Betavoltaic Cell*, Journal of Applied Physics, Vol. 120, Art. No. 144501.

Butera, S., Gohil, T., **Lioliou, G.**, Krysa, A.B., and Barnett, A.M., 2016, *Temperature Study of $Al_{0.52}In_{0.48}P$ Detector Photon Counting X-ray Spectrometer*, Journal of Applied Physics, Vol. 120, Art. No. 024502.

Butera, S., Whitaker, M.D.C., **Lioliou, G.**, and Barnett, A.M., 2016, *AlGaAs ^{55}Fe X-ray Radioisotope Microbattery*, Scientific Reports, Vol. 6, Art. No. 38409.

Chapter 1 Introduction

1.1 Brief history of semiconductor radiation detectors

Until 1960s, the main use of semiconductors detectors was for nuclear and atomic physics experiments (Lowe & Sareen, 2014). Ionisation detectors (ionisation chambers, proportional counters and Geiger-Muller counters) and scintillation counters were also used in these applications (Leo, 1994) (Kamal, 2014). The ready availability of material and their properties made Silicon (Si) and Germanium (Ge) the only viable semiconductor detectors until 1957, when cadmium telluride (CdTe) started to be studied as radiation detector. For both Si and Ge radiation detectors, the main material-related problem was impurities which limited the depletion depth and hence quantum detection efficiency. In 1960, when lithium ion (Li^+) movement under an applied electric field (drift) in Si was studied (Pell, 1960), it was found that the pairing of the mobile Li^+ to the impurities present in Si and Ge could result in near-intrinsic material. Lithium compensation (Mann et al., 1962), evolution of detector geometries (Brown, 1969), and advances in amplifiers (Harris & Shuler, 1967) opened new horizons in the use of semiconductor radiation detectors.

1.2 Traditional (narrow bandgap) semiconductor radiation detectors

It has been claimed that more than 99 % of X-ray and γ-ray semiconductor spectrometers, in 2014, were made of Si and Ge (Lowe & Sareen, 2014). Photodiode detectors made of lithium drifted Si, Si(Li), and high purity germanium, HPGe, are the classical high-resolution semiconductor detectors, achieving near Fano-limited energy resolutions (defined in **Section 2.3.2**) (e.g. 130 eV at 5.9 keV) when operating at cryogenic temperatures (-173 °C) (Lowe, 1997) (Strüder et al., 1999)) (Tsuji et al., 2004). The bulk of the material of these devices is characterised by a very low concentration of free carriers, which is achieved through lithium compensation of p-type Si in the case of Si(Li) and the use of extremely pure material in the case of HPGe photodiode detectors (Van Grieken & Markowicz, 2002). However, complex, bulky, and expensive cryogenic systems impose limitations in the deployability of such detectors in portable equipment and applications outside the laboratory environment (Gauglitz & Vo-Dinh, 2006). This led to the development of semiconductor detectors with reduced cooling requirements thus reducing or eliminating the need for liquid nitrogen. Even so, thermoelectric cooling – sometimes to near cryogenic temperatures, e.g. -120 °C (Abbey et al., 2003) – is still commonly required for optimum operation of these detectors where they are based on Si or other narrow bandgap materials.

Si p^+-i-n^+ photodiodes are one of the most common semiconductor detectors (Renker & Lorenz, 2009) (Lowe & Sareen, 2014). The Si p^+-i-n^+ photodiode is a development from the simple p-n junction which consists of an intrinsic i layer (high resistivity, pure semiconductor with negligible impurities) between a p^+ type (acceptor doped semiconductor with positive charged holes in the valence band) and n^+ type (donor doped semiconductor with negative charged electrons in the conduction band) semiconductor layer (White, 1982). Although the depletion layer can extend throughout the i layer and penetrate into both the p^+ type and n^+ type layers depending on the doping density in these layers, the depletion width is approximately equal to the intrinsic layer width for very highly doped (low resistivity) p^+ and n^+ regions. Energy resolutions of 149 eV at 5.9 keV have been achieved with a Si p^+-i-n^+ photodiode, when thermoelectrically cooled at -43 °C (Pantazis et al., 2010).

Charge Coupled Devices (CCDs) were initially developed as imaging devices by Boyle and Smith (1970) to replace the light sensitive film in cameras, but CCDs are now also used as particle tracking detectors (Damerell, 1998) and X-ray spectrometers and imaging devices (Akimov, 2007) (Lowe & Sareen, 2014). The use of CCDs as X-ray spectrometers was first proposed by Catura and Smithson (1979). The pixels of the CCD are manufactured by an n-type implant on a p-type Si wafer or on a p-type epitaxial Si layer grown on a wafer to form a channel buried under the surface (Lowe & Sareen, 2014). Metal-oxide-semiconductor (MOS) technology (Abbey et al., 2003) and p-n technology (Meidinger et al., 2005) have been applied to the manufacture of X-ray CCDs, with the latter achieving full depletion and being more radiation resistance than the former (Meidinger et al., 1995) (Strüder et al., 1999). Fully depleted CCDs can benefit from back side illumination, eliminating the attenuation of X-rays by the top surface structures (Knoll, 2010). When operating at -80 °C, pn-CCDs have been shown to achieve a full width at half maximum (*FWHM*) (defined in **Section 2.3.2**) at 5.9 keV of 138 eV (Meidinger et al., 2005). However, event pile-up, occurring when two or more photons are absorbed in the same pixel or nearby pixels of an X-ray CCD detector within a short period of time, and are thus interpreted as one single event, can produce spectral artefacts which may complicate analysis (Jethwa et al., 2015). A related limitation of CCDs is their readout speed which is limited due to the serial readout nature of conventional CCDs (Liu et al., 2005).

Si Drift Detectors (SDDs) were first introduced by Gatti and Rehak (1983). A unique electrode configuration allows semiconductor p-n junctions to be formed at both faces of the wafer (Knoll, 2010). When the p-n structure of the SDD is reverse biased, full depletion is achieved creating a minimum electrostatic potential energy which acts as a collection channel for carriers generated by ionizing radiation (Lowe & Sareen, 2014). An energy resolution of 128 eV at 5.9 keV has been achieved with a thermoelectrically cooled to -33 °C SDD (Redus et al., 2011), whereas at a

temperature of 0 °C, an energy resolution (*FWHM*) of 158 eV at 5.9 keV has been reported with 38 mm^2 drift square cells (Gianoncelli et al., 2016). Work to reduce the anode current density of SDDs in order to permit operation at room temperatures has also been reported; recently, an energy resolution (*FWHM*) of 136 eV at 5.9 keV at room temperature was reported (Bertuccio et al., 2016).

The Depleted P-Channel Field Effect Transistors (DEPFETs) structure was first proposed in 1986 and its functional principle was experimentally confirmed in 1990 (Kemmer et al., 1990). It consists of a p-type channel Field Effect Transistor (FET) working on a depleted high resistivity (low doped) n-type Si substrate (Tsuji et al, 2004). The detector is depleted in such a way as to create a potential minimum under the channel of the FET in which signal charge carriers (electrons) created by the incident radiation (see **Section 2.3.2** for charge generation by radiation in semiconductors), can be collected and stored. This local potential minimum serves as the "internal gate" of the transistor resulting in holes being induced in the DEPFET channel, increasing the transistor current (Tsuji et al, 2004). The overall effect is the integration of the first amplification stage (input FET of the preamplifier) on the detector chip. An energy resolution of 250 eV at 5.9 keV was reported for a DEPFET at room temperature when it was first experimentally characterised (Kemmer et al., 1990). A near Fano-limited energy resolution of 131 eV at 5.9 keV was more recently reported with a DEPFET operating at room temperature (Wermes et al., 2003).

Pixel array detectors are radiation detectors consisting of an array of photodiode devices on a single wafer (Lowe & Sareen, 2014). Although they overcome the disadvantage of high capacitance per device (as for example the p^+-i-n^+ diodes), the complexity of readout electronics is increased. Much work has been conducted to develop pixel array readout electronics, typically an application specific integrated circuit (ASIC) is connected to the detector array by flip-chip bump bonding (Wermes, 2003). Medipix1 (a large prototype chip (Di Bari et al., 1997)), Medipix2 (a Medipix1 successor with reduced pixel dimension (Llopart et al., 2001)), Timepix (an evolution of Medipix2 with a different functionality at the level of the single pixel (Llopart et al., 2007)), and Medipix3 (a successor of Medipix2 permitting colour imaging (Ballabriga et al., 2011)) are CMOS readout ASICs which have been designed and developed for use with pixel array detectors.

1.3 The limitations of the traditional narrow bandgap semiconductors

A variety of radiation detection applications require operation in harsh environments. Harsh environments may include high temperatures (> 20 °C), e.g. 482 °C at the surface of Venus (Kolawa et al., 2007), and the presence of intense radiation, e.g. doses as high as 6 MRad at

Jupiter and the Galilean moons (Atzei et al., 2007). The properties of Si and Ge when used for semiconductor detectors are limiting in these regards. The narrow bandgaps of Si (=1.12 eV (Bludau et al., 1974)) and Ge (=0.67 eV (Spieler, 2005)) have a direct effect on their intrinsic carrier concentrations and consequently on their leakage current densities achievable with such devices (Neudeck et al., 2002). The intrinsic carrier concentration, n_i, refers to the thermal electron and hole charge carriers present in any semiconductor material, excluding the dopant carriers; it has an exponential dependence upon temperature. The intrinsic carrier concentration is also a function of the bandgap of each semiconductor, such that,

$$n_i \propto e^{-E_G/2kT}, \tag{1.1}$$

where E_G is the bandgap in eV, k is the Boltzmann constant, and T is temperature in K. At a given temperature, the greater the bandgap, the lower the intrinsic carrier concertation. As an example, at room temperature, the intrinsic carrier concentrations for Si and Ge are ~10^{10} cm^{-3} and ~10^{13} cm^{-3}, respectively (Lowe & Sareen, 2014). The leakage currents of p-n junctions and of energy barriers (in Schottky diodes, see **Section 2.4.1**) are fundamentally tied to the intrinsic carrier concentration (Neudeck et al., 2002). The leakage current of a p-n junction is directly proportional to (and dominated by) the intrinsic carrier concentration (Lowe & Sareen, 2014) and thus, the use of narrow bandgap materials results in leakage current densities which can limit the performance of such diodes at room and high temperatures. The Schottky barrier height in Schottky diodes depends upon the metal, the semiconductor, and process by which the junction was formed, but it cannot be higher than the semiconductor bandgap (Neudeck et al., 2002). Consequently, narrow bandgap semiconductor detectors with Schottky contacts have limited Schottky barrier heights which may result in significant junction leakage current densities (see **Section 2.4** for further discussion of leakage current in p-n and Schottky diodes).

Another limitation of traditional narrow bandgap semiconductor detectors arises from their propensity to radiation damage. Semiconductor devices are required to operate in and after exposure to different radiation regimes, depending on the application. The radiation in a space environment is mostly composed of protons and electrons trapped in the Van Allen belts of Earth, heavy ions trapped in magnetospheres of Earth and other planets, cosmic-ray photons and heavy ions, and protons, electrons, and heavy ions from Solar flares (Claeys & Simoen, 2002). In High Energy Physics (HEP) experiments, electron and proton beams of energies as high as 500 GeV are the primary reason of potential radiation damage. γ-rays and both thermal and fast neutron irradiation are usually present in nuclear environments with higher fluxes and doses compared to many space applications. Even in natural environments, the presence of radiation from

radioactive materials, including certain lead isotopes, can be of possible harm to the semiconductor devices. As an example, the inevitable presence of the radioactive ^{40}K (89.44 % probability of 1.31 MeV β emission and 10.6 % probability of 1.46 MeV γ emission, for each decay) in the glass of microchannel plate (MCP) detectors was found to account for most of the observed background and dark current noise of MCP detectors (Fraser et al., 1987) (Siegmund et al., 1988) (Mitchell et al., 2016).

The main radiation damage mechanism in semiconductor detectors is displacement. Displacement occurs when a particle of sufficiently high energy knocks an atom from its lattice site within the semiconductor detector with the consequence that a defect within the lattice structure is created (Leo, 1994). Such radiation defects give rise to trapping levels in the normally forbidden bandgap which affect the electrical behaviour and properties of the semiconductor device. Increases in leakage current, due to changes in the resistivity of the material, and degradation of energy resolution, due to incomplete charge collection noise (**Section 3.5**), are the main effects of radiation damage (Lindström, 2003) (Leroy & Rancoita, 2007) (Jafari & Feghhi, 2016).

The use of semiconductor radiation detectors made of Si and Ge in harsh environments may for certain applications be achieved with a trade-off. Such radiation detection systems commonly require cooling facilities to bring the temperature of the detectors to ≤ 20 °C (sometimes near to cryogenic temperatures (Abbey et al., 2003)) to reduce the number of carriers generated by thermal excitation, as well as to mitigate radiation damage effects, and radiation shielding to protect against radiation damage. All these increase the mass, volume, and power requirements, and subsequently increase the total cost of the instrumentation. Furthermore, there are applications which cannot accommodate the mass, volume, and power requirements of such additional equipment, regardless of cost.

An alternative to using narrow bandgap semiconductor detectors in harsh environment applications is to develop new semiconductor materials (and detectors made from them) with favourable characteristics under extreme environments, in order to eliminate or reduce the need for cooling and radiation shielding. The development of such materials and detectors and instrumentation made from them, is the subject of much ongoing research world-wide. Semiconductor materials with wide bandgaps that can withstand high temperatures and intense radiation have already shown much promise and suitability for such applications, but the state-of-the-art and maturity of the technologies still means that much research is required if such devices are ever to displace Si from its dominant position within the broader field of radiation detectors. Numerous applications would benefit from the development of practical wide bandgap

semiconductor radiation detectors, with some of the most demanding applications being found in space science and astronomy, where electron, ultra-violet (UV), and X-ray detectors are required for many of the likely missions to be attempted in the 21st century. An introduction to wide bandgap semiconductor materials is given in **Section 1.5**, but first a discussion of some key semiconductor electron, UV, and X-ray detectors being presently employed in space applications is presented in **Section 1.4**.

1.4 Space missions employing semiconductor electron, UV, and X-ray detectors

This section focuses on space applications utilising semiconductor detectors for electron, UV, and X-ray detection. It includes planetary orbiters and landers, as well as Earth and Sun orbiting observatories.

1.4.1 Semiconductor electron detectors

Planetary electron spectroscopy, along with ion spectroscopy, can be used to help understanding the Solar wind and its interactions with planetary atmospheres and magnetospheres (Livi et al, 2003). The Solar wind, in conjunction with a sufficiently strong magnetic dipole moment, which is true in the Solar system for Mercury, Earth, Jupiter, Saturn, Uranus, and Neptune, results in space plasma activity (Schindler, 2007). Observation and characterisation of such interactions have been amongst the science objectives of various instruments and space missions.

The Energetic Particle Spectrometer (EPS) (mass of ~1.5 kg) on board the MESSENGER spacecraft launched in 2004 to Mercury, measured in situ the energy, angular and compositional distributions of the high-energy components of electrons (> 20 keV) using semiconductor detectors (Livi et al, 2003) (Andrews et al., 2007). The main objective of the MESSENGER EPS was to determine the origin and structure of Mercury's magnetic field. Electron measurements across the energy range of 15 keV to 1 MeV were achieved with a semi-circular collimator and a total of 12 detector regions (pixels), mounted on 6 individual substrates (2 pixels per detector, one 40 mm^2, and one 2 mm^2). The detectors were 500 μm thick ion-implanted Si solid state detectors (SSDs). They were coated with a 1 μm Al layer to attenuate protons of energies ≤ 110 keV. They were cooled to < -5 °C (Andrews et al., 2007).

An electron spectrometer, the Pluto Energetic Particle Spectrometer Science Investigation (PEPSSI), with instrument heritage from the MESSENGER EPS, was included on the NASA New Horizons mission to Pluto (McNutt et al., 2008). With a total mass of 1.475 kg and an average power consumption of 2.49 W, PEPSSI measured in situ energetic electrons with energies from 25 keV to 500 keV in the near-Pluto environment and in the Pluto-interaction region. It consisted of a collimator and a 500 μm thick SSD array assembly (3 out of 12 pixels

were measuring electrons). The electron detectors were coated with an Al layer to block the protons and ion particles with energies less than 100 keV. PEPPSI had an electron energy resolution of 5 keV, over the energy range of interest (McNutt et al., 2008).

The Jupiter Energetic Particle Detector Instruments (JEDI) on board JUNO (arrived at Jupiter in July 2016), is used along with other space physics instruments to characterise and understand the space environment of Jupiter's polar regions and the Jovian aurora (Mauk et al., 2013). JEDI can measure the energy and angle distribution (directional distribution of the intensity) of electrons from 25 keV to 1 MeV, using SDDs, similarly to the MESSENGER EPS and the New Horizons PEPSSI. The electron SSDs (same structure and configuration as the MESSENGER EPS electron SSDs) are covered with a 2 μm thick Al layer to stop protons of energies ≤ 250 keV. The electron energy resolution of JEDI is 20 % over the electron energy range of interest, according to Mauk et al. (2013), although details of the achieved energy resolution were not included.

1.4.2 Semiconductor UV detectors

Space observations in the UV region of the electromagnetic spectrum enable study of the origins of large scale structures in the universe, the formation and evolution of galaxies, as well as the origin of stellar systems, and the interstellar medium (Green, 2001). The Hubble Space Telescope (HST) with its UV instruments has resulted in many major scientific discoveries (Green et al., 2012). Three of its instruments, the Space Telescope Imaging Spectrograph (STIS) (Kimble et al., 1998), the Cosmic Origins Spectrograph (COS) (Green et al., 2012) and the Wide Field Camera 3 (WFC3) (Dressel, 2016), cover together the UV range from 115 nm to visible light (1 μm). The STIS covers the far-UV band with a microchannel plate detector with an opaque CsI photocathode on its front, and the near-UV with a microchannel plate detector with a semi-transparent CsTe photocathode on its inside. The COS, complementing the STIS, covers the far-UV band with a windowless microchannel plate detector (Vallerga et al., 2002). The WFC3 consists of thinned, backside illuminated and UV optimized Si based CCDs to cover the UV range from 200 nm to visible region of the electromagnetic spectrum.

UV observations utilising semiconductor detectors are also possible with the Swift space observatory. Its Ultraviolet/Optical Telescope (UVOT) is designed to observe γ-ray bursts, from the early afterglow to long term observations, as well as all kind of astronomical sources (Roming et al., 2005) (Page et al., 2014). UV and optical observations between 2005 and 2010 resulted in the detection of more than 6 million unique sources. The two detector assemblies of the telescope are microchannel-plate intensified CCDs operating in a photon-counting mode.

Astrophysical UV missions can also enhance our understanding of heliophysics, encompassing the interactions of the Sun with the Solar system, fundamental physical processes of space plasma systems (including the Solar plasma), the Solar corona, Solar wind, and the flow of energy and matter from the Sun and through Heliosphere. The Interface Region Imaging Spectrograph (IRIS) spacecraft, launched into Sun-synchronous Earth orbit in June 2013, enables study of the Solar surface and corona (De Pontieu et al., 2014). It provides simultaneous spectra and images of the Sun's photosphere, chromosphere, transition region, and corona. Its imaging spectrograph consists of three back-thinned CCD sensors, two for far-UV (133.2 nm to 140.7 nm) and one for near-UV (278.3 nm to 283.5 nm).

1.4.3 Semiconductor X-ray detectors

Analysis of planetary and related surfaces can be benefit from semiconductor radiation detectors. It can be achieved with both in situ analysis using landers, and remote sensing using orbiting spacecraft (Fraser, 2008). Different missions have different objectives and depending on the environment, mission duration and science goals, different approaches to fulfil the mission objectives may be followed. The progress achieved by multiple groups in development of X-ray fluorescence (XRF) instrumentations for in situ analysis of planetary surfaces emphasizes the need for miniaturised instruments which require less cooling, can achieve better energy resolution, and that are not damaged by radiation. A discussion of some key missions to the Moon, Mars, Mercury, asteroids and comets for planetary analysis, utilising X-ray semiconductor radiation detectors is presented below.

The SMART-1 mission to the Moon (launched in 2004) was the first Lunar mission employing semiconductor X-ray detectors. The D-CIXS (Demonstration of a Compact Imaging X-ray Spectrometer) instrument carried by SMART-1 conducted global X-ray fluorescence mapping of the Lunar surface resulting in measurements of absolute elemental abundances (Swinyard et al., 2009). The exciting source for XRF of the Lunar surface was Solar X-rays (see **Section 2.1.3**). The instrument, including collimator, had a mass of 5.2 kg and a total power consumption of 18 W (Foing et al., 2003). The spectrometer consisted of a matrix of swept charge device (SCD) solid state X-ray detectors to perform spatially localised XRF, and Si p^+-i-n^+ photodiodes for the X-ray Solar monitor (Grande et al., 2003). The swept charge device was a variant form of CCD. It had an energy resolution of better than 250 eV *FWHM* at Mg (Kα = 1.25 keV (Thompson et al., 2009)), Al (Kα = 1.48 keV (Thompson et al., 2009)), and Si (Kα = 1.74 keV (Thompson et al., 2009)) lines at launch (Grande et al., 2005) which degraded to ~420 eV at 1.48 keV (Al Kα) after the 15 month journey due to the radiation damage, emphasising that even missions to relatively benign environments such as the Moon would benefit from radiation hard instrumentation. Despite its degraded energy resolution, it successfully demonstrated the

technology, which led to significantly improved design for similar instruments (e.g. C1XS, see below), and resulted in high quality scientific data, for example, the first Lunar XRF observations of the Ti Kα line were achieved with D-CIXS. Importantly, it also demonstrated that even X-ray spectrometers of modest energy resolution can return valuable and high quality data.

The SELENE (SELenological and ENgineering Explorer) spacecraft (launched in 2007) also performed X-ray spectroscopic remote observations of the Lunar surface making valuable contributions which advanced understanding of the Moon's origin and evolution (Shirai et al., 2008). The X-ray fluorescence spectrometer (XRS) on-board SELENE, including the collimators and the radiators used to cool the detectors, had a mass of 20.67 kg and a power consumption of 46.3 W. Included within this were three components; the Lunar X-ray fluorescence detector (XRF-A), the Solar X-ray monitor and calibrator (SOL-B, SOL-C), and the electronics package. The CCD based XRF-A detector had an energy resolution of better than 200 eV at 5.9 keV when cooled at -50 °C with the aid of a passive radiator (Shirai et al., 2008). The two Si p^+-i-n^+ photodiodes (300 μm thick depletion layer) of SOL-B, covered an energy range of 1 keV to 20 keV and had energy resolutions of 430 eV and 580 eV respectively at 5.9 keV when cooled to 0 °C.

An improved version of the SMART-1 D-CIXS was carried by the Chandrayaan-1 spacecraft to the Moon (launched in 2008) (Grande et al., 2009). The performance of the Chandrayaan-1 X-ray Spectrometer (C1XS) (mass 5.5 kg; power consumption 25.5 W) surpassed its predecessor, D-CIXS. Measurements of absolute and relative abundances of major rock-forming elements in the Lunar crust were achieved with 24 SCD detectors, and a high purity Si (HPSi) p^+-i-n^+ detector (X-ray Solar monitor) having an energy resolution (*FWHM*) of 200 eV at 5.9 keV. The SCD detectors had an energy resolution of 85 eV at 1.487 keV (Al Kα) during calibration with an additional energy resolution degradation of 30 eV due to radiation damage during the Earth-Moon transit, based on data from Lunar commissioning work (Howe et al., 2009).

The use of X-ray fluorescence spectroscopy on Mars enables the determination of its surface geology and many recent Mars landers and rovers have included X-ray spectrometers. Measurement of the chemical composition of rocks and soils, identification of local surface anomalies and searches for past and current water activity on its surface contributing to the search of life, are all science objectives for the exploration of Mars with XRF. The Sojourner rover (launched in 1996; landed in Ares Vallis, in 1997 (Golombek et al., 1999)), which was part of the Mars Pathfinder (MPF) mission, was the first lander to use semiconductor detectors for in situ XRF (Rieder et al., 1997) (Bruckner et al., 2003). The Alpha Proton X-ray Spectrometer (APXS) instrument head, containing nine ^{244}Cm radioisotope α particle sources (emitting 5.8 MeV

α particles, and having a total activity of 1.7 GBq) and the detectors (α particle detector, X-ray detector, background detector, and proton detector), was attached to the APXS deployment device at the rear of Sojourner with the objective to determine the elemental composition of the soils and rocks it encountered on the surface of Mars. The APXS instrument head diameter and length were 52 mm and 80 mm, respectively. It had an overall instrument mass (including electronics) of 0.6 kg and a power consumption of 0.4 W (Bruckner et al., 2003). The X-ray detector was a Si p^+-i-n^+ diode with an energy resolution of 260 eV at 6.4 keV when operated at temperatures below -50 °C (Bruckner et al., 2003). Such temperatures were achieved by operating the spectrometer during the Martian night without any cooling (Bruckner et al., 2003).

Another notable X-ray fluorescence spectrometer was developed for the Beagle 2 Mars lander. Beagle 2 was deployed from the Mars Express Orbiter (launched in 2003 (Chicarro et al., 2004)) to a landing site in Isidis Planitia in 2003. Although communications from Beagle 2 were not received after its deployment from Mars Express, the Beagle 2 X-ray Fluorescence Spectrometer (B2 XRS) incorporated a number of notable and innovative design features (Talboys et al., 2009). Having a total mass of 0.34 kg and power consumption of 5 W (Fraser, 2008), the XRS consisted of two ^{55}Fe radioisotope X-ray sources (Mn Kα = 5.9 keV and Kβ = 6.49 keV; activity of 105.6 MBq) and two ^{109}Cd radioisotope X-ray sources (Ag Kα = 22.16 keV and Kβ = 24.94 keV; activity of 8.77 MBq), and a Si p^+-i-n^+ diode (thickness of 300 μm, area of 7 mm^2) coupled to the B2 XRS back end electronics (BEE). The B2 XRS had an energy resolution (*FWHM*) of 340 eV at 5.9 keV when cooled to -23 °C.

A new generation APXS instrument with instrument heritage from the instrument used on the Sojourner rover was included on the two Mars Exploration Rovers (MER), Spirit and Opportunity (launched in 2003), landed in 2004 at Gusev crater and Meridiani Planum, respectively (Rieder et al., 2003) (Desai & Knocke, 2004) (Fraser, 2008). The new APXS had a slightly decreased measurement geometry (30 mm mean distance between sources/detectors and sample c.f. 50 mm for the MPF APXS), less radioactive material (six radioactive ^{244}Cm radioisotope α particle sources emitting 5.8 MeV α particles, with a total activity of 1.1 GBq). The most notable improvements included better energy resolution (160 eV *FWHM* at 5.9 keV when operated at a temperature of -35 °C) and improved sensitivity in the X-ray mode (an improvement factor of >10 was found for elements Na to Fe, when comparing the X-ray photopeak areas of the MER APXS with the MPF APXS). The MER APXS instrument head, including the door mechanism, microswitches, one X-ray and two α channels and the shielding, had a length of 90 mm, diameter of 53 mm, a total mass of 0.25 kg, and 0.6 W power consumption (Rieder et al., 2003).

The MER APXS was further improved for Mars Science Laboratory (MSL) rover Curiosity, which launched in 2011 and landed in 2012 at the Gale crater. The science payload of Curiosity includes the CheMin X-ray diffractometer, and the MSL APXS instrument for in situ determination of rock and soil chemistry (Grotzinger et al., 2012). CheMin was the first instrument to combine XRF with X-ray diffraction in order to provide information about the identity and crystal structure of solids (mineralogy). It uses an active 600 × 582 pixel CCD cooled with a cryocooler to achieve temperatures between -48 °C and -22 °C for dark current reduction (Blake et al., 2012). Although the same SDD X-ray detector is used in the APXS in MSL as in MER, an energy resolution improvement at low temperatures (~140 eV at 5.9 keV) and good energy resolution at higher temperatures (-5 °C c.f. -40 °C for the MER APXS) was achieved (Gellert et al., 2009). Other improvements include higher sensitivity (counts per second from calibrated reference samples) in the X-ray mode due to closer proximity of sample and detector (19 mm c.f. 30 mm in MER APXS), the elimination of α particle detectors, and the use of additional conventional sealed ^{244}Cm radioisotope α particle sources.

Missions to comets enable investigation of the Solar system's origins (Glassmeier et al., 2007). Comets are commonly considered to contain the least processed material in the Solar system, and even pre-Solar grains, thus their compositional properties can potentially provide information of the formation of the Solar system. The Rosetta mission to comet 67P/Churyumov-Gerasimenko (launched in 2004) was a cooperative project between ESA, NASA, and various European national space agencies. It was comprised of 25 experiments. The prime scientific objectives of the Rosetta orbiter, and the Rosetta lander, Philae, were the characterisation of the comet's nucleus, and determination of its surface morphology and composition. One of the instruments of Philae was the Rosetta APXS. The Rosetta APXS was a successor of the MPF APXS. The Rosetta APXS, provided data on the chemical composition of the comet's surface and of the dust components, which together with results from other measurements made by the lander and orbiter, could determine changes in the comet as it approached the Sun (Klingelhöfer et al., 2007). However, results from Rosetta APXS have not yet published. The Rosetta APXS had a total mass of 0.64 kg and used 1.5 W of power. The cylindrical instrument head had a length of 84 mm and a width of 52 mm. An improved energy resolution was achieved with the Rosetta APXS (180 eV *FWHM* at 6.4 keV) which employed a SDD for X-ray detection, compared to the MPF APXS (250 eV *FWHM* at 6.4 keV), both when operated at temperatures < -40 °C.

Missions to Mercury enable key questions regarding the formation and evolution of the inner Solar system to be addressed (Solomon et al., 2001). MESSENGER (launched in 2004, Mercury orbital insertion in 2011 (McNutt et al., 2014)) was the first mission to Mercury which used semiconductor X-ray detectors. Key geological topics to be addressed by MESSENGER's X-ray

Spectrometer (XRS) included the nature of Mercury's geological evolution, the state of its core, and the origin of its anomalously high ratio of metal to silicide. The XRS was used to measure the elemental composition of Mercury's surface (Schlemm et al., 2007). As is the case for the Moon, the exciting source for XRF of Mercury's surface from orbit is Solar X-rays (see **Section 2.1.3**). X-ray measurements of the planet's surface over the energy range 1 keV to 10 keV were taken with three gas proportional counters, whereas a 500 μm thick Si p^+-i-n^+ detector cooled to < -20 °C measured the incident Solar X-rays over the same energy range to support quantitative analysis of the X-ray fluorescence measurements of Mercury's surface. Thus, whilst a semiconductor X-ray spectrometer was used on the mission, it was not used to measure X-ray fluorescence from the surface. The XRS had a total mass of 3.4 kg, including the inter-box cables, and a power consumption of 6.85 W. The surface and Solar X-ray detectors had energy resolutions of 880 eV and 598 eV at 5.9 keV, respectively.

BepiColombo will be the next mission to orbit Mercury. It will use the Mercury Imaging X-ray Spectrometer (MIXS), with two complimentary instruments, the MIXS-C (collimator) and MIXS-T (telescope) for planetary remote sensing by measuring fluorescent X-ray emissions in the energy range 0.5 keV to 7.5 keV using microchannel plate X-ray optics and Si Macropixel DEPFET arrays (a detailed analysis of MIXS was provided by Fraser et al. (2010)). BepiColombo will also include the Solar Intensity X-ray and particle Spectrometer (SIXS) (Huovelin et al., 2010). SIXS, with three identical p^+-i-n^+ X-ray detectors, will measure the Solar spectrum (from 1 keV to 20 keV) incident on the surface of Mercury. Such observations will complement the observations of the X-ray emissions of the Mercury surface with MIXS and enable comparison between theoretical models and observations. GaAs p^+-i-n^+ X-ray detectors were initially chosen for SIXS because of the significantly better radiation tolerance of GaAs compared to Si (Huovelin et al., 2010). However, due to unstable performance of the GaAs detectors during early development, the detectors were changed to high-purity Si in 2009 (Lehtolainen et al., 2011). Ground calibration of the Si p^+-i-n^+ X-ray detectors, which have i layer thicknesses of 300 μm, was conducted in 2012 and showed an energy resolution (*FWHM*) ranging from 145 eV to 165 eV at 6 keV over the temperature range -20 °C to 0 °C (Lehtolainen et al., 2014).

Missions to asteroids can provide information on their surface composition and on their formation and thermal evolution (Prettyman et al., 2012). In addition, asteroids are thought to preserve information from the Solar system's formation and thus they can provide better understanding of the origin and evolution of the Solar system. The Hayabusa mission to the near-Earth asteroid Itokawa (Nakamura et al., 2011) was launched in 2003 (arrived at Itokawa in 2005), and included an X-ray fluorescence spectrometer. Initially, the Hayabusa X-ray spectrometer (XRS) performed remote sensing measurements of the whole Itokawa surface and then descended to land

and capture dust particles from Itokawa. XRF spectrometry was performed (for the first time for such a purpose) using a CCD X-ray detector with an energy resolution of 160 eV at 5.9 keV, when cooled at -60 °C, and a low energy threshold of detection at 2.37 keV (Miyaguchi et al., 1999) (Okada et al., 2006).

CCD X-ray detectors are also carried by Earth orbiting observatories for astrophysical X-ray spectroscopy. Astrophysical X-ray spectroscopy provides information regarding all classes of astrophysics X-ray sources, including thermal processes in plasmas and non-thermal processes such as synchrotron emission and scattering from hot or relativistic electrons (Weisskopf et al., 2002). The importance of X-ray spectroscopy of astrophysical plasmas resides in the fact that X-ray emitting plasmas are not in local thermodynamic equilibrium except at very high densities. Hence, spectral analysis provides information about various microphysical, as well as macrophysical properties of the source (Kahn et al., 2002). The electron temperature and density, the relative abundances and the intensities of the hydrogenic (one electron) and helium-like (two electrons) lines of plasma's elements, the degree of thermal and ionisation equilibrium, are all determinable from astrophysical X-ray spectroscopy (Bavdaz et al., 2001).

Recent key astrophysical X-ray instruments include those for the Chandra X-ray observatory (Weisskopf et al., 2002), XMM-Newton (Strüder et al., 2001), Swift (Burrows et al., 2005), Suzaku (Mitsuda et al., 2007), ASTROSAT (Singh at el., 2014), and Hitomi (Takahashi et al., 2016). They all employ or employed Wolter telescopes and CCD type X-ray detectors (Trümper and Hasinger, 2008).

The Chandra X-ray Observatory, launched in July 1999, has a sub-arcsecond angular resolution over the band 0.08 keV to 10 keV allowing useful observations of a wide variety phenomena (Weisskopf et al., 2002). It has enabled high resolution studies of the structure of supernova remnants, astrophysical jets, hot gas in galaxies and clusters of galaxies, and is also an essential tool for determining conditions in hot plasmas. XMM-Newton, launched in December 1999, benefits from the largest collecting area of all X-ray telescopes, 4260 cm^2 at 1 keV, and has an upper energy limit of 15 keV (Strüder et al., 2001). Swift, launched in November 2004, carries three instruments: the Ultraviolet/Optical telescope (UVOT) (see **Section 1.4.2**), the X-ray telescope (XRT), and the burst alert telescope (BAT) (Burrows et al., 2005). The XRT is an autonomous X-ray imaging spectrometer which measures fluxes, spectra and lightcurves of γ-ray bursts, enabling determination of their position to within a few arcseconds. It covers the energy range of 0.2 keV to 10 keV and has an energy resolution of 140 eV *FWHM* at 5.9 keV. Hard X-rays, over the energy range 15 keV to 150 keV, are detected by the BAT with a CdZnTe imager (energy resolution of 6.2 keV at 122 keV), comprised of 256 CdZnTe modules operating at 20 °C,

allowing the initial detection and localization of γ-ray bursts followed by observations using the UVOT and XRT (Barthelmy et al., 2005). Suzaku, launched in July 2005, was designed to be complementary to Chandra and XMM-Newton. It had four sets of X-ray Telescopes, each one with an X-ray imaging CCD covering the energy range 0.2 keV to 12 keV and providing an energy resolution of ~ 130 eV *FWHM* at 6 keV (Mitsuda et al., 2007). Advantages of Suzaku included the lowest background count rate for many X-ray energies among the existing missions, and good low energy (< 1 keV) CCD response. ASTROSAT, launched in September 2015, is capable of simultaneously observations of broad-band X-ray energies from 0.3 keV to 100 keV (Singh at el., 2014). The soft X-ray telescope which uses a CCD (energy range 0.3 keV to 8 keV, with an energy resolution (*FWHM*) of 150 eV at 6 keV) has a heritage from XMM-Newton and Swift. It is able to perform spectroscopic observations of hot plasmas in galaxies, clusters of galaxies, quasars, stellar coronae, and supernova remnants. Hard X-rays, up to 100 keV, are detected with a CdZnTe imager (energy resolution of ~ 8 keV at 100 keV) comprised of 64 CdZnTe modules operating at 0 °C, allowing the detection of γ-ray bursts (Singh at el., 2014).

For Hitomi (launched in 2016), a soft X-ray imager was designed based on previous missions (Chandra, XMM-Newton, Swift, and Suzaku) using CCDs cooled by single stage sterling coolers to -120 °C. However, satellite attitude control failure led to loss of the spacecraft within a few weeks (Tsunemi et al., 2010) (Takahashi et al., 2016).

The Athena X-ray observatory is a proposed ESA future mission targeted for launch in 2028. It would address two key questions for astrophysics: how ordinary matter assembled into the large scale structures we see today and how black holes grow and shape the universe (Barret et al., 2013). Instruments proposed for Athena include the Wide Field Imager (WFI) (Meidinger et al., 2016) and the X-ray Integral Field Unit (X-IFU) (Barret et al., 2016). The WFI, having an unprecedented large field of view (40 arcminute × 40 arcminute), would cover energies from 0.2 keV to 15 keV using DEPFET active pixel sensors (*FWHM* of ≤ 170 eV at 7 keV) operated at temperatures between -80 °C and -60 °C (Meidinger et al., 2016). The X-IFU, having a very high energy resolution (*FWHM* of 2.5 eV at < 7 keV), would cover energies from 0.3 keV to 12 keV, using cryogenic (50 mK) microcalorimeters (Barret et al., 2016).

Semiconductor X-ray detectors are also a key technology for Solar Orbiter, a heliophysics observatory planned to launch in September 2018 (Müller et al., 2013). Solar Orbiter will investigate the relationship between the Sun and the heliosphere. One of its instruments, the Spectrometer/Telescope for Imaging X-rays will provide imaging spectroscopy of Solar thermal and non-thermal X-ray emissions over the energy range 4 keV to 150 keV. Solar flare X-ray observations will enhance understanding of energy release processes in Solar flares (Benz et al.,

2012). The intensity, spectrum, timing, and location of accelerated electrons near the Sun will be determined by a spectrometer with 32 CdTe X-ray detectors, one behind each of the 32 subcollimators of the imager. The detectors will operate at temperatures between -50 °C to -20 °C, and will have an energy resolution (*FWHM*) of 1 keV at 6 keV.

1.5 Wide bandgap semiconductor materials for radiation detection

The bandgap of any semiconductor detector material has a direct effect on the number of thermally generated carriers within it (as has already been discussed, see Equation 1.1) and an indirect effect on its expected intrinsic energy resolution (Fano-limited energy resolution, see **Section 3.1**) when operating in spectroscopic photon counting mode. Although, narrower bandgaps suggest improved Fano-limited energy resolutions, wide bandgap semiconductor detectors have the potential to be used at high temperatures due to their fundamentally lower thermally generated leakage current compared to narrower bandgap semiconductor detectors at a given temperature. Another advantage of WBG semiconductors is that their required energy for defect formation is larger than for NBG materials (e.g. Si and Ge) resulting in enhanced radiation tolerance for WBG detectors (Spieler, 2005). This thesis follows the same convention as Owens (2012a), in distinguishing between wide bandgap (WBG) and narrow bandgap (NBG) materials: semiconductors with bandgap energies $\geq$ 1.4 eV are considered WGB, whereas those with bandgap energies < 1.4 eV are considered NBG.

To date, a wide variety of WBG compound semiconductor materials have been studied for their suitability as radiation detectors at temperatures $\geq$ 20 °C. WBG compound semiconductor materials for radiation detectors under development include GaAs, SiC, GaN, AlGaAs, AlInP, CdTe, CdZnTe, HgI_2, and TlBr. This thesis focuses on SiC and GaAs radiation detectors. A review of recent developments related to these two materials but excluding the work presented in this thesis, is given below.

A broader introduction to present detection systems employing WBG compound semiconductor detectors can be found in Owens (2012a). The reader is also referred to Owens et al. (2012b) and Gohil (2016) for more recent developments regarding GaN radiation detectors, Barnett et al. (2012) and Whitaker et al. (2016) for AlGaAs detectors, Butera et al. (2016) and Auckloo et al. (2016) for AlInP detectors, Hansson et al. (2014) and Owens (2002a) for CdTe and CdZnTe detectors, Owens (2002b) for HgI_2 detectors and Kozlov et al. (2008) for TlBr detectors.

1.5.1 SiC photodiode radiation detectors

SiC has a bandgap energy which ranges from 2.3 eV to 3.3 eV depending on polytype (Harris, 1995). Of the polytypes, 4H-SiC (E_G = 3.27 eV) is preferred for radiation detection applications

since it has the highest electron mobility (Owens, 2012a). Much work has been reported regarding the development of 4H-SiC for UV and soft X-ray detectors suitable for harsh environments.

4H-SiC has several advantages over Si. Its large bandgap (almost three times that of Si) yields low thermally generated currents permitting operation at high temperatures. SiC Au and Ni Schottky diodes have been reported with leakage current densities as low as 1 pA/cm^2 at room temperature, and 1 nA/cm^2 at 100 °C, even at very high internal electric fields (103 kV/cm) (Bertuccio et al., 2011). A further benefit comes from the strong interatomic bonding in SiC and its correspondingly high displacement threshold energy (= 21.8 eV) (Owens, 2012a), which increases device radiation hardness (Nava et al., 2003) (Prasai et al., 2013). As such, SiC suffers less from device aging due to radiation damage (Monroy et al., 2003). Consequently SiC detectors can have much longer lifetimes than Si detectors when subjected to intense energetic radiation, as would be required for space missions to intense radiation environments. Additionally, the intrinsic insensitivity (visible-blindness) of 4H-SiC to photons of energy < 3.2 eV (wavelength = 380 nm) allows 4H-SiC UV photodiodes to operate even in high flux visible and IR backgrounds without the use of filters (Yan et al., 2004).

The relatively low electron affinity for 4H-SiC (3.17 eV) (Davydov, 2007) results in a high Schottky barrier height (which in the ideal case equals the difference between the metal work function and the electron affinity of the semiconductor (Sze & Ng, 2007)), and consequently in reduced thermionic emission current, minimizing the parallel white noise of the X-ray spectrometer system (see **Chapter 3**) (Bertuccio & Casiraghi, 2003). For instance, a Schottky barrier height of 1.93 eV and 1.98 eV was calculated for Au/4H-SiC and Ni/4H-SiC contacts, respectively (the metal work functions of Au and Ni are 5.1 eV and 5.15 eV, respectively (Michaelson, 1978)). It is informative to compare this to the same contact metalisations on Si (electron affinity of Si is 4.05 eV (Sze & Ng, 2007)); a Schottky barrier height of 1.05 eV and 1.10 eV was calculated for the Au/Si and Ni/Si contacts, respectively.

High electric field strengths can be applied to SiC detectors because of the material's high breakdown field (eight times that of Si) and high saturation electron drift velocities (almost twice that of Si), resulting to short charge carrier transit times (Owens, 2012a) (Bertuccio et al., 2013). Thus, the incomplete charge collection noise of a SiC X-ray spectrometer (see **Chapter 3**) can be favourably reduced.

A variety of device structures have been reported for high performance 4H-SiC UV photodiodes in the past. The first UV 4H-SiC p^+-i-n^+ photodetectors were reported by Chen et al. (2006), where photocurrent measurements under UV illumination as a function of applied reverse bias

and responsivity measurements were reported in arbitrary units showing a peak responsivity at 275 nm. More recently, electrical characterisation and photoresponsivity measurements on 4H-SiC p^+-i-n^+ photodetectors have been reported by Cai et al. (2014), showing a leakage current density of 99.5 nA/cm^2 at 100 kV/cm internal electric field, and a peak responsivity of 0.15 A/W at 268 nm, both at a temperature of 176.85 °C. 4H-SiC Schottky UV photodiodes of different sizes were reported by Yan et al., (2004), having a leakage current density of 80 pA/cm^2 at 13.5 kV/cm internal electric field, at room temperature and a nearly flat quantum detection efficiency of ≥ 30 % from 240 nm to 320 nm. Hu et al. (2006) reported 4H-SiC Schottky UV photodiodes with a 4.5 nm thick semitransparent Ni film deposited on top of the devices as the Schottky contact. These devices showed a leakage current density of 0.4 pA/cm^2 at 8 kV/cm internal electric field at "room temperature" (no exact temperature was defined), and a peak quantum detection efficiency of 65 % at 276 nm, with the devices in photovoltaic mode. Photoresponsivity measurements on 4H-SiC p-n UV photodiodes at temperatures up to 300 °C were reported by Watanabe et al. (2012). The results showed a temperature independent response at a wavelength which depended on the applied reverse bias.

Work has also been conducted on 4H-SiC Schottky UV detectors employing vertical nickel silicide (Ni_2Si) interdigitated contacts. The vertical interdigit Schottky photodiodes (a vertical Schottky contact is created when the front electrodes are short cut and polarised with respect to the back-side contact), first reported by Sciuto et al. (2006), enabled high UV responsivity, e.g. 0.16 A/W at 256 nm corresponding to a 78 % internal quantum detection efficiency (see **Section 2.3.2**), compared with the same area planar interdigit metal-semiconductor-metal 4H-SiC photodiodes (a planar Schottky contact is created when the polarisation is applied between two front electrodes while the back Ohmic contact is floating), which had a maximum UV responsivity of 0.07 A/W at 310 nm. The vertical interdigit photodiodes had two times higher optically active area due to more efficient depletion of the interdigit structures compared to the planar interdigit photodiodes (Sciuto et al., 2006).

Temperature dependent photoresponsivity measurements of vertical Ni_2Si 4H-SiC Schottky UV photodiodes were subsequently reported by Mazzillo et al. (2009) which showed a strong dependency of the long wavelength (280 nm to 380 nm) UV responsivity on temperature. The increased UV responsivity at the long wavelength range (280 nm to 380 nm) with temperature was attributed to the enhanced optical generation via indirect band transition with increased temperature due to the increased phonon population and minority carrier lifetime as the temperature increased. This temperature dependent optical generation via indirect band transition became negligible at short wavelengths (< 280 nm) where the direct band transition dominated (Mazzillo et al., 2009). The effect of different Ni_2Si interdigitated strip pitch sizes (8 μm, 10 μm,

and 20 μm) on the responsivity of the 4H-SiC Schottky UV photodiodes was investigated by Adamo et al. (2014). It was found that the devices with a pitch size of 10 μm had the highest UV responsivity due to the device's wider space to strip width ratio than the devices with a pitch size of 8 μm, while the devices with a pitch size of 20 μm did not reach fully depletion at the highest investigated reverse bias (-10 V).

The first experimental results with 4H-SiC Schottky X-ray detectors were reported by Bertuccio et al. (2001). Following this, rapid development of prototype single pixel spectroscopic systems using SiC epitaxial layers and ultra-low-noise electronics followed (Bertuccio et al., 2004). To date, the best experimental results (best energy resolution) with single pixel SiC X-ray detectors reported were by Bertuccio et al. (2011); 4H-SiC Schottky diodes with circular Au Schottky contacts of 200 μm diameter were used. The 4H-SiC epitaxial layer had a thickness of 70 μm and an n-type doping concentration of 5×10^{14} cm^{-3}. The devices were coupled to ultra-low-noise preamplifier electronics, and the resultant spectrometer had a *FWHM* at 5.9 keV of 196 eV at 30 °C, which increased to 233 eV at 5.9 keV at 100 °C. Studies on semi-insulating 4H-SiC X-ray detectors have shown poorer energy resolution compared to epitaxial SiC layers, primarily due to higher leakage currents and lower charge collection efficiencies (Bertuccio et al., 2013).

Work has also been conducted to develop SiC Schottky diodes with thin (18 nm) Schottky contacts, with the intention of improving the soft X-ray quantum detection efficiency and as an alternative technology to interdigitated contacts. An energy resolution (*FWHM* at 22 keV) of 1.47 keV at room temperature was been reported for such a device (Lees et al., 2007), with photon counting spectroscopic measurements at temperatures up to 80 °C (2.5 keV *FWHM* at 5.9 keV at 80 °C (Barnett, 2011)), and after proton irradiation (Stevens et al., 2011) also presented.

1.5.2 GaAs photodiode radiation detectors

GaAs has been investigated with a view to its use as a potential material for X-ray detectors at high temperature (≥ 20 °C) and in intense radiation environments, as well as for hard X-ray detection.

One of the favourable attributes of GaAs is that its bandgap energy (1.42 eV at room temperature (Bertuccio & Maiocchi, 2002)) results in less leakage current density (and thus less parallel white noise, see **Section 3.2**) at a given temperature compared to narrower bandgap semiconductors (see Equation 1.1), such as Si, while its relatively low electron-hole pair creation energy (4.184 eV (Bertuccio & Maiocchi, 2002) provides similar charge carrier creation statistics and Fano-limited spectroscopic resolution as Si (see **Section 2.3.2**). Also, the density of GaAs (5.32 g/cm^3, which is more than twice that of Si density = 2.33 g/cm^3 (Owens et al., 2003)) and its effective atomic

number (more than twice that of Si) result in better stopping power and higher quantum detection efficiency per unit thickness compared to Si, especially at high X-ray energies (Owens, 2012a).

Additionally, GaAs has been demonstrated to be radiation resistant. Researchers have demonstrated a high radiation resistance of GaAs detectors to γ-rays (Ly Anh et al., 2006) (Dixit et al., 2015), fast neutrons (Ladzianský et al., 2009), and high energy electrons (Šagátová et al., 2014). GaAs detectors are more radiation-resistant than Si for γ-rays, electrons and for low energy protons and neutrons (Rossi et al., 2006). This is because the radiation induced defects in n-GaAs are point defects or pairs of primary defects, in contrast with impurity related radiation defects in Si (Claeys & Simoen, 2002). Impurity-related radiation defects are formed in GaAs under high flux or high temperature irradiation, most of which anneal at relatively low temperatures. However, it should be noted that GaAs is less radiation resistant than Si for high energy hadrons (Rossi et al., 2006) (Sellin & Vaitkus, 2006).

The best experimental results with GaAs X-ray detectors reported to date are by Owens et al. (2001). Owens et al. (2001) reported a 5 × 5 GaAs diode array structure of 200 μm × 200 μm pixels. The pixel structure included a 40 μm thick ultrapure epitaxial planar layer, forming p^+-i-n^+ structure, Au/Pt/Ti Schottky contacts at the p^+ layer, and guard ring surrounding the pixel array structure. Low dark current densities (<6 nA/cm^2) and an energy resolution (*FWHM*) of 266 eV at 5.9 keV at room temperature were reported with these devices, after coupling them to ultra-low-noise preamplifier electronics. Following this, larger devices (250 μm × 250 μm) with a thicker epilayer (325 μm) and similar structure to the detectors reported by Owes et al. (2001) in a 32 × 32 pixel array have been reported with an energy resolution of 300 eV *FWHM* at 5.9 keV at room temperature (Erd et al., 2002). Mesa detectors with both 40 μm and 400 μm thick epilayers have also been fabricated with similar structures as was used by Owens et al. (2001) and Erd et al. (2002), and results for the mesa detectors with 40 μm thick epilayers at room and low temperatures were reported by Owens et al. (2003). These devices showed typical leakage current densities of < 4nA/cm^2 but a poorer energy resolution at room temperature (572 eV at 5.9 keV) compared to the earlier pixel detectors. Despite considerable international effort, energy resolutions as good as those reported by Owens et al. (2001) have never been replicated.

Research has also been conducted on GaAs p^+-i-n^+ mesa X-ray photodiodes. GaAs p^+-i-n^+ photodiodes with a 2 μm thick i-layer were coupled to low-noise preamplifier electronics. The resulting spectrometer had an energy resolution (*FWHM*) at 5.9 keV of 800 eV at room temperature, rising to 1.5 keV at 80 °C (Barnett et al., 2011). Subsequent studies on thicker (3 μm) GaAs p^+-i-n^+ mesa photodiodes performed by Barnett (2014) showed the X-ray detection characteristics of the devices over the energy range 4.95 keV to 59.5 keV, at 33.3 °C. A

fabrication study of GaAs mesa photodiodes regarding the effects of the wet chemical etchants and etch depths on the dark currents has also been reported (Ng et al., 2014).

1.6 Contribution of this work

In this thesis, wide bandgap semiconductor photodiodes have been examined for their suitability as radiation detectors for harsh environment applications. More specifically, three families of photodiodes have been investigated: 4H-SiC Schottky UV photodiode detectors with Ni_2Si interdigitated contacts; 4H-SiC Schottky photodiode detector arrays with planar NiSi contacts for X-ray spectroscopy; and GaAs p^+-i-n^+ mesa photodiode detectors for X-ray spectroscopy. The latter were also investigated for visible and infrared light detection as well as β^- particle (electron) spectroscopy. The work presented compares the performance of randomly selected diodes of each family. The results are related back to the material and geometry of the detectors, and to the environment under which the detectors were investigated, as well as to previously published work. This systematic study complements existing knowledge and advances the understanding of such devices with a view to their future use in space science instrumentation. The X-ray and electron spectroscopic measurements are supported by a comprehensive treatment of the noise components in charge sensitive preamplifiers for spectroscopy, and the first calculations showing the potential benefits of using a SiC, rather than Si, JFET as the input transistor of such a preamplifier, are presented.

1.7 Thesis organization

A review of relevant detector physics is presented in **Chapter 2**. The different radiation production processes are discussed with a focus on those used in this thesis. The relevant radiation interactions with matter are described, as are the main components of a semiconductor spectrometer of the type considered in this thesis. The two types of semiconductor photodiode detectors used in the thesis (the Schottky diode and the p^+-i-n^+ diode) are also reviewed in detail, and the experimental techniques used for the measurements presented in the thesis are described. **Chapter 3** describes the different noise components in semiconductor X-ray and electron spectrometers, with a focus on the contribution of both the charge sensitive preamplifier's input JFET, and the detector itself.

Chapter 4 presents and discusses results characterising 4H-SiC interdigitated Schottky photodiodes as room temperature UV detectors. **Chapter 5** reports and discusses high temperature electrical characterisation and X-ray detection measurements at 33 °C of 4H-SiC planar-contact Schottky diode arrays. **Chapter 6** describes and discusses measurements and analysis characterising the performance of two GaAs X-ray mesa p^+-i-n^+ photodiodes with i layer thicknesses of 7 μm at room temperature. The same photodiodes were then electrically

characterised over the temperature range 0 °C to 120 °C, and one of the diodes was characterised as a photon counting spectroscopic X-ray detector over the temperature range 0 °C to 60 °C. For **Chapter 7**, 22 GaAs X-ray mesa p^+-i-n^+ photodiodes having i layer thicknesses of 10 μm at room temperature, and diameters of 200 μm and 400 μm, were electrically characterised. The mean value and rms deviance among all 22 devices for the measured and calculated parameters are reported and results are shown for a representative device of each diameter. Two of the diodes (one device of each diameter) are then further characterised as detectors for X-ray spectroscopy. One of the diodes was also characterised as a detector for β^- particle (electron) spectroscopy at room temperature. Furthermore, this chapter reports multi-energy (4.95 keV to 21.17 keV) X-ray calibration of one of the 10 μm i layer GaAs X-ray mesa p^+-i-n^+ photodiodes, along with results characterising its suitability for XRF spectroscopy for elemental analysis of deep seabed minerals. An inventory of the photodiodes reported in the experimental part of the thesis (**Chapter 4** to **Chapter 7**) can be seen in **Table 1.1**.

Chapter 8 provides a summary of the key findings of the work reported in the thesis and draws conclusions. Possible future research is also discussed.

Material	Type of photodiode	Active layer thickness	Dimensions	Naming	Chapter
4H-SiC	Schottky	6 μm	1.2 × 1.2 mm^2	D1	4
4H-SiC	Schottky	6 μm	1.2 × 1.2 mm^2	D2	4
4H-SiC	Schottky	6 μm	1.2 × 1.2 mm^2	D3	4
4H-SiC	Schottky	6 μm	1.2 × 1.2 mm^2	D4	4
4H-SiC	Schottky	20 μm	250 × 250 μm^2	D1	5
4H-SiC	Schottky	20 μm	250 × 250 μm^2	D2	5
4H-SiC	Schottky	20 μm	250 × 250 μm^2	D3	5
4H-SiC	Schottky	20 μm	250 × 250 μm^2	D4	5
4H-SiC	Schottky	20 μm	250 × 250 μm^2	D5	5
GaAs	p^+-i-n^+	7 μm	200 μm diam.	D1	6
GaAs	p^+-i-n^+	7 μm	200 μm diam.	D2	6
GaAs	p^+-i-n^+	10 μm	200 μm diam.	D1	7
GaAs	p^+-i-n^+	10 μm	400 μm diam.	D2	7

Table 1.1. Summary of the photodiode detectors used in the present work. For **Chapter 7**, a total of 22 devices were characterised but only the representative devices identified in the chapter are included in the table.

Chapter 2 Detector Physics Background

2.1 Radiation production

This thesis concentrates on the detection of fast electrons (β^- particles emitted in nuclear decay and high energy electrons) and on the electromagnetic radiation range from infrared (~ 1 eV) to X-rays (35 keV). An introduction to the production of fast electrons, infrared, visible and UV light, and X-rays is given in this section.

2.1.1 Fast electrons

Anthropogenic laboratory fast electron sources include radioisotope sources and electron guns producing energetic electrons (Ahmed, 2007). In this thesis, a ^{63}Ni radioisotope β^- particle source was used to produce a continuous spectrum of β^- particles with energies up to 66 keV (the ^{63}Ni endpoint energy).

Two types of radioisotope decay can produce fast electrons: β^- decay and internal conversion. The former occurs when a radioisotope with a neutron rich nucleus decays with the transformation of a neutron into proton, with the emission of a β^- particle and an antineutrino (Leo, 1994). Because the available energy for the β^- decay is shared between the emitted particles (β^- particle and antineutrino) the energy of β^- particle varies from decay to decay resulting in a continuous energy spectrum ranging up to the nuclide-specific endpoint energy (Knoll, 2010). In contrast with many β^- emitting radioisotopes which decay to an excited state of the nucleus, and then subsequently further decay with, for example, emission of γ-rays, ^{63}Ni (and others such as ^{3}H, ^{14}C, ^{99}Tc) decay directly to the ground state of the product (Leo, 1994) (Knoll, 2010).

In internal conversion radioisotope decay, the nuclear excitation energy is transferred to an atomic electron which is then ejected with a kinetic energy equal to the difference of the excitation energy and the bonding energy of the electron (Knoll, 2010). Although internal conversion is a source of monoenergetic electrons (Leo, 1994), the conversion electron spectrum of a single radioisotope source, including ^{109}Cd, ^{113}Sn, ^{137}Cs, and others, can contain several groups of electrons' energies because the nuclear excitation energy can be transferred to any electron shell within the atom.

Intense beams of energetic electrons can also be produced using electron guns. Their principle of operation relies on a stimulated process, such as heating in thermionic electron guns (Goldstein et al., 2003), application of high electric fields of the order of 10^9 V/m in field emission electron guns (Molokovsky & Sushkov, 2005), and photon illumination in photo-emission electron guns (Sinclair, 2003), to provide enough kinetic energy to liberate atomic electrons.

Naturally occurring radioisotope β^- emitters include the intermediate radionuclides of the decay chains of the three most abundant naturally occurring unstable isotopes: ^{238}U, ^{235}U, and ^{232}Th (Lottermoser, 2005). Th occurs together with U in some uranium ore deposits, including volcanic uranium deposits, Vein-type uranium deposits, and metasomatite deposits (Dahlkamp, 1993). Since U and Th isotopes have half-lives comparable to the age of Earth, they are still present in such minerals. ^{238}U, ^{235}U, and ^{232}Th decay to intermediate nuclides via β^- (and α) decay with the final, stable, non-radioactive daughter nuclides being ^{206}Pb, ^{207}Pb, and ^{208}Pb, respectively.

Cosmic-rays are also a natural source of electrons. Although there is limited knowledge of cosmic-ray production mechanisms, it has been determined that 1 % of cosmic-rays observed during space based cosmic-ray experiments consist of electrons (Berdugo, 2016). Electrons in the energy range of 1 GeV to 625 GeV have been measured and a small number of sources in the Solar neighbourhood, exotic sources such as dark matter particles, and astrophysical objects such as pulsars, have all proposed as potentially significant sources of cosmic-ray electrons (Adriani et al., 2011).

2.1.2 Infrared, visible and UV light

Numerous anthropogenic light sources covering the range of infrared, visible, and UV light have been produced and are still being developed for multiple applications. Such light sources include incandescent light sources, electrical gas discharge light sources, light-emitting diodes (LEDs), and light amplification by stimulated emission of radiation (lasers) (Kitsinelis, 2015). In this thesis, a spectrophotometer employing a W-halogen incandescent lamp and a ^2H gas discharge lamp is used to cover the wavelength range of interest, i.e. 200 nm to 980 nm.

Incandescent light sources use a filament which radiates as it is being heated, at an energy depending on the filament's temperature, from infrared to visible emission as the temperature increases (Kitsinelis, 2015). Commonly, incandescent lamps use W filaments due to the element's high melting point (3387 °C) which allows operation at relatively high temperatures (2527 °C for a typical incandescent lamp). Such lamps emit a continuous spectrum. The W-halogen incandescent lamp employs a halogen gas in addition to the tungsten filament, and has an increased average lifetime, operation at higher temperatures, and thus radiation up to near-UV, compared to W incandescent lamps.

The basic principle of electrical gas discharge lamp is the excitation of valence electrons from collisions with other electrons followed by de-excitation and the emission of electromagnetic radiation (Kitsinelis, 2015). Hg vapour is the most commonly used active medium in gas

discharge lamps due to its low ionisation potential and high vapour pressure. The most intense Hg emission line is 254 nm (i.e. within the UV band), and depending on the requirements of the application, and whether UV emission is required or not, a phosphor can be used to convert the UV light into visible light, thus producing a so called fluorescent lamp. The noble gases, He, Ne, Ar, Kr, and Xe, (the radioactive Rn is not a practical option), can also be used instead of Hg. Discharge lamps using these elements emit in the visible and UV bands of the electromagnetic spectrum. For applications which require lamps with high outputs' fluences at short UV wavelengths, ^{2}H gas discharge lamps are commonly used (McCluney, 2014).

Discussion of the production of infrared, visible, and UV light by LEDs and lasers is out of the scope of this thesis. Instead, the reader is referred to Ahmed (2007) and Kitsinelis (2015) for an extensive discussion on the different types, operation, and applications of LEDs and lasers.

Solar radiation is the main natural source of infrared, visible, and UV light on Earth. Although the Sun's emission spectrum covers the whole of the infrared region, visible region and UV region, Earth's atmospheric gases absorb Solar radiation in particular wavelength bands and fully absorb UV light of < 300 nm (Fu, 2003).

2.1.3 X-rays

There are a variety of anthropogenic and natural X-ray sources which produce continuous X-ray radiation (i.e. emission of all wavelengths within a range, rather than discrete energies), X-rays of characteristic energy, or both, depending on their principle of operation. In this thesis, an ^{55}Fe radioisotope X-ray source was used to produce characteristic Mn Kα (5.9 keV) and Mn Kβ (6.49 keV) lines (Schötzig, 2000). A Mo target X-ray tube was also used to produce a continuous spectrum of X-rays of energy ≤ 35 keV, with additional characteristic Mo Kα (17.4 keV) and Mo Kβ (19.6 keV) X-ray emission lines from the Mo target (Thompson et al., 2009). For some measurements, high purity metal foil samples of known composition, and geological samples of previously unknown composition, were subsequently fluoresced by the Mo target X-ray tube.

Emission of continuous X-rays occurs when electrons, or other energetic charged particles such as protons or α particles, lose energy in passing through the Coulomb field of a nucleus (Van Grieken & Markowicz, 2002). This type of radiation, in the form of bremsstrahlung radiation with a continuous energy spectrum (i.e. no quantised energy transitions), can be explained by classical electromagnetic theory: the de-acceleration of the high energy electrons in the target material is correspondingly accompanied by the emission of radiation (Ahmed, 2007). The emitted radiation (X-ray photon) energy extends as high as the initial electron energy (Knoll, 2010). The operation of conventional X-ray tubes relies on the process of bremsstrahlung

radiation production; their cathode material is used to de-accelerate electrons emitted from the tube's anode, where the X-ray emission intensity is determined by the current of the X-ray tube, and the maximum energy of the X-ray emission is determined by the tube's potential difference.

The process by which the electrons of an X-ray tube cause the production of the characteristic X-ray emission lines of the cathode is also deserving of further comment. Characteristic X-rays may be generated when a source of radiation of sufficient energy (e.g. an electron beam or X-rays) is incident upon a target. Incident radiation when absorbed by a target atom causes the excitement (and potentially, ejection) of an atomic electron from its shell within the atom. The vacancy of the ionised atom is subsequently filled through the rearrangement of the electrons of other shells of the atom, in order to improve atomic stability. The transition from the excited to the ground state results in the emission of energy from the atom in the form of an X-ray fluorescence photon of characteristic energy (Knoll, 2010). The energy of the characteristic X-rays equals the difference between the corresponding atomic energy levels involved in the process, and hence the target material becomes a source of characteristic X-rays itself. For example, when an L shell electron fills a vacancy in the K shell, a Kα characteristic photon is emitted. Similarly, when the K shell vacancy is filled by an electron from the M shell, a Kβ characteristic photon is emitted (Van Grieken & Markowicz, 2002). When the atom in question contains sufficient electrons, vacancies in the L and M shells may also be filled from electrons from higher energy levels. Because the allowed energy levels in an atom are unique to each individual element, and hence their characteristic X-rays are also correspondingly unique, this phenomenon may be used as a technique for elemental analysis samples; this is termed X-ray fluorescence spectroscopy. When the generated electrons in X-ray tubes are of sufficient energy to cause the rearrangement of the electron shells of the atoms of the cathode, or other materials in the X-ray tube in this manner, the resulting X-ray tube spectrum has characteristic X-ray emission lines superimposed on the continuous bremsstrahlung spectrum (Knoll, 2010).

Whilst not an X-ray source used in this thesis, synchrotron X-ray radiation is continuous and, in contrast with bremsstrahlung X-rays, extremely intense, highly collimated, and polarised. X-rays are produced when charged particles, such as energetic electrons, are accelerated at relativistic velocities using magnetic fields in circular orbits (Ahmed, 2007). These emissions can also be explained by classical electromagnetic theory: a small fraction of the beam of energetic charged particles bent into a circular orbit is radiated away during each cycle of the beam (Knoll, 2010).

Radioisotope X-ray emitters are also important sources of X-rays. Such sources emit X-rays as a consequence of radioactive decay, through electron capture and internal conversion (Knoll, 2010). In electron capture, an electron from one of the atomic orbitals (most likely from the K shell)

captured by the nucleus of a proton-rich atom causes an atomic shell vacancy which may be filled by another atomic electron from higher energy levels, giving rise to the emission of a characteristic X-ray (Leo, 1994). The product nucleus of the electron capture nuclear decay can either be in the ground state or in an excited state (de-excitation may involve emission of γ-rays). Internal conversion, as defined earlier (see **Section 2.1.1**), results in a vacancy being left in one of the atom's inner shells, with the electron in the K shell being more probably converted (Knoll, 2010). Rearrangement of atomic electrons to achieve atomic stability can result in the emission of characteristic lines. Along with the de-excitation of the nuclear state with internal conversion, γ-ray emission is always a competing process (Magill & Galy, 2005). When a pure X-ray source is needed, a radioactive material decaying by electron capture to the ground state of the product nucleus is required, one such material is ^{55}Fe which decays with characteristic X-ray emissions of Mn Kα (5.9 keV) and Mn Kβ (6.49 keV) photons (Schötzig, 2000).

It should be noted that there is an alternative, competing process that may occur following the transition from the excited to the ground state of the atom, through the rearrangement of the electrons, instead of the emission of characteristic X-rays. The excess energy from the rearrangement of the electrons to fill the vacancy of the ionised atom can be given to one of the atom's electrons, with a binding energy less than the available energy, which is ejected from the atom. Such electrons are called Auger electrons (Van Grieken & Markowicz, 2002). As a result, fewer X-ray photons are produced for a given quantity of material than would otherwise be expected. The fluorescence yield is the probability that a vacancy in an atomic shell is filled with a subsequent radiative emission (characteristic X-rays), rather than ejection of an Auger electron. As an example, the fluorescence yield of the K shell is given by the ratio of total number of characteristic X-rays emitted to the total number of primary K shell vacancies.

X-rays can originate also from natural sources, such as astronomical sources. Most X-rays from astronomical sources cannot penetrate the Earth's atmosphere and thus they are impossible to be detected from ground-based observatories (Seward & Charles, 2010). The dominant astrophysical mechanisms for generating X-rays are thermal, synchrotron, and blackbody radiation (Seward & Charles, 2010). The thermal radiation emission, which occurs from the acceleration of thermally energetic electrons due to collisions with positive ions in a hot gas, is a continuum and its shape is only determined by the temperature of the hot gas. The synchrotron radiation occurs from relativistic electrons traveling through a magnetic field whose direction changes resulting in acceleration and emission of electromagnetic radiation. The blackbody radiation, originating from stars, neutron stars, and pulsars, is a continuum with peak emission at an energy which only depends on the temperature of the emitting object. Cosmic X-rays are also

generated when planets, moons and comets are bombarded with cosmic X-rays with subsequent emission of characteristic fluorescent X-rays.

The strongest X-ray source in the Solar system is the Sun and more specifically its corona, which emits thermal X-rays (Seward & Charles, 2010). X-rays have also been detected from Earth, Jupiter, Saturn, Venus, and Mars, as well as from Earth's and Jupiter's moons, and asteroids and comets. The principle production mechanisms of such X-rays are scattering of and fluorescence by Solar X-rays, synchrotron radiation due to the presence of a magnetosphere (Earth and Jupiter), and energetic Solar-wind particle collisions with material. Beyond the Solar system, the hot material of the interstellar medium is a source of diffuse emission of soft X-rays and interstellar dust is source of scattered cosmic X-rays. Similarly to Sun, all stars, apart from some red giants (these cooler than class K1) and two types of dwarfs (these in the mid-A range where there is no convection and these cooler than type M5), are X-ray sources. Other astrophysical X-ray sources include supernovae, supernova remnants, neutron stars with high rates of rotational energy loss, and dwarf novae. The variety of astrophysical X-ray sources is extensive and a more detailed discussion is out of the scope of this thesis; the reader is referred to Seward & Charles (2010).

2.2 Radiation (photons and charged particles) interaction with matter

In this section, a comprehensive analysis of the different processes taking place when radiation interacts with solids is presented. The discussion focuses on the dominant mechanisms of interest in this thesis for electrons, and photons in the infrared, visible, UV, and X-ray regions.

2.2.1 Electrons

Electrons, as charged particles, are subject to Coulomb and nuclear interactions (Ahmed, 2007). They do not lose their energy in a single event; instead they lose energy along their path through matter. Their paths (sometimes called their tracks or trajectories) are subject to large deviations because their individual masses are equal to the masses of the orbital electrons with which they interact (Knoll, 2010) (Nikjoo et al., 2012). As a result, the total path length for an electron is much greater than the distance of penetration along the initial velocity unit vector. Depending on their energy, electrons can undergo ionisation, elastic scattering or emission of bremsstrahlung when interacting with matter.

Moving electrons interact with atomic electrons through electromagnetic force and may transfer energy to these electrons (Nikjoo et al., 2012). An orbital electron can be ejected when the transferred energy is sufficient, thus resulting in ionisation of the atom; alternatively, an orbital electron can be moved to an excited state. If the ejected electron carries enough energy it can produce secondary ionisations. This process can continue until the energy of the ejected electron

is less than that required for ionisation (Ahmed, 2007). **Figure 2.1** shows this process. The probability in which an electron can cause ionisation largely depends on its energy and the type of target atom.

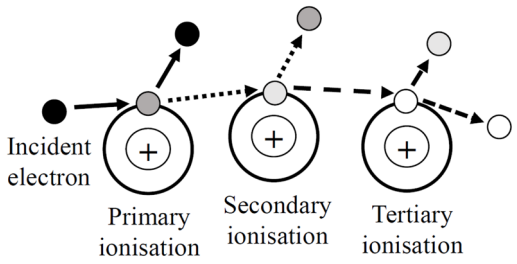

Figure 2.1. Cascade ionisation process initiated from an incident electron of a sufficient energy to eject an atomic electron. Ionisation is one mode of electrons interaction with matter.

Scattering may also be significant when incident electrons interact with a material. The elastic scattering of an electron from another electron as a consequence of Coulomb repulsion is known as Moeller scattering whereas the elastic scattering of an electron from a positron resulting from Coulomb attraction is called Bhabha scattering (Nikjoo et al., 2012).

Incident electrons are also subject to scattering upon interaction with the nucleus. The deviation of their path by the electrical attractions of the nucleus results in their deceleration which gives rise to bremsstrahlung emission (no direct electronic or nuclear transitions involved) as explained by classical electromagnetic theory (Leo, 1994). Radiative energy loses in the form of bremsstrahlung radiation becomes more significant compared to collisional energy losses, for high energy electrons (Nikjoo et al., 2012). The cross section of energy loss by bremsstrahlung also depends on the atomic number of the material, Z; the number of atomic electrons surrounding the nucleus plays an important role in determining the strength of the electric field with which the incident electrons interact, and therefore on the probability of radiative energy loss. The intensity of bremsstrahlung emitted radiation depends on the atomic number of the material squared, Z^2 (Leroy & Rancoita, 2009).

2.2.2 Photons

Photons behave differently when traversing an absorber compared to electrons due to their charge neutrality (Nikjoo et al., 2012). The number of photons of any beam of monochromatic photons reduces exponentially when traveling in matter (Leroy & Rancoita, 2009). Mechanisms by which photons may lose (deposit) energy include photoelectric absorption, Compton scattering and pair production, whereas Thomson and Rayleigh scattering do not involve energy deposition.

2.2.2.1 Photoelectric absorption

The photoelectric absorption is the predominant mode of interaction of photons of relatively low energy and the dominant mechanism of interest in this thesis. In this process, the photon's energy is required to be at least equal to the binding energy of the most loosely bound electron in the atom. The photon's energy is transferred to an orbital electron, and the photon ceases to exist (Sherer et al., 2014). The electron is then ejected. This electron, called photoelectron, has an energy equal to the incident photon energy less its binding energy.

The K shell, which can contain the two most tightly bound electrons to the nucleus, is the most probable origin of the photoelectron for photons of sufficient energy (Knoll, 2010). Immediately after the ejection of an inner shell electron, a vacancy is left in that shell of the atom. This represents an unstable energy situation. Consequently, the electrons of the atom are rearranged, with an electron from a higher atomic energy level filling the vacancy (Lowe & Sareen, 2014). The energy difference between these two atomic levels may be carried away by either emission of a characteristic X-ray photon (fluorescence), or the ejection of another orbital electron (Auger electron) provided its energy is equal to the binding energy of the electron. This process is summarised in **Figure 2.2**.

The emitted X-ray photon can be absorbed by a secondary photoelectric interaction involving less tightly bound electrons from another atom. The overall effect, which is the fundamental for photon detection with semiconductor detectors (see **Section 2.3**), is a cascade production of X-rays, Auger electrons, and photoelectrons. These resulting electrons (and holes) may cause further excitations and ionisations leaving secondary electrons (and holes) along their path until none of them have sufficient energy to produce any more (Lowe & Sareen, 2014). When the production of electrons and holes from the absorption of a photon finishes, electrons transition to the bottom of the conduction band and holes transition to the top of the valence band.

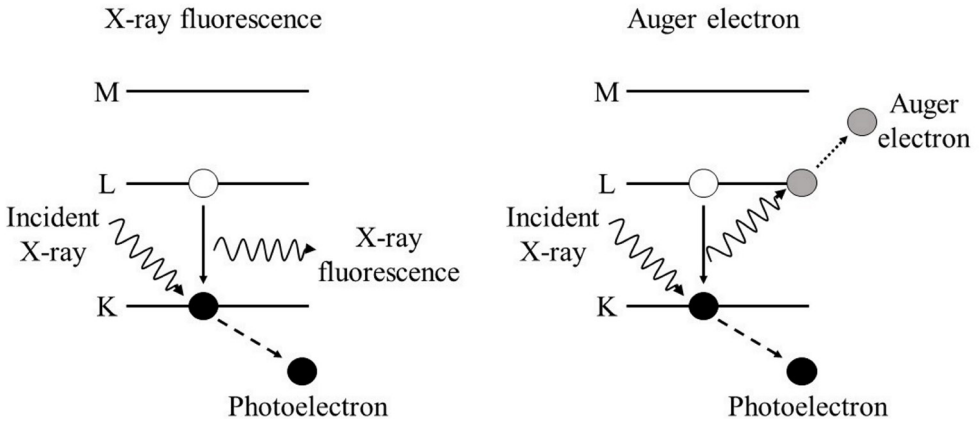

Figure 2.2. Emission of photoelectron as a result of photoelectric absorption followed by an emission of a characteristic X-ray or an Auger electron, during the rearrangement of the electrons involving different atomic energy levels (such as K, L or M shell) to achieve stability. Photoelectric absorption is one mode of photon interaction with matter.

2.2.2.2 Compton scattering

Compton scattering takes place between an incoming photon and an electron in the absorbing material assumed to be initially at rest. The photon transfers part of its energy to the electron. As a result of such a collision, the energy and momentum of the photon decreases and the electron is ejected at a forward angle (Nikjoo et al., 2012). The energy of the recoil electron can vary from zero to a large fraction of the photon energy. Since this process involves a change in photon energy it is an inelastic scattering process. The cross section of Compton scattering depends on the energy of the incoming photon and the atomic number of the absorbing material (Leroy & Rancoita, 2009).

2.2.2.3 Pair production

In pair production, the incoming photon disappears and is replaced by an electron-positron pair (Knoll, 2010). This interaction takes place in the Coulomb field of a nucleus and is energetically possible only when the photon has at least the required energy (=1.02 MeV) to create an electron-positron pair. The recoil energy of the heavy nucleus is negligible and thus any excess energy carried by the photon is transferred into kinetic energy and shared by the pair.

2.2.2.4 Rayleigh and Thomson scattering

Thomson scattering is a process between an incoming photon of low energy and a free electron (Ahmed, 2007). The free electron oscillates in response to the electric vector of the electromagnetic wave (photon) and emits radiation of the same frequency as the incident wave. The result of such collisions is a change in the angle of deflection with no energy loss being

involved (elastic scattering) (Nikjoo et al., 2012). Rayleigh scattering is a process of elastic scattering between an incoming photon and an atom. When the radius of the target atom is much smaller than the wavelength of incident photon, there is minimal coupling between the incident photon and the internal structure of the target atom. Thus, there is extremely small energy transfer during Rayleigh scattering (the scattered photon has almost the same energy as the incident photon).

2.2.2.5 Passage of photons through matter

The attenuation of a photon beam is given by the Beer-Lambert law

$$I_x = I_0 \exp(-\mu x) \tag{2.1}$$

where I_x is the beam intensity at a depth x, I_0 is the beam intensity just before it enters the material and μ is the linear attenuation coefficient of the target material (Lowe & Sareen, 2014). The linear attenuation coefficient, μ, is the probability per unit length that a photon is removed from the beam and depends on both the photon energy of interest and on the density, ρ, of the absorber (Knoll, 2010). Instead, the mass attenuation coefficient, μ_ρ, can be used

$$\mu = \mu_\rho \rho. \tag{2.2}$$

The mass attenuation coefficient increases with increased atomic number and for comparison, the linear attenuation coefficient of three semiconductor materials, GaAs, 4H-SiC, and Si, extracted from Henke et al. (1993), as a function of photon energy can be seen in **Figure 2.3**. The inverse of the linear attenuation coefficient ($1/\mu$) is called the mean free path and is defined as the average distance required for an interaction in the absorber to take place. As an example, the mean free path of a 20 keV X-ray photon beam is 105 mm in Si and 4 mm in GaAs.

Broadly, the linear attenuation coefficient decreases with increased energy for the same material. However, there are abrupt jumps in linear attenuation coefficient at certain energies. These discontinuities, the absorption edges, occur at energies equal to the binding energies of the atom (Ahmed, 2007). At that energies, the absorption of the photon increases resulting in a linear attenuation coefficient jump to a higher value than it is for an energy slightly less than the absorption edges.

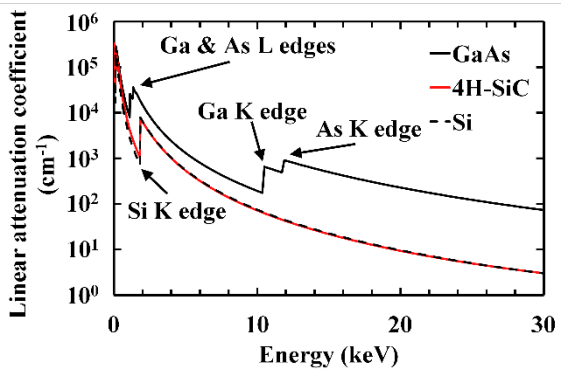

Figure 2.3. Linear attenuation coefficient (extracted from Henke et al. (1993)) as a function of photon energy for GaAs (black line), 4H-SiC (red line) and Si (dashed black line). The corresponding absorption edges are also shown.

2.3 Semiconductor radiation detection system

2.3.1 The overall semiconductor radiation detection system

The block diagram of a spectroscopic system employing a semiconductor detector can be seen in **Figure 2.4**. The incident radiation, here X-ray photons or β^- particles, interact with the semiconductor detector which converts the energy deposited by each radiation quantum to an electrical signal charge, Q (see **Section 2.3.2** for charge generation by radiation in semiconductors) (Spieler, 2005). This burst of charge, Q, is ideally proportional to the energy deposited. As an example, the signal charge created by a single 5.9 keV X-ray photon in a GaAs detector is 2.25×10^{-16} C on average, with this being subject to statistical fluctuations, as well as electronic noise (see **Chapter 3**). The next component in the signal processing chain is the charge-sensitive preamplifier. The function of the charge sensitive preamplifier is not to amplify the signal but to serve as an interface between the detector and the subsequent processing electronics and to produce a voltage step proportional to Q by integrating the current pulses. The function of the charge sensitive preamplifier is described in **Section 2.3.3**.

The charge sensitive preamplifier's output is a tail pulse, with a rapid rise and slow return to baseline (Knoll, 2010), which is not suitable for direct measurement of peak height (Gilmore, 2008). The preamplifier's output is delivered to a shaping amplifier, whose primary function is to change the pulse shape to achieve peak height measurements and improve the signal-to-noise ratio. A signal-to-noise ratio improvement can be achieved by tailoring the frequency response to attenuate the noise and strengthen the signal since the signal power of the pulses is distributed in both time and frequency domain and the frequency spectra between the signal and the noise differ (Spieler, 2005). However, improving the signal-to-noise ratio results in an increase of the pulse duration (reduced bandwidth) thus imposing limitations on the count rate and thus care should be taken to find a balance between these conflicting requirements. Shaping amplifiers

may also provide other functions apart from pulse shaping, such as pole-zero cancellation, baseline restoration, and pile-up rejection (Gilmore, 2008).

The multi-channel analyser (MCA) (**Figure 2.4**) converts the pulse amplitude, which is an analogue signal, to an equivalent digital number, bins the pulses based on their height, and counts the number of pulses within individual pulse height intervals (bins or channels) (Gilmore, 2008). The result is a record of the amplitude distribution of pulses (a spectrum) as accumulated by the instrumentation. Information regarding the incident radiation may then be deduced from the positions, shapes, and areas of peaks and other features present in the recorded spectrum.

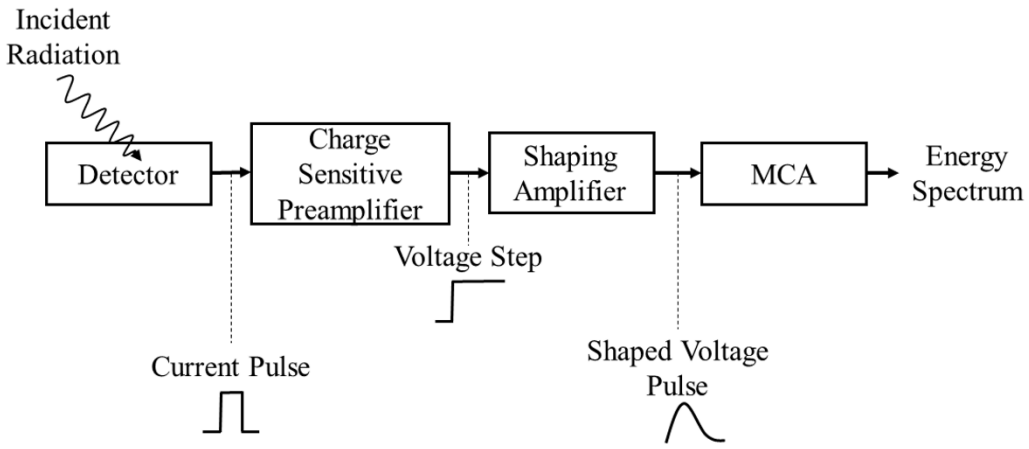

Figure 2.4. Schematic diagram of a semiconductor spectroscopic system.

2.3.2 Charge generation by radiation in semiconductor photodiodes

The mechanisms of interest in this thesis are the ionisation process resultant from β^- particles interacting with the semiconductor material and the photoelectric effect when X-ray photons are absorbed in the semiconductor material. Both processes result in the generation of a number of electron-hole pairs proportional to the energy of the interacting radiation quanta.

The electric field present in the depletion region (commonly assumed to be the active region, unless otherwise specified) of a reverse biased semiconductor photodiode sweeps out the generated electrons and holes in opposite directions, towards their respective electrode (Lowe & Sareen, 2014). The movement of these generated charges induces charge on the contacts of the semiconductor photodiode and produces the signal, which is fully developed once the last of the carriers arrives at its collecting electrode (Knoll, 2010). The induced charge on electrodes can be calculated by the Shockley-Ramo theorem (Shockley, 1938) (Ramo, 1939).

The charge generated in the semiconductor photodiode by a given radiation quantum, the amplitude of the detector pulse formed by the charge induced on its electrodes, the tail pulse output of the preamplifier, and the amplitude of the shaping amplifier's output would be expected to be all proportional to the energy of the incident radiation and constant from one event to the next. However, the pulse at each point of the detection and processing chain (discussed in **Section 2.3.1**) is subject to statistical variations. As such, the accumulated energy spectrum of a monoenergetic radiation beam becomes a distribution of pulse heights, rather than an energy spectrum with all counts confined to a single channel.

The ability of a spectroscopic system to distinguish between quanta of different energies is termed energy resolution. For a Gaussian peak, it is commonly quantified by measurement of the full width at half maximum (*FWHM*) of that peak. The potential sources of fluctuation (noise) in the response of a spectroscopic system resulting in the broadening of the *FWHM* and not related to the charge generation statistics in the semiconductor photodiode, are discussed in **Chapter 3**. The fluctuation of the charge generation in the photodiode is described in the next paragraphs.

Not all of the energy of the incident radiation goes into production of electrons and holes, but a proportion may stimulate optic lattice vibration (dissipated as direct heat) (Lifshin, 1999) (Lowe & Sareen, 2014). This has two effects. First, the number of electron-hole pairs generated, n, is less than the ratio of the incident radiation quantum energy, E_{rad}, to the bandgap of the material, E_G. Instead, the number of electron-hole pairs generated, N, is

$$N = \frac{E_{rad}}{\omega}, \tag{2.3}$$

where ω is the average energy consumed in the generation of an electron-hole pair (commonly called the electron-hole pair creation energy). The electron-hole pair creation energy depends on the semiconductor material (increases with increased bandgap) and the temperature. **Table 2.1** shows the electron-hole pair creation energy of Si, GaAs, and 4H-SiC.

The second effect is that the number of mobile charge carriers generated is not always the same for a given radiation quantum energy but is subject to statistical fluctuations, as suggested by Equation 2.3 describing the average rather than absolute number of electron-hole pairs created. The standard deviation, σ, characterising the statistical fluctuations of the total number of the generated charge carriers (= N) would be $\sqrt{N}$ for a Poissonian process (Knoll, 2010). However, the events in the ionisation process are not independent of each other, and thus the process is not Poissonian. As a result, the observed statistical variance (σ^2) is less than the Poisson predicted

variance, with the Fano factor, F, quantifying the extent to which the distribution is tightened, such that

$$F = \frac{observed\ variance}{Poisson\ predicted\ variance} = \frac{observed\ variance}{N} . \quad (2.4)$$

The Fano factor lies between 0, for no fluctuations, and 1, for Poissonian process. **Table 2.1** gives the Fano factor of Si, GaAs and 4H-SiC. The standard deviation, σ, of the distribution of the electron-hole pairs generated takes the form $\sqrt{FN}$. The equivalent energy broadening due to the statistical fluctuations of the total number of electron-hole pairs generated, called the Fano noise, gives the fundamental resolution limit for a semiconductor spectroscopic system (Lowe & Sareen, 2014). For a Gaussian distribution, the Fano noise in terms of *FWHM*, ΔE, is related to the electron-hole pairs creation energy, ω, the Fano factor, F, and the energy of the incident radiation, E_{rad}, such that

$$\Delta E\ [\text{eV}] = 2.355\omega\sqrt{FE_{rad}/\omega} . \quad (2.5)$$

It is clear, from Equation 2.5, that semiconductor materials with low electron-hole pair creation energy and Fano factor are favourable because of their high fundamental statistical resolution (low ΔE).

Unlike β^- particles, X-ray photons are absorbed in a single collision and therefore, might be absorbed in a dead layer, and not detected at all. When a photon of a monoenergetic beam is absorbed in the depletion layer of the detector, an event will contribute to the photopeak, at an energy equal to the energy of the incoming beam. However, this is true only when both the ejected photoelectron and emitted characteristic fluorescence X-ray of the semiconductor detector, as a result of the photoelectric effect, are absorbed in the active layer of the detector.

When either the photoelectron or the fluorescence X-ray photon is not absorbed in the active layer of the detector, the result is an event added to the fluorescence or the escape peaks, respectively, in the obtained energy spectrum. For relatively high energy incoming photons, the ejected photoelectron might have enough energy to leave the active volume of the detector and be absorbed elsewhere. In this situation, only the energy of the emitted characteristic X-ray photon is absorbed, and an event is added at an energy equal to the characteristic X-ray energies of the semiconductor material in the spectrum, forming the fluorescence peaks. There is also the possibility that the photoelectron is fully absorbed in the active layer of the detector but the fluorescence X-ray photon escapes and does not contribute to the absorbed energy. This is

unavoidable mostly near the sides of the detector as well as the front and the rear surfaces of the detector (Lowe & Sareen, 2014). In this situation, an event is added at an energy equal to the energy of the incoming photon reduced by the energy of the lost fluorescence X-ray photon, forming the escape peaks.

Parameter	Si	GaAs	4H-SiC
Density (g/cm^3)	2.3	5.4	3.12
Mean atomic number	14	31.3	10
Bandgap (eV)	1.12	1.42	3.27
Electron-hole pair creation energy (eV)	3.65	4.184	7.8
Fano factor	0.11	0.12	0.1

Table 2.1. Values of key parameters of Si, GaAs and 4H-SiC at room temperature.

The parameters of the semiconductor material (i.e. its electron-hole pair creation energy and Fano factor) of the photodiode not only affect the fundamental statistical resolution of the detector (Equation 2.5), but also determine the number of photons absorbed in the active layer of the detector at a given photon energy (Knoll, 2010). The intrinsic quantum detection efficiency, QE_{int}, is defined as

$$QE_{int} = \frac{number\ of\ radiation\ quanta\ absorbed\ in\ the\ active\ layer}{number\ of\ radiation\ quanta\ incident\ on\ detector\ face} \tag{2.6}$$

and should be distinguished from the absolute quantum detection efficiency, QE_{abs}, defined as

$$QE_{abs} = \frac{number\ of radiation\ quanta\ absorbed\ in\ the\ active\ layer}{number\ of\ radiation\ quanta\ emitted\ by\ source}. \tag{2.7}$$

For isotropic sources, the intrinsic and absolute quantum detection efficiencies are related by

$$QE_{int} = QE_{abs} * (4\pi/\Omega) \tag{2.8}$$

where Ω is the solid angle of the photodiode seen from the radiation source.

The intrinsic quantum detection efficiency, QE_{int}, of the detector can be further differentiated into external quantum detection efficiency, $QE_{external}$, and internal quantum detection efficiency, $Q_{internal}$. Their difference is that the former accounts for the loss of incident to the detector face photons due to the reflectance at the air-photodiode interface. Hence, the external and internal (both intrinsic) quantum detection efficiencies are related by

$$QE_{external} = (1 - r)QE_{internal} \tag{2.9}$$

where r is the reflectance at each photon energy at the air-photodiode interface (Sze & Ng, 2007) and it can be calculated using the refractive indices of air, n_{air}, and the semiconductor material of the detector, n_d,

$$r = \left(\frac{n_d - n_{air}}{n_d + n_{air}}\right)^2. \tag{2.10}$$

The internal quantum detection efficiency, $QE_{internal}$, of a semiconductor photodiode depends on the density and the bandgap of the material as well as on its geometry (Spieler, 2005). Having Equation 2.1 as a starting point for the absorption of photons in matter, the internal quantum detection efficiency of a semiconductor photodiode of a known geometry can be calculated as a function of photon energy using

$$QE_{internal} = [\prod_m \exp(-\mu_m x_m)][1 - \exp(-\mu_a x_a)]. \tag{2.11a}$$

The first term accounts for the absorption of photons in a total of m dead layers before they reach the active layer (Fraser, 1989). In Equation 2.11a, μ_m and x_m are the linear attenuation coefficient and the thickness of the m^{th} dead layer, respectively. Dead layers before the active layer of the semiconductor detector may include the electrode structure (top contact) used to apply the bias voltages and any dead layers between the surface of the detector and the depletion layer. The latter can be the p^+ layer of a p^+-i-n^+ photodiode or any recombination layer close to the surface of the diode. The second term of Equation 2.11a accounts for the absorption of photons in the active layer of the detector having a thickness, x_a, and a linear attenuation coefficient, μ_a. The carriers generated outside the active layer of the detector from the absorption of photons in the bulk of the semiconductor, and diffused into the reverse biased junction may also contribute to the recorded pulses in the spectroscopic system (Sze & Ng, 2007). As such, the internal quantum detection efficiency becomes

$$QE_{internal} = [\prod_m \exp(-\mu_m x_m)]\left[1 - \frac{\exp(-\mu_a x_a)}{1 - \mu_a L_p}\right] \tag{2.11b}$$

where L_p is the hole diffusion length, to account for both the photons absorbed in the active layer and the contributing photons absorbed in the diffusion region. Combining Equation 2.9 and Equation 2.11 gives

$$QE_{external} = (1 - r)[\prod_m \exp(-\mu_m x_m)]\left[1 - \frac{\exp(-\mu_a x_a)}{1-\mu_a L_p}\right]. \quad (2.12)$$

A related to the external quantum detection efficiency, $QE_{external}$, figure of merit is the responsivity, R'. It is measured in A/W and is defined as the ration of the photocurrent to the optical power. The responsivity, R', is given by (Sze & Ng, 2007)

$$R' = \frac{QE_{external}\lambda[\mu m]}{1.24}. \quad (2.13)$$

2.3.3 The charge sensitive preamplifier

Although voltage sensitive preamplifiers are commonly used in many electronic applications (Knoll, 2010), their use has disadvantages for high energy resolution spectroscopy utilising semiconductor detectors. The output of a voltage sensitive preamplifier depends not only on the charge, Q, liberated by the incident radiation but also on the capacitance of the detector, C_{det} (Leo, 1994). Since the capacitance of semiconductor photodiodes may change with operating parameters, such as temperature, the use of a voltage sensitive preamplifier is undesirable. Charge sensitive preamplifiers are therefore used instead. The charge, Q, induced on the detector's contacts is integrated on charge sensitive preamplifier's feedback capacitor, C_f, and the voltage across C_f is amplified. The preamplifier used to obtain spectra reported in this thesis was charge sensitive and its principle of operation is described in the following paragraphs.

A schematic diagram of the charge sensitive configuration can be seen in **Figure 2.5**. It consists of a feedback capacitor, C_f, a feedback resistor, R_f, and an inverting voltage amplifier with an ideally infinite input resistance, to prevent any detector signal current flowing in the inverting voltage amplifier. The input of the preamplifier, node G in **Figure 2.5**, should maintained at a virtual ground potential. The detector signal charge, Q, produces a potential difference, v_{in}, (input voltage) between the input of the preamplifier and ground. Potential also appears at the output of the preamplifier. The inverting voltage amplifier has a voltage gain, defined as the ratio between the output voltage, v_{out}, (potential difference between the output of the preamplifier and ground) and input voltage, v_{in}, of $-A$ (Spieler, 2005), such that

$$v_{out} = -Av_{in}. \quad (2.14)$$

The feedback capacitance, C_f, is connected from the input to the output of the preamplifier. The potential difference across the feedback capacitor, v_f, as a response to the input voltage, v_{in}, (effectively as a response to the detector signal charge, Q) becomes

$$v_f = v_{in} - v_{out} = v_{in} + Av_{in} = v_{in}(1 + A) \tag{2.15}$$

and the charge, Q_f, deposited on the feedback capacitance equals

$$Q_f = C_f v_f = C_f v_{in}(1 + A). \tag{2.16}$$

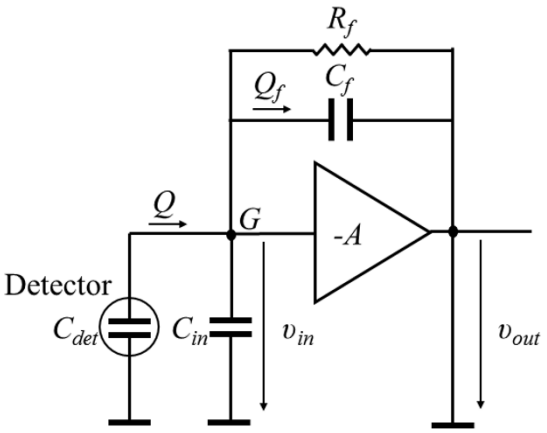

Figure 2.5. Schematic diagram of a detector connected to a charge sensitive preamplifier.

Since no current can flow into the preamplifier, the preamplifier reacts to the charge, Q, accumulated at the node G and in order to maintain node G at the virtual ground, induces an equal charge on the feedback capacitor, C_f, thus $Q_f = Q$. Effectively, the detector signal charge, Q, is integrated on the feedback capacitor, C_f.

The voltage, v_{in}, at the input of the preamplifier and the incoming charge from the detector, Q, makes the preamplifier input to appear as a dynamic input capacitance, $c_{in} = Q/v_{in}$. Substituting the input voltage, v_{in}, from rearrangement of Equation 2.16, into the input capacitance, it is found that

$$C_{in} = C_f(A + 1). \tag{2.17}$$

Combining Equation 2.14 and Equation 2.17 the output voltage, v_{out}, per unit detector charge, Q, becomes

$$\frac{v_{out}}{Q} = \frac{Av_{in}}{C_{in}v_{in}} = \frac{A}{C_{in}} = \frac{A}{C_f(A+1)} \approx \frac{1}{C_f}, \text{ for } A >> 1 \tag{2.18}$$

and hence

$$v_{out} = \frac{Q}{C_f}. \tag{2.19}$$

The potential difference, v_{out}, between the preamplifier output and ground would remain at this level in the absence of a resistive path for the charge, Q, to leak away (Gilmore, 2008). A feedback resistor, R_f, connected in parallel with the feedback capacitor, as seen in **Figure 2.5**, is used to discharge the integrated to the feedback capacitor charge. Consequently, the output of a resistive charge sensitive preamplifier as a response to the detector signal charge, Q, is a voltage step with an amplitude, v_{out}, independent of the detector capacitance, C_{det}, (Equation 2.18) which slowly decays with a time constant $C_f R_f$.

The feedback resistor, R_f, also serves as a discharge path for the detector's leakage current. However, R_f may be the main source of noise in the preamplifier circuit, which limits the energy resolution of the system (Bertuccio et al., 1993). Although, removing the feedback resistor improves the system's resolution, a conventional charge sensitive preamplifier cannot work properly without it because there is no DC feedback path to stabilize the working point of the preamplifier. Furthermore, without a feedback resistor, the leakage current of the detector along with its signal current would eventually fully charge the feedback capacitance of the preamplifier. Among the different configurations which have been proposed for feedback resistorless charge sensitive preamplifiers, the one presented by Bertuccio et al. (1993), was utilised in the work presented in this thesis, and its input circuit diagram can be seen in **Figure 2.6**.

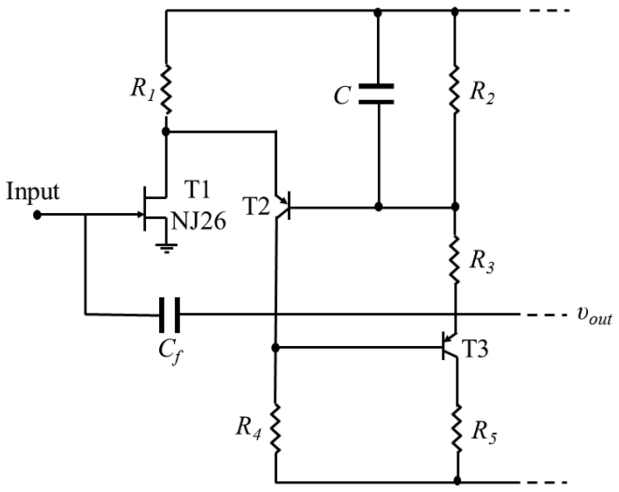

Figure 2.6. Circuit diagram of the input of the feedback resistorless charge sensitive preamplifier used in the work presented in this thesis (Bertuccio et al., 1993).

The elimination of the feedback resistor in the above configuration is achieved with an additional feedback loop for stabilizing the working point of the preamplifier and utilising a slightly forward

bias n-type Junction Field Effect Transistor (JFET), as a path for the feedback capacitor discharge. Based on the detector resistance, the input transistor can be chosen such that to minimise the preamplifier noise (Dakin & Brown, 2006). For low detector resistance (< 1 kΩ), a bipolar transistor, with relatively low series white noise (see Section 3.2.3) is advantageous. However, within the range of typical semiconductor detector resistances (> 1 kΩ), the realtively high parallel white noise (see Section 3.2.3) of bipolar transistors is unfavourable; JFETs and MOSFETs are preffered (Konczakowska & Wilamowski, 2011). Additionally, JFETs have lower 1/*f* noise (see Section 3.2.3) compared to MOSFETs which results in better energy resolution (Levinzon & Vandamme, 2011) (Bertuccio, 2012). Thus, a JFET is often chosen to be the input transistor of a low-noise charge sensitive preamplifier for X-ray spectroscopy (Bertuccio et al., 1993) (Bertuccio et al., 1995) (Fazzi et al., 2000). The photodiode detector is connected to input n-type JFET so that the detector's current enters into the preamplifier input. Although a p-type JFET can also be used with the detector connected so that its current comes out of the preamplifier input, the present discussion regards the use of an n-type JFET.

The detector current, I_D, consists of the photocurrent, I_{PH}, which is the charge induced at the electrodes of the photodiode due to the movement of the generated charges from the interaction of radiation quanta with the semiconductor's active volume (Shockley-Ramo theorem, **Section 2.3.2**), plus the reverse dark current (leakage current), I_R (see **Section 2.4**). The JFET used is a Si Vishay 2N4416A JFET of a NJ26 type (Siliconix, 2001). Since the detector current enters the preamplifier input (p-type gate of the n-type JFET T1) and the source of the JFET is grounded, the gate to source junction is forward biased.

The leakage current of the detector, I_R, which is the DC component of the detector's current, along with the leakage current of the drain to gate junction of the input JFET, flows through the gate to source junction and sets a positive potential difference, V_{GS}, between the preamplifier input (gate of the input JFET) and ground (source of the input JFET). This voltage, which is the DC operating point of the preamplifier, can vary in the range of few hundreds of mV (Bertuccio et al., 1993). The variations of the DC voltage at the input of the preamplifier are related to the variations of the leakage current of the detector. The DC and low frequency gain, G_0, of the preamplifier, defined as

$$G_0 = \frac{v_{out}}{v_{in}}, \tag{2.20}$$

should be reduced to increase the dynamic range of the DC input voltage. This is done using a feedback loop consisting of R2, R3, and C between the preamplifier's output and the base of T2

(**Figure 2.6**). This feedback loop introduces very high DC input resistance at the emitter of T2 resulting in lowering the DC gain of the preamplifier. As an example, a variation of two orders of magnitude of the current flowing in the gate of the JFET results in $|\Delta v_{out}| < 1.2$ V (Bertuccio et al., 1995). Another connected function of this feedback loop (R2, R3, and C) is imposing a well-defined voltage across the node where transistors T2, T3, and R4 are connected and ground, defining the DC operating point of transistors T2, T3, and T4 (Bertuccio et al., 1994).

In the frequency range of the signal charge, I_{PH}, the feedback loop, consisting of R2, R3, and C between the preamplifier's output and the base of T2 (**Figure 2.6**), does not play any role. The capacitor C grounds the base of T2 and it behaves as in the common base configuration. JFET T1 and BJT T2 consists the input cascode amplifier. With this configuration, the characteristics of each device are exploited (Khan & Dey, 2006). In more specific terms, the input JFET provides high input impedance and the BJT provides large voltage gain. The combination of these transistors ensures a high open loop gain which results in accumulating all the charge in feedback capacitor, C_f.

The pnp transistor T3 along with R4 and R5 is the voltage follower stage. The potential difference between the emitter of T3 the base of T3 is zero, hence there is no voltage gain. Effectively, it is used for impedance matching purposes (Boylestad & Nashelsky, 2006). The impedance at its input (base) is high whereas the impedance at its output (emitter) is low. The impedance of the output of the preamplifier is further lowered using an npn transistor T4 as an emitter follower network, which can be seen in **Figure 2.7**. The capacitor C1 is used for impedance multiplication (bootstrapping) of the load resistor of the input cascode amplifier, JFET T1 and BJT T2. A high load resistance at the emitter of T4 is guaranteed by the current source network, consisting transistor T5, which also supplies power to the preamplifier circuit.

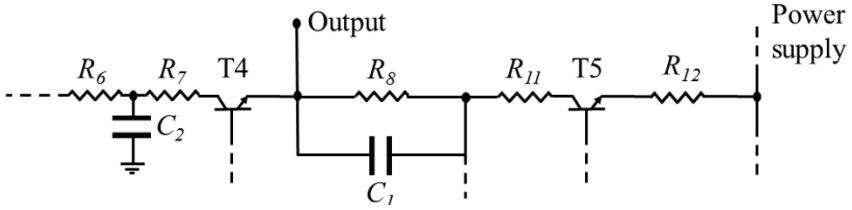

Figure 2.7. Circuit diagram of the output of the feedback resistorless charge sensitive preamplifier used in the work presented in this thesis (Bertuccio et al., 1993).

The output voltage, v_{out}, taken at the emitter of T4, shows a maximum proportional to the charge, Q, as in the conventional charge sensitive preamplifiers (Equation 2.19). With the above

configuration, it decays exponentially with two time constants. For an input charge signal pulse, Q, the output voltage pulse equals

$$v_{out}(t) = \left(-\frac{Q}{C_f}\right)\left(\frac{\tau_s\tau_l}{\tau_l-\tau_s}\right) \times \left[\frac{\tau_d-\tau_s}{\tau_d\tau_s}\mathrm{e}^{-1/\tau_s} + \frac{\tau_l-\tau_d}{\tau_d\tau_l}\mathrm{e}^{-1/\tau_l}\right]. \quad (2.21)$$

The time constant, τ_d, and the short time constant, τ_s, of the preamplifier output voltage pulse decay are determined by the values R2, R3, and C. The longer time constant, τ_l, is determined by the total capacitance at the input of the preamplifier and the dynamic resistance of the gate to source junction of the input JFET (Bertuccio et al., 1993).

2.4 Physics of semiconductor photodiodes

In this thesis, two types of semiconductor photodiodes are used for the detection of β^- particles and photons (from infrared (~ 1 eV) to X-ray energies (≤ 35 keV)); they are the Schottky diode and the p^+-i-n^+ diode. Knowledge of the fundamental physics governing the operation of the diodes is essential to understand their performance, and hence progress the development of semiconductor detectors. A review of the physics of Schottky and p^+-i-n^+ diodes required for the discussion and interpretation of the experimental part of this thesis is presented in the following paragraphs.

2.4.1 Schottky diode

A Schottky diode is a metal-semiconductor device, where the contact at the metal-semiconductor interface has rectifying properties (Grundmann, 2006). A barrier is formed at the metal-semiconductor interface. Figure 2.8 shows the energy band diagram of a metal and an n-type semiconductor when being in separate systems and when being connected into one system (Sze & Ng, 2007). The work function is defined as the energy difference between the vacuum level and the Fermi level. The metal has a work function of $q\varphi_m$, (φ_m in V) and the semiconductor has a work function of $q(\chi+V_n)$, where $q\chi$ is the electron affinity of the semiconductor and qV_n is the energy difference between the conduction band and the Fermi level. The electron affinity is defined as the energy difference between the conduction band and the vacuum level. As an example, Si has an electron affinity of 4.05 eV (Sze & Ng, 2007), whereas 4H-SiC has a relatively low electron affinity of 3.17 eV (Davydov, 2007).

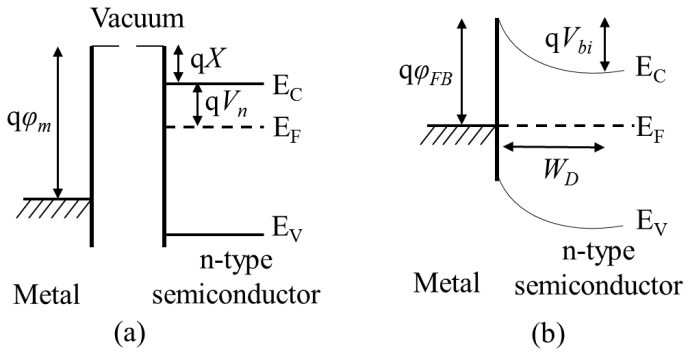

Figure 2.8. Energy band diagram of a metal and an n-type semiconductor (a) in separate systems and (b) connected into one system (Schottky diode).

After the connection of the metal and n-type semiconductor is made, thermal equilibrium is established, and the Fermi levels of the metal and the semiconductor are lined up (Figure 2.8 (b)). A barrier is formed at the metal-semiconductor interface. Ideally, the barrier height equals the difference between the metal work function and the electron affinity of the semiconductor (Sze & Ng, 2007).

The current in Schottky diodes is mainly due to majority carriers and arises from 1) the transport of carriers from the semiconductor into the metal over the potential barrier (thermionic emission), 2) quantum-mechanical tunnelling of carriers through the barrier, 3) recombination-generation in the depletion region (identical to the recombination-generation process in p^+-i-n^+ diodes, refer to Equation 2.33 and Equation 2.34), 4) carrier diffusion in the depletion region, 5) carrier diffusion from the metal to semiconductor, 6) edge leakage current due to high electric field at the contact periphery, and 7) interface current due to traps at the metal-semiconductor interface (Sze & Ng, 2007). A generalized thermionic emission – diffusion theory can adequately describe the current transport in Schottky diodes when the edge leakage current and the interface current are negligible. According to this combined theory, the complete expression of the current, I_F, as a function of applied forward bias, V_{AF}, which is equal to the voltage drop across the diode, $V_D = V_{AF}$, is

$$I_F = I_{sat}\left(e^{\mathrm{q}V_D/n\mathrm{k}T} - 1\right) \tag{2.22}$$

where q is the charge of an electron, n is the ideality factor used to take into account any deviations of a real diode from the ideal Schottky diode, and I_{sat} is the saturation current. For $V_{AF} > 3\mathrm{k}T/\mathrm{q}$, Equation 2.22 can be approximated to

$$I_F = I_{sat} e^{qV_D/nkT}. \quad (2.23)$$

The saturation current,

$$I_{sat} = SA^* T^2 e^{-q\varphi_{0B}/kT}, \quad (2.24)$$

where S is the area of the diode, A^* is the effective Richardson constant, and φ_{0B} is the barrier height at zero applied bias called the zero band barrier height, is the extrapolated current at zero applied bias. The zero band barrier height can thus be computed rearranging Equation 2.24, from the extrapolated saturation current, I_{sat},

$$\varphi_{0B} = \frac{kT}{q} \ln\left(\frac{SA^* T^2}{I_{sat}}\right). \quad (2.25)$$

For high forward applied biases, where the Schottky diode carries large forward current, I_F, the series resistance, R_{ser}, is critical (Sze & Ng, 2007). The diode is modelled with a series combination of a diode and a resistor, R_{ser}, where the forward current, I_F, flows (Cheung & Cheung, 1986). The voltage drop across the diode, V_D, is not equal to the applied forward bias, V_{AF}, as it was for Equation 2.22, but $V_D = V_{AF} - I_F R_{ser}$. Substituting the voltage drop across the diode, V_D, with the applied forward bias minus the voltage drop at the resistor, rearranging and differentiating Equation 2.23, it becomes

$$\frac{d(V_{AF})}{d(lnI_F)} = R_{ser} I_F + n\frac{kT}{q}. \quad (2.26)$$

When there is little or no depletion layer recombination-generation, n is close to unity. An ideality factor, n, closer to two suggests that the recombination-generation current dominates over the thermionic emission – diffusion current (Sze & Ng, 2007).

For applied reverse bias, $V_{AR} < 0$ V the barrier height is smaller than the zero band barrier height, φ_{0B}. The Schottky-barrier lowering and the depletion layer generation are the dominant effects for the reverse current. The reverse current,

$$I_R = SA^* T^2 e^{-E_A/kT}, \quad (2.27)$$

is a function of the activation energy, E_A, of the reverse behaviour. The activation energy is a function of temperature, T, and applied reverse bias, V_{AR}. Rearranging Equation 2.27, it becomes

$$\ln I_R = \ln(SA^*T^2) - \frac{E_A}{\mathrm{k}T}. \tag{2.28}$$

Thus, the activation energy, E_A, at a given applied reverse bias, V_{AR}, can be calculated from the gradient of the $\ln I_R$ as a function of $1/T$ graph. An activation energy lower but comparable with the zero band barrier height, φ_{0B}, reveals that the Schottky thermionic emission current dominates, whereas an activation energy equal to known defect energy levels suggests that the leakage current originates from these defects.

In an n-type semiconductor, the electron concentration almost equals the ionised donor concentration, N_D^+, at a given temperature. At relatively high temperatures, all donors with a concentration of N_D are assumed ionised. Under the approximation that the electron concentration for n-type Schottky diode (hole concentration for p-type Schottky diode) within the depletion layer width, W_D, is constant and equals the doping concentration in the epilayer, N_D, and that the electric field outside the depletion layer is zero, the depletion layer capacitance, C_{DL}, of an n-type Schottky diode

$$C_{DL} = S\sqrt{\frac{\mathrm{q}\varepsilon\varepsilon_0 N_D}{2(|V_{bi}| - V_{AR} - \mathrm{k}T/\mathrm{q})}}, \tag{2.29}$$

where ε is the dielectric constant of the semiconductor material, ε_0 is the permittivity of free space, and V_{bi} (< 0) is the built-in potential of the metal-semiconductor contact, is inversely proportional to the depletion layer width, W_D,

$$C_{DL} = \frac{S\varepsilon\varepsilon_0}{W_D}, \tag{2.30}$$

and both are functions of the applied reverse bias, V_{AR} (Schroder, 2006). Rearranging Equation 2.29, it can be written in the form

$$N_D = \frac{2}{q\varepsilon\varepsilon_0 S^2}\left[-\frac{1}{d\left(1/C_{DL}^2\right)/dV_{AR}}\right]. \tag{2.31}$$

If the doping concentration, N_D, is constant throughout the depletion region, assuming all donors are ionised and their concentration almost equals the electron concentration in the depletion layer, a plot of $1/C_{DL}^2$ as a function of applied reverse bias, V_{AR}, will yield a straight line which gradient can be used to determine N_D (Equation 2.31). For a non-constant doping concentration, $N_D(W_D)$, (i.e. when the epilayer has a nonuniform doping profile) the differential capacitance method may be used to calculate the doping concentration as a function of depletion layer width, $W_D(V_{AR})$,

using the same equation (Sze & Ng, 2007). It should be noted that the doping profiles of the epilayer of a Schottky diode determined by the capacitance measurements as functions of applied reverse bias (and using Equation 2.31) have a spatial resolution of the order of one Debye length. This is because the capacitance measurements as functions of applied reverse bias are insensitive to changes in the doping concentration that occur in a distance less than one Debye length. The physical meaning of the Debye length is the distance (screening radius) over which local electric field affects the distribution of free charge carriers; it is a function of the semiconductor material, doping concentration, and temperature (Cazaux, 2016).

The intercept point of the $1/C_{DL}^2$ as a function of applied reverse bias, V_{AR}, plot gives the intercept voltage, $V_i = V_{bi} - \mathrm{k}T/q$. The flat band barrier height, φ_{FB}, can be extracted from the capacitance measurements, since it is a function of V_{bi}, thus

$$\varphi_{FB} = \frac{\mathrm{k}T}{\mathrm{q}} \ln\left(\frac{N_C}{N_D}\right) + V_{bi} = \frac{kT}{q} \ln\left(\frac{N_C}{N_D}\right) + V_i + \frac{\mathrm{k}T}{\mathrm{q}}, \tag{2.32}$$

where N_C is the effective density of states in the conduction band of the semiconductor (Schroder, 2006). The flat band barrier height, φ_{FB}, extracted from capacitance measurements is determined from V_i which is the voltage where $1/C_{DL}^2 \to 0$ or $C_{DL}^2 \to \infty$ indicating sufficient forward bias to cause flat band conditions in the semiconductor.

2.4.2 p^+-i-n^+ diode

A p^+-i-n^+ diode is a variation of the p-n junction. It consists of an intrinsic i layer (high resistivity, pure semiconductor with negligible impurities) between a p^+ type (acceptor doped semiconductor with positive charged holes in the valence band) and n^+ type (donor doped semiconductor with negative charged electrons in the conduction band) semiconductor layer (White, 1982).

The current transport in p-n junctions, as well as in p^+-i-n^+ diodes, is mainly due to minority carriers, in contrast with Schottky diodes where the majority carriers are responsible (Sze & Ng, 2007). It arises mainly from 1) carrier diffusion, and 2) generation-recombination of carriers in the depletion layer. Other processes such as tunnelling of carriers between states in the bandgap, high injection condition, surface effects, and the effect of the parasitic series resistance, deviate the measured current from the theoretical predictions. The effect of series resistance is considered important at high forward current, due to the finite resistivity of the regions outside the depletion region (Sze & Ng, 2007). Similarly to Equation 2.23 for Schottky diodes, current, I_F, as a function of applied forward bias, V_{AF}, (for $V_{AF} >$ kT/q) which is equal to the voltage drop across the diode, $V_D = V_{AF}$, for a p-n diode can be approximated to,

$$I_F = I_{sat} e^{qV_D/nkT} = Sqn_i^2 \left(\frac{1}{N_D} \sqrt{\frac{D_p}{\tau_p}} + \frac{1}{N_A} \sqrt{\frac{D_n}{\tau_n}} \right) (e^{\frac{qV_D}{kT}}) + Sq \frac{n_i}{2\tau_g} W_D (e^{\frac{qV_D}{2kT}}) \quad (2.33)$$

The first term in Equation 2.33 is the diffusion current, I_{diff}, and the second term is the recombination current, I_{rec}. The saturation current, I_{sat}, and ideality factor, n, can be extracted from the semi logarithm current, I_F, as a function of applied forward bias, V_{AF}, plot. The ideality factor, n, equals 1 when the diffusion current, I_{diff}, dominates and 2 when the recombination current, I_{rec}, dominates. It lies between 1 and 2 when both currents are comparable. The saturation current of a p-n junction, which is notably different from that of the Schottky diode (Equation 2.24), represents the reverse current,

$$I_R \approx I_{sat} = Sqn_i^2 \left(\frac{1}{N_D} \sqrt{\frac{D_p}{\tau_p}} + \frac{1}{N_A} \sqrt{\frac{D_n}{\tau_n}} \right) + Sq \frac{n_i}{2\tau_g} W_D = I_{diff} + I_{gen}. \quad (2.34)$$

The first term in Equation 2.34 is the diffusion current, I_{diff}, and the second term is the generation current, I_{gen}. The reverse current might not be described by Equation 2.34 when surface effects dominate. In Equation 2.34, N_D and N_A are the donor and acceptor impurity concentrations respectively, D_p and D_n are the diffusion coefficient for holes and electrons respectively, τ_p and τ_n are the carrier lifetime for holes and electrons respectively, and τ_g is the carrier generation lifetime. The diffusion current scales with n_i^2 and the generation current scales with n_i. Since

$$n_i \propto e^{-E_G/2kT} \quad (2.35)$$

and

$$n_i^2 \propto e^{-E_G/kT}, \quad (2.36)$$

a plot of $\ln(I_R)$ as a function of $1/kT$ can be expected to yield a straight line whose slope determines whether the generation or the diffusion current dominates (Sze & Ng, 2007). More specifically, a slope of approximately $-E_G/2$ suggests that the dominant leakage current mechanism is generation, whereas a slope of approximately $-E_G$ suggests that the diffusion current dominates (Spieler, 2005).

The p-n junction capacitance consists of the diffusion capacitance, C_{Diff}, and the depletion layer capacitance, C_{DL}. The former, which is due to the rearrangement of the minority carrier density,

is directly proportional to the forward current, I_F. Thus, it significantly contributes to the junction capacitance at forward bias conditions.

The junction capacitance of a p-n junction at reverse bias conditions is mostly defined by the depletion layer capacitance, C_{DL}, which similarly to that of a Schottky diode, is inversely proportional to the depletion layer width, W_D,

$$C_{DL} = S\sqrt{\frac{\mathrm{q}\varepsilon\varepsilon_0 N_B}{2(|V_{bi}|-V_{AR}-2\mathrm{k}T/\mathrm{q})}} = \frac{S\varepsilon\varepsilon_0}{W_D}. \tag{2.37}$$

In Equation 2.37, N_B is the doping concentration of the lightly doped side of the p-n junction, i.e. N_D when $N_D << N_A$ and N_A when $N_A << N_D$, under the approximation that all dopants are ionised and the doping concentration equals the majority carrier concentration. For a p^+-i-n^+ diode, N_B can be substituted with the effecting doping concentration of the intrinsic layer, N_{eff}, which almost equals the concentration of the majority carriers in the intrinsic layer. Rearranging Equation 2.37,

$$N_{eff} = \frac{2}{q\varepsilon\varepsilon_0 S^2}\left[-\frac{1}{d(1/C_{DL}^2)/dV_{AR}}\right]. \tag{2.38}$$

For a constant effecting doping concentration, N_{eff}, the $1/C_{DL}^2$ as a function of applied reverse bias, V_{AR}, plot is a straight line whose gradient can be used to determine the effective doping concentration in the i layer and the voltage axis intercept point, $V_i = V_{bi} - 2\mathrm{k}T/\mathrm{q}$, gives the built in voltage, V_{bi}. Similarly to the Schottky diode, for a non-constant (arbitrary shaped profile) effective doping concentration in the i layer, N_{eff}, the differential capacitance method may be used (Equation 2.38) to determine the effective doping concentration as a function of depletion layer width, $N_{eff}(W_D)$. The spatial resolution of the doping profiles of the intrinsic layer determined by the capacitance measurements as functions of applied reverse bias (and using Equation 2.38) is of the order of one Debye length. This is because variations in the doping profile of the intrinsic layer occurring in a scale less than one Debye length cannot be resolved, similarly to the variations in the doping profile of the epilayer of a Schottky diode (**Section 2.4.1**).

2.5 Experimental techniques

In this section, the experimental techniques for the electrical and optical characterisation of the devices presented in the thesis are discussed. The procedures followed for dark current, dark capacitance, and photocurrent measurements are described.

2.5.1 Current measurements as a function of bias

Forward and reverse biased dark current measurements were performed for all three families of photodiodes being investigated in the thesis. The dark current as a function of forward applied bias enables the extraction of key parameters of the devices (see **Section 2.4**) such as the saturation current, I_{sat}, the zero band barrier height, φ_{0B}, and the ideality factor, n. The measurements of dark current as a function of reverse applied bias enables the determination of the photocurrent-to-dark current contrast, in photocurrent measurements, and in part the noise contribution of the detector to the *FWHM* in spectroscopic measurements.

Both the application of the bias and the measurement of the current were performed with the Keithley 6487 Picoammeter/Voltage Source (Keithley Instruments, 2011). The Keithley 6487 had a source voltage range from ± 200 μV to ± 505 V, and a current reading range from ± 10 fA to ± 21 μA. The uncertainty associated with the current reading depended on the current range, and it can be seen in **Table 2.2**.

Current range	**Uncertainty**
2 nA	0.3 % + 400 fA
20 nA	0.2 % + 1 pA
200 nA	0.15 %0 + 10 pA
2 μA	0.15 % + 100 pA
20 μA	0.1 % + 1 nA
200 μA	0.1 % + 10 nA
2 mA	0.1 % + 100 nA
20 mA	0.1 % + 1 μA

Table 2.2. Uncertainties associated with current measurements using the Keithley 6487 Picoammeter/Voltage Source (Keithley Instruments, 2011).

Each diode detector was mounted in a metal box enclosure, an aluminium chassis, to eliminate light and provide shielding; electrostatic interference was prevented. The Voltage Source Output (VSO) of the Keithley 6487 was connected to the cathode of each diode detector. The current was measured from the anode of each diode detector.

The leakage current arising from the cables connecting each detector to the Keithley 6487 can dominate the current measurements, especially at low signal levels (Keithley Instruments, 2013). Thus, any such unwanted effects need to be eliminated. Instead of using a coaxial cable between the anode of the device under test and the input of the Keithley 6487, which would have a leakage resistance parallel with the device under test, a triax cable was used as appropriate. The signal

line (force) of a triax cable was surrounded by the guard line, connected at the same potential as the signal line, and hence reducing the effects of leakage currents.

The input triax connector of the Keithley 6487 had an Input High, an Input Low and a Chassis Ground. This Input Low was the guard terminal of the Keithley 6487 Picoammeter/Voltage Source, and was at the same potential as the Input High. The VSO of the Keithley 6487 Picoammeter/Voltage Source was a standard banana connector for both the HI and LO. The aluminium box enclosure, serving as the ground plane of the measurement system, had a female triax connector with a Force, Guard, and Shield, and an SMA connector. The connections between the Keithley 6487 Picoammeter/Voltage Source and each diode detector can be seen in **Figure 2.9**.

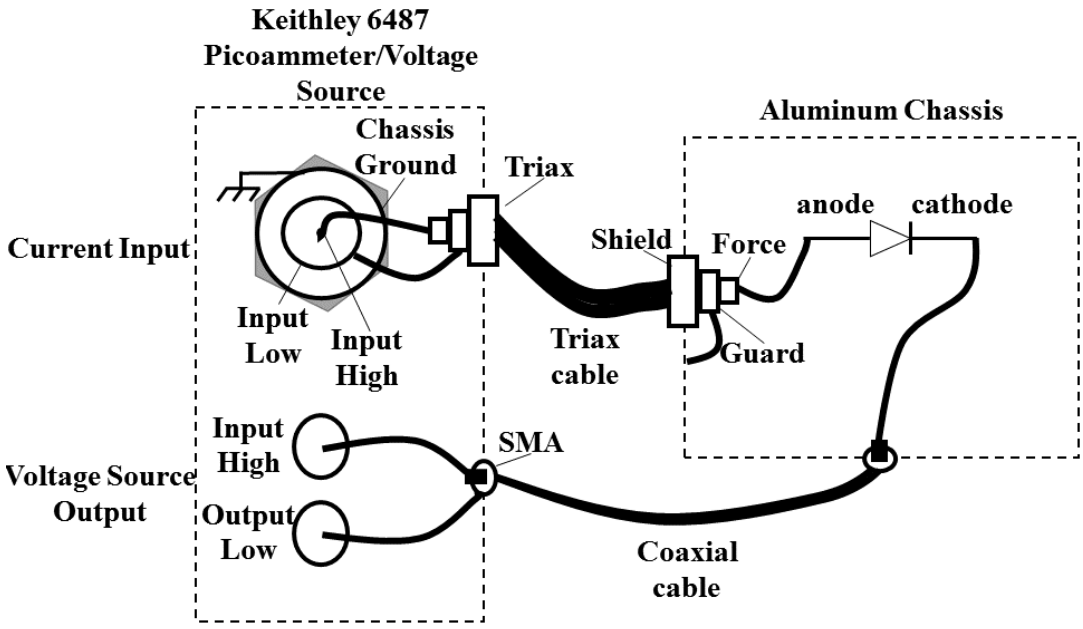

Figure 2.10. Diagram shown the experimental set up of the current measurements using a Keithley 6487 Picoammeter/Voltage Source.

The triax cable used was terminated at both ends with 3-slot male triax connector. The middle conductor (guard, between the force and shield) of the triax cable was connected to the guard terminal (Input Low) of the Keithley 6487 Picoammeter/Voltage Source. The aluminium enclosure, the triax cable shield, and the shield terminal (Chassis Ground) of the Keithley 6487 Picoammeter/Voltage Source were all maintained at the same ground potential. A double banana plug to BNC adapter and a BNC to SMA adapter were used to connect the VSO of the Keithley 6487 Picoammeter/Voltage Source and the SMA connector of the aluminium enclosure with a coaxial cable.

2.5.2 Capacitance measurements as a function of bias

Forward and reverse biased dark capacitance measurements were performed for all three families of photodiodes being investigated in the thesis. Capacitance measurements enable the determination of the flat band barrier height, φ_{FB}, of a Schottky diode, the depletion layer width, W_D, the doping concentration, N_D, of a Schottky diode, and the effective doping concentration of the intrinsic layer, N_{eff}, of a p^+-i-n^+ diode (see **Section 2.4**). The measurements of capacitance as a function of reverse applied bias enables the determination (in part) of the noise contribution of the detector to the *FWHM* in spectroscopic measurements.

The measurement of the capacitance was performed with a HP 4275A Multi-frequency LCR meter (Hewlett Packard, 1979). The application of the bias was performed with the Keithley 6487 Picoammeter/Voltage Source (Keithley Instruments, 2011); the Keithley 6487 was connected at the rear of the HP 4275A LCR meter. The capacitance range of the HP 4275A LCR meter was from 1000 fF to 100 μF. The uncertainty associated with the capacitance reading was (0.1% of reading + 3 counts) × 1.2. The input of the HP 4275A LCR meter was a four terminal pair with guard; LCUR, LPOT, HPOT, and HCUR.

Each diode detector was mounted in a metal box enclosure, an aluminium chassis, similar to the current measurements, to eliminate light and provide shielding; electromagnetic interference was prevented. The connections between the HP 4275A LCR meter and each diode detector can be seen in **Figure 2.10**.

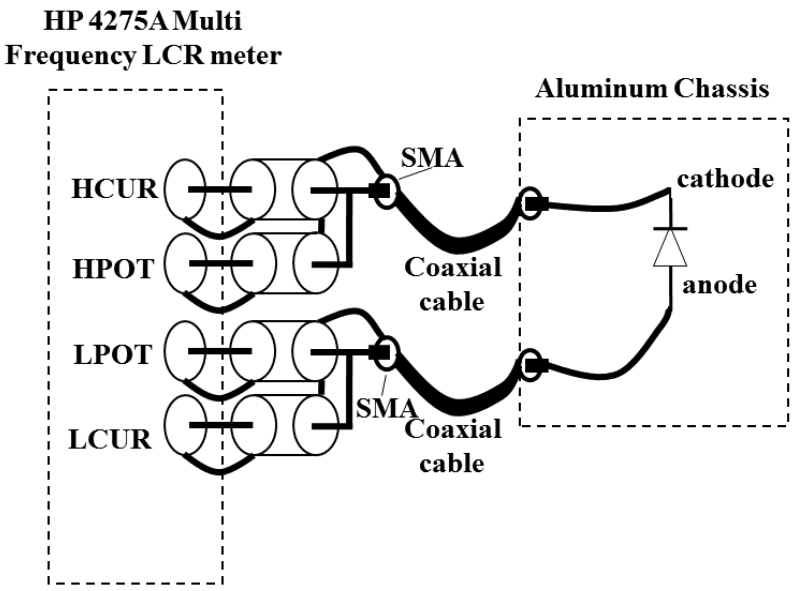

Figure 2.10. Diagram shown the experimental set up of the capacitance measurements using a HP 4275A Multi Frequency LCR meter.

The cables and wires connecting the photodiode detector under test to the LCR meter have individual inherent stray capacitances, residual inductances and resistances. In order to compensate for such factors, zero offset adjustments were performed prior to any capacitance measurements. Setting the test sinusoidal signal to 1 V rms magnitude and 1 MHz frequency, and without connecting anything to the test wires, the ZERO OPEN check was performed; the stray capacitance and conductance was measured. Following this, and after shorting the test wires, the ZERO SHORT check was performed; residual inductance and resistance was measured. The magnitude of the test signal was then set to the desired level, 50 mV, and the photodiode under test was connecting to the test wires for capacitance measurements.

Another precaution taken for the capacitance measurements was the measurement of the capacitance of the package, C_{pack}, of each photodiode. Since all photodiode detectors being investigated in the thesis were packaged, the measured capacitance included the capacitance of the package, in addition to the capacitance of the photodiode itself. Thus, separate measurements of the capacitance of the empty package were performed following the same procedure as the measurements of the packaged devices, and the resulted capacitances, C_{pack}, were subtracted from the measured total capacitance.

It should be noted here that the uncertainties associated with the capacitance measurements were not exclusively related to the accuracy of the LCR meter. The capacitance uncertainties in each case were estimated taken into account the accuracy of the LCR meter, the error arising from the

connection of the photodiode under test to the test wires (calculated from multiple capacitance measurements of the same device), and the rms error of the capacitance of the package (calculated from capacitance measurements of multiple empty packages, when possible).

2.5.3 Photocurrent measurements

To investigate the performance of the 4H-SiC UV Schottky photodiodes under UV illumination, and of the 7 μm i layer GaAs mesa p^+-i-n^+ photodiodes under visible and near infrared light illumination, photocurrent measurements were performed. In each case, the responsivity, $R^{'}$, of the photodiodes (Equation 2.13) as a function of wavelength was calculated.

A ThermoSpectronic Unicam UV300 UV-VIS spectrophotometer was used to provide the optical power (Unicam, 2000). The UV-VIS spectrophotometer had a Tungsten and a Deuterium lamp to cover the UV (210 nm to 500 nm) and the visible and near infrared (580 nm to 980 nm) wavelength range of interest. An internal monochromator and UV grating allowed the selection of the wavelength, with a chosen bandwidth of 1.5 nm. The photocurrent measurements were performed using a Keithley 6487 Picoammeter/Voltage Source (see **Section 2.5.1**). A diagram of the experimental set up can be seen in **Figure 2.11**.

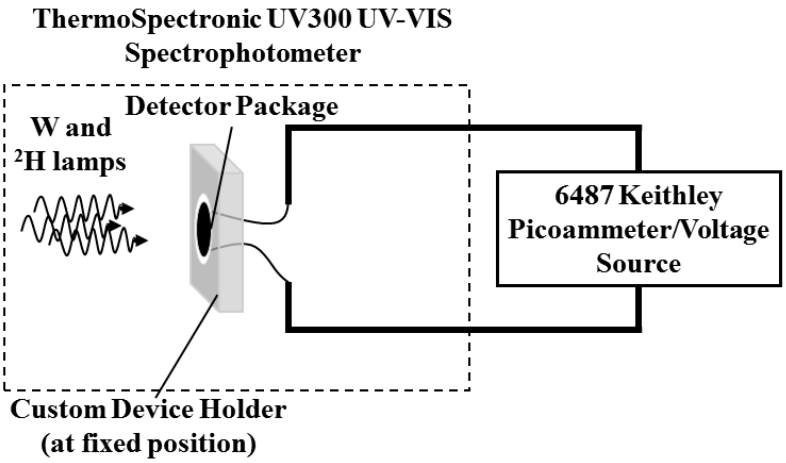

Figure 2.11. Diagram shown the experimental set up of the UV, visible, and near infrared photocurrent measurements using a ThermoSpectronic UV300 UV-VIS spectrophotometer.

Custom baffles were used to prevent external light influencing the measurements. Also, a custom device holder, made of PTFE, was used for accurate device position, with respect to the input optical power. The device holder was kept at a fixed position. To achieve absolute responsivity measurements, $R^{'}$[A/W], such as the ones in **Section 4.4**, the optical power incident on each detector was measured, in addition to the photocurrent measurements as a function of wavelength. This was achieved using photodiode detectors with known responsivities; two SG Lux SiC

photodetectors with different areas (SGlux SolGel Technologies GmbH, SG01D-18) (SGlux SolGel Technologies GmbH, SG01L-18) were chosen. These reference photodiodes were positioned in the custom device holder, and their photocurrent, I_{PH}, as a function of wavelength was measured. Taking into account the area of each reference photodiode, and their known responsivities, the optical power at the fixed position of the device holder was deduced.

Chapter 3 Noise in Semiconductor Radiation Detection Systems for X-ray Spectroscopy

3.1 Introduction to noise components

The energy resolution, ΔE, (quantified by the *FWHM* of the photopeak) of a non-avalanche semiconductor detector coupled to a charge sensitive preamplifier is defined by the quadratic sum of three independent terms, such that,

$$\Delta E[\text{eV}] = 2.355\omega\sqrt{\frac{FE_{rad}}{\omega} + R^2 + A^2}. \quad (3.1)$$

The first term under the square root, the Fano noise, is related to the statistical nature of the ionisation process and has been discussed in **Section 2.3.2**. The second term, *R*, is the equivalent noise charge (in e^- rms) representing the incomplete charge collection noise and is discussed in **Section 3.5**. The third term, *A*, is the equivalent noise charge (in e^- rms) representing the broadening of the photopeak due to electronic noise. The characteristics of the detector, input transistor of the preamplifier (a JFET is usually chosen, see Section 2.3.3), and the shaping amplifier, all affect the electronic noise.

3.2 Electronic noise components

There are five main components which constitute the electronic noise, *A*. These are series white noise, parallel white noise, 1/*f* series noise, dielectric noise, and induced gate current noise (Bertuccio et al., 1996). In this section, these sources are introduced in turn.

3.2.1 Series white noise

The series white noise, ENC_{WS}, arises from the thermal noise of the current flowing at the channel of the preamplifier's input JFET. It commonly dominates at short shaping time due to its inversely proportional relationship with the shaping time, τ (Bertuccio et al., 1996). The equivalent noise charge (*ENC*) for the series white noise in units of e^- rms, is given by,

$$ENC_{WS} = \frac{1}{q}\sqrt{\frac{A_1}{2}S_{WS}C_T^2\frac{1}{\tau}}. \quad (3.2)$$

In Equation 3.2, A_1 is a constant shape factor for the series white noise depending on the type of the shaping amplifier and equals 1.85 for an RC-CR shaping amplifier (Gatti et al., 1990). C_T is the total capacitance at the preamplifier input. This includes the detector capacitance, C_{det}, the

feedback capacitance, C_f (see **Section 2.3.3**), the test capacitance, C_t (used to inject charge at the input of the preamplifier to simulate a charge pulse of a detector), the stray capacitance, C_s (widely distributed capacitance arising from parallel conductors of a printed circuit board or conductors near ground planes (Glisson, 2011)), and the input transistor capacitance, C_i. The latter, also referred as intrinsic gate capacitance, consists of the gate to source capacitance, C_{gs}, and the drain to gate capacitance, C_{dg}, and they are both voltage dependent capacitances. They arise due to the depletion layer of the junctions which act as dielectrics and therefore they depend on the source to gate voltage, V_{GS}, and the drain to gate voltage, V_{GD}. In most amplifier applications, the drain to gate voltage is greater than the source to gate voltage. The capacitance of an abrupt junction is an inverse function of the square root of the junction voltage (Evans, 1981). Thus, C_{gs} is higher than C_{dg}, this difference becomes even larger when the source to gate junction is forward biased because its depletion layer decreases.

The time parameter, τ, is the shaping time of the shaping amplifier. This time parameter is proportional to the width of the δ-response of the filter, $h(t)$ (Gatti et al., 1990). Since the series white noise is a continuous signal in the frequency domain, its spectrum may be referred to as a power spectral density with units of V^2/Hz (Norton & Karczub, 2003). That is to say that its integral over all possible frequencies equals the average signal power (Howard, 2002). The series white noise power spectral density, S_{WS}, (also known as spectral voltage noise density of thermal noise) can be approximated to the thermal noise of a noise resistance, R_s, in series with the gate (Radeka, 1973) such that,

$$S_{WS} = 4\mathrm{k}TR_s = 4\mathrm{k}T\frac{\gamma}{g_m} \tag{3.3}$$

where g_m is the FET transconductance which determines the change in drain current, I_{Dr}, due to a change in gate to source voltage, V_{GS} (Boylestad and Nashelsky, 2006), such that

$$g_m = \frac{\Delta I_{Dr}}{\Delta V_{GS}}. \tag{3.4}$$

The parameter γ is the dimensionless product of noise resistance, R_s, and transconductance, g_m (Klaassen, 1971). The noise resistance, R_s, is a function of the drain to source voltage, V_{GS}, and the velocity saturation parameter, γ'. The velocity saturation parameter is a constant dependant on the JFET bias condition and the channel (also known as the gate) length l. Specifically, γ' is given by

$$\gamma' = \frac{V_p}{lE_0}, \tag{3.5}$$

where V_p is the pinch-off voltage. The pinch-off voltage, V_p, is the corresponding voltage value of drain to source voltage, V_{DS}, plus the built in voltage V_{bi} (described in **Section 3.4** in the model calculations) where the channel is fully depleted and saturation current flows through the channel, with the gate shorted. Its value depends on the doping density in the n-type channel, N_D, and the geometry of the device, such that

$$V_p = \frac{qh^2 N_D}{2\varepsilon\varepsilon_0}, \tag{3.6}$$

where h is the height (also known as the depth) of the channel (i.e. the distance between the p-type materials that are connected to the gate terminals in an n-type channel JFET) (Sze & Ng, 2007). The parameter E_0 in Equation 3.5 is an empirically determined constant which relates the experimental measurements of the carrier mobility, μ_c, in a uniform channel JFET with the electric field, thus it is material dependent. For example, the E_0 has been found to be equal to 8.5×10^5 V/cm for n-type Si (Trofimenkoff, 1965). Hence, γ' is also material dependent. For example, for the n-type channel Si JFET, 2N4338, with l = 12 μm and V_p = 1 V, the velocity saturation parameter γ' equals to 0.098 (Levinzon & Vandamme, 2011). According to Klaassen (1971), γ may be approximated to

$$\gamma = 0.7 + \frac{V_p - V_{GS}}{2lE_0}. \tag{3.7}$$

Alternatively, substituting lE_0 of Equation 3.7 with its equal from Equation 3.5, and rearranging, the dimensionless product of noise resistance, R_s, and transconductance, g_m, produces

$$\gamma = 0.7 + \frac{\gamma'}{2}\left(1 - \frac{V_{GS}}{V_p}\right). \tag{3.8}$$

3.2.2 Parallel white noise

Parallel white noise arises from the shot noise of the FET gate current, I_G, and detector's leakage current, I_{LD} (Bertuccio et al., 1996). This is due to the discrete nature of electric charge (Vasilescu, 2005). Another source of the parallel white noise is the feedback resistor, R_f, in preamplifiers that have them.

The *ENC* of the white parallel noise is given by

$$ENC_{WP} = \frac{1}{\mathrm{q}}\sqrt{\frac{A_3}{2}S_{WP}\tau} \tag{3.9}$$

where A_3 is a constant shape factor for the parallel white noise depending on the type of the shaping amplifier and equals 1.85 for an RC-CR shaping amplifier (Gatti et al. 1990) (Bertuccio et al., 1996). The parallel white noise power spectral density, S_{WP}, which is also known as the spectral current noise density of shot noise, is given by,

$$S_{WP} = 2\mathrm{q}\alpha'(I_{LD} + I_G) + \frac{4\mathrm{k}T}{R_f}, \tag{3.10}$$

in which α' = 1 for full shot noise (Bertuccio et al., 1996). Full shot noise is present when the motion of electrons can be regarded randomly and independently of each other and hence Poissonian statistics describe the transfer of electrons. Parallel white noise dominates at long shaping times, whereas it can be considered less important than other types of noises at short shaping times (Equation 3.9).

3.2.3 1/f series noise

The 1/*f* series noise arises from the flicker noise of the drain current of the preamplifier input transistor. This is due to the generation and recombination of carriers in the two depleted regions from impurity atoms and lattice defects. The fluctuation in the depleted regions' charge changes the width of the channel which results in fluctuations of the drain current, I_{Dr} (Vasilescu, 2005). If the trapping and releasing of carriers were purely random, the noise spectrum would be uniform. Since this process occurs independently in time, the noise spectrum deviates from white noise, in a certain frequency range (Spieler, 2005). In the rare situation where only one time constant is involved in these events, the power spectral density has a $1/f^2$ distribution and when more than one time constants are involved, the distribution of the power spectral density becomes a nearly ideal 1/*f* response.

The *ENC* of the 1/*f* series noise is given as

$$ENC_{1/f} = \frac{1}{\mathrm{q}}\sqrt{A_2\pi A_f C_T^2} \tag{3.11}$$

where A_2 is a constant shape factor for the 1/*f* noise depending on the type of the shaping amplifier and equals 1.18 for an RC-CR shaping amplifier (Gatti et al., 1990) (Bertuccio et al., 1996). The corresponding spectral voltage noise density is A_f/f, where A_f is a constant characteristic of the transistor that can be expressed as

$$A_f = \frac{H_f}{C_i} = \frac{\left(\gamma 2\mathrm{k}T/\pi\right)\left(f_c/f_T\right)}{C_i} \tag{3.12}$$

in which f_T is the transition frequency and f_c is the corner frequency of the JFET. The transition frequency, f_T, is the frequency where the unity current gain is achieved, i.e. $i_0 = i_i$ (Levinzon & Vandamme, 2011),

$$f_T = \frac{g_m}{2\pi C_i}. \tag{3.13}$$

The corner frequency, f_c, is where the white spectral density and the $1/f$ spectral density are equal. The ratio f_c/f_T depends only on the bias of the transistor, as is discussed in **Section 3.4**. For a given JFET technology and fixed bias conditions, H_f is constant for JFETs that differ only in channel width, W, (Bertuccio et al., 1996). *1/f* noise is τ independent (Equation 3.11).

3.2.4 Dielectric noise

Dielectric noise arises from thermal fluctuations in insulators that are close to, or in contact with, the preamplifier input (Bertuccio et al., 1996). Polarisation in lossy dielectrics can cause fluctuations in electric charge density. The field that is consequently set up, draws current from the external circuit (Lowe & Sareen, 2014). This current can add substantially to the noise. In other words, the dielectric material is inserted into a stray capacitance and its distribution in the vicinity of the FET gate affects the dielectric noise. The feedback capacitance, test capacitance, the dielectrics of the transistor, any passivation layers on the detector or JFET, as well as the packaging materials of the detector and JFET, the material of the preamplifier's printed circuit board, and the detector and JFET themselves all contribute to the dielectric noise (Pullia & Bertuccio, 1996). The dielectric noise might also arise due to the increased capacitive coupling of the preamplifier input electrode to the surrounding dielectrics, when the input electrode is extended in the connection to the detector (Bertuccio et al., 2003).

The *ENC* of the dielectric noise is given by

$$ENC_{DN} = \frac{1}{\mathrm{q}}\sqrt{A_2 2\mathrm{k}TDC_{die}}, \tag{3.14}$$

where C_{die} is the capacitance of the lossy dielectrics with a (dimensionless) dissipation factor, D, and the rest of the symbols have been previously defined. The dissipation factor is defined as

$$D = \frac{G(\omega')}{\omega' C_{die}}, \tag{3.15}$$

where $G(\omega')$ is the loss conductance at an angular frequency ω' associated with the lossy capacitance C_{die} (Lowe & Sareen, 2014). Each capacitance in the system can be regarded as lossy, with an associated dissipation factor and is considered separately. The dissipation factor for low loss dielectrics is in the range of 10^{-5} (Lowe & Sareen, 2014), whereas lossy materials exhibit higher D resulting in higher dielectric noise. The dissipation factor is not only a function of the material but also of frequency, temperature as well as its conductivity representing all the various loss terms in the medium (effectively, its quality) (Kaiser, 2005). Krupka et al. (2006) measured the dissipation factor for high resistivity p-type Si at 6.8 GHz and reported an increment from 2×10^{-4}, at temperatures below -247 °C, to 2×10^{-3}, at 26 °C, whereas a dissipation factor increase from 1.6×10^{-6}, at -263 °C, to 2×10^{-3}, at 26 °C, was reported by Jung et al. (2014) for undoped n-type Si at 13.7 GHz. The dissipation factor of semi-insulating 4H-SiC was measured at near 40 GHz to increase from 9×10^{-7} at -233 °C to 4×10^{-4} at 22 °C (Hartnett et al., 2011), whereas the dissipation factor of undoped 4H-SiC at 8.7 GHz was reported to be 1×10^{-2}, at -263 °C, by another group (Jung et al, 2014). The dissipation factor of 6H-SiC could not be found in the literature, possibly because it has been measured to be an anisotropic material (Patrick & Choyke, 1970). Measurements of the dissipation factor of Cr-doped semi-insulating GaAs as functions of frequency and temperature were reported by Courtney (1977); it varied from 2×10^{-4} at 2.5 GHz to 6×10^{-4} at 36 GHz, both at 26 °C. The dissipation factor of semi-insulating GaAs bulk crystals was also measured by Krupka et al. (2008), as a function of frequency and temperature. A value of 2×10^{-4} at 12.4 GHz, at a temperature of 26 °C was reported.

Lossy dielectrics generate a noise current spectrum in parallel with the input, proportional to f, which when integrated on the input capacitance becomes $1/f$ noise (Radeka, 1973). The dielectric noise contribution is independent the shaping time constant τ (Equation 3.14). Eliminating the package of the FET by integrating the FET's die onto the detector is clearly advantageous (Bertuccio et al., 1995) as is integrating the FET with the detector as in a DEPFET detector (Zhang et al., 2006).

3.2.5 Induced gate current noise

Induced gate current noise arises from fluctuations in the gate charge due to fluctuations in the drain current (Vasilescu, 2005). This is caused from capacitive coupling between the gate and the channel of the JFET. Since both the fluctuations in the gate charge and in the drain current stem from the same noise origin, the random motion of carriers in the JFET's channel, the induced

gate current noise, S_{ig}, is correlated with the drain current noise, S_{WS}, with an imaginary coefficient $c = jc_o$ (Bertuccio et al., 1996).

The power spectral density of the induced gate current noise is proportional to frequency, ω, and is given by

$$S_{ig} = S_{WS}\omega^2 C_{gs}^2 \delta, \tag{3.16}$$

where both δ and c_0 are experimentally measured factors (Bertuccio et al., 1996). The factor δ, which is dimensionless and depends upon the bias condition, was calculated for a simplified FET model to be $\delta \approx 0.25$ (Bertuccio et al., 1996).

The correlation factor, c_0, between the drain current, I_{Dr}, and the induced gate charge is a function of the pinch-off voltage, V_p, the voltage at the gate, V_{GS}, the voltage at the drain, V_{DS}, and the diffusion potential of the gate-channel junction, V_{dif} (also known as the built in voltage (Bar-Lev, 1993)) (Van der Ziel, 1963). By definition, it can be calculated once the gate current noise, S_{ig}, and the drain current noise, S_{WS}, are calculated. In saturation, c_0 has been previously calculated using an approximation method which allowed the calculation of S_{ig} and S_{WS}, resulting in a value of $c_0 \approx 0.4$ (Van der Ziel, 1963). The corresponding equivalent noise charge, ENC_{WSc}, which takes into account S_{WS}, S_{ig}, and their correlation equals

$$ENC_{WSc} = \frac{1}{\mathrm{q}}\sqrt{A_1 S_{WS} G_c C_T^2 \frac{1}{\tau}} = ENC_{WS}\sqrt{G_C} \tag{3.17}$$

where,

$$G_C = \left[1 + \left(\frac{C_{gs}\delta}{C_d' + C_i}\right)^2 - \frac{2c_0 C_{gs}\delta}{C_d' + C_i}\right]. \tag{3.18}$$

G_C is a correction factor which enhances or reduces the contribution of the white series noise (Equation 3.17) (Bertuccio et al., 1996). In Equation 3.18, C_d' which is the input load capacitance, equals the total capacitance, C_T, excluding the input transistor capacitance, C_i.

The induced gate current noise can be important at short shaping times where the white series noise can be dominant.

3.3 Electronic noise squared equivalent noise charge

The squared equivalent noise charge (Bertuccio and Pullia, 1993) is useful for computing the total *ENC* from all noise sources, such that

$$ENC^2 = \frac{1}{\mathrm{q}^2}\left(aC_T^2A_1\frac{1}{\tau} + bA_3\tau + 2\pi a_f C_T^2 A_2 + \frac{b_f}{2\pi}A_2\right). \tag{3.19}$$

The total squared equivalent noise charge simply originates from summating the *ENC* from all noise components in quadrature. The first term inside the parenthesis in Equation 3.19 is the series white noise, the second term is the parallel white noise, the third term is the 1/*f* noise, and the fourth term is the dielectric noise (the induced gate current noise has been excluded). The dependency of the ENC^2 on the shaping time, τ, is emphasized in Equation 3.19.

In Equation 3.19, *a* (measured in V^2/Hz) is the contribution of the white series noise and is given by

$$a = \gamma\frac{2\mathrm{k}T}{g_m}. \tag{3.20}$$

This is derived by comparing Equation 3.19 with Equation 3.2, and Equation 3.3.

In Equation 3.19, *b* (measured in A^2/Hz) is the contribution of the white parallel noise, such that

$$b = \mathrm{q}(I_{LD} + I_G). \tag{3.21a}$$

This is derived by comparing Equation 3.19 with Equation 3.9 and Equation 3.10, for the case where the preamplifier does not have a feedback resistor, R_f. However, when there is feedback resistor R_f, the contribution of the white parallel noise becomes

$$b = \mathrm{q}(I_{LD} + I_G) + \frac{2\mathrm{k}T}{R_f}. \tag{3.21b}$$

In Equation 3.19, a_f is the coefficient of the 1/*f* noise, where

$$a_f = \frac{\left(\gamma 2\mathrm{k}T/\pi\right)\left(f_c/f_T\right)}{2C_i}, \tag{3.22}$$

this is derived by comparing Equation 3.19 with Equation 3.11 and Equation 3.12.

Lastly, in Equation 3.19, b_f is the coefficient for the dielectric noise and equals

$$b_f = 4\mathrm{k}T\pi DC_{die}. \tag{3.23}$$

This is derived by comparing Equation 3.19 with Equation 3.14.

3.4 Contribution of the input JFET

3.4.1 Contribution of the input transistor to the total noise in summary

The overall *ENC* is calculated using Equation 3.19. The intention of this section is to elucidate which JFET parameters affect the noise and how they do so. The first approximation to the problem is by assuming that the detector capacitance, C_{det}, is negligible and only the transistor's input capacitance, C_i, is regarded as the total capacitance, C_T. Also, the detector's leakage current, I_{LD}, is assumed to be zero. Making all other sources of noise ideal, the *ENC* which arises only from the input JFET is computed. Hence, Equation 3.19 becomes

$$ENC^2 = \frac{1}{\mathrm{q}^2}\left(\gamma\frac{2\mathrm{k}T}{g_m}C_i^2A_1\frac{1}{\tau} + \mathrm{q}I_GA_3\tau + (\gamma 2\mathrm{k}T)\left(\frac{f_c}{f_T}\right)C_iA_2 + 2\mathrm{k}TDC_iA_2\right). \tag{3.24}$$

The parameters of the input FET that directly affect the overall *ENC* are its gate current, I_G, its input capacitance, C_i, the ratio between the corner and transition frequency, f_c/f_T, its transconductance, g_m, and the dissipation factor, D, of the JFET's material.

The *ENC* contribution of some different FETs due to the white parallel noise was plotted by Bertuccio et al. (1996), using Equation 3.9; the equivalent noise charge was plotted as a function of FETs' gate leakage current (which is part of gate current I_G as is explained in **Section 3.4.3**) with τ as a parameter. The transistor's gate leakage current is a source of parallel white noise and should be minimised. It can be clearly seen from Figure 1 of Bertuccio et al. (1996) that the parallel white noise is the dominant source of noise at long shaping times and can be negligible at short τ.

The *ENC* contribution of different FETs due to the series white noise was plotted by Bertuccio et al. (1996) using Equation 3.2. The equivalent noise charge was plotted as a function of K_s with τ as a parameter, where $K_s = C_T(S_{ws})^{1/2}$, was calculated for comparison purposes. An increase in the transistor's gate intrinsic capacitance, C_i, (included in the total capacitance, C_T) causes larger drain current shot noise contributions at the output. Hence, C_i should be kept as small as possible to

limit the series white noise. As can be seen from Figure 2 of Bertuccio et al. (1996), C_i is a significant source of noise at short shaping times and can be negligible at long shaping times.

Regarding the ratio f_c/f_T, it can be seen from Equation 3.24 that it should be minimised for the $1/f$ noise to be minimised. This ratio is given by the following equation (Levinzon & Vandamme, 2011),

$$\frac{f_c}{f_T} = \frac{\mathrm{q}|V_{GS}-V_p|a_{1/f}}{\mathrm{k}T} \tag{3.25}$$

in which $\alpha_{1/f}$ is a dimensionless $1/f$ parameter (also known as the Hooge parameter) which depends on the quality of the semiconductor material and any damage present in the FET. For instance, this parameter depends on whether or not the current in the JFET flows through a region damaged by implantation (Levinzon & Vandamme, 2011). Hence, this parameter cannot be directly analytically calculated in theory, but it can be calculated, once f_c is experimentally observed, using the equation,

$$a_{1/f} = \frac{f_c 2\pi \mathrm{k}T C_i}{\mathrm{q}g_m|V_{GS}-V_p|}. \tag{3.26}$$

The corner frequency, f_c, can be obtained by measuring the equivalent input spectral voltage noise density squared (in V^2/Hz) of the JFET. This noise includes both the white series noise (**Section 3.2.1**) and the $1/f$ noise (**Section 3.2.3**). The $1/f$ parameter, $\alpha_{1/f}$, should be as small as possible to minimise the ratio f_c/f_T, as can be seen from Equation 3.25. This consequently results in requiring the transistor input capacitance, C_i, to be as low as possible, and the transistor transconductance, g_m, to be as high as possible. This is in agreement with Equation 3.24, where, by having a large value of transconductance, the series white noise spectral density is decreased and the overall *ENC* is also decreased.

Two other transistor parameters which indirectly affect the noise are the gate length, l, and the channel width, W. Both the transconductance and the transistor input capacitance are proportional to the channel width such that

$$g_m = \frac{Wh\mathrm{q}\mu_c N_D}{l}\left(1 - \sqrt{\frac{-V_{GS}+V_{bi}}{V_p}}\right), \tag{3.27}$$

where μ_c is the carrier mobility, V_{bi} and V_p are the built in voltage and the pinch off voltage respectively; both are defined in **Section 3.4.4**, in model calculations. The capacitance for a one-sided abrupt junction, as the gate to channel junction can be regarded, is given by

$$C_i = \frac{Wl\varepsilon\varepsilon_0}{H(x)}, \tag{3.28}$$

where $H(x)$ is the width of the depletion region at a distance x from the source and is function of V_{GS} (Sze & Ng, 2007).

Since the goal is to have transistor input capacitance, C_i, as small as possible and the transconductance, g_m, as high as possible, as has been made clear above, there is a trade off in selecting the ideal channel width.

When the detector capacitance dominates ($C_{det} > C_i$), increasing the channel width results in only negligible increment of transistor input capacitance, while the increased transconductance leads to lower (improved) *ENC* (Spieler, 2005). When the transistor input capacitance dominates ($C_{det} < C_i$) and the width of the channel is increased, the positive contribution of the higher transconductance to the total noise is overridden by the increased transistor input capacitance, C_i. It should be noted here that in the capacitively matched case ($C_{det} = C_i$), the total *ENC* is minimized (see **Section 3.4.2**).

Since the transistor input capacitance, C_i, is proportional to the gate length (Equation 3.28), it is decreased as gate length, l, is decreased resulting in higher transition frequency, f_T (Equation 3.13). Furthermore, a smaller gate length results in a higher transconductance (Equation 3.27). Hence, decreasing the channel length has a positive effect at both the series white noise and 1/f noise. However, the smaller the gate length, the higher the drain current, I_{Dr}, becomes (Bar-Lev, 1993), i.e.

$$I_{Dr} \propto \frac{1}{l}. \tag{3.29}$$

Since part of the gate to channel leakage current (which is part of I_G as explained in **Section 3.4.3**) is a linear function of drain current, I_{Dr}, it increases with decreased gate length, l, (Oxner, 1989) (the total I_G is analysed in **Section 3.4.3**). This results in increased parallel white noise.

Moreover, the transition frequency, f_T, in the non-saturated case, f_{Tns}, is given by (Sze, 1981) as

$$f_{Tns} = \frac{\mu_c V_{DS}}{2\pi l^2}, \tag{3.30a}$$

and in the saturation case as

$$f_{Ts} = \frac{v_s}{2\pi l}, \tag{3.30b}$$

where μ_c is the majority carrier mobility (electron mobility in an n-type channel and hole mobility in a p-type channel JFET (Bar-Lev, 1993)). The non-saturated case refers to relatively low internal (to the device) electric field, E, where the proportionality of the carrier velocity, v_c, to the magnitude of the electric field still holds (Bar-Lev, 1993). For higher electric fields, the carrier velocity equals the saturation velocity, v_s, and does not further increase with electric field increment. The trade off in selecting the gate length, l, has been already discussed. Maintaining a high transition frequency requires high carrier mobility in the channel (Equation 3.30a). However, for short channel length JFETs, the carrier velocity saturates at low drain to source voltages, V_{DS}, and the transition frequency becomes proportional to the saturation velocity (Equation 3.30b). Hence, materials with higher carrier saturation velocity are advantageous.

3.4.2 Matching detector and transistor capacitance

The requirements for the JFET's parameters in the case where the detector's capacitance, C_{det}, was negligible were discussed in **Section 3.4.1**. However, in this section, the detector capacitance, C_{det}, is assumed to be non-zero. Hence,

$$C_T = C_{det} + C_f + C_t + C_s + C_i = C_d' + C_i \tag{3.31}$$

where C_T is the total capacitance at the preamplifier input comprising of the input load capacitance, C_d' (the sum of detector capacitance, C_{det}, the feedback capacitance, C_f, the test capacitance, C_t, and the stray capacitance, C_s) and the input transistor capacitance, C_i.

Starting from Equation 3.2, it can be shown that input transistor capacitance C_i, should match the input load capacitance C_d'. Substituting the series white noise spectral density (Equation 3.3) into Equation 3.2, ENC_{WS} is shown to be

$$ENC_{WS} = \frac{1}{\mathrm{q}}\sqrt{\frac{A_1}{2}\gamma\frac{4\mathrm{k}T}{g_m}C_T^2\frac{1}{\tau}}. \tag{3.32a}$$

Substituting the transconductance from Equation 3.13 into the above Equation 3.32a and rearranging, it is found that

$$ENC_{WS} = \frac{1}{\mathrm{q}}\sqrt{\frac{A_1}{2\tau}\gamma\frac{4\mathrm{k}T}{f_T 2\pi}}\frac{C_T}{\sqrt{C_i}}. \tag{3.32b}$$

Substituting C_T from Equation 3.31 into Equation 3.32b gives

$$ENC_{WS} = \frac{1}{\mathrm{q}}\sqrt{\frac{A_1}{2\tau}\gamma\frac{4\mathrm{k}T}{f_T 2\pi}}\frac{C_d'+C_i}{\sqrt{C_i}}. \tag{3.32c}$$

Taking the square root, squaring C_d' and C_i, and rearranging, it can be shown that

$$ENC_{WS} = \frac{1}{\mathrm{q}}\sqrt{\frac{A_1}{2\tau}\gamma\frac{4\mathrm{k}T}{f_T 2\pi}}\left(\sqrt{C_d'}\sqrt{\frac{C_d'}{C_i}}+\sqrt{C_i}\sqrt{\frac{C_i}{C_i}}\right). \tag{3.32d}$$

Substituting the fraction C_i/C_i (= 1) with the fraction C_d'/C_d' (= 1) gives

$$ENC_{WS} = \frac{1}{\mathrm{q}}\sqrt{\frac{A_1}{2\tau}\gamma\frac{4\mathrm{k}T}{f_T 2\pi}}\sqrt{C_d'}\left(\sqrt{\frac{C_d'}{C_i}}+\sqrt{\frac{C_i}{C_d'}}\right), \tag{3.32e}$$

and further substitution of the fraction C_d'/C_i with the parameter m results in

$$ENC_{WS} = \frac{1}{\mathrm{q}}\sqrt{\frac{A_1}{2\tau}\gamma\frac{4\mathrm{k}T}{f_T 2\pi}}\sqrt{C_d'}\left(m^{1/2}+m^{-1/2}\right). \tag{3.33}$$

Substituting A_f (Equation 3.12) into Equation 3.11 and rearranging as above, gives

$$ENC_{1/f} = \frac{1}{\mathrm{q}}\sqrt{A_2\gamma 2\mathrm{k}T\frac{f_c}{f_T}C_d'}\left(m^{1/2}+m^{-1/2}\right). \tag{3.34}$$

In order to minimise the white series noise and the 1/f noise, transistors with high f_T (Equation 3.13) and low ratio f_c/f_T (Equation 3.25) are required. Regarding the ideal transistor, high f_T is achieved with high transconductance, g_m, and low input capacitance, C_i, as seen from Equation 3.13.

However, it can be seen from Eqs. 3.33 and 3.34, that low white series and 1/f noise requires capacitively matching the transistor with the input load capacitance, C_d'. Consequently, the ideal

transistor has an input capacitance, C_i, which depends on the detector and all other input capacitances.

Hence, when

$$C_i = C_d' = C_{det} + C_f + C_t + C_s, \tag{3.35}$$

m = 1, and consequently lower (improved) white series and 1/f noises are achieved. Overall, the aim is to decrease C_d' as much as possible and then match the transistor input capacitance C_i to that value.

3.4.3 Gate current

The characteristics of the ideal input FET, in terms of noise, have been discussed in the previous sections. However, the requirements for the input JFET are also affected by the specific application. In preamplifier circuits where an n-type channel JFET is used in the forward bias mode (a p-type channel JFET can also be employed in the forward bias mode) there is no feedback resistor (Bertuccio et al., 1993) and consequently the parallel white noise is reduced. However, the operating bias point (V_{GS}) in this specific configuration sets the gate current, I_G, the transconductance, g_m, and the transistor input capacitance, C_i.

In the conventional (i.e. reverse bias) mode of a JFET, ideally, the current flowing at the gate, I_{GRM}, is zero. However, in a real transistor, there are three components which constitute the gate current (Evans, 1981). Two of them are the leakage current flowing at the gate to drain junction, I_{DGl}, and the leakage current flowing at the gate to source junction, I_{GSl}, whose directions depend on whether the JFET has an n-type channel or p-type channel. Leakage current flows from drain to gate and from source to gate region at an n-type channel JFET, and from gate to drain and gate to source at a p-type channel JFET. They result from two processes: thermal ionisation (generation) of carriers within the depletion regions of the junctions and diffusion of minority carriers due to reverse biasing. The third component, I_3, results from carriers generated in the drain to gate depletion region from impact ionisation by the drain current carriers. This current, I_3, is linear function of I_{Dr} and an exponential function of V_{DG} (Evans, 1981). The summation of the drain to gate leakage current, I_{DGl}, and I_3 is termed the total drain to gate current,

$$I_{DG} = I_{DGl} + I_3, \tag{3.36}$$

and the total gate current , I_{GRM}, when the JFET operates in the reverse (conventional) mode is given by

$$I_{GRM} = I_{GSl} + I_{DG}. \tag{3.37}$$

When the JFET is used in forward bias mode (i.e. with the gate slightly positive), in a feedback resistorless preamplifier, the gate to source junction conducts like a normal diode, and I_{GS} is formed from majority carriers (rather than being the leakage current I_{GSl} resulting from the diffusion of minority carriers). The drain to source junction is still reverse biased, and leakage current, I_{DGl}, flows. The third component, I_3, is still present. The gate to channel current, I_{GFM}, consists of the summation of these three components, and all of them contribute to the parallel white noise (Equation 3.10).

In this mode, the input FET is forward biased by the leakage current of the detector, I_{LD}, which enters the preamplifier at the gate of the FET and also the current from drain to gate I_{DG}. Both currents flow from gate to source junction, and their summation is termed the total gate to source current,

$$I_{GS} = I_{LD} + I_{DG}. \tag{3.38}$$

The total gate current when the JFET is used in the forward bias mode, I_{GFM}, is given by

$$I_{GFM} = I_{GS} + I_{DG} = I_{GS} + I_{DGl} + I_3. \tag{3.39}$$

By combining Eqs. 3.38 and 3.39, I_{GFM} can be obtained such that,

$$I_{GFM} = I_{LD} + 2I_{DG}. \tag{3.40}$$

A reduction of the total noise of the system is achieved by minimising all three components of Equation 3.39. The drain to gate leakage current, I_{DGl}, can be kept to a minimum by keeping the junction at low temperature but unfortunately this might not always be a practical option; as a consequence, wide bandgap JFETs (**Section 3.4.4**) are expected to find much use in preamplifiers for high temperature environments. As an approximation in Si, thermal ionisation of carriers double in magnitude for each 10° C temperature increase (Evans, 1981). The third component of Equation 3.39, I_3, is decreased as the drain current, I_{Dr}, decreases. Since the input JFET is used in the saturation region, and the drain current in saturation is proportional to drain to source saturation current with gate shorted, I_{DSS}; thus a JFET with relatively small I_{DSS} should be used (Bar-Lev, 1993).

3.4.4 Wide bandgap materials

In this section, the advantages of a JFET made from a wide bandgap material such as 6H-SiC (E_G = 3.08 eV (Shur et al., 2006)) (rather than Si, E_G = 1.12 eV (Bludau et al., 1974)) are examined. This is done by computing the noise contributions of JFETs of identical geometry made from different materials (6H-SiC and Si). The noise arising from a previously reported n-type channel 6H-SiC JFET was computed at different shaping times and room temperature when operating with V_{DS} in the saturation region and slightly forward bias V_{GS}. Thereinafter, the noise arising from the same geometry JFET made of Si was calculated and compared to the former case.

An epitaxial n-type channel 6H-SiC JFET was considered (Neudeck et al., 2009). Its channel length, width and height were l = 10 μm, w = 100 μm, and h = 0.3 μm respectively; the donor concentration in the channel, N_D, and the acceptor concentration in the gate, N_A, were 1×10^{17} cm^{-3} and 2×10^{19} cm^{-3}, respectively (Neudeck et al., 2009).

3.4.4.1 Model calculations

The noise contribution was computed using Equation 3.24. The input capacitance, C_i, was calculated using Equation 3.28; it was assumed that only the gate to source junction capacitance contributes to the transistor's input capacitance (see **Section 3.2.1**). Hence,

$$C_i \approx \frac{W(l/2)\varepsilon\varepsilon_0}{W_{GS}} \tag{3.41}$$

where W_{GS} (depletion region width of the slightly forward biased gate to source junction) was calculated, in accordance with Sze and Ng (2007), by

$$W_{GS} = \sqrt{\frac{2\varepsilon\varepsilon_0}{\mathrm{q}N_D}(-V_{GS} + V_{bi})}. \tag{3.42}$$

The built in potential between the gate to channel p-n junction, V_{bi}, equals

$$V_{bi} = \frac{\mathrm{k}T}{\mathrm{q}} \ln \frac{N_D N_A}{n_i^2} \tag{3.43}$$

in which N_A is the doping concentration of the p-type gate (in an n-channel JFET) and n_i is the intrinsic carrier concentration given by

$$n_i = \sqrt{N_C N_V} e^{-E_G/2\mathrm{k}T}. \tag{3.44}$$

N_c and N_v are the effective density of states in the conduction and valence bands respectively (Sze & Ng, 2007). The transconductance, g_m, was calculated using Equation 3.27. The ratio f_c/f_T was calculated using Equation 3.25.

The dimensionless $1/f$ parameter, $a_{1/f}$, depends on the quality of the JFET's material and material damage (Levinzon & Vandamme, 2011), as has been discussed in **Section 3.4.1**. The $a_{1/f}$ values often observed after 1980 for Si JFETs are $10^{-8} < a_{1/f} < 10^{-6}$ (Levinzon & Vandamme, 2011). For SiC JFETs, this value has typically been measured to be higher, reaching a value of $a_{1/f} \approx 10^{-6}$ after proper annealing (Palmour et al., 1996) (Levinshtein et al., 2002). Since this dimensionless parameter cannot be analytically calculated based on the geometry and the material of each device, moderate values of 10^{-7} and 10^{-6} were used for the Si and 6H-SiC JFETs, respectively.

The gate current was computed from Equation 3.40 taking into account only the contribution of the input JFET ($I_{LD} = 0$) such that

$$I_{GFM} = 2I_{DG} = 2(I_{DGl} + I_3), \tag{3.45}$$

where the leakage current at the drain to gate junction was computed by

$$I_{DGl} = A_{DG}\left(\frac{\mathrm{q}D_p n_i^2}{L_p N_D} + \frac{\mathrm{q}D_n n_i^2}{L_n N_A} + \frac{\mathrm{q}n_i W_{DG}}{\tau_g}\right) \tag{3.46}$$

where A_{DG} is the cross sectional area of that junction (Sze & Ng, 2007). The sum of the first two terms in Equation 3.46 is the saturation current due to diffusion, I_{diff}, (holes diffuse to n-type and electrons to p-type). The third term is the generation current due to reduction in carrier concentration under reverse bias, I_{gen} (Sze & Ng, 2007). The hole diffusion coefficient, D_p, and the electron diffusion coefficient, D_n, were computed from the Einstein relations

$$D_p = \frac{\mathrm{k}T}{\mathrm{q}}\mu_h \tag{3.47a}$$

and

$$D_n = \frac{\mathrm{k}T}{\mathrm{q}}\mu_e, \tag{3.47b}$$

where μ_h and μ_e are the hole and electron mobility in the semiconductor material. The hole diffusion length, L_p, and the electron diffusion length, L_n, were computed using the hole lifetime, τ_p, and electron lifetime, τ_n, (Sze & Ng, 2007), such that

$$L_p = \sqrt{D_p \tau_p} \tag{3.48a}$$

and

$$L_n = \sqrt{D_n \tau_n}. \tag{3.48b}$$

The generation current takes place in the depletion region at the reverse biased drain to gate junction, which has a depletion layer width,

$$W_{DG} = \sqrt{\frac{2\varepsilon\varepsilon_0}{qN_D}(V_{DG} + V_{bi})}. \tag{3.49}$$

The generation carrier lifetime τ_g in Equation 3.46 was calculated by

$$\tau_g = \left(1 + \frac{n_{con}}{n_i}\right)\tau_p + \left(1 + \frac{p_{con}}{n_i}\right)\tau_n \tag{3.50}$$

where p_{con} and n_{con} are the hole and electron concentrations in the depletion region and are both functions of the applied voltage and the distance from the two boundaries of the depletion region and the n and p sides (Sze & Ng, 2007). For a given applied voltage, V_{DG}, the electron concentration, n, starts from a maximum value of n_n (= N_D) at the boundary of the depletion region with the n side and decreases to a minimum value of n_p at the boundary of the depletion region with the p-type side, where, in accordance with Sze (1981),

$$n_p = \frac{n_i^2}{N_A} e^{\left(qV_{DG}/kT\right)}. \tag{3.51}$$

Similarly, for a given applied voltage, V_{DG}, the hole concentration, p, starts from a maximum value of p_p (= N_A) at the boundary of the depletion region with the p side and decreases to a minimum value of p_n at the boundary of the depletion region with the n-type side, where, as per Sze (1981),

$$p_n = \frac{n_i^2}{N_D} \mathrm{e}^{\left(\mathrm{q}V_{DG}/\mathrm{k}T\right)}. \quad (3.52)$$

Since the product $n_{con}p_{con}$ of the electron and hole concentration is constant for a given applied voltage at both the boundaries of the depletion region as well as at all the intermediate points, the electron and hole concentration at the boundary of the depletion region with the n-type side was used to calculate the generation lifetime, τ_g (Equation 3.50).

The impact ionisation current, I_3, is normally negligible at low V_{DG}, where the leakage current of the junction is dominant (Evans, 1981). Moreover, I_3 decreases with increasing temperature due to its dependant on carrier mobility. For simplicity reasons, the impact ionisation current I_3 is considered negligible in the present calculations. The impact ionisation multiplication process is characterised by the impact ionisation coefficient defined as the number of electron-hole pairs generated by a carrier per unit distance travelled (Sze & Ng, 2007). This coefficient (differs between electrons and holes) is a strong function of the material, the temperature, the electric field strength and it decreases with increasing bandgap. As an example, the hole impact ionisation coefficient was calculated to be ~10^4 cm^{-1} at an internal electric field of 2.7 × 10^6 V/cm and 0.4 × 10^6 V/cm for 6H-SiC (Raghunathan & Baliga, 1999) and Si (Massey et al., 2006) at room temperature, respectively. Hence, the impact ionisation current, I_3, is smaller at a 6H-SiC JFET compared to a Si JFET operating under the same bias conditions and temperature. The linear function of the impact ionisation current with the drain to source current, I_{Dr}, implies that JFETs with lower I_{Dr} are favourable. The drain current at saturation region I_{Dsat} was computed by

$$I_{Dsat} = \frac{W\mu_c \mathrm{q}^2 h^3}{6\varepsilon\varepsilon_o l} N_{Deff} n_{ch} \left[1 - 3\left(\frac{(-V_{GS}+V_{bi})}{V_p}\right) + 2\left(\frac{(-V_{GS}+V_{bi})}{V_p}\right)^{3/2}\right], \quad (3.53)$$

where the effective donor concentration N_{Deff} at the channel is approximately equal to N_D, and n_{ch} is the electron concentration at the channel region which equals to N_D for Si at room temperature (where the carrier concentration is fully activated). The ionised carrier concentration in the channel, n_{ch}, is much lower than N_D, for the 6H-SiC JFET, at room temperature (not all carriers are activated); it was computed to be 9 × 10^{15} cm^{-3} based on experimental results according Neudeck et al. (2009).

3.4.4.2 Material properties

The values of the materials' properties used in the modelling can be seen at **Table 3.1**. It should be noted that the parameters given are temperature, T, and dopant concentration dependent. Consequently, the used values should be adjusted for conditions other than those stated.

3.4.4.3 Computed parameters

In this paragraph, the computed JFET's parameters using the equations described in Model calculations paragraph of **Section 3.4.4** are presented and discussed. For equality of comparison, both JFETs are assumed to have the same geometry and doping concentrations. All calculations are done for T = 25 °C, V_{GS} = 0.2V (slightly positive gate as required in a feedback resistorless preamplifier (Bertuccio et al., 1993)) and V_{DS} = 9 V (JFET operating in saturation region i.e. $V_{DS} \geq V_p - V_{bi}$ and thus $I_{Dr} = I_{Dsat}$), unless otherwise specified. A comparison between the computed parameters for the two JFETs is presented in **Table 3.2**.

Parameter	Si	6H-SiC
Dielectric constant	11.90	9.66
Bandgap (eV)	1.12	3.08
Effective density of states in the conduction band (m^{-3})	2.8×10^{25}	9.0×10^{24}
Effective density of states in the valence band (m^{-3})	2.65×10^{25}	2.5×10^{25}
Electron mobility (m^2/Vs)	0.1500	0.0400
Hole mobility (m^2/Vs)	0.0480	0.0100
Electron lifetime (s)	$>10^{-3}$	5×10^{-7}
Hole lifetime (s)	10^{-3}	7×10^{-7}
Dissipation Factor	2×10^{-3}	4×10^{-4}

Table 3.1. Values of properties used in this study for Si and 6H-SiC for T = 25 °C, $N_D = 1 \times 10^{17}$ cm^{-3} and $N_A = 2 \times 10^{19}$ cm^{-3} (Patrick & Choyke, 1970) (Tuagi & Overstraeten, 1982) (Levinshtein et al., 2001) (Shur et al., 2006) (Sze & Ng, 2007) (Hartnett et al., 2011) (Owens, 2012a) (Jung et al., 2014). The electron lifetime, hole lifetime, and dissipation factor of 4H-SiC was used instead of 6H-SiC.

	Si JFET	6H-SiC JFET
Intrinsic carrier concentration (m^{-3})	9.69×10^{15}	1.97×10^{-1}
Built in voltage (V)	0.97	2.96
Input Capacitance (pF)	0.52	0.25
Transconductance (mS)	4.47	0.82
Corner frequency over transition frequency	2.57×10^{-5}	3.18×10^{-4}
Gate current (pA)	0.11	9×10^{-32}
Drain current (mA)	11.3	0.2

Table 3.2. Comparison between computed parameters for the Si and the 6H-SiC devices.

Due to its wider bandgap, 6H-SiC has much lower intrinsic carrier concentration n_i (Equation 3.44) compared to Si at a given temperature (here T = 25 °C). In other words, fewer carriers are thermally generated in 6H-SiC than in Si. This has a number of effects.

First of all, smaller n_i results in higher built in voltage V_{bi} (Equation 3.43) which in turns results in lower input capacitance, C_i (Equation 3.41), i.e. the gate to source depletion region is wider in the 6H-SiC JFET compared to Si JFET when operating with V_{DS} in the saturation region and slightly forward bias V_{GS} (normal conditions in a feedback resistorless charge sensitive preamplifier). The biggest effect of the intrinsic carrier concentration is at the gate current (Equation 3.46), as it can be seen in **Table 3.2**. The gate current (with the impact ionisation current, I_3, excluded) in the SiC JFET is 30 orders of magnitude lower than the Si JFET at a temperature of 25 °C. For higher drain to source voltages, V_{DS}, where the impact ionisation component dominates, the difference between the gate current in the Si and SiC JFETs becomes even bigger due the linear dependency of the impact ionisation current on the drain current I_{Dr} (~ 50 times greater in the Si JFET than in the 6H-SiC JFET). The effect of the gate length, l, on the equivalent noise charge was discussed in **Section 3.4.1**. Although decreasing the gate length results in higher drain current at saturation region I_{Dsat} (Equation 3.53), which in turn increases the gate current (due to larger I_3), this effect is smaller in wide bandgap semiconductor JFETs than it is in Si JFETs.

As far as the transconductance is concerned, the higher electron mobility in Si has a more positive effect in its transconductance compared to the 6H-SiC transconductance (Equation 3.27). Also, the ratio between the corner and transition frequency, f_c/f_T, has been found to be higher in the SiC JFET than in the Si JFET, resulting in poorer (greater) 1/f noise. This is due to the lower 1/f parameter, $\alpha_{1/f}$, in Si compared to 6H-SiC.

3.4.4.4 Equivalent noise charge

The equivalent noise charge, *ENC*, arising from the input JFET was calculated using Equation 3.24, and the parameters computed for both JFETs using the equations from **Section 3.4.4**. The calculated overall *ENC* for both JFETs as a function of the shaping time, τ, at T = 25 °C can be seen in **Figure 3.1**.

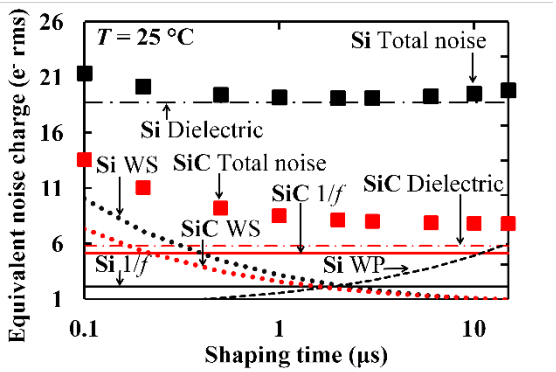

Figure 3.1. Calculated equivalent noise charge for the 6H-SiC JFET reported in Neudeck et al. (2009) (red symbols) and a Si JFET (black symbols) having the same geometry at a temperature, T, of 25 °C (contribution of only the input JFET is included). Total noise (squares); White parallel (WP) noise (square dots); White series (WS) noise (round dots); $1/f$ noise (solid line); Dielectric noise (long dash dots). The white parallel noise of the 6H-SiC JFET is not included in the graph since its contribution is less than 1 e^- rms.

For the Si JFET, its sub-microsecond *ENC* is limited by its dielectric noise and by its white series noise (arising from the ratio C_i^2/g_m). As the shaping time increases ($\tau > 3$ μs), the white parallel noise (arising from the gate current) becomes higher than the white series noise, with the dielectric noise being the dominant source of noise.

The 6H-SiC JFET is also limited by its white series noise in the sub-microsecond shaping time range. Although the $1/f$ series noise is higher in the 6H-SiC JFET than in Si JFET, the overall computed *ENC* of the 6H-SiC device is less than that of the Si device due to the lower input capacitance and lower dissipation factor of 6H-SiC compared to Si resulting in lower white series noise and dielectric noise.

In contrast with the Si JFET, as the shaping time becomes longer, the overall *ENC* for the 6H-SiC JFET decreases. At long shaping times the white parallel noise dominates. Since the gate current in the 6H-SiC JFET is negligible, a shaping time increase reduces the equivalent noise charge arising from the 6H-SiC device, reaching the lower limit set by the dielectric and $1/f$ noise, as shown in **Figure 3.1**.

The contribution of the white parallel noise to the overall *ENC* for the Si JFET is emphasized below. The ENC_{WP} was computed for the Si device at $T = 25$ °C using the parameters stated at **Table 3.1**. Although these parameters are temperature dependent, they can be regarded unchanged for small temperature changes. Hence, making the assumption that the parameters of **Table 3.1** are stable for the temperature range 25 °C ± 10 °C, the equivalent noise charge

contribution due to white parallel noise was calculated at the same temperature range for the Si JFET and τ = 10 μs. The calculated ENC_{WP} for the Si device at different temperatures and bias conditions can be seen in **Figure 3.2**.

At room temperature, the generation current, I_{gen}, dominates in Si, rather than the diffusion current, I_{diff} (Sze & Ng, 2007). At a given temperature, I_{gen} is proportional to the gate to drain depletion layer width, W_{DG}, (Equation 3.46) which, in turn, is proportional to the square root of the applied voltage, V_{DG} (Equation 3.49). It can be further seen that ENC_{WP} is highly dependent on T. For a 10 °C temperature rise (from 25 °C to 35 °C), the equivalent noise charge contribution due to white parallel noise (arising from gate current) increased from 5 e^- rms to 10 e^- rms, when τ = 10 μs and the JFET is under normal operating conditions (i.e. in saturation region with the gate slightly positive). The dependency of the ENC_{WP} to T can be explained as follows: the generation current, I_{gen}, which dominates at this temperature range, highly depends on the intrinsic carrier concentration n_i (Equation 3.46). The temperature dependence of the intrinsic carrier concentration (Equation 2.35) shows its relation with the bandgap, E_G.

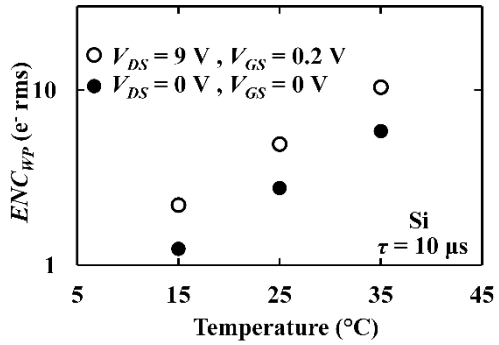

Figure 3.2. Calculated equivalent noise charge contribution due to white parallel noise for the Si JFET at τ = 10 μs under two bias conditions; V_{DS} = 9 V, V_{GS} = 0.2 V (open circles) and V_{DS} = 0 V, V_{GS} = 0 V (filled circles).

Including the function of the generation carrier lifetime, τ_g, (Equation 3.50) with temperature, the current at the drain to gate junction of the Si JFET used in this study, biased at V_{DS} = 9 V and V_{GS} = 0.2 V, quintupled increasing from 0.1 pA to 0.5 pA as the temperature increased from 25 °C to 35 °C. The current in the drain to gate junction of the 6H-SiC JFET, under the same biasing conditions, remained negligible at 35 °C (as it was at 25 °C), resulting in a white parallel ENC < 1 e^- rms.

3.4.4.5 Conclusion

To elucidate the JFETs contribution to noise in charge sensitive preamplifiers for X-ray and electron spectroscopy, and demonstrate the importance of wide bandgap material for the preamplifier input transistor as well as for the detector, a model for computing the equivalent noise charge contribution of the input JFET of a charge sensitive preamplifier without the feedback resistor has been presented, with examples computed for 6H-SiC and Si JFETs of identical geometry. Given the material and geometry of the JFET (channel length, width, and height), and the doping concentration at the channel and gate, the model enabled computation of the equivalent noise charge with varied temperature, shaping time and bias condition of the JFET. Using this model, it has been shown that a JFET made of 6H-SiC has lower noise contribution compared to the same geometry JFET made of Si. This was mostly attributed to the higher dissipation factor and gate current presented in the Si device compared to 6H-SiC at $T = 25$ °C, with the latter being limited by its dielectric and $1/f$ noise. Also, the large dependence of the white parallel noise to small increments in temperature has been underlined which makes the use of a wide bandgap JFET at elevated temperatures particularly advantageous. It should be noted here that the above results are based on analytical theory, and experimentally determined values might be different due to non-idealities in the devices.

3.5 Contribution of detector

As it has already been discussed, the detector itself sets the fundamental energy resolution limit of a non-avalanche semiconductor spectrometer, given the detector's Fano noise (see **Section 2.3.2**). Furthermore, this statistical limit may be further degraded by noise from incomplete charge collection (see Equation 3.1). This is a result of carrier trapping and recombination (Owens, 2012a) (Lowe & Sareen, 2014). Crystal imperfections, also termed as defects, such as impurity atoms, vacancies, and dislocations introduce state into the crystal which can either trap one charge (electron or hole), or trap both an electron and a hole (recombination), in which this latter case the carriers annihilate each other (Spieler, 2005). The result of carrier trapping and recombination may be the loss of generated carriers from the radiation detection. Hence, the charge that is induced at the electrodes, Q_i, is less than the generated charge, Q. The fraction Q_i/Q is described as the charge collection efficiency, *CCE*, and it depends on the distance of the charge creation to the corresponding electrode and on the carrier drift lengths. The carrier drift lengths are directly proportional to the carrier mobilities, lifetimes, and applied electric field. Consequently, it can be said that materials with high mobility-lifetime product present less trapping than materials with low mobility-lifetime product. The degradation of the mobility-lifetime product can be explained by the presence of impurities, vacancies, dislocations as well as plastic deformation for the softer materials (Owens, 2012a). An increased applied electric field improves the carrier drift lengths and hence their transport resulting in less trapping

and incomplete charge collection noise. It should be noted that, although when trapped carriers are released in a time shorter than the charge collection time they contribute to the signal, they still introduce fluctuations in the signal.

Compared to Fano noise and to the different electronic noise contributions, the incomplete charge collection noise is more difficult to predict/calculate. This is because it depends on the trapping centre density and the charge collection and diffusion properties of the semiconductor detector. Although the broadening of detected spectral lines due to incomplete charge collection is an asymmetric process (Fraser, 1989), since incomplete charge collection noise is directly proportional to the energy of the incoming photons, the distribution of the incomplete charge collection noise, R, is regarded normal (symmetric) for low to intermediate energies (Owens, 2012a). Semiempirical formulas, determined by best fitting for planar detectors (Henck et al., 1970), coaxial detectors (Owens, 1985) and a general analytical expression including the effects of geometry (Kozorezov et al., 2005) have been proposed.

The detector itself also contributes to the electronic noise. Its capacitance, C_{det}, is included in the total capacitance of the system, C_T (see **Section 3.2.1** and Equation 3.31). Hence, it directly affects the white series noise and 1/f noise contributions (Equation 3.19). Both the white series and 1/f noise are minimised with a low detector capacitance (Eqs. 3.33 and 3.34). Also, they are further reduced when the input load capacitance, C_d', which includes the detector capacitance, is matched with the preamplifier's input transistor capacitance.

The leakage current of the detector, I_{LD}, impacts the white parallel noise (Equation 3.19). Detector leakage current, I_{LD}, can vary from < 1 pA (Bertuccio & Caccia, 2007) to ~ nA or more, depending on detector type and temperature. The white parallel noise is minimised by using a detector with low leakage current. In the forward biased mode of t he input transistor of the preamplifier (feedback resistorless preamplifier (Bertuccio et al., 1993)), the leakage current of the detector, I_{LD}, flows at the gate to source junction of the input JFET consisting part of the noisy gate current, I_{GFM} (Equation 3.40). The contributions of these two components to the parallel white noise (Equation 3.10), I_{LD} and I_{GFM}, are regarded separately due to there being two statistically independent shot noises which arise from them (i.e. shot noise of I_{LD} and shot noise of I_{GFM}).

Chapter 4 4H-SiC UV Schottky Photodiodes

4.1 Introduction and background

UV detection using 4H-SiC photodiodes may lead to a variety of advantages, due to its inherent properties. Its wide bandgap (E_G = 3.27 eV) results in low intrinsic carrier concentration (Equation 1.1) and effectively in lower leakage current density at a given temperature, compared to narrower bandgap materials. Reduced thermionic emission leakage current in Schottky photodiodes can also be achieved with 4H-SiC due to its relatively low electron affinity (3.17 eV (Davydov, 2007)) resulting in relatively high Schottky barrier heights (Equation 2.24) compared to Si, which has an the electron affinity of 4.05 eV (Sze & Ng, 2007). 4H-SiC UV photodiodes can operate in visible and IR backgrounds without the use of filters due to their intrinsic insensitivity to photons of energy smaller than (photons of wavelength longer than) their bandgap (3.27 eV = 380 nm) (Yan et al., 2004). Additionally, 4H-SiC should be more radiation hard than Si due to 4H-SiC high displacement threshold energy (21.8 eV (Owens, 2012a)), making it suitable for operation in intense radiation environments. Indeed, experimental results showed that no significant degradation of the charge collection efficiency and compensation of the conductivity of 4H-SiC epitaxial layers was observed after irradiation with α particles, electrons, γ-rays even at very high doses as well as with 8 MeV protons (up to 3×10^{14} p/cm^2 fluency) and 1 MeV neutrons (up to 5×10^{13} n/cm^2 fluency), as it is summarized by Nava et al. (2008).

Work has been conducted for the development of high performance 4H-SiC UV photodiode detectors. Results for both 4H-SiC p^+-i-n^+ UV photodiodes (Chen et al., 2006) (Cai et al., 2014) and 4H-SiC UV photodiodes (Yan et al., 2004) (Hu et al., 2006) (Watanabe et al., 2012) have been reported which showed their performance under dark and UV illumination.

In 2006, a new UV photodiode detector structure was introduced; vertical 4H-SiC Schottky UV detectors employing self-aligned nickel silicide (Ni_2Si) interdigit contacts showed higher UV responsivity (0.16 A/W at 256 nm) and internal quantum detection efficiency (78 % at 256 nm) than the same area planar semiconductor-metal 4H-SiC photodiodes (Sciuto et al., 2006). Following this, temperature dependent photoresponsivity measurements of vertical Ni_2Si 4H-SiC Schottky UV photodiodes showed a strong function of the long wavelength (280 nm to 380 nm) UV responsivity with temperature (Mazzillo et al., 2009). The effect of different Ni_2Si interdigitated strip pitch sizes (8 μm, 10 μm and 20 μm) on the responsivity of the 4H-SiC Schottky UV photodiodes was investigated by Adamo et al. (2014), with the photodiodes having a 10 μm pitch size showing the best results (highest photoresponsivities).

In this chapter, electrical and optical characterisation of prototype vertical 4H-SiC Schottky UV detectors with nickel silicide (Ni_2Si) interdigitated contacts are reported. Four ostensibly identical devices were randomly selected to be characterised. The interdigitated contacts allowed the active region of the devices to be directly exposed to the UV radiation, enabling high internal quantum detection efficiency. The vertical configuration allowed more efficient depletion of the interdigit structures compared to a planar configuration. An extensive electrical characterisation including forward and reverse bias dark current and capacitance measurements was conducted at temperatures from 20 °C to 120 °C, the highest reported temperature for similar devices. Responsivity measurements as a function of wavelength and applied bias are also reported and examined. The photodiodes were fabricated by researchers at STMicroelectronics-Catania (Italy) using a 4H-SiC wafer purchased from Cree Inc. Subsequent characterisation was conducted at University of Sussex.

4.2 Device structure and fabrication

The 4H-SiC wafer was supplied by Cree with a 6 μm thick n-type epitaxial layer grown on an n-type substrate. The doping concentration of the substrate was 10^{19} cm^{-3}. The dopant was N. The doping concentration of the epilayer was stated by the supplier to be 10^{14} cm^{-3}. 200 nm thick Ni Ohmic contacts were formed by sputtering followed by a rapid annealing at 1000 °C. Schottky contacts on the device front were obtained by defining Ni_2Si interdigitated structures. The interdigitated structure was chosen to allow the active region of the devices to be directly exposed to the UV radiation, enabling high internal quantum detection efficiency. The vertical configuration allowed more efficient depletion of the interdigit structures compared to a planar configuration; a vertical Schottky contact is created when the front electrodes are short cut and polarised with respect to the back-side contact, whereas a planar Schottky contact is created when the polarisation is applied between two front electrodes while the back Ohmic contact is floating. The definition of 3 μm wide Ni_2Si stripes was obtained by combining standard optical lithography and a highly selective metal etch. The pitch of the Ni_2Si stripes was 10 μm. A rapid thermal processing at 700 °C was used for the formation of Ni_2Si to improve the uniformity of the Schottky barrier with respect to that of pure Ni (Sciuto et al., 2006). A 1 μm thick AlSiCu metal layer was sputtered on the top side of the devices defining the anode contact pad and a metallic multilayer Ti-Ni-Au (100 nm/500 nm/50 nm) was sputtered on the rear of the wafer defining the cathode contact pad. **Figure 4.1** shows a simplified not to scale schematic of the device, an illustrative layers structure, and an optical microscopy top view image: photodiodes had a square geometry, each with area of (1.2 × 1.2) mm^2. The top face of each device had an area of 1 mm^2 uncovered by the contact and thus directly exposable for illumination (70 % of fill factor). The photodiodes were packaged in TO-18 cans with a suitable UV transparent quartz window.

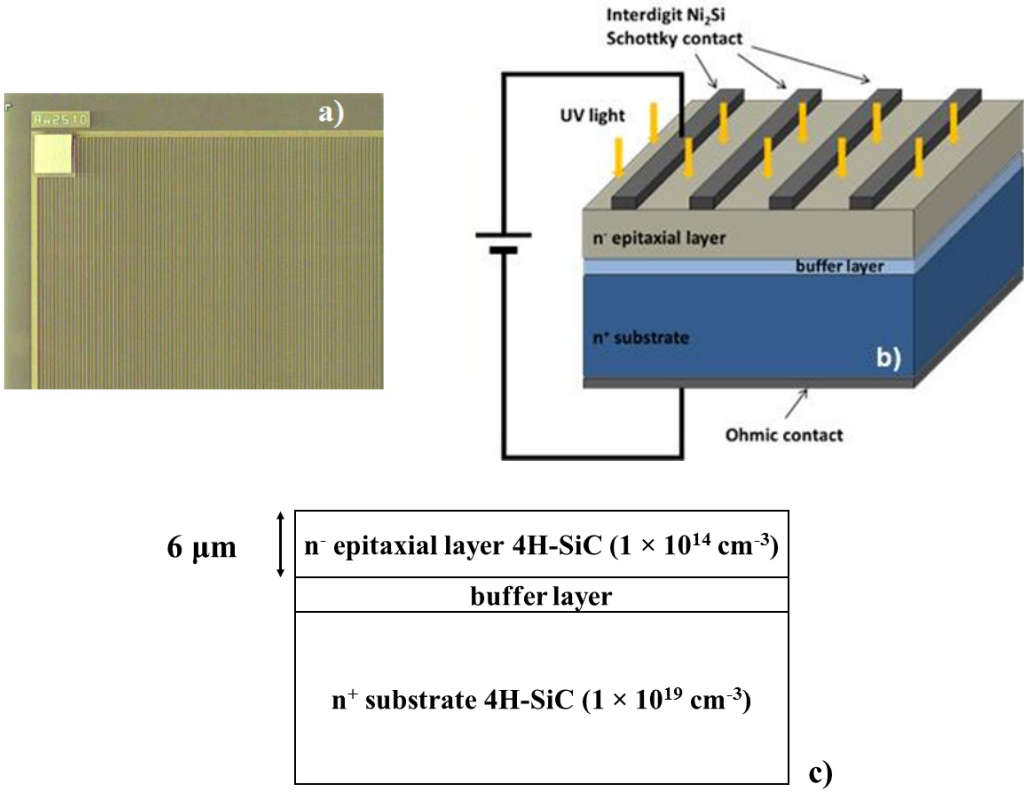

Figure 4.1. (a) An optical microscopy image, (b) a schematic side drawing, and (c) an illustrative layers structure (not in scale) of the 4H-SiC UV Schottky photodiode (Mazzillo et al., 2012) (Lioliou et al., 2015).

4.3 High temperature electrical characterisation

4.3.1 Current measurements as a function of bias

Forward and reverse biased dark current measurements as functions of applied voltage were made for the four 4H-SiC UV Schottky photodiodes (D1 to D4) at temperatures between 20 °C and 120 °C, with 20 °C steps, using a Keithley 6487 Picoammeter/Voltage Source (see **Section 2.5.1**) and a TAS Micro MT climatic cabinet. The photodiodes were packaged. To ensure thermal equilibrium, the photodiodes were left to stabilize at each temperature for 30 minutes before the measurements were started at each temperature. **Figure 4.2** shows the measured current as a function of applied forward bias for the photodiodes at room temperature. The temperature dependent current measurements as a function of applied forward bias of a representative diode, D4, are presented in **Figure 4.3**.

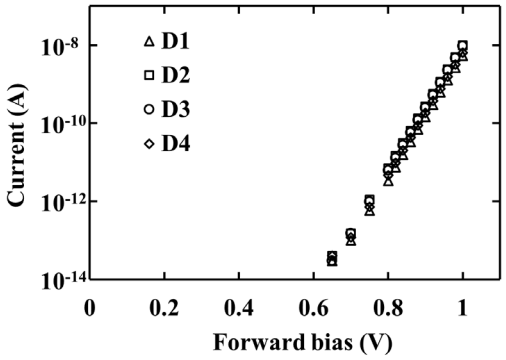

Figure 4.2. Current as a function of forward bias measured at a temperature of 20 °C for the four 4H-SiC UV Schottky photodiodes, D1 to D4. D1 (open triangles); D2 (open squares); D3 (open circles); D4 (open diamonds).

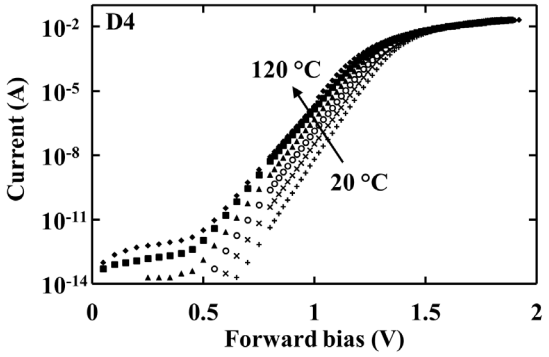

Figure 4.3. Current as a function of forward bias measured at a temperature range of 20 °C to 120 °C, for the 4H-SiC UV Schottky photodiode D4. 120 °C (filled diamonds); 100 °C (filled squares); 80 °C (filled triangles); 60 °C (open circles); 40 °C (× symbols); 20 °C (+ symbols).

The saturation current, I_{sat}, was found from extrapolating the linear region of the dark current as a function of forward bias, to the intercept point ($V_{AF} = 0$V) (Equation 2.23). Using the determined values of the saturation current for each diode, the zero band barrier height, φ_{0B}, was extracted (Equation 2.25) and using the Cheung method (Cheung & Cheung, 1986). The ideality factor, n, was extracted from the dark current as a function of forward bias measurement (Equation 2.26). As an example, the saturation current, I_{sat}, for D2 was found to be 20×10^{-25} A $\pm$ 1×10^{-25} A at 20 °C, from a single current as a function of applied forward bias measurement and linear least squares fitting, taking into account the standard deviation of the intercept. The mean saturation current, I_{sat}, of the four photodiodes, calculated using the same procedure, was 12×10^{-25} A $\pm$ 5×10^{-25} A at 20 °C. The mean zero band barrier height, φ_{0B}, of the four photodiodes was found to be 1.70 eV $\pm$ 0.01 eV at 20 °C. The computed zero band barrier height and ideality factor of D4, as a function of temperature can be seen in **Figure 4.4**.

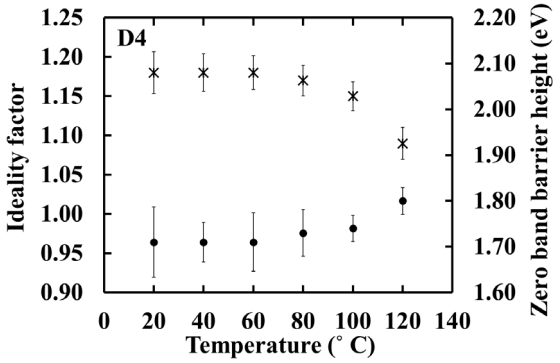

Figure 4.4. Ideality factor (stars) and zero band barrier height (filled circles) extracted from current as a function of forward bias measurements in the temperature range 20 °C to 120 °C for the 4H-SiC UV Schottky photodiode D4.

The ideality factor, n, of D4 improved from 1.18 ± 0.03 at 20 °C to 1.09 ± 0.02 at 120 °C and the zero band barrier height, φ_{0B}, increased from 1.71 eV ± 0.07 eV at 20 °C to 1.80 eV ± 0.03 eV at 120 °C. As the temperature decreased, there was a bigger deviation from the ideal (i.e. n = 1), with the barrier height to appearing to be lowered. This observation suggested the presence of an inhomogeneous barrier (Roccaforte et al., 2003a). Tung (1991) showed that the current through an inhomogeneous Schottky barrier may be expressed as the sum of currents flowing in an assortment of Schottky barrier height (SBH) patches that have low height. Tung (1991) provided an analytical form of the current flowing to and from a small SBH low patch which explains these and similar widely reported experimental results (such as from Özer et al. (2007) and Çakıcı et al. (2015)). Current transport across the metal-semiconductor interface at low temperatures is dominated by electrons surmounting the lower barriers, resulting in a larger ideality factor and a lower apparent Schottky barrier height. However, as the temperature increases, electrons have more energy to overcome higher barriers, resulting in an increase of the dominant barrier height. Tung's theory (1991) shows that the observed changes in ideality factor with temperature and barrier height with temperature are a natural result of an inhomogeneous SBH. For the investigated photodiodes reported here, the improvement of the ideality factor and the increment of the barrier height as the temperature increased can be similarly explained. The improved ideality factor, n, at 120 °C may also be attributed to the increased thermal energy of electrons as the temperature increased. This could result in the effect of traps/defects becoming less important at 120 °C compared to lower temperatures and hence, the recombination-generation current in the depletion region to decreasing at the high temperatures investigated.

The measured current, I_R, as a function of applied reverse bias, V_{AR}, of all four 4H-SiC UV Schottky photodiodes when measured at a temperature of 20 °C are shown in **Figure 4.5**. It should be noted that due to the devices' 6 µm thick epilayers, applied (reverse) biases of -50 V

created a mean electric field of 83 kV/cm across the depletion region. However, even at this field strength (83 kV/cm), the leakage current at 20 °C remained ≤ 0.2 pA (13 pA/cm^2) for three of the tested devices (D2 to D4), with D1 showing a leakage current of 2.5 pA (173 pA/cm^2). It should be noted that the leakage current measured for three of the tested devices (D2 to D4) was smaller than the uncertainty of the measurement (0.3% of the current measurement plus 0.4 pA) (see **Section 2.5**), and hence their actual leakage current was believed to be smaller than these presented in **Figure 4.5**. The higher leakage current of diode D1 measured at room temperature and applied reverse bias > -30 V, compared to the leakage current measured for the rest of the diodes (D2 to D4) suggests that a different conduction mechanism gave rise to the leakage current of D1 compared to that of the rest of the diodes (D2 to D4). Generation current in the depletion region of D1 originated from defects and edge leakage current due to high electric field at the contact periphery (see **Section 2.4.1**) could both contribute to the leakage current of D1 and further investigation is required to detangle the different conduction mechanisms as functions of applied reverse bias and temperature. These leakage current densities are much lower than typical values for Si diodes (1 nA/cm^2 at room temperature (Bertuccio et al., 2014)).

For a representative device, D4, from the set of three diodes that showed the lowest leakage currents, temperature dependent leakage current measurements as functions of applied reverse bias are shown in **Figure 4.6**. The maximum investigated temperature, 120 °C, was chosen in order to exceed the previously reported maximum temperature for leakage current measurements of similar devices (100 °C (Mazzillo et al., 2012)) but to avoid possible device damage at high temperatures under an internal electron field of 83 kV/cm (corresponding to an applied reverse bias of -50 V). At low biases, the leakage current densities for these detectors are lower than had previously been reported for similar devices with similar epilayer thicknesses; for example, Mazzillo et al. (2009) reported a leakage current density, J_R, of ~242 pA/cm^2 at -5 V, whereas device D4 from the currently reported devices had a current density of 187 pA/cm^2 at -5 V, both at 100 °C.

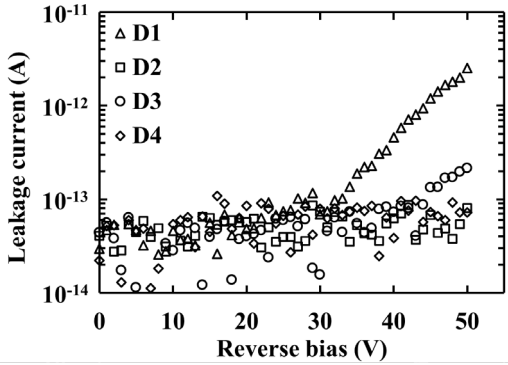

Figure 4.5. Leakage current as a function of applied reverse bias measured at a temperature of 20 °C for the four 4H-SiC UV Schottky photodiodes, D1 to D4. D1 (open triangles); D2 (open squares); D3 (open circles); D4 (open diamonds).

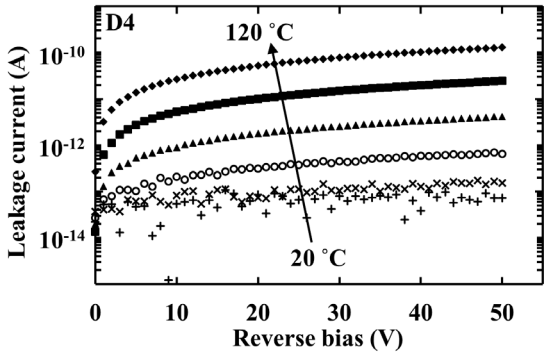

Figure 4.6. Leakage current as a function of applied reverse bias measured at a temperature range of 20 °C to 120 °C, for the 4H-SiC UV Schottky photodiode D4. 120 °C (filled diamonds); 100 °C (filled squares); 80 °C (filled triangles); 60 °C (open circles); 40 °C (× symbols); 20 °C (+ symbols).

The ideality factor of the devices was found to be close to unity suggesting that the prevailing current mechanism was thermionic emission-diffusion, excluding| tunnelling, recombination-generation, surface and metal-semiconductor interface current (see **Section 2.4.1**). Thus, the measured leakage current per unit area, i.e. the leakage current density, J_R, for one representative device, D4, as a function of temperature at three internal electric fields, was calculated and is shown in **Figure 4.7**. At the highest investigated temperature (120 °C), the current density of D4 was still low (3.6 nA/cm^2 at 33 kV/cm, 5.4 nA/cm^2 at 50 kV/cm and 8.9 nA/cm^2 at 83 kV/cm) despite the relatively high internal electric field. For comparison purposes, the leakage current of all four devices was found to be 1.7 nA/cm^2 ± 0.1 nA/cm^2, at 100 °C at a mean internal electric field of 83 kV/cm, which is comparable with those reported for other high quality Au/4H-SiC Schottky devices (e.g. ~1 nA/cm^2 at 100 °C at a mean internal electric field of 103 kV/cm (Bertuccio et al., 2011)). Although the current density showed an exponential increase as temperature increased from 40 °C to 120 °C, as a consequence of more thermally generated

carriers being present as the temperature increases, the measurement system (accuracy of the Keithley 6487 Picoammeter/Voltage Source) limited the current measurements at lower temperatures. At the highest investigated temperature (120 °C) and applied reverse bias (-50 V, corresponding to an internal electric field of 83 kV/cm), the leakage current densities of D1, D2, and D3 were measured to be 8.2 nA/cm^2, 8.3 nA/cm^2, and 8.3 nA/cm^2, respectively.

The low leakage current densities measured can be attributed in part to the high quality of the epitaxial material. The Schottky contact can also have an effect on the leakage current of the devices. The barrier height of the Ni_2Si/4H-SiC Schottky contact was measured to be 1.71 eV at 20 °C, and 1.80 eV at 120 °C. These high values resulted from the work function (see **Figure 2.8**) of Ni_2Si being ~4.8 eV (Kittl et al., 2006). Since the leakage current of a Schottky diode arises from the majority carriers (in this case e^-) at the metal side overcoming the barrier height (see **Section 2.4.1**), the low leakage currents measured is also attributable to the high barrier height formed from the Ni_2Si/4H-SiC contact. A similar explanation was given by Roccaforte et al. (2003b), where Ni_2Si/4H-SiC Schottky diodes had a higher barrier height and significantly lower leakage current than Ti/4H-SiC Schottky diodes.

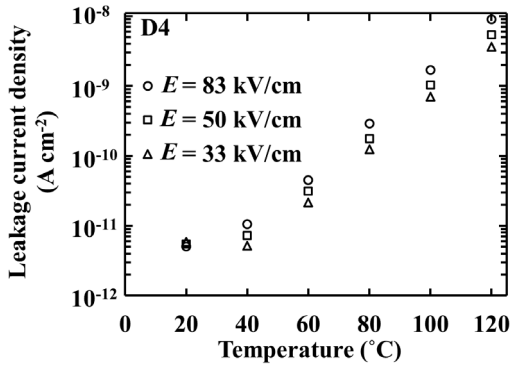

Figure 4.7. Measured leakage current density as a function of temperature at three electric fields of the 4H-SiC UV Schottky photodiode, D4.

4.3.2 Capacitance measurements as a function of bias

To determine the depletion width and the doping concentration of the photodiodes, the devices' capacitances were investigated as functions of applied forward and reverse bias and temperature (20 °C to 120 °C) using an HP 4275A Multi Frequency LCR meter (see **Section 2.5.2**), and a TAS Micro MT climatic cabinet. The LCR meter test signal was sinusoidal with a 50 mV rms magnitude and 1 MHz frequency. Capacitance measurements were made at forward biases between 0 V and 1 V and at reverse biases between 0 V and -50 V. The capacitance of the package was determined by measuring three empty pins at empty packages of identical type; the packaging capacitance was found to be 0.61 pF ± 0.02 pF. **Figure 4.8** shows the measured

capacitance as a function of applied forward and reverse bias of the four photodiodes (packaging capacitances subtracted) when measured at 20 °C, and **Figure 4.9** shows the measured capacitance for one representative device, diode D4, at temperatures from 20 °C to 120 °C.

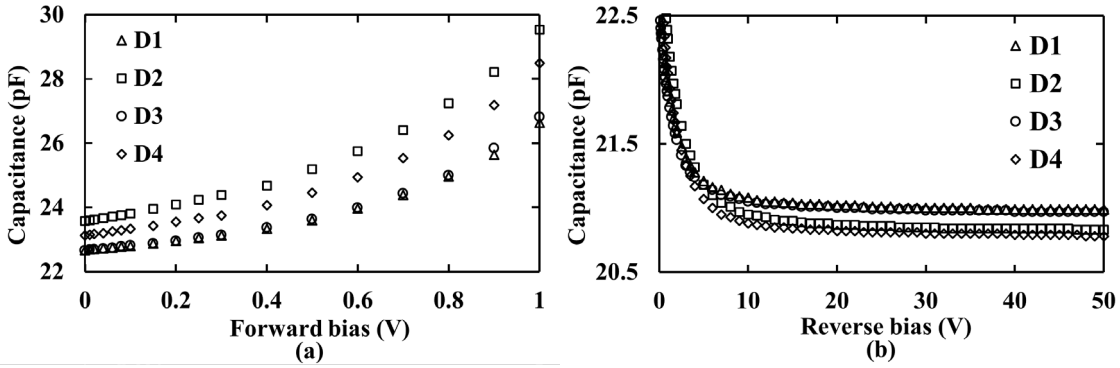

Figure 4.8. Measured capacitance as a function of (a) forward and (b) reverse bias at a temperature of 20 °C for the four 4H-SiC UV Schottky photodiodes, D1 to D4. D1 (open triangles); D2 (open squares); D3 (open circles); D4 (open diamonds).

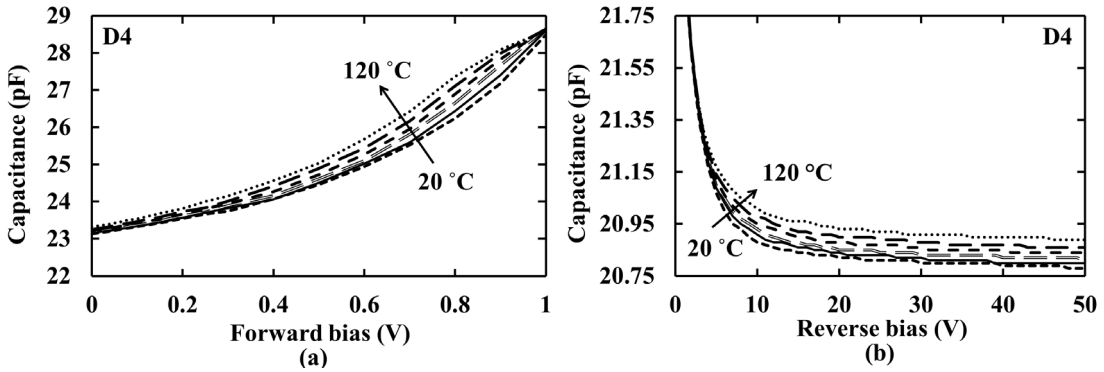

Figure 4.9. Measured capacitance as a function of (a) forward and (b) reverse bias at a temperature range of 20 °C to 120 °C, for the 4H-SiC UV Schottky photodiode D4. 120 °C (round dots); 100 °C (long dashes); 80 °C (dashes); 60 °C (double long dashes); 40 °C (solid line); 20 °C (thick square dots). The data points have been replaced by lines for clarity.

At 20 °C, as the reverse bias was increased in magnitude from 0 V to -5 V, the capacitance of all the diodes decreased by 1.8 pF ± 0.4 pF (rms deviance). Increasing the reverse bias further resulted in only a small additional decrease in capacitance: there was an additional reduction of 0.17 pF ± 0.04 pF in capacitance as the reverse bias was increased from -5 V to -10 V, and a 0.10 pF ± 0.01 pF reduction as the reverse bias was further increased from -10 V to -50 V. The small decrease in capacitance at reverse biases beyond -10 V indicates that the epitaxial layer was almost fully depleted at this voltage. At each applied reverse bias, the capacitance increased as the temperature increased. This may be attributed to the increasing doping concentration in the space charge region with temperature; similar effects have been explained by the presence of deep

level defects and the carriers trapped by them (Gramberg, 1971) (Mazzillo et al., 2012) (Cai et al., 2014).

The depletion width, W_D, was calculated based on the measured depletion layer capacitance, C_{DL}, (Equation 2.30). The depletion widths of the four photodiodes were found to increase from 5.35 µm ± 0.08 µm at 0 V to 5.89 µm ± 0.02 µm at -50 V reverse bias, at 20 °C. Similarly, the depletion widths of the four devices was found to increase from 5.32 µm ± 0.09 µm at 0 V to 5.86 µm ± 0.02 µm at -50 V reverse bias, at 120 °C.

The doping concentration (under the approximation that it equals the majority carrier concentration) as a function of depletion width, $N_D(W_D)$, with a spatial resolution of the order of a Debye length, was calculated using the differential capacitance method (suitable for an arbitrary doping profile) and Equation 2.31 (**Section 2.4.1**). **Figure 4.10** shows the extracted doping concentration, N_D, for a representative 4H-SiC UV Schottky photodiode (D4) at 20 °C and 120 °C.

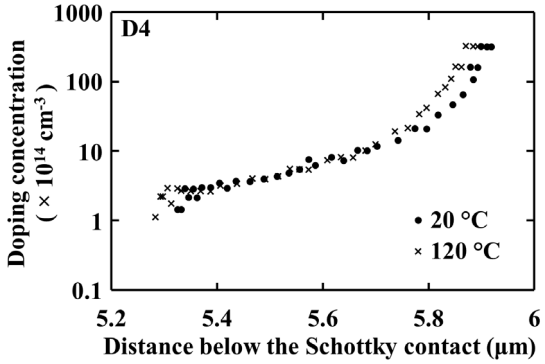

Figure 4.10. Calculated doping concentration as a function of depletion layer width of a representative 4H-SiC UV Schottky photodiode (D4) at 20 °C (filled circles) and 120 °C (× symbol).

The doping concentration was determined to vary from 1.9×10^{14} cm^{-3} ± 0.3×10^{14} cm^{-3} at 5.35 µm ± 0.08 µm below the Schottky contact to 3.21×10^{16} cm^{-3} ± 0.04×10^{16} cm^{-3} at the interface between the n epilayer and the substrate, at 20 °C. Similarly, the doping concentration was determined to vary from 1.4×10^{14} cm^{-3} ± 0.3×10^{14} cm^{-3} at 5.32 µm ± 0.09 µm below the Schottky contact to 3.26×10^{16} cm^{-3} ± 0.03×10^{16} cm^{-3} at the interface between the epilayer and the substrate, at 120 °C. It should be noted that although the uncertainties of the distance below the Schottky contact at which the doping concentrations were calculated were smaller than one Debye length, which has been calculated for 4H-SiC at room temperature to be 0.36 µm (Sze & Ng, 2007), the lower limit of a doping profile change that can be resolved using Equation 2.31 is

one Debye length (Sze & Ng, 2007). The doping profile of the devices, as is shown in **Figure 4.10**, follows an exponential trend, rather than an abrupt change between the epilayer and substrate.

4.4 Room temperature UV characterisation

To investigate the performance of the detectors under UV illumination, responsivity measurements were made using a ThermoSpectronic UV300 UV-VIS spectrophotometer with Tungsten and Deuterium lamps to cover the wavelength range 210 nm to 500 nm. The selection of the wavelength of interest was performed using an internal monochromator and UV grating. Two SG Lux SiC photodetectors with different areas and known responsivities (SGlux SolGel Technologies GmbH, SG01D-18) (SGlux SolGel Technologies GmbH, SG01L-18) were used as reference photodiodes to calibrate the apparatus. Custom baffles were made and used to ensure that no external sources of light could influence the measurements. Description of the UV photocurrent measurements can be found in **Section 2.5.3**.The incident UV power illuminating the devices was small (less than 2 nW) in the investigated wavelength range of 210 nm to 500 nm, while the photocurrent measured with the devices reported here was from ~1 pA to 108 pA. The dark leakage current for all photodiodes was measured to be < 0.07 pA at -15 V reverse bias at room temperature. Hence, even with small UV power illuminating the devices, the photocurrent-to-dark current contrast reached almost four orders of magnitude.

UV responsivity spectra of the four devices are shown in **Figure 4.11** as a function of the incident photons' wavelengths measured at room temperature and in photovoltaic operation condition (i.e. V_{AR} = 0 V). A responsivity peak value of 0.037 A/W ± 0.007 A/W ($QE_{external}$ = 16 %, using Equation 2.13 and $QE_{internal}$ = 20 % using Equation 2.9) was measured at 280 nm at room temperature when no reverse bias was applied for all four photodiodes. The responsivity did not have an abrupt spectral cutoff since 4H-SiC is indirect semiconductor and does not have a sharp cutoff band edge (Chen et al., 2007). The linear attenuation coefficient, μ, of the 4H-SiC is inversely proportional to wavelength and, in part, determines the quantum detection efficiency (Sze & Ng, 2007). It increases from 380 nm ((= 3.27 eV = E_G) to shorter wavelengths and as a result, the responsivity follows the same trend (Sridhara et al., 1998). The responsivity slowly increased from 380 nm to shorter wavelengths, as the attenuation coefficient, μ, increased (Sridhara et al., 1998). The penetration depth, $1/\mu$, at 380 nm was much larger (~ 625 μm) than the width of the space charge region of the devices (6 μm) (Chen et al., 2007). Hence, most of the incident photons penetrated through the active region resulting in low photocurrent. As the wavelength became shorter, the penetration depth decreased and more photons were absorbed and generated electron-hole pairs in the detector. The maximum photoresponsivity was achieved at around 280 nm, with shorter wavelengths showing decreased photoresponsivity. This may be

attributed to the fact that for λ < 280 nm the penetration length (< 1 μm (Chen et al., 2007)) becomes comparable with the dead zone introduced by the surface recombination resulting in the generated carriers recombining and thus not contributing to the photoresponse (Chen et al., 2007). An increased responsivity at the long wavelength range (> 280 nm) can be achieved with a vertical 4H-SiC Schottky UV photodiode with the same structure but thicker epitaxial layer (> 6 μm) compared to the devices presented here.

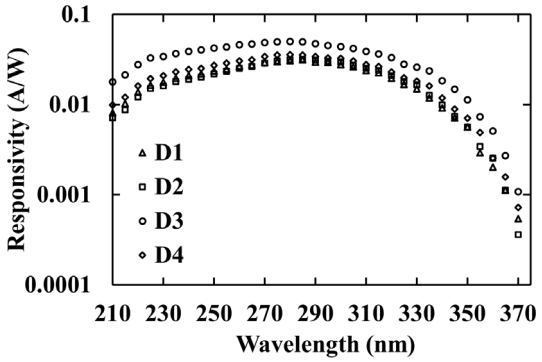

Figure 4.11. Responsivity as a function of wavelength (210 nm to 380 nm) measured for each 4H-SiC Schottky photodiode, D1 to D4, at room temperature and at 0 V applied bias.

The expected responsivity, R'_{Th}, as a function of wavelength, was computed based on the calculated external quantum detection efficiency, $QE_{external}$ (Equation 2.13) and compared with the measured responsivity, R'. The external quantum detection efficiency was calculated (see **Section 2.3.2**) using the reflectance, r, at each wavelength at the air-photodiode interface and the internal quantum detection efficiency, $QE_{internal}$ (Equation 2.9). The reflectance, r, was calculated using Equation 2.10 and the refractive indices for the detector material (4H-SiC), n_d, (= 2.3 at 270 nm (Park, 1997)) and air, n_{air}. The internal quantum detection efficiency, $QE_{internal}$, calculated as a function of wavelength using Equation 2.11a (see below), accounts for the absorption of photons before reaching the depletion region (first term of Equation 2.11a) as well as the absorption in the active depletion region (second term of Equation 2.11a).

In the detectors' geometry, there is an attenuating layer in front of the active region of the 4H-SiC UV Schottky photodiodes. This is the interdigitated Ni_2Si Schottky contacts, which covers 30 % of each diodes face. Consequently, the first term of Equation 2.11a, taking into account attenuation in the Ni_2Si Schottky contacts, becomes $\left[\left(1-f_{geo}\right)\mathrm{e}^{(-\mu_1 x_1)}+f_{geo}\right]$, where f_{geo} is the geometrical fill factor of the devices which equals the area directly exposed to the incoming light (= 70 % for these devices) and μ_1 and x_1 are the linear attenuation coefficient of Ni_2Si and the thickness of the Ni_2Si layer, respectively (Fraser, 1989). In the wavelength of interest, all photons

falling on this are of the diode face are attenuated at the Ni_2Si Schottky contacts. Consequently, the first term of Equation 2.11a, is simplified to f_{geo}.

Using the attenuation coefficient, μ, reported by Cha and Sandvik (2008) for 4H-SiC (17000 cm^{-1} at 270 nm), the depletion layer width, W_D, found from the capacitance measurements as a function of reverse bias and the procedure described above, the expected responsivity, R'_{th}, was calculated.

The expected value of the maximum R'_{Th} (270 nm) was constant between 0 V and -15 V applied reverse bias, and equal to 0.128 A/W. **Figure 4.12** shows a comparison between the measured and theoretical photoresponsivity at 270 nm as a function of applied reverse bias. **Figure 4.13** shows photoresponsivity spectra for a representative 4H-SiC UV Schottky photodiode, D2, with the applied reverse bias as parameter. The peak responsivity at 0 V and -5 V reverse bias occurred at 280 nm whereas the responsivity showed a peak value at 270 nm when the diode was reverse biased at -10 V and -15 V.

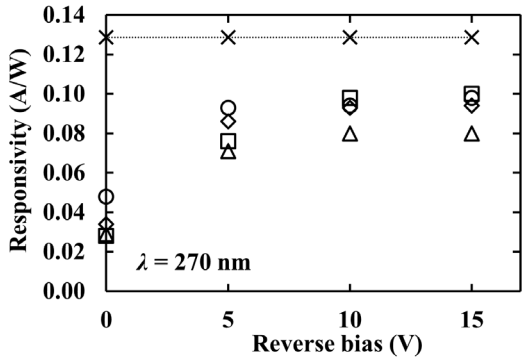

Figure 4.12. Theoretical (crosses) and measured photoresponsivity for D1 (open triangles), D2 (open squares), D3 (open circles), and D4 (open diamonds) as a function of applied reverse bias, at room temperature.

Although the calculated expected responsivity at 270 nm was 0.128 A/W for all investigated biases, the measured responsivity was well below this value for unbiased devices and increased with applied voltage. The measured responsivity increased when the photodiodes were reverse biased at -5 V compared to 0 V. There was a further improvement in photoresponsivity at -10 V, but the responsivity increase at reverse biases beyond this (-15 V) was comparatively small. The increase in the responsivity as the reverse bias increased from 0 V to -5 V could not be attributed to the increased depletion layer width at the same bias range. The depletion layer width increased from 5.35 μm ± 0.08 μm at 0 V to 5.82 μm ± 0.01 μm at -5 V. The increase in the responsivity as the reverse bias increased from 0 V to -5 V as well as the difference between the theoretical and measured responsivities at 270 nm and 0 V may be attributed to charge trapping and losses

present in the active region of the device at low internal electric field (zero applied bias). As the internal field increased with increased reverse bias, the improved charge transport resulted in less trapping and less charge loss, with the consequence of more charge being induced on the contacts; there was an additional internal electric field of 8.59 kV/cm ± 0.02 kV/cm at -5 V reverse bias compared to the one at 0 V. At -15 V reverse bias, the measured photoresponsivity was much closer to the computed value, consistent with reduced charge transport losses at higher fields.

As the reverse bias was increased in magnitude, the depletion layer width also increased. Hence, a red-shift (towards longer wavelengths) of the responsivity was expected (enhanced absorption of the long-wavelength photons) with increased reverse bias. However, a red-shift was not observed. This was attributed to the small change of the depletion layer width as the reverse bias increased from 0 V (W_D = 5.2 μm) to -15 V (W_D = 5.9 μm). The peak expected responsivity was also computed to be invariant with this change in depletion layer width. A blue-shift of the responsivity peak was observed instead, with increased reverse bias. The improved charge transport with increased reverse bias might enhance the collection of charge carriers generated close to the surface (short-wavelength photons), which explains the blue-shift of the responsivity peak.

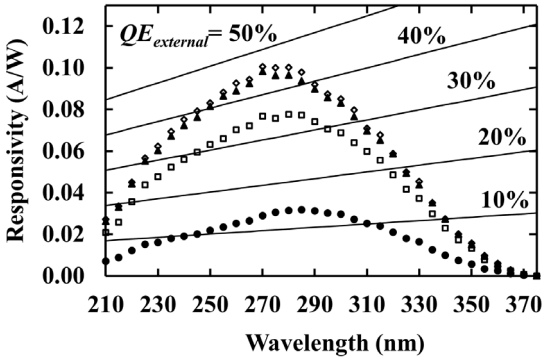

Figure 4.13. Photoresponsivity spectra measured with a representative 4H-SiC UV Schottky photodiode, D2, at room temperature at reverse biases of 0 V (filled circles); -5 V (open squares); -10 V (filled triangles); -15 V (open diamonds).

The photoresponsivity of diode D2 had a peak value of 0.100 A/W ($QE_{external}$ = 46 %, using Equation 2.13 and $QE_{internal}$ = 55 % using Equation 2.9) at 270 nm when the device was reverse biased at -15 V. This value is comparable with previous reported results of similar devices (Mazzillo et al., 2009) (Adamo et al., 2014) and better than 4H-SiC UV Schottky diodes employing thin metal Schottky contacts, rather than interdigitated Schottky contacts, (e.g. $QE_{internal} \leq 45$ % at 270 nm (Xin et al., 2005) and $QE_{internal} \approx 30$ % at 253 nm (Blank et al., 2005)).

The measured photoresponsivity at 270 nm and reverse bias of -15 V was 0.080 A/W, 0.098 A/W, and 0.094 A/W for diode D1, D3, and D4, respectively.

The visible blindness, as defined by the peak responsivity in the UV range divided by the responsivity at 500 nm, was measured using a 500 nm light with a power of 105 pW. While irradiating a device with the 500 nm light, no photocurrent could be detected with the Keithley 6487 picoammeter suggesting that the photocurrent was < 0.01 pA. When illuminating the devices with a 270 nm light providing a power of 864 pW, a photocurrent of 81 pA ± 7 pA was measured. Due to the low power of the 500 nm light, only the maximum boundary of the UV-visible rejection ratio between the photoresponsivity at 500 nm and at 270 nm could be estimated. This ratio was found to be 10^{-3}. The real degree of visible blindness of the photodiode is expected to be better, as for previously reported similar devices (Mazzillo et al., 2009) (Sciuto et al., 2014). The high visible blindness found for the Ni_2Si/4H-SiC Schottky UV devices is a result of the inherent insensitivity of 4H-SiC to photons of longer than 380 nm wavelength, as well as to the Schottky structure, which has been found to be more effective than the p^+-i-n^+ structure for visible light rejection (Sciuto et al., 2006).

4.5 Conclusion

Four 4H-SiC Schottky UV detectors employing Ni_2Si interdigitated contacts have been characterised for their electrical and optical behaviour within the temperature range 20 °C to 120 °C. The devices' dark currents as functions of applied forward and reverse bias and temperature were measured. The devices' leakage current densities were found to remain ≤ 13 pA/cm^2 (limited by the accuracy of the Keithley 6487 picoammeter) for three of the tested devices (D2 to D4), with D1 showing a leakage current density of 173 pA/cm^2, all at 20 °C and an internal electric field of 83 kV/cm. Similarly, the leakage current densities of all devices were found to remain ≤ 8.9 nA/cm^2 at 120 °C and an internal electric field of 83 kV/cm. Forward and reverse biased capacitance measurements showed comparable performance between the diodes. The depletion width and effective doping density calculations based on the capacitance measurements showed that the diodes were almost fully depleted at -10 V reverse bias, due to the high quality of the epilayer.

UV photoresponsivity measurements at room temperature have been performed as a function of applied reverse bias. The peak responsivity of all four detectors was at 280 nm, when operating in photovoltaic mode. Although the devices had modest responsivities (mean of 0.037 A/W ± 0.007 A/W) at 0 V applied reverse bias, the mean responsivity increased to 0.093 A/W ± 0.007 A/W when the detectors were reverse biased at -15 V. This was attributed to charge trapping and possibly recombination in the active region of the photodiodes at low internal

electric fields. The dark leakage current for all photodiodes was measured to be < 0.07 pA at -15 V reverse bias at room temperature.

The internal quantum detection efficiency (as defined in **Section 2.3.2**, Equation 2.9) of the detectors was measured to be 55 % at 270 nm for the best performance device, with the detector reverse biased at -15 V. Also, the UV-visible rejection ratio (photoresponsivity at 500 nm divided by photoresponsivity at 270 nm) was measured to be at least 10^{-3}, although the true UV-visible rejection ratio is likely to be far better.

Overall, the high quality of the 4H-SiC epitaxial material and the relatively high work function of Ni_2Si, resulted in low leakage current densities measured for up to 120 °C at an internal electric field of up to 83 kV/cm. These results are comparable with the lowest leakage current densities ever reported for 4H-SiC Schottky diodes (Bertuccio et al., 2011) and are much lower than typical values for Si diodes (1 nA/cm^2 at room temperature (Bertuccio et al., 2014)). The low dark currents of the Ni_2Si/4H-SiC Schottky diodes resulted in almost four orders of magnitude UV photocurrent-to-dark current contrast, at small (less than 2 nW) UV power, suggesting that they could operate even at low UV light intensities. The interdigitated Ni_2Si Schottky contacts resulted in an increased internal quantum detection efficiency, compared to 4H-SiC UV Schottky diodes employing thin metal Schottky contacts. The inherent properties of 4H-SiC and the Schottky structure resulted in high visible blindness (at least 10^{-3}), suggesting that they could be suitable for UV detection even at high visible and IR backgrounds without the use of filters.

The results reported here along with previous reports on 4H-SiC radiation tolerance makes these devices a potential attractive option for future UV detection in applications such as space science and harsh terrestrial environments.

Chapter 5 4H-SiC Schottky Diode Arrays for X-ray Detection

5.1 Introduction and background

The physical properties of 4H-SiC and its potential advantages over Si as detector material for X-ray spectrometers operating under harsh environments (high temperature and intense radiation environment) have been introduced in **Section 1.5.1**.

The first experimental results of SiC photodiodes for X-ray spectroscopy were reported by Bertuccio et al. (2001). These results were obtained with 4H-SiC Schottky diodes having 30 μm epilayer thickness and 1.8×10^{15} cm^{-3} dopant concentration. Although the main X-ray lines (Np Lα at 13.9 keV and Lβ at 17.8 keV) and γ-ray lines (at 26.3 keV and 59.5 keV) of the acquired ^{241}Am spectrum were clearly detected, the separation of the low energy lines was limited by the high detector capacitance (16 pF at -500 V reverse bias) contributing to its energy resolution degradation (Bertuccio et al., 2001). A ^{241}Am spectrum with improved energy resolution using a 4H-SiC detector fabricated onto a 70 μm thick low doped (9×10^{14} cm^{-3}) 4H-SiC epilayer at 26 °C was reported by Bertuccio and Casiraghi (2003) which was attributed to its lower capacitance (below 1 pF) compared to the previously reported 4H-SiC Schottky detector (Bertuccio et al., 2001). A study of SiC X-ray detectors in comparison to Si X-ray detectors was also reported in the same journal article (Bertuccio & Casiraghi, 2003), showing that under some conditions of operating temperature and detector active area, superior energy resolution can be achieved using SiC detectors. Following this, further development of 4H-SiC epitaxial layers and ultra-low-noise electronics resulted in experimental proof that 4H-SiC Schottky X-ray detectors can operate at a temperature range of 27 °C to 100 °C (Bertuccio et al., 2004). The best experimental results on single pixel SiC X-ray detectors were reported by Bertuccio et al. (2011) with 4H-SiC Schottky diodes with circular (200 μm diameter) Au Schottky contacts, and a 4H-SiC epitaxial layer of 70 μm thickness and 5×10^{14} cm^{-3} dopant concentration, having a *FWHM* at 5.9 keV of 196 eV at 30 °C which was increased to 233 eV at 5.9 keV at 100 °C. Studies on semi-insulating 4H-SiC X-ray detectors (Mandal et al., 2011) (Bertuccio et al., 2013) have shown poorer energy resolution compared to epitaxial SiC layers primarily due to high leakage currents and low charge collection efficiencies (Bertuccio et al., 2013).

Work has also been conducted to develop 4H-SiC Schottky diodes with thin (18 nm) NiSi Schottky contacts, with the intention of improving the soft X-ray quantum detection efficiency and as an alternative technology to interdigitated contacts. An energy resolution (*FWHM* at 22 keV) of 1.47 keV at room temperature has been reported for such a device with a 20 μm

epilayer thickness (Lees et al., 2007). Photon counting spectroscopic measurements at temperatures up to 80 °C (2.5 keV *FWHM* at 5.9 keV at 80 °C) for a 4H-SiC Schottky diode with thin NiSi Schottky contacts and 45 μm epilayer thickness (Barnett, 2011), and after proton irradiation of a 4H-SiC Schottky diode with thin NiSi Schottky contacts and 20 μm epilayer thickness (Stevens et al., 2011) showed promising results for their use in harsh environments.

In this chapter, a comparable study including electrical characterisation and X-ray detection using five 4H-SiC Schottky diodes with thin NiSi Schottky contacts in a combined 2 × 2 and 1 × 3 pixel configuration are reported. Two of the diodes are part of both arrays (further details can be found in **Section 5.2** Device structure). The electrical characterisation included measurements of the forward and reverse bias dark currents and capacitances of the five diodes at room temperature. One of the diodes was characterised over a temperature range of 20 °C to 140 °C, the highest reported temperature for similar devices. The photogenerated current of all diodes in the presence of X-ray photons from a Mo X-ray tube was measured as a function of applied reverse bias, demonstrating operation of the devices as current mode X-ray detectors. Each diode was then coupled to a low-noise charge-sensitive preamplifier, and their performance as spectroscopic photon counting X-ray detectors were investigated. The 4H-SiC Schottky diodes (250 μm × 250 μm) were fabricated at Newcastle University using a 4H-SiC wafer purchased from Cree Inc. Subsequent characterisation was conducted at University of Sussex.

5.2 Device structure

The 4H-SiC wafer was supplied by Cree. It had an n-type 20 μm epitaxial layer (doping concentration of 4×10^{14} cm^{-3} as stated by the supplier), on a resistive n-type 350 μm SiC substrate (doping concentration of 2×10^{18} cm^{-3}). A drawing of the layers structure can be seen in **Figure 5.1**. The substrate had a diameter of 76.2 mm, a resistivity of 25 mOhm cm and an off axis surface orientation of 8.0°. After an RCA clean (Kern and Puotinen, 1970), oxidation at 1150 °C in dry oxygen followed to form the 25 nm thick passivation layer. A common NiSix Ohmic contact, at the rear of the array, was formed from 5 nm Ti and 100 nm Ni layers which were sintered at 1100 °C in vacuum. Windows were opened in this thermal oxide using buffered hydrofluoric acid prior to deposition of the Schottky contacts. The NiSi Schottky contacts on the active side of the array for each pixel were formed by depositing 3 nm of Ti and 12 nm of Ni using e-beam evaporation and then annealing the samples at 600 °C. This thin Schottky contact was chosen such that to improve the soft X-ray quantum detection efficiency (minimise the X-ray attenuation). The bond pads were formed by depositing a 200 nm thick Au layer on top of a 5 nm thick Cr adhesion layer.

The diodes were fabricated in a combined 2 × 2 and 1 × 3 array pattern as per the mask layout is shown in **Figure 5.1**. Four diodes constitute the 2 × 2 array and three constitute the 1 × 3 array. Due to the mask layout, two of the diodes are part of both arrays. The devices were mounted in a ceramic package and wire bonded.

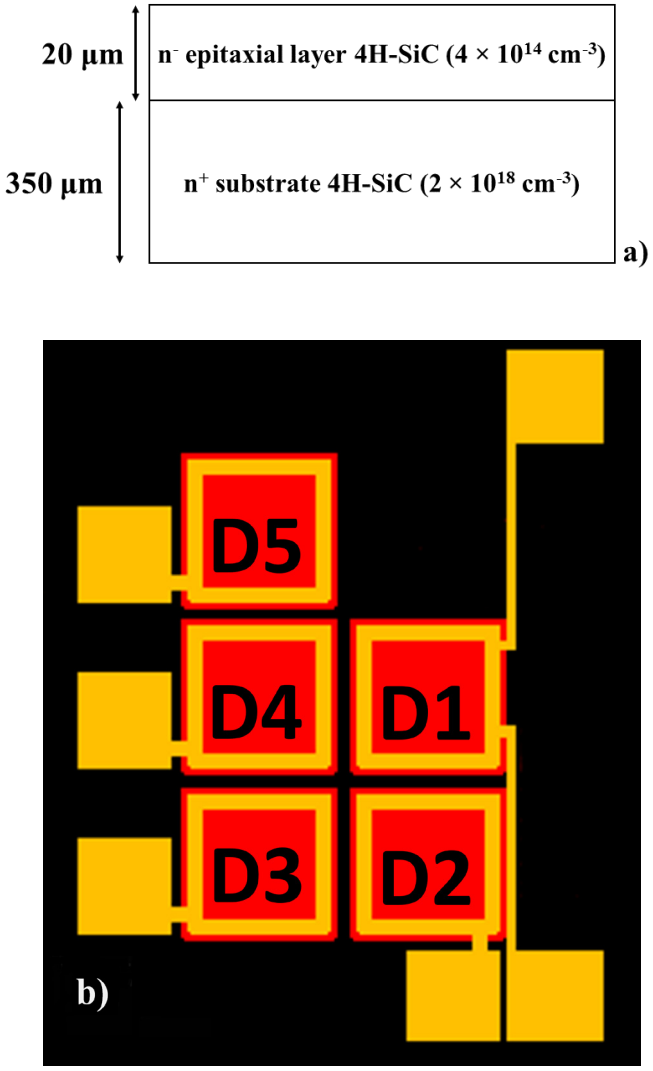

Figure 5.1. a) Illustrative layers structure (not in scale) of each 4H-SiC Schottky photodiode and b) mask layout showing the combined 2 × 2 and 1 × 3 4H-SiC Schottky photodiode array.

5.3 High temperature electrical characterisation

5.3.1 Current measurements as a function of bias

Forward and reverse biased dark current measurements as functions of applied voltage were made for the five 4H-SiC Schottky photodiodes (D1 to D5) at 20 °C using a Keithley 6487 Picoammeter/Voltage Source (see **Section 2.5.1**). **Figure 5.2** shows the measured current as a function of applied forward bias (0 V to 2 V) and reverse bias (0 V to -200 V) for the photodiodes.

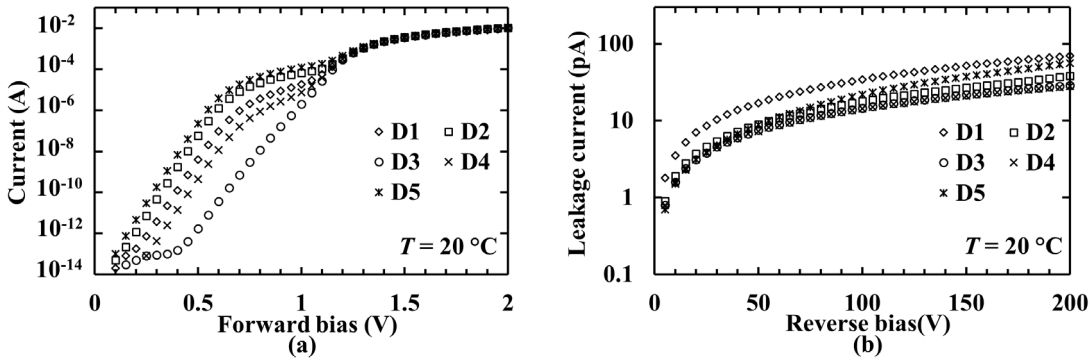

Figure 5.2. Current as a function of (a) forward and (b) reverse bias measured at a temperature of 20 °C for the five 4H-SiC Schottky photodiodes, D1 to D5. D1 (open diamonds); D2 (open squares); D3 (open circles); D4 (× symbols); D5 (stars).

As can be seen in **Figure 5.2a**, the shape of the forward current as a function of applied voltage of diode D3 is different compared to the rest of the devices. Diodes D1, D2, D4, and D5 exhibited anomalous behaviour (double barrier behaviour) in the form of a knee in the forward bias regime, for $V_{AF} < 1$ V. The excess forward current of diodes D1, D2, D4, and D5 at low applied forward biases (< 1 V), resulting in a non-ideal behaviour, can be explained using a Schottky barrier height inhomogeneity concept (Tumakha et al., 2005) (Ma et al., 2006) (Grekov et al., 2008). This concept accounts for two Schottky barriers connected in parallel. The double barrier height observed for D1, D2, D4, and D5 can be similarly explained. Work has been previously done to identify the causes of the double barrier formation and various phenomena have been suggested including crystallographic defects, surface defects (Defives et al., 1999) (Tumakha et al., 2005), doping non-uniformity and contaminations. Surface preparation methods have been correlated with the Schottky barrier height and non-ideal behaviour (Roccaforte et al., 2003c) and defects (growth pits) located in the thin layer of epitaxial surface have been regarded as the main cause of Schottky barrier inhomogeneities by Ma et al. (2006).

The saturation current, I_{sat}, was found by extrapolating the linear region of the dark current as a function of forward bias, to the intercept point ($V_{AF} = 0$V) (Equation 2.23). Using the determined values of the saturation current for each diode, the zero band barrier height, φ_{0B}, for each diode was extracted (Equation 2.25). The Cheung method (Cheung & Cheung, 1986) was used to obtain the ideality factor, n, which was extracted from the dark current as a function of forward bias measurements (Equation 2.26). Diode D3 was found to have the highest zero band barrier height (1.25 eV) whereas D5 had the lowest zero band barrier height (1.04 eV). A mean zero band barrier height of 1.14 eV ± 0.07 eV (rms deviance) was found for all five diodes. This value is comparable with the zero band barrier height extracted for similar devices (1.21 eV) (Stevens et al., 2011). However, the mean zero band barrier height found for the five NiSi/4H-SiC Schottky

diodes was smaller than the mean zero band barrier height found for the four Ni_2Si/4H-SiC UV Schottky diodes (=1.70 eV ± 0.07 eV) (**Chapter 4**), both at 20 °C. This was attributed to the higher metal work function of Ni_2Si (4.8 eV) compared to the metal work function of NiSi (4.5 eV) (Kittl et al., 2006), since the Schottky barrier height ideally equals the difference between the metal work function and the electron affinity of the semiconductor (= 3.17 eV for 4H-SiC (Davydov, 2007)) (Sze & Ng, 2007)) (see **Figure 2.8**). A mean ideality factor of 2.1 ± 0.1 (rms deviance) was found for all diodes with diode D1 showing the lowest (best) ideality factor (1.9). The variance of the ideality factor among the diodes was found to be within the uncertainty introduced by the current measurement as a function of applied forward bias (± 0.1). Although previous reports of similar devices have shown ideality factors close to unity (Stevens et al., 2011), the ideality factor values of the currently reported diodes suggest that the current mechanism is dominated by recombination (Sze & Ng, 2007). The exact reason for the ideality factor values close to two is currently unknown, but it could be attributed to peripheral or surface leakage current components added to the thermionic component, as it was by Woods and Hall (1994).

All the diodes were reverse biased at up to -200 V at a temperature of 20 °C. All five diodes showed leakage currents ≤70 pA (112 nA/cm^2) at -200 V reverse bias. Diode D4 exhibited the lowest reverse dark current across the investigated applied reverse bias range with a leakage current of 28 pA (44.8 nA/cm^2) at 170 kV/cm (-200 V). The leakage current density of diode D4 was 13.9 nA/cm^2 (8.7 pA) at an internal electric field of 105 kV/cm (-60 V), whereas a leakage current density of 1.6 nA/cm^2 (1 pA) has been previously reported for a similar device at the same electric field and at room temperature (Lees et al., 2011). The leakage current mechanism, resulting in unexpected high leakage current densities for all five diodes at room temperature is discussed below. The presently reported detectors have much higher room temperature leakage currents than the lowest reported in the literature for SiC detectors (1 pA/cm^2 (Bertuccio et al., 2011) at 103 kV/cm) and commercial 4H-SiC Schottky diodes (347 pA/cm^2 at 403 kV/cm (Zhao et al., 2016)).

To characterise the performance of the detectors with temperature, one of the diodes, D3, was installed inside a TAS Micro MT climatic cabinet and its forward and reverse dark currents measured as a function of applied bias over the temperature range 20 °C to 140 °C. Diode D3 was selected due to the absence of a double barrier height and its leakage current being the lowest of the five diodes. **Figure 5.3** shows the temperature dependency of the dark current as a function of applied bias of this diode.

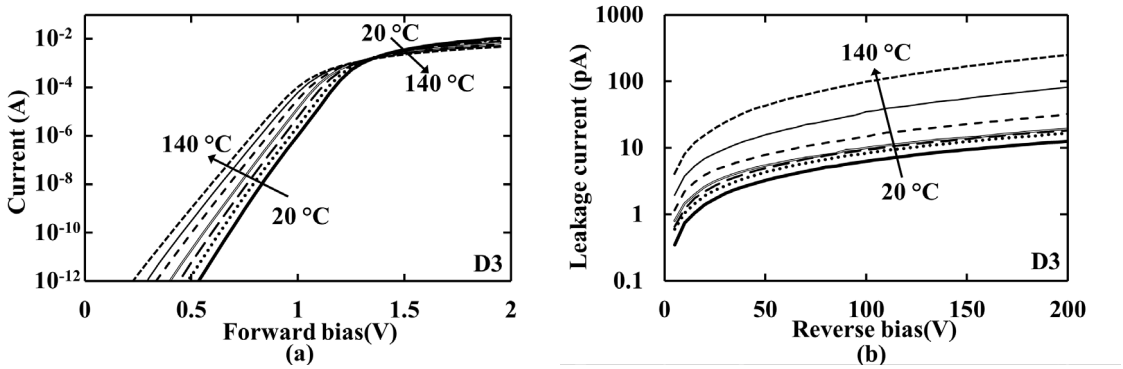

Figure 5.3. Current as a function of (a) forward and (b) reverse bias measured at a temperature range of 20 °C to 140 °C, for the 4H-SiC Schottky photodiode D3. 140 °C (square dots); 120 °C (thin solid line); 100 °C (dashes); 80 °C (long dash dot); 60 °C (long dashes); 40 °C (big round dots); 20 °C (thick solid line). The data points have been replaced by lines for clarity.

For applied forward biases up to 1.35 V, the measured current increased with increased temperature due to recombination being the main current generation mechanism. Recombination in the depletion region of Schottky diodes is (identically to recombination in p^+-i-n^+ diodes) proportional to the intrinsic carrier concentration, n_i (Equation 2.34). However, a different behaviour was observed at forward applied biases greater than 1.35 V; the measured current decreased with increased temperature. Here, it is hypothesized that optical phonon scattering resulted in the reduction of the electron mobility which influenced the electrical behaviour at high current values region (La Via et al., 2005).

The ideality factor, n, and the zero band barrier height, φ_{0B}, were extracted for diode D3 over the temperature range 20 °C to 140 °C following the same procedure as described above. The results are presented in **Figure 5.4**. The ideality factor improved from 1.99 at 20 °C to 1.81 at 140 °C and the zero band barrier height increased from 1.32 eV at 20 °C to 1.49 eV at 140 °C. The improvement in ideality factor and the increase in the zero band barrier height as the temperature was increased can be explained by the presence of an inhomogeneous barrier (Tung, 1991) (Roccaforte et al., 2003a), as was the case for the UV photodiodes reported in **Chapter 4**. The current through an inhomogeneous barrier can be expressed as the sum of currents flowing in lower Schottky barrier height patches (Tung, 1991). The low apparent Schottky barrier height (1.32 eV) at 20 °C was attributed to the current being dominated by electrons surmounting the lower barriers. As the temperature increased, electrons had more energy to overcome higher barriers resulting in a higher zero band barrier height and improved ideality factor.

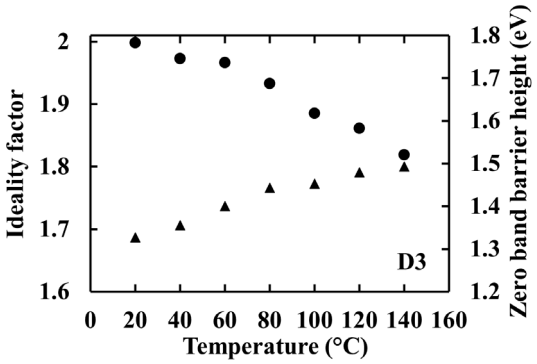

Figure 5.4. Ideality factor (circles) and zero band barrier height (triangles) extracted from forward current – voltage graph in the temperature range 20 °C to 140 °C for the 4H-SiC Schottky photodiode D3.

As expected, the leakage current of the 4H-SiC Schottky photodiode D3 was found to be greater at higher temperatures at all investigated reverse biases. **Figure 5.5** shows the measured leakage current as a function of temperature at -200 V and -80 V reverse bias. The current exponentially increased at temperatures above 100 °C, which was consistent with Schottky-barrier lowering (Sze & Ng, 2007). However, within the temperature range 20 °C to 80 °C, the dominant mechanism of the measured leakage current was different compared to that at higher temperatures, as shown by the measured leakage current of the 4H-SiC Schottky photodiode D3 as a function of temperature, at the temperature range 20 °C to 80 °C (**Figure 5.5**).

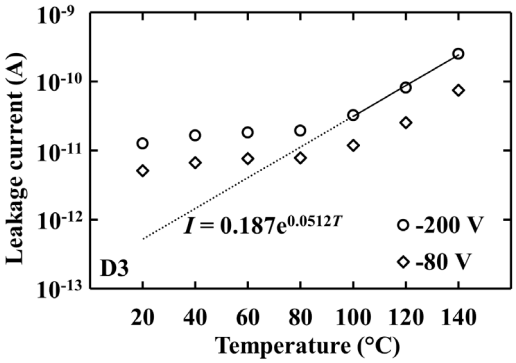

Figure 5.5. Leakage current as a function of temperature at -200 V (circles) and -80 V (diamonds) reverse bias for the 4H-SiC Schottky photodiode D3. The line of best fit calculated using linear least squares fitting for the temperature range 100 °C to 140 °C and 200 V reverse bias is also shown (solid line) along with the extrapolated line for the temperature range 20 °C to 100 °C (dots).

To further investigate the leakage current mechanisms at different temperatures, the activation energy, E_A, was extracted from the Arrhenius plot (Equation 2.28) (Bertuccio et al., 2013). For the temperature range where the activation energy was constant, the $\ln I_R$ as a function of $1/T$

graph, shown in **Figure 5.6**, yielded a straight line. Two linear regions can be seen in **Figure 5.6**. The activation energy was found to be 0.06 eV in the temperature range 20 °C to 80 °C and 0.67 eV in the temperature range 100 °C to 140 °C. The energy level for the activation energy at low temperatures was associated with nitrogen (n-type epilayer dopant) atoms with ionisation energy of 0.052 eV in 4H-SiC (Lebedev, 1999). When 4H-SiC is doped with nitrogen, various complexes may be formed in association with intrinsic defects of the SiC or background impurities. A donor level of 0.6 eV, similar to the activation energy found at high temperatures, has been reported for Ti-N pairs in 4H-SiC having a different position in the lattice compared to a single nitrogen atom. The low activation energy at low temperatures (=0.06 eV), suggests a weak dependence of leakage current upon temperature. At high temperatures, the leakage current of diode D3 was comparable with a previously reported similar device (Lees et al., 2011). As an example, both the currently reported device, D3 and the device reported by Lees et al. (2011) had a leakage current < 10 pA at -80 V reverse bias and 80 °C. However, the leakage current of D3 only slightly decreased from 8 pA at 80 °C to 5 pA at 20 °C, both at -80 V reverse bias.

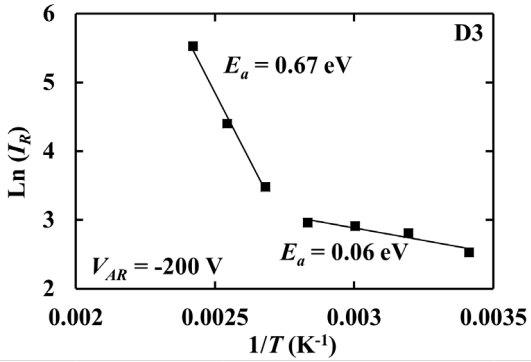

Figure 5.6. Arrhenius plot (ln I_R as a function of 1/T) to extract the activation energy for the 4H-SiC Schottky photodiode D3 at -200 V applied reverse bias.

5.3.2 Capacitance measurements as a function of bias

The depletion widths, the doping concentrations, and the flat band barrier heights of the diodes were determined from measurements of capacitance as a function of applied forward and reverse bias using an HP 4275A Multi frequency LCR meter (see **Section 2.5.2**). The test signal was sinusoidal with a 50 mV rms magnitude and 1 MHz frequency. The measured capacitance consisted of the device capacitance, C_{DL}, (regarded as the depletion layer capacitance) and the capacitance of the package, C_{pack}. Due to the nature of the packaging, each diode had a different C_{pack}. An estimation of each C_{pack} (± 0.1 pF) was made based on capacitance measurements of empty pins of the package. **Figure 5.7** shows the measured capacitance (C_{pack} subtracted) of all five diodes at a temperature of 20 °C.

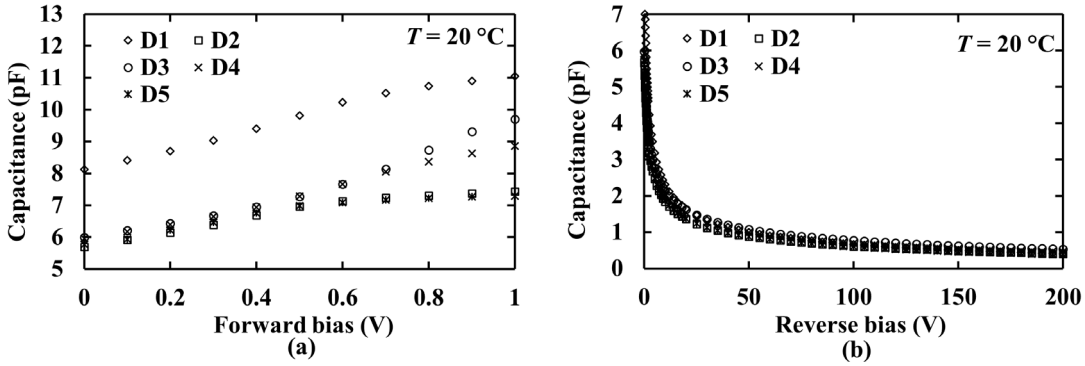

Figure 5.7. Measured capacitance as a function of (a) forward and (b) reverse bias at a temperature of 20 °C for the five 4H-SiC Schottky photodiodes, D1 to D5. D1 (open diamonds); D2 (open squares); D3 (open circles); D4 (× symbols); D5 (stars).

At 0 V applied bias and at a temperature of 20 °C, comparable capacitances were recorded for four devices (D2 to D5), with a mean value of 5.83 pF ± 0.22 pF (rms deviance). Diode D1 showed a higher capacitance of 8.0 pF ± 0.1 pF. As the applied reverse bias, V_{AR}, increased, the capacitance, C_{DL}, of all five diodes, was found to decrease as expected. More specifically, as the reverse bias increased from 0 V to -50 V, the capacitance of four diodes (D2 to D5) decreased by 4.87 pF ± 0.09 pF to 0.96 pF ± 0.15 pF, whereas the other diode, D1, showed a larger decrease of 7.05 pF to 1.00 pF. As the reverse bias was further increased in magnitude from -50 V to -100 V, there was an additional reduction in capacitance of 0.30 pF ± 0.04 pF for all diodes. For all diodes, a 0.23 pF ± 0.04 pF reduction in capacitance was recorded as the reverse voltage increased in magnitude from -100 V to -200 V. The depletion width, W_D, was calculated based on the measured depletion layer capacitance, C_{DL}, (Equation 2.30) and can be seen in **Figure 5.8**. Additionally, the calculated internal quantum detection efficiency, $QE_{internal}$, (see **Section 2.3.2**) of the detectors for 17.4 keV X-ray photons as a function of applied reverse bias, taking into account the 3 nm Ti and 12 nm Ni dead layers, and assuming that only the depletion layer width is the active layer, can be seen in **Figure 5.8**; X-ray detection with the devices is discussed in **Section 5.4**.

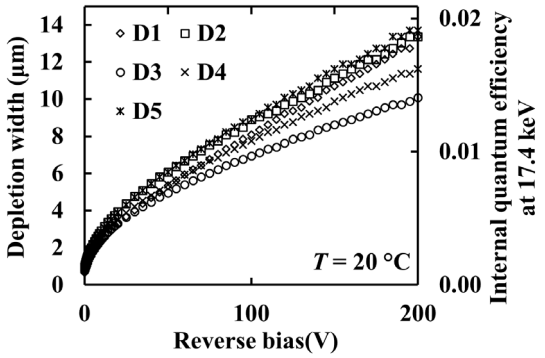

Figure 5.8. Calculated implied depletion width and internal quantum detection efficiency at 17.4 keV for the five 4H-SiC Schottky photodiodes, D1 to D5, as functions of reverse bias and at a temperature of 20 °C. D1 (open diamonds); D2 (open squares); D3 (open circles); D4 (× symbols); D5 (stars).

The implied depletion widths of the diodes were found to range from 10 μm to 14 μm at -200 V reverse bias, with a mean value of 12 μm ± 1 μm. The variation in the depletion width of the diodes was attributed to the uncertainty of the capacitance of the package, C_{pack}. The different measured capacitance change, ΔC, among the five diodes as the voltage increased from 0 V to -200 V reverse bias suggested that possible variations of the doping concentration in the epilayer across the wafer may also have contributed to the apparent variation in the depletion width of the diodes seen in **Figure 5.8**.

The doping concentration in the epilayer, N_D, and the flat band barrier height, φ_{FB}, were computed at 20 °C from $1/C_{DL}^2$ as a function of applied reverse bias, V_{AR}, for one representative diode, D3 (see **Figure 5.9**).

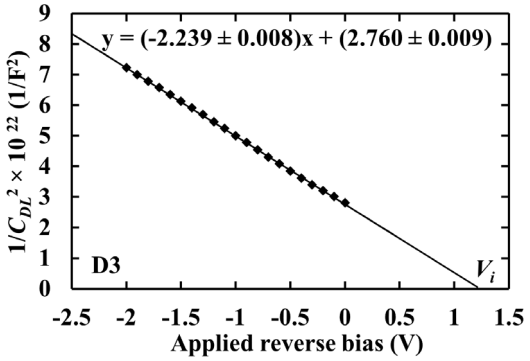

Figure 5.9. $1/C_{DL}^2$ plot as a function of applied reverse bias, V_{AR}, for the 4H-SiC Schottky photodiode D3 at a temperature of 20 °C. The line of best fit as determined by linear least squares fitting is also shown.

The electron concentration, which was effectively the donor concentration in the n-type epilayer assuming all donors were ionised, was found to be 16.7×10^{14} cm^{-3} using Equation 2.31. The flat band barrier height, φ_{FB}, for diode D3 at 20 °C, computed using Equation 2.32 (4H-SiC $N_c = 1.5 \times 10^{19}$ cm^{-3} at room temperature based on the electron effective masses (Son et al., 1995)) was found to be $\varphi_{FB} = 1.48$ eV and the built in voltage, $V_{bi} = 1.26$ V (corresponding to a value of $V_i = 1.24$ V).

To investigate the capacitance characteristics of the devices at elevated temperatures, the same diode as it was used for the temperature dependent current measurements (i.e. D3) was placed inside a TAS Micro MT climatic cabinet and connected to an HP 4275A Multi frequency LCR meter with a sinusoidal test signal of 50 mV rms magnitude and 1 MHz frequency. The diode's capacitance at both forward and reverse biases was measured over the temperature range 20 °C to 140 °C. **Figure 5.10** shows the temperature dependence of the measured device capacitance for diode D3, with the packaging capacitance (temperature independent) subtracted, as a function of applied bias. It should be noted that for comparison purposes, and since the reported measurements are for one device, the uncertainty of capacitance of the empty package, C_{pack}, was excluded from the total uncertainty of the capacitance readings (reduced to ± 0.03 pF).

Different behaviour was observed at different bias and temperature ranges. At each applied forward bias (**Figure 5.10a**), and at the reverse bias range from 0 V to -5 V (0 V shown in **Figure 5.10b**), the capacitance of D3 was measured to be greater at higher temperatures, over the whole investigated temperature range 20 °C to 140 °C. As an example, the capacitance of D3 increased from 5.28 pF ± 0.03 pF at 20 °C to 5.69 pF ± 0.03 pF at 140 °C, at 0 V. The small increase of the capacitance at forward bias and at reverse biases up to - 5V was attributed to the progressive ionisation with temperature of non-ionised donors in a thin region around the depletion layer (Mazzillo et al., 2012). The ratio between the thickness of this possible thin layer and the depletion layer would be smaller at high reverse biases, explaining the unchanged measured capacitance at higher (in magnitude) than -5 V applied reverse bias over the temperature range 20 °C to 80 °C (**Figure 5.10c**). At higher (in magnitude) than -5 V applied reverse, the capacitance of D3 was measured to be greater at higher temperatures over the temperature range 80 °C to 140 °C. This was attributed to a possible increase of the charge density in the depletion layer as the temperature increased from 80 °C to 140 °C due to the presence of deep centres whose occupancy was temperature dependent, similarly to as was reported by Gramberg (1971).

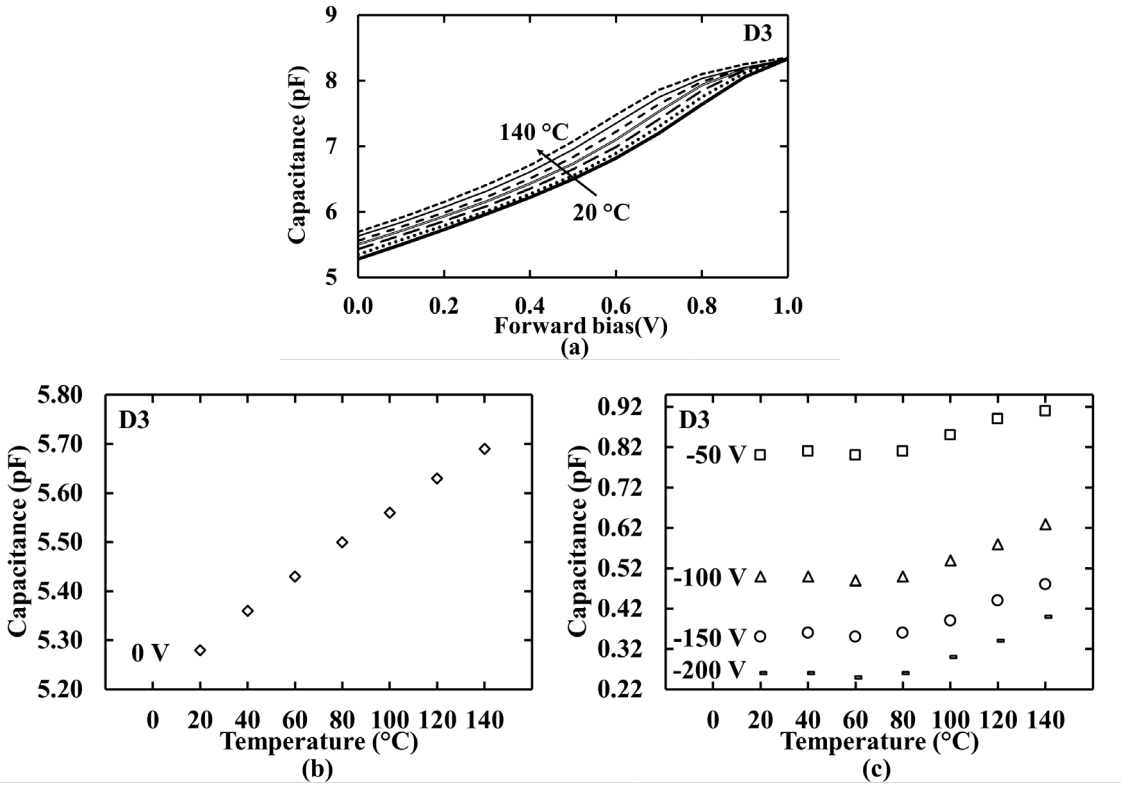

Figure 5.10. Measured capacitance for the 4H-SiC Schottky photodiode D3 (a) as a function of applied forward bias at a temperature range of 20 °C to 140 °C; 140 °C (square dots); 120 °C (thin solid line); 100 °C (dashes); 80 °C (long dash dot); 60 °C (long dashes); 40 °C (large round dots); 20 °C (thick solid line), and as a function of temperature (b) at 0 V (open diamonds) and (c) at applied reverse biases of -50 V (open squares), -100 V (open triangles), -150 V (open circles), and -200 V (dashes). The data points in (a) have been replaced by lines for clarity.

5.4 X-ray detection measurements

To characterise the five diodes for their response to X-ray illumination, they were installed in an LD Didactic GmbH X-ray apparatus which had a Mo target X-ray tube. Each diode was positioned inside a custom test fixture with a 4 μm Al window, directly in-line with aperture to the X-ray tube. A diagram of the experimental set up can be seen in **Figure 5.11**. Description of the current measurements, using the Keithley 6487 Picoammeter/Voltage Source, can be found in **Section 2.5.1**.

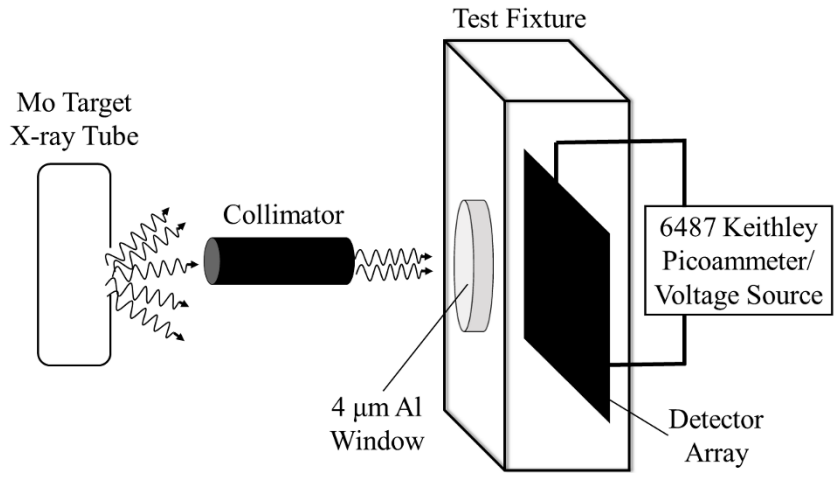

Figure 5.11. Diagram shown the experimental set up of the X-ray photocurrent measurements with the 4H-SiC Schottky photodiode array.

The leakage current of each diode was measured as a function of applied reverse bias at 25 °C (the ambient temperature of the LD Didactic GmbH X-ray apparatus with the Mo target X-ray tube switched off). Then, the X-ray tube, with its voltage and current being 35 kV and 1 mA respectively, was switched on. The total current (dark plus photocurrent) was recorded as a function of applied reverse bias for each diode one minute after the X-ray tube was switched on to eliminate any changes in the operating temperature (25 °C). **Figure 5.12** shows the measured dark and illuminated currents at 25 °C for diode D5 at the reverse bias range 0 V to -200 V.

The leakage current was subtracted from the total current, to give the photogenerated current which can be seen for each of the five diodes as a function of reverse bias in **Figure 5.13**. The photocurrent was measured to range from 4 pA to 8 pA for all diodes at reverse biases up to -100 V. However, a sign of breakdown for three of the devices (D1, D2, and D4) at high reverse biases (> -100 V) as a possible result of thermal runaway (Buttay et al., 2012) can be seen at **Figure 5.13**. None of the devices was reverse biased at > -100 V for the subsequent X-ray measurements.

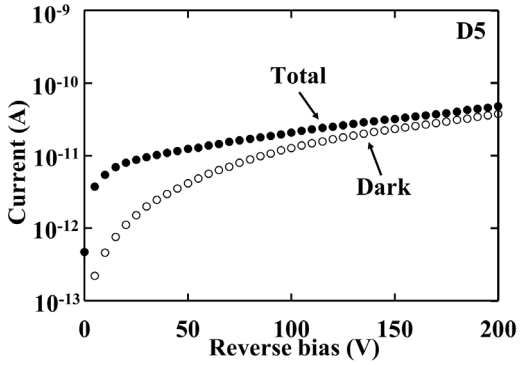

Figure 5.12. Measured current of the 4H-SiC Schottky photodiode D5 as a function of reverse bias for X-ray tube (with a voltage of 35 kV and a current of 1 mA) being switched off (dark current) (open circles) and on (total current) (filled circles) at a temperature of 25 °C.

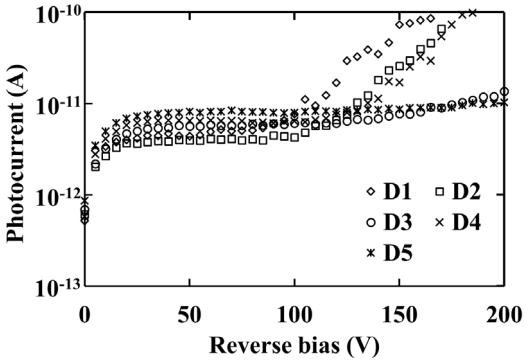

Figure 5.13. Measured photogenerated current as a function of reverse bias from X-ray photons from a Mo target X-ray tube (with a voltage of 35 kV and a current of 1 mA), of all five 4H-SiC Schottky photodiodes at a temperature of 25 °C; D1 (open diamonds); D2 (open squares); D3 (open circles); D4 (× symbols); D5 (stars).

Following the photocurrent measurements, X-ray spectra were obtained using the five diodes. The Mo target X-ray tube, with a voltage of 35 kV and a current of 1 mA, was powered for 3 hours prior to any measurements in order for the temperature of the system to stabilize; the ambient Mo target X-ray tube temperature was 33 °C. Each diode was connected in turn to a single-channel custom-made charge sensitive preamplifier of feedback resistorless design (Bertuccio et al., 1993). The diodes and the preamplifier were both housed in a custom test fixture with a 4 μm Al window, which was positioned inside the X-ray apparatus in-line with the X-ray tube aperture. The output signal of the preamplifier was shaped using an Ortec 572A shaping amplifier. The output of the shaping amplifier was connected to a multi-channel analyser (MCA) for digitisation. The live time of each accumulated spectrum was 300 s.

Spectra were accumulated using D5 at different shaping times (τ = 0.5 μs, 1 μs, 2 μs, 3 μs, 6 μs, and 10 μs), with the diode being reverse biased at -60 V. The selection of the applied reverse bias

of the detector is a trade off between high quantum detection efficiency, improved charge transport, low capacitance (high reverse biases needed) and low leakage current (low reverse biases needed). Operating the diodes at -60 V reverse bias, improved charge transport, reduced capacitance (by 7.1 pF for D1 and a mean of 4.9 pF ± 0.1 pF for D2 to D5, **Fig. 5.7b**) and a moderate increase in leakage current (by 20 pA for D1 and a mean of 10 pA ± 1 pA for D2 to D5, **Fig. 5.2b**) was achieved, compared to 0 V. Operating the diodes at a higher reverse bias, e.g. -200 V, higher count rate (due to larger depletion width, **Fig. 5.8**) and a further reduction in capacitance (by a mean of 0.44 pF ± 0.07 pF for didoes D1 to D5, **Fig. 5.7b**) could be achieved but at the expense of an increase in leakage current (by a mean of 30 pA ± 10 pA for diodes D1 to D5, **Fig. 5.2b**), compared to -60 V reverse bias. Hence, the -60 V applied reverse bias was a compromise between increasing the quantum detection efficiency, improving the charge transport, reducing the capacitance, while maintaining low leakage current.

Gaussians were fitted to the detected Mo Kα (= 17.4 keV) and Kβ (= 19.6 keV) peaks of the accumulated spectra. The positions of the zero energy noise peak and the Mo Kα peak were used to energy calibrate each spectrum. The measured *FWHM* at 17.4 keV as a function of shaping time (reverse biased at -60 V) can be seen in **Figure 5.14**. The uncertainty of the *FWHM* associated with fitting a Gaussian to the photopeak was estimated to be ± 0.03 keV for the five 4H-SiC Schottky photodiodes reported in this section.

The energy resolution (*FWHM* at 17.4 keV) at the optimum shaping time (τ_{opt} = 1 μs) was found to be 1.43 keV. Spectra of the Mo X-ray tube were then subsequently obtained using the other diodes operated at 1 μs shaping time. The diodes were kept reverse biased at -60 V. As stated in **Section 5.3.2**, a mean depletion layer width of 6.1 μm ± 0.5 μm (rms deviance) had been found for the diodes at -60 V reverse bias during the electrical characterisation (**Figure 5.8**) and the apparent variance of depletion width among the diodes, described by the rms deviance was found to be within the uncertainty of the measurements (i.e. ± 2 μm), thus a quantum detection efficiency of 0.85 % at 17.4 keV was implied for the diodes when reverse biased at -60 V (**Figure 5.8**).

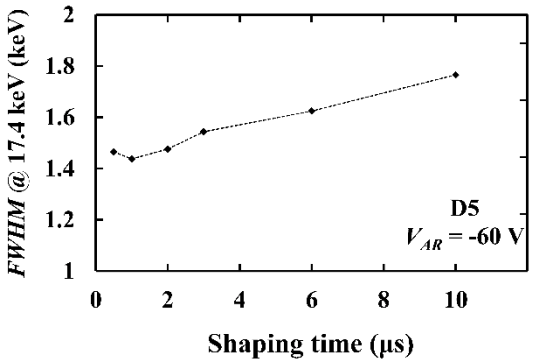

Figure 5.14. Energy resolution (*FWHM* at 17.4 keV) as a function of shaping time for the 4H-SiC Schottky photodiode D5 when reverse biased at -60 V and at a temperature of 33 °C (the temperature at which the photodiode and preamplifier stabilised when in proximity to the Mo target X-ray tube). The dotted lines are guides for the eye only.

The best energy resolution was achieved with diode D4 (*FWHM* at 17.4 keV = 1.36 keV, corresponding to *ENC* of 73 e^- rms, excluding Fano noise), whereas the poorest energy resolution was found to be 1.68 keV (*ENC* of 90 e^- rms, excluding Fano noise) using diode D1, which had the highest leakage current (20.4 pA, see **Figure 5.2**) and capacitance (2.2 pF, including the packaging capacitance) at -60 V reverse bias. An energy resolution of 1.52 keV (*ENC* of 82 e^- rms, excluding Fano noise), 1.42 eV (*ENC* of 76 e^- rms, excluding Fano noise) and 1.43 eV (*ENC* of 77 e^- rms, excluding Fano noise) was achieved using diode D2, D3 and D5 respectively. The spectrum of the Mo target X-ray tube obtained using all five diodes, D1 to D5, at 1 μs and -60 V reverse bias can be seen in **Figure 5.15**. The spectrum of the Mo target X-ray tube seen in **Figure 5.15** has the characteristic X-ray emission lines of the X-ray tube's cathode (Mo Kα at 17.4 keV and Mo Kβ at 19.6 keV) superimposed on the continuous bremsstrahlung spectrum emitted by the X-ray tube (see **Section 2.1.3**). The maximum energy of the X-ray continuous spectrum was determined by the tube's potential difference; 35 keV in this case. The presence of counts with energies >35 keV suggested pulse pile-up; there were 1252 counts (mean value among the diodes), ranging from 998 to 1328, with energies >35 keV. The dead time of the spectroscopic system was ranging from 9 % with D1 to 13 % with D4, with a mean value of 10 %.

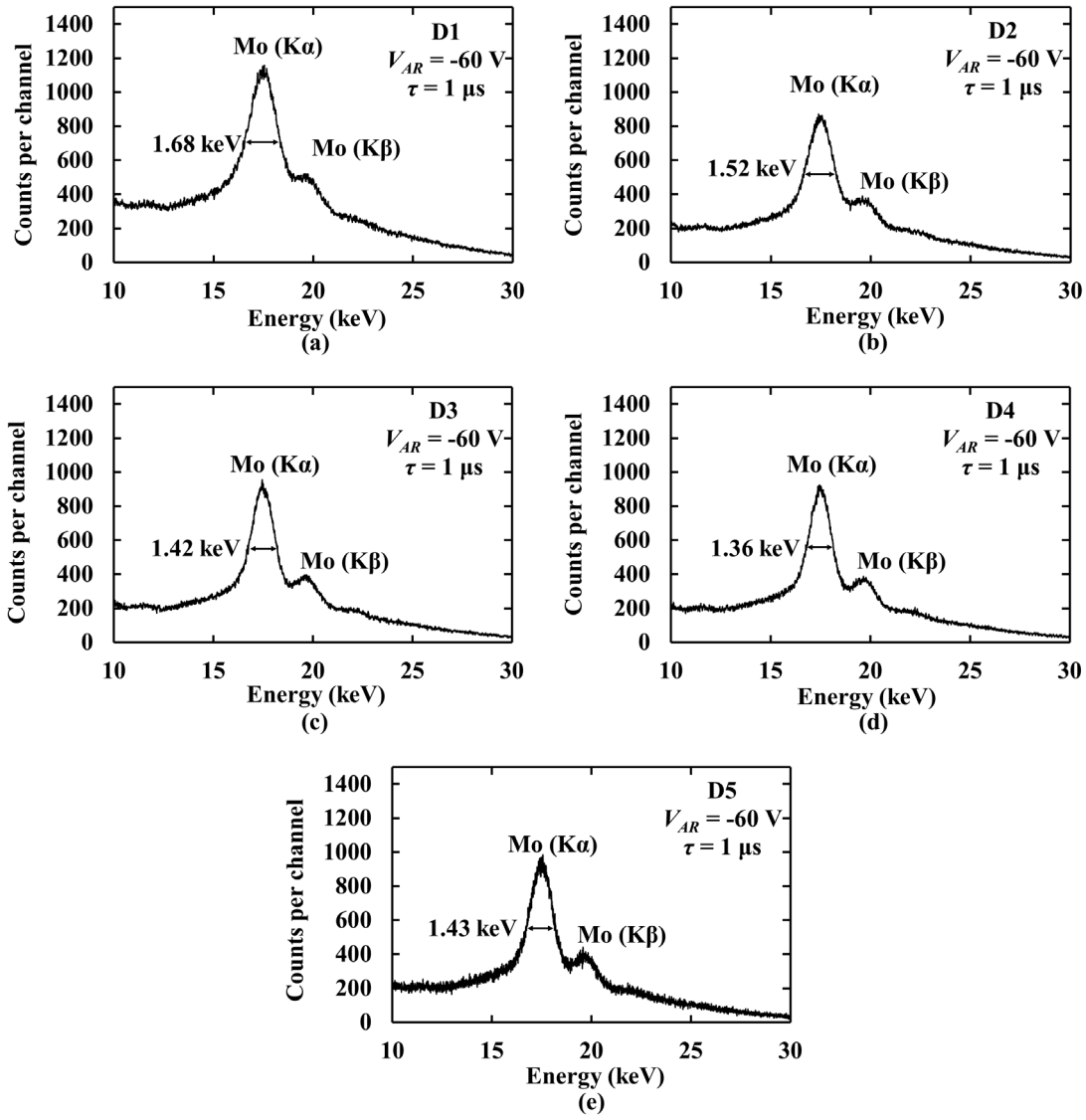

Figure 5.15. Spectra of the Mo target X-ray tube accumulated with the 4H-SiC Schottky photodiode a) D1, b) D2, c) D3, d) D4, and e) D5, at 1 µs shaping time and -60 V reverse bias.

The leakage currents of the detector and preamplifier's input JFET give rise to the parallel white noise, *WP* (see Equation 3.10). The capacitance of the detector and of the input JFET of the preamplifier give rise to the series white noise, *WS* (see Equation 3.2). Each component of the electronic noise (parallel white noise, series white noise, 1/*f* noise) was calculated as described in **Section 3.2**. The Fano noise was calculated to be equivalent to a *FWHM* of 274 eV at 17.4 keV, assuming F = 0.1 (Bertuccio et al., 2011) and ω = 7.8 eV (Bertuccio & Casiraghi, 2003). By subtracting the expected Fano noise, along with the calculated white series, white parallel, and 1/*f* noise contributions in quadrature from the determined energy resolution as quantified by the *FWHM*, the remaining was attributed to stray capacitances (unknown white series noise) and dielectrics (dielectric noise, *DN*) in close proximity to the input of the preamplifier. The total

noise along with the calculated contributions for each different noise source can be seen in **Figure 5.16** for each of the diodes.

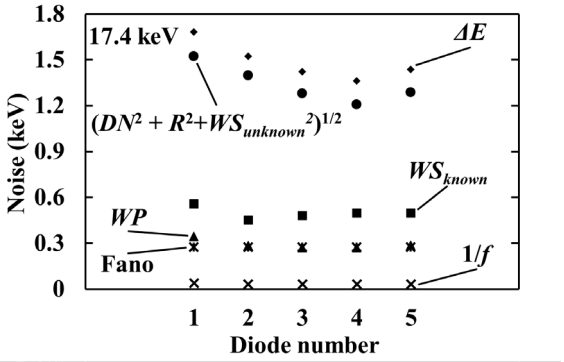

Figure 5.16. The calculated noise contributions for all five 4H-SiC Schottky photodiodes, at 1 μs shaping time and -60 V reverse bias. 1/*f* noise (crosses); Fano noise (stars); white parallel noise (filled triangles); known white series noise (filled squares); quadratic sum of dielectric noise, incomplete charge collection noise and unknown white series noise (filled circles); total noise (energy resolution as quantified by the *FWHM* at 17.4 keV) (filled diamonds).

The analysis presented in **Figure 5.16** indicates that the noise arising from stray capacitances and dielectrics at the input of the preamplifier was the dominant source of noise in the reported system; 1.34 keV ± 0.11 keV (equivalent to 73 e^- rms ± 6 e^- rms) *FWHM* at 17.4 keV. This result is comparable with similar previously reported preamplifier systems, which have a dielectric noise of 70 e^- rms (Barnett et al., 2012a) and 72 e^- rms (Lioliou et al., 2016) (see **Chapter 6**). Due to the pinout of the package of the devices, the connection of each device to the preamplifier was different resulting in a different unknown stray capacitance for each diode. Consequently, both the unknown white series noise and the dielectric noise varied among the diodes, with the dielectric noise being dependent on the total capacitance at the input of the preamplifier. The incomplete charge collection noise, *R*, was assumed to be negligible at -60 V reverse bias due to improved charge transport at electric field strengths of 98 kV/cm compared to lower electric fields. However, the presence of the incomplete charge collection noise cannot be directly measured. Hence, the incomplete charge collection noise was included in the sum of the unknown noise components: the unknown series white noise and dielectric noise, in **Figure 5.16**.

The *FWHM* at 17.4 keV ranged from 1.36 keV (D4) (corresponding to 74 e^- rms) to 1.68 keV (D1) (corresponding to 92 e^- rms), at 33 °C. These results are comparable with previously reported semi-transparent 4H-SiC Schottky diodes (1.49 keV at 5.9 keV at 23 °C (Lees et al., 2007) and 1.5 keV at 5.9 keV (Barnett, 2011)) and better than commercial 4H-SiC UV Schottky diodes (1.8 keV at 5.9 keV (Zhao et al., 2016)) repurposed as X-ray detectors and connected to

similar preamplifier systems. However, they are not as good as the best experimental reports on single pixel 4H-SiC X-ray detectors (196 eV *FWHM* at 5.9 keV at 30 °C (Bertuccio et al., 2011)); which were achieved using 4H-SiC epitaxial layers of exceptional quality and ultra-low-noise electronics.

It should be noted that compared to systems employing detectors made from Si or materials with narrow bandgaps, the electronic noise of the preamplifier used with a wide bandgap semiconductor detector, such as SiC, is more critical due to the typically greater electron hole pair creation energy of wide bandgap materials (7.8 eV for 4H-SiC (Bertuccio & Casiraghi, 2003) as opposed to 3.65 eV for Si (Fraser et al., 1994)) (see **Section 2.3.2**). For example, a total equivalent noise charge of 70 e^- rms (excluding Fano noise) at the input of a preamplifier results in a *FWHM* of 600 eV when a Si detector is used, and 1300 eV when a SiC detector is used. However, the lower white parallel noise in systems employing SiC detectors compared to that using Si detectors allows to overcompensate the greater electron hole pair creation energy of SiC under specific operating conditions. Bertuccio and Casiraghi (2003) showed that, depending on the area of the detector, there is a crossing temperature at which the *FWHM* of SiC becomes lower than that of Si for both pad and drift detectors. Interestingly, the larger the detector area the lowest this crossing temperature was found to be. Theoretical calculations showed that a better energy resolution (*FWHM*) can be achieved with a SiC detector than a Si detector for areas larger than 1 mm^2 at room temperature and above (Bertuccio & Casiraghi, 2003).

5.5 Conclusion

A 2 × 2 and a 1 × 3 4H-SiC diode array, consisting of five diodes in total, have been electrically characterised at room temperature. In addition, one representative diode was electrically characterised at elevated temperatures (up to 140 °C). Use of the diodes as X-ray detectors in both current mode and spectroscopic X-ray photon counting mode was demonstrated for all diodes at a temperature of 33 °C.

The forward current characteristics suggested that four diodes (D1, D2, D4, and D5) had double barrier heights. The double barrier height observed for D1, D2, D4, and D5 was attributed to the presence of two Schottky barriers connected in parallel based on the Schottky barrier height inhomogeneity concept (Tumakha et al., 2005) (Ma et al., 2006) (Grekov et al., 2008). The extracted zero band barrier height was found to be 1.14 eV ± 0.07 eV (rms deviance). The ideality factor (2.1 ± 0.1) deviated from unity, indicating that, at room temperature, the main current mechanism was not thermionic emission. Possible peripheral or surface leakage current component could contribute to the measured leakage current which can result in ideality factor values close to 2 (Woods & Hall, 1994). All the diodes were reverse biased at up to -200 V

(161 kV/cm) and had leakage currents less than 70 pA at -200 V reverse bias, at room temperature.

Forward and reverse bias current measurements on D3 at elevated temperatures (up to 140 °C) revealed the possible presence of an inhomogeneous barrier. Over the investigated temperature range, the ideality factor of D3 improved from 1.99 at 20 °C to 1.81 at 140 °C, and the zero band barrier height increased from 1.32 to 1.49 at the same temperatures. It was also found that the origin of the leakage current in the temperature range of 20 °C to 80 °C was different to that in the temperature range 80 °C to 120 °C. The leakage current at low temperatures was attributed to nitrogen (n-type epilayer dopant) carrier generation. The leakage current at high temperatures was attributed to carrier generation from Ti-N pairs in 4H-SiC having a different position in the lattice compared to a single nitrogen atom. The low activation energy at low temperatures (0.06 eV), suggested a weak dependence of leakage current upon temperature, at the temperature range 20 °C to 80 °C.

Comparable capacitances (5.83 pF ± 0.22 pF at 0 V) were measured for four of the five devices, (i.e. D2 to D5), at both forward and reverse biases, but one device, D1 showed a moderately higher capacitance at 0 V (8.0 pF ± 0.1 pF) and at forward biases. The implied depletion width was found to range from 10 μm to 14 μm among the diodes, with a mean value of 12 μm ± 1 μm, at the highest investigated reverse bias (-200 V), however this was mostly attributed to the uncertainty of each packaging capacitance. The effective carrier concentration and flat band barrier height at room temperature was calculated for one representative diode, D3, and were found to be 16.7×10^{14} cm^{-3} and 1.48 eV respectively. The temperature dependence of the same diode's capacitance was also measured. It was found that its capacitance slightly increased as the temperature increased at each applied forward bias and at the reverse bias range from 0 V to -5 V, possibly due to the progressive ionisation with temperature of non-ionised donors in a thin region around the depletion layer (Mazzillo et al., 2012), whose thickness would be a smaller fraction of the depletion layer at higher than -5 V reverse bias. This latter could explain the invariant capacitance measured at higher than -5 V applied reverse bias, over the temperature range 20 °C to 80 °C. The measured increase in capacitance with increased temperature at higher than -5 V applied reverse bias over the temperature range 80 °C to 140 °C was attributed to an increase in the effective charge density at the same temperature range which was related to the occupancy of deep level defects (Gramberg, 1971).

The X-ray response of the diodes as a function of reverse bias was studied by measuring the photogenerated current in the devices when they were illuminated with a Mo X-ray tube. All five

diodes were sensitive to X-rays and showed comparable photogenerated currents in the range of 4 pA to 8 pA at -100 V reverse bias at a temperature of 25 °C.

To evaluate the devices for photon counting X-ray spectroscopy, the diodes were coupled to a custom-made low noise charge sensitive preamplifier. Spectra were obtained using the same Mo X-ray tube as was used for the current mode X-ray measurements. The *FWHM* of the Mo Kα peak was measured; using diode D5, it was found that the optimum shaping time was 1 μs. The diodes were reverse biased at -60 V and the energy resolution (*FWHM* at 17.4 keV) achievable with each diode was measured; it ranged from 1.36 keV ± 0.03 keV (D4) (corresponding to 74 e^- rms) to 1.68 keV ± 0.03 keV (D1) (corresponding to 92 e^- rms), at 33 °C and 1 μs shaping time, where the uncertainties of the *FWHM* were associated with fitting a Gaussian to the photopeak. These results are comparable with previously reported 4H-SiC Schottky diodes having thin NiSi Schottky contacts (1.49 keV at 5.9 keV at 23 °C (Lees et al., 2007) and 1.5 keV at 5.9 keV (Barnett, 2011)) and better than commercial 4H-SiC UV Schottky diodes (1.8 keV at 5.9 keV (Zhao et al., 2016)) repurposed as X-ray detectors and connected to similar preamplifier systems. Although, they are not as good as the best experimental reports on single pixel 4H-SiC X-ray detectors (196 eV *FWHM* at 5.9 keV at 30 °C (Bertuccio et al., 2011)); which were achieved using 4H-SiC epitaxial layers of exceptional quality and ultra-low-noise electronics, it was found then the energy resolution of the system was limited by the noise arising from the dielectric noise and stray capacitances present at the proximity of the preamplifier's input at the reported temperature (33 °C), reverse bias (-60 V) and shaping time (1 μs).

Although the pixels of the 2 × 2 and 1 × 3 4H-SiC diode arrays reported here showed unexpected high leakage current at room temperature, double barrier heights and high ideality factors, it has been shown that they can operate as detectors for photon counting X-ray spectroscopy at 33 °C with modest energy resolution. The slight increase in leakage current as the temperature increased from 20 °C to 80 °C (**Figure 5.5**) and in capacitance as the temperature increased from 20 °C to 140 °C (**Figure 5.10b**) for the reported 4H-SiC Schottky diodes with thin NiSi Schottky contacts, along with the noise analysis of the energy resolution of the detector/preamplifier system (limited by the preamplifier noise, **Figure 5.16**) suggest they are likely to operate at high temperatures. The importance of developing the electronics to which the detectors were connected, due to higher electron hole pair creation energy of 4H-SiC compared to Si and GaAs, was highlighted. However under some conditions (e.g. at high temperatures and for large area devices) when the energy resolution is expected to be limited by the detector leakage current, the wide bandgap of 4H-SiC may become beneficial.

Chapter 6 7 μm i Layer GaAs Mesa p^+-i-n^+ Photodiodes

6.1 Introduction and background

GaAs, with its wider bandgap (1.42 eV (Bertuccio & Maiocchi, 2002) c.f. 1.12 eV of Si (Bludau et al., 1974)) and only slightly greater electron-hole pair creation energy (4.184 eV (Bertuccio & Maiocchi, 2002) c.f. 3.65 eV of Si (Fraser et al., 1994)), higher density, higher effective atomic number, and greater radiation hardness than Si, can be exploited as a material for X-ray detectors at harsh environments.

GaAs has already been studied for its performance as X-ray detector at room temperature and up to 80 °C, as well as for its radiation resistance to γ-rays (Ly Anh et al., 2006) (Dixit et al., 2015), fast neutrons (Ladzianský et al., 2009), and high energy electrons (Šagátová et al., 2014). The best energy resolution (*FWHM* at 5.9 keV) using GaAs X-ray photodiode detectors reported by Owens et al. (2001). An energy resolution of 266 eV at 5.9 keV, at 23 °C, was achieved with GaAs devices in a 5 × 5 pixel array structure of 200 μm × 200 μm pixel size and 40 μm ultrapure epitaxial planar layer grown by chemical vapour phase deposition (CVPD), forming p^+-i-n^+ structure, and having Au/Pt/Ti Schottky contacts at the p^+ layer, and a guard ring (Owens et al., 2001). The GaAs devices were wire bonded to the same low loss substrate and close to the input JFET of the ultra-low-noise frond-end electronics. One year later, Erd et al. (2002) reported an energy resolution of 300 eV at 5.9 keV, at room temperature, using larger devices (250 μm × 250 μm) with a thicker epilayer (325 μm) and similar structure to the detectors reported by Owes et al. (2001) in a 32 × 32 pixel array. Despite these results, there are no reports for X-ray detection at higher than room temperature using such devices.

GaAs X-ray photodiodes operating at temperatures up to 80 °C have been studied by Barnett et al. (2011). An energy resolution of 800 eV at 5.9 keV, at room temperature, rising to ~1.5 keV at 80 °C, was achieved using GaAs p^+-i-n^+ mesa photodiodes grown by molecular beam epitaxy, with a 2 μm thick i layer (Barnett et al., 2011). GaAs p^+-i-n^+ mesa photodiodes with thicker i layer (3 μm), were characterised for their X-ray detection performance as a function of incident photon energy (from 4.95 keV to 59.5 keV) at a temperature of 33.3 °C (Barnett, 2014).

In this chapter, results from two (D1 and D2) fully etched 200 μm diameter GaAs p^+-i-n^+ mesa X-ray photodiodes with 7 μm thick i layers are presented. The wafer was grown by metal organic chemical vapour deposition at the EPSRC National Centre for III-V Technologies and the devices were fabricated at University of Sheffield. The devices reported in this chapter were randomly selected from the wafer. In **Section 6.2**, the device structure is described. In **Section 6.3**, both

devices are electrically characterised in terms of their current and capacitance at room temperature and key parameters are calculated. The devices are further characterised for their visible and near infrared responsivity without any external bias applied, and the results are presented in **Section 6.4**, along with theoretical calculations. The spectroscopic X-ray photon counting performance achieved with one GaAs p^+-i-n^+ mesa photodiode (D1) coupled with low-noise front-end electronics, operating at room temperature is reported and analysed in **Section 6.5**. In **Section 6.6**, the electrical characterisation of both diodes at the temperature range 0 °C to 120 °C is reported. X-ray spectra accumulated with one GaAs p^+-i-n^+ mesa photodiode (D1) coupled with low-noise front-end electronics operated in the temperature range 0 °C to 60 °C are presented and discussed in **Section 6.7**.

6.2 Device structure

GaAs epilayers were grown on a 350 μm thick heavily doped, n^+ GaAs substrate by metal organic vapour phase epitaxy (MOVPE) at the EPSRC National Centre for III-V Technologies, Sheffield. A p^+-i-n^+ structure was grown with a 0.5 μm p^+ type GaAs layer, a 7 μm unintentionally doped i layer and a 1 μm n^+ type GaAs layer. The thicknesses of the p^+ and i layers were designed so as to improve the X-ray quantum detection efficiency of the photodiode by keeping the p^+ layer as thin as possible and the i layer as thick as possible, while maintaining the quality of the semiconductor. The p^+ and n^+ type dopants used were C and Si, and the doping density of both n^+ type and p^+ type layers was 2×10^{18} cm^{-3}. The wafer's layer structure is summarised in **Table 6.1** and a drawing of the structure can be seen in **Figure 6.1**. Mesa diodes with diameters of 200 μm were chemically etched using H_3PO_4:H_2O_2:H_2O as the chemical etchant. The etched depth, as measured from the top of the wafer, was 8.3 μm. The Ohmic contact of the p^+ side was formed from Ti (20 nm thickness) and Au (200 nm thickness) layers.

Material	Type	Thickness (nm)	Doping density (cm^{-3})
Ti		20	
Au		200	
GaAs	p^+	10	1×10^{19}
GaAs	p^+	500	2×10^{18}
GaAs	i	7000	undoped
GaAs	n^+	1000	2×10^{18}
GaAs	n^+ (substrate)	-	-

Table 6.1. Layers structure of the GaAs p^+-i-n^+ wafer.

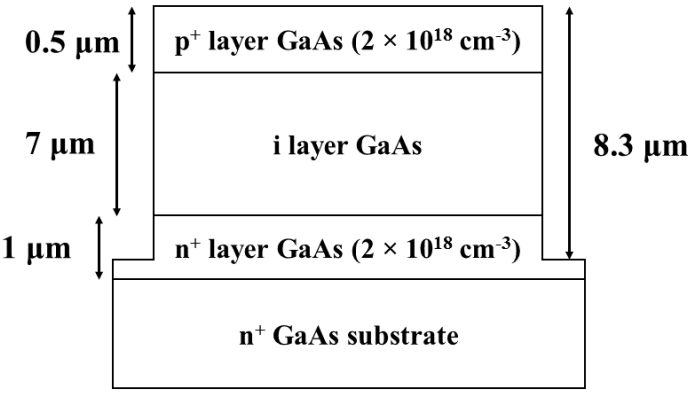

Figure 6.1. Illustrative layers structure (not in scale) of the GaAs p^+-i-n^+ photodiode.

The internal quantum detection efficiency of the devices was calculated for photon energies up to 30 keV using Equation 2.11a (see **Section 2.3.2**) and can be seen in **Figure 6.2**. For these calculations, it was assumed that there was a dead region in the p^+ layer, close to the surface with a width of 0.16 µm (see **Section 6.4**). The rest of the p^+ layer and the i layer was assumed to be the active region of the devices.

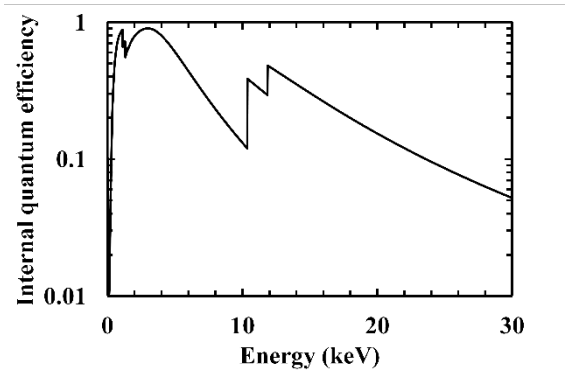

Figure 6.2. Calculated quantum detection efficiency of the GaAs p^+-i-n^+ mesa photodiodes as a function of photon energy.

6.3 Room temperature electrical characterisation

6.3.1 Current measurements as a function of bias

Forward and reverse bias dark current measurements as functions of applied voltage were performed using a Keithley 6487 Picoammeter/Voltage Source (see **Section 2.5.1**). The dark current at room temperature was measured for both diodes when forward biased in the range 0 V to 1.5 V, and when reverse biased in the range 0 V to -15 V. **Figure 6.3** shows the forward current, I_F, as a function of applied forward bias, V_{AF}, of diodes D1 and D2.

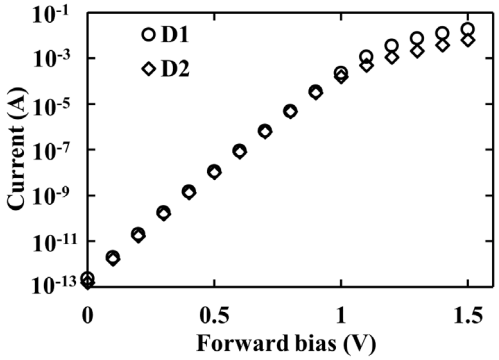

Figure 6.3. Current as a function of applied forward bias of the two GaAs p^+-i-n^+ mesa photodiodes, D1 (open circles) and D2 (open diamonds), measured at room temperature.

The ideality factor, n, and the saturation current, I_{sat}, were both calculated from the measured semi-logarithmic forward current, I_F, as a function of applied forward bias, V_{AF}, of the devices (see Equation 2.33). These extracted values, as well as their temperature dependence reveal the nature of the conduction mechanism (thermionic emission, diffusion, recombination and tunnelling).

There are two distinct regions of the plots shown in **Figure 6.3**. The first region is linear and corresponds to applied voltages $V_{AF} \leq 0.9$ V. The saturation current, I_{sat}, was found to be 0.312 pA ± 0.032 pA and 0.258 pA ± 0.030 pA for diode D1 and diode D2, respectively. The ideality factor was computed to be 1.91 ± 0.01 for D1 and 1.89 ± 0.01 for D2. Ideality factor values close to 2 suggest that recombination current dominated (Sze & Ng, 2007). Further investigation of the relationship between the ideality factors of each photodiode with temperature could give a better indication of the conduction process (Sellai, 2008); such measurements and analysis are reported in **Section 6.6**. The second region of the semi-logarithmic forward current, I_F, as a function of applied forward bias, V_{AF}, which corresponds to applied voltages $V_{AF} > 0.9$ V deviates from linearity. As the applied voltage increased, the semi-logarithm forward current, I_F, as a function of applied forward bias, V_{AF}, of the devices bend down (**Figure 6.3**), resulting in a non-linear relationship between the logarithm of forward current and the applied voltage and indicating that the effect of series resistance, R_{ser}, became significant. Indeed, at high current levels, the finite resistivity of the regions outside the depletion region may absorb an amount of the applied bias at the diode terminals, resulting in deviation of the measured current from the theoretical predictions (**Section 2.4.2**).

The leakage current, I_R, as a function of applied reverse bias, V_{AR}, of the two GaAs p^+-i-n^+ mesa photodiodes are shown in **Figure 6.4**. Both GaAs p^+-i-n^+ mesa photodiodes showed low leakage current densities when reverse biased at -15 V (mean electric field of 22 kV/cm across the i

region). At room temperature, the leakage current densities of 17.4 nA/cm^2 and 1.08 nA/cm^2 were measured for D1, and D2, respectively, at -15 V reverse bias. These values are comparable with other high quality GaAs p^+-i-n^+ photodiodes (e.g. ~10 nA/cm^2 at 30 °C, at a similar internal electric field (Bertuccio et al., 2003)), and are better than other reported similar GaAs p^+-i-n^+ mesa photodiodes having the same i layer thickness (20 nA/cm^2 to 100 nA/cm^2 at similar electric field and at room temperature (Ng et al., 2014)), possibly due to better wafer quality and diode fabrication.

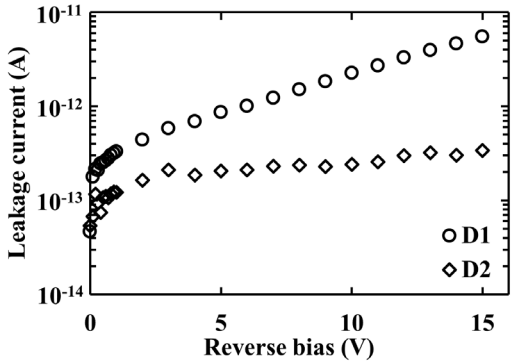

Figure 6.4. Leakage current at room temperature as a function of applied reverse bias for the two GaAs p^+-i-n^+ mesa photodiodes, D1 (open circles) and D2 (open diamonds).

The stability of the leakage current with time was investigated. Initial measurements at room temperature showed that the leakage current of diode D1 increased from 5.47 pA to 28.35 pA over a period of 90 s when reverse biased at -15 V. Under these conditions, the diode was not reverse biased at -15 V for more than 90 s in order to ensure that it was not damaged. The leakage current of diode D2 was found to increase from 0.33 pA to 4.5 pA over a period of 300 s when reverse biased at -15 V. Both devices, D1 and D2, were then annealed up to a final temperature of 120 °C in a TAS Micro MT climatic cabinet. After annealing, they were gradually cooled to 20 °C, over a period of 205 minutes. The leakage current measurements as a function of applied reverse bias of the diodes were then repeated, and when reverse biased at -15 V the leakage current of both devices was measured to remain stable with time, over a period of 600 s. Additionally, the first leakage current measurement (at 0 s) of D1 at -15 V reverse bias was found to be reduced after annealing; it decreased from 5.47 pA before annealing to 3.86 pA after annealing. **Figure 6.5** shows the measured leakage current of diodes D1 and D2 as a function of time, at -15 V reverse bias, both before and after annealing. The precise mechanism of leakage current reduction and leakage current stabilization over time, after heating the devices at 120 °C, is currently unknown, but the improvement can probably be attributed to the presence of shallow and/or deep level traps in GaAs being partially annealed by the heating. During the annealing process, the number of defects in a semiconductor material decreases with time (Vavilov, 1965).

The reestablishment of the semiconductor disturbed by defects (annealing) occurs when structural point defects (vacancies and interstitial atoms) and chemical impurities interact with each other. Crystal defects that might have been introduced during the growth or the processing of the devices, may be acting as trapping and/or recombination centres and affecting the leakage current. Radiation induced defects have been previously shown to be annealed at -23 °C and at 227 °C (Stein, 1969), and at 40 °C (Dixit et al., 2015) resulting in the recovery of the device properties. Similarly to this, crystal defects might have been partially annealed at 120 °C resulting in leakage current reduction.

The leakage current reduction of the GaAs photodiodes after they were heated to 120 °C may also be related to the reduction of the surface leakage current. Surface dangling bonds can act as recombination/generation and trapping centres (Holt & Yacobi, 2007) (Owens, 2012a). In practice, the dangling bonds combine with any atoms they encounter; most likely with hydrogen and oxygen in the atmosphere (Lowe & Sareen, 2014). When bias is applied, the field at the surface (bare walls) of the device causes current flowing in the surface channels that have been formed. The bonds between the surface of the semiconductor and atoms in the atmosphere can break at elevated temperatures (becoming dangling bonds again), resulting in possible leakage current reduction.

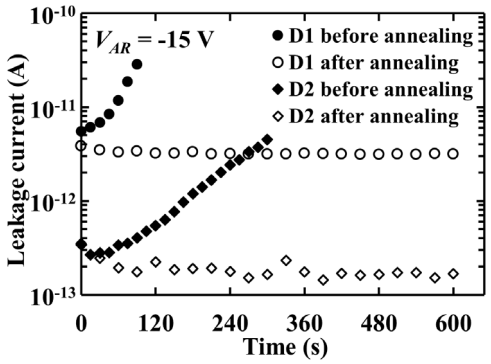

Figure 6.5. Leakage current of two GaAs p^+-i-n^+ mesa photodiodes, D1 and D2, measured at 20 °C at -15 V reverse bias, as a function of time, before and after annealing at 120 °C.

6.3.2 Capacitance measurements as a function of bias

The depletion layer width, W_D, and the effective doping concentration, N_{eff}, in the intrinsic layer of the devices were determined from capacitance measurements. The capacitance was measured as a function of applied forward and reverse bias, using an HP 4275A Multi Frequency LCR meter (see **Section 2.5.2**). The test signal was sinusoidal with a 50 mV rms magnitude and 1 MHz frequency. Capacitance measurements were made at forward bias between 0 V and +1 V and at reverse bias between 0 V and -15 V. The capacitance of the empty packaging was also measured

and subtracted from the measured capacitance of the packaged diodes. The capacitance of the package was determined by measuring two empty packages and was found to be 0.6 pF. **Figure 6.6** shows the forward and reverse bias capacitance measurements of the two GaAs p^+-i-n^+ mesa photodiodes with the packaging capacitances subtracted.

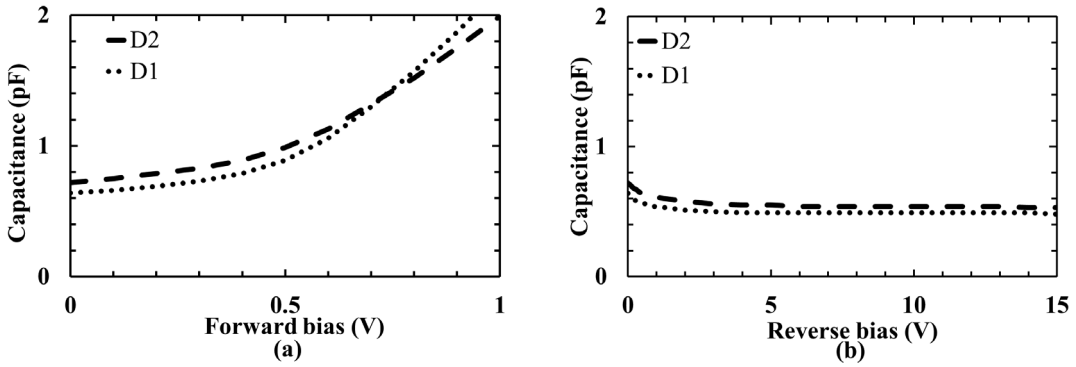

Figure 6.6. Capacitance as a function of (a) forward and (b) reverse bias of the two GaAs p^+-i-n^+ mesa photodiodes, D1 (dashes) and D2 (round dots), measured at 20 °C. The data points have been replaced by lines for clarity.

The depletion layer width of the diodes as a function of applied reverse voltage was calculated using Equation 2.37 and is presented in **Figure 6.7**. Once the lightly doped intrinsic layer was fully depleted, the capacitance was independent of the applied reverse bias. This occurred at -4 V reverse bias for D1, suggesting a depletion width of 7.3 μm ± 0.4 μm and at -6 V reverse bias for D2, suggesting a derived depletion width of 6.6 μm ± 0.4 μm. The depletion width at 0 V bias was measured to be 5.6 μm ± 0.3 μm for D1 and 5.0 μm ± 0.2 μm for D2. The uncertainties of the calculated depletion widths were related to the uncertainty in the capacitance measurements (± 0.03 pF). Although **Figure 6.7** shows a small increase in the depleted depth from -14 V to -15 V reverse bias, this increase is insignificant because the spatial resolution of profiles determined by capacitance as a function of applied reverse bias measurements are of the order of a Debye length, which has been calculated for GaAs with a doping concentration of 10^{14} cm^{-3} at room temperature to be 0.4 μm (Sze & Ng, 2007).

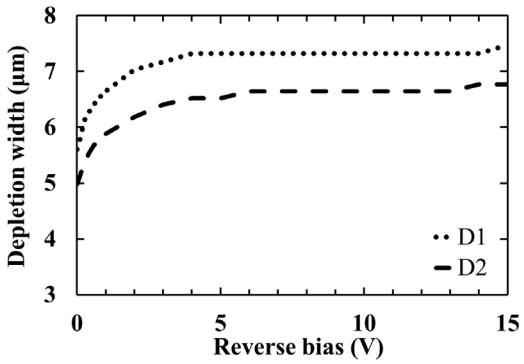

Figure 6.7. Calculated depletion layer width for the two GaAs p^+-i-n^+ mesa photodiodes, D1 (round dots) and D2 (dashes), calculated from capacitance measurements as a function of applied reverse bias. The depletion layer widths of D1 and D2 for applied reverse biases > -2 V were the same within the uncertainties (error bars were omitted for clarity). The data points have been replaced by lines for clarity.

The build-in potential, V_{bi}, along with the effective doping concentration of the i layer, N_{eff}, was calculated using Equation 2.38. **Figure 6.8** shows the measured $1/C_{DL}^2$ as a function of applied bias, V_{AB}, for the two fully etched GaAs p^+-i-n^+ mesa photodiodes, D1 and D2. The uncertainties shown in **Figure 6.8** associated with the measured $1/C_{DL}^2$ were related to the estimated uncertainty of a single capacitance measurement (± 0.03 pF). It should be noted that the measured $1/C_{DL}^2$ as a function of applied bias, V_{AB}, for each diode resulted from a single set of measurements and thus had correlated errors.

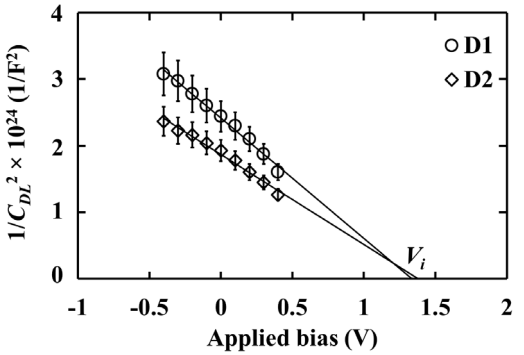

Figure 6.8. $1/C_{DL}^2$ as a function of applied bias for the GaAs p^+-i-n^+ mesa photodiode D1 (open circles) and D2 (open diamonds) at the bias range -0.4 V to 0.4 V where the relationship is linear. The line of best fit, for each set of data, calculated using linear least squares fitting, is also shown. The error bars were calculated based on the uncertainties in the capacitance measurements (± 0.03 pF).

A line of best fit was calculated for the $1/C_{DL}^2$ (V_{AB}) data presented in **Figure 6.8** using linear least squares fitting. The value of V_{bi} was extracted from the voltage axis intercept point, V_i, and the *i* layer effective doping concentration, N_{eff}, from the gradient of the line. The measured built-in potential was found to be the same (within the uncertainties) for D1 and D2, 1.39 V ± 0.05 V for D1 and 1.43 V ± 0.06 V for D2. This is comparable with the theoretical built-in voltage (1.39 V) based on the acceptor and donor density of the p^+ and n^+ layer respectively (Sze & Ng, 2007). Furthermore, the majority carrier concentration, effectively being the i layer doping density, was calculated to be 6×10^{13} cm^{-3} ± 1×10^{13} cm^{-3} for D1 and 8×10^{13} cm^{-3} ± 1×10^{13} cm^{-3} for D2.

Due to the high doping concentrations of the p^+ and n^+ layers, the extension of the depletion region to the p^+ and n^+ sides was negligible for the devices reported here. The effective doping concentration as a function of depletion layer width, $N_{eff}(W_D)$ was calculated using the differential capacitance method, based on Equation 2.38 and is shown in **Figure 6.9**.

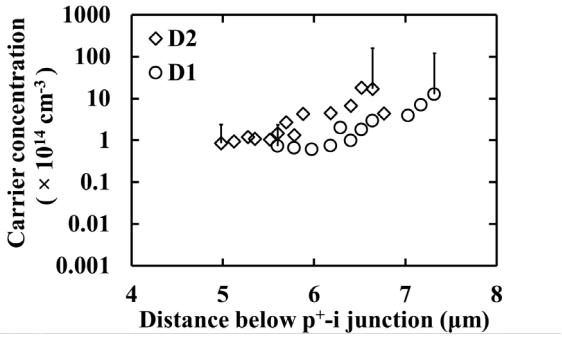

Figure 6.9. Calculated effective doping concentration as a function of depletion layer width of the GaAs p^+-i-n^+ mesa photodiode D1 (open circles) and D2 (open diamonds) at room temperature. The error bars were calculated propagating the uncertainty in the capacitance measurements (± 0.03 pF). Negative error bars cannot be plotted due to the y axis being on a logarithmic scale.

The lowest effective doping concentration in the i layer was found to be 1×10^{14} cm^{-3} for both diodes, up to 6.2 μm below the p^+-i junction for D1 and up to 5.0 μm below the p^+-i junction for D2. The uncertainty of the lowest effective doping concentration in the i layer was found to be ± 2×10^{14} cm^{-3} propagating the uncertainty in the capacitance measurements (± 0.03 pF), and considering that it encompasses only 2/3 of the effective doping concentration values (assuming a Gaussian distribution), the lowest effective doping concentration in the i layer was determined to be $\leq 4 \times 10^{14}$ cm^{-3}. These results were consistent with the *i* layer effective doping concentration, N_{eff}, calculated from the gradient of the $1/C_{DL}^2$ (V_{AB}); 6×10^{13} cm^{-3} ± 1×10^{13} cm^{-3} for D1 and 8×10^{13} cm^{-3} ± 1×10^{13} cm^{-3} for D2.

At deeper distances (closer to i-n^+ junction), the effective doping concentration in the i layer increased reaching a maximum value of 10×10^{14} cm^{-3} at the i-n^+ interface for both diodes, where the i-n^+ interface was determined from the capacitance measurements as a function of applied bias. The uncertainty of the effective doping concentration at the i-n^+ interface was found to be $\pm 100 \times 10^{14}$ cm^{-3}, which suggested an effective doping concentration at the i-n^+ interface $\leq 160 \times 10^{14}$ cm^{-3}.

6.4 Room temperature visible and near infrared responsivity

6.4.1 Photocurrent measurements

To investigate the performance of the detectors under visible and near infrared light illumination, and their suitability for use in applications where visible and near infrared detectors are required, photocurrent measurements were made using a ThermoSpectronic UV300 UV-VIS spectrophotometer with a Tungsten lamp to cover the wavelength range 580 nm to 980 nm, in 5 nm intervals (see **Section 2.5.3**). The selection of the wavelength of interest was performed using an internal monochromator and UV grating. Custom baffles were used in order to ensure that no external sources of light could influence the measurements. The measured photocurrent, in the investigated wavelength range of 580 nm to 980 nm, ranged from ≤ 1 pA to 35 pA.

Responsivity measurements of the two devices, in arbitrary units, are shown in **Figure 6.10** as a function of the incident photons' wavelengths, measured at room temperature and at 0 V reverse bias. The responsivity is a function of the wavelength, λ (see **Section 6.4.2**). This is due to the dependence of the linear attenuation coefficient of the material, μ, on the incident light's wavelength (Saleh & Teich, 1991).

The responsivity of the detectors exhibited abrupt spectral cutoff (GaAs direct bandgap = 1.42 eV (Bertuccio & Maiocchi, 2002), corresponding to 870 nm), as other semiconductors with direct bandgaps (Torvik et al., 1999). The long wavelength cutoff was 870 nm for both detectors, where the maximum responsivity was recorded. This was established by the bandgap; for wavelengths longer than 870 nm, the photon energy was smaller than the bandgap energy so that no photoelectron was generated (Sze & Ng, 2007). The photoresponsivity decreased with shortening wavelength, from a maximum at 870 nm. This was attributed to the fact that photons with wavelength $\leq$ 870 nm (corresponding to energy $\geq$ 1.42 eV) were absorbed near to the surface (penetration depth $\leq$ 1.25 μm). The recombination lifetime is short near the surface (Saleh & Teich, 1991), and hence some photocarriers recombined before being collected.

6.4.2 Calculated expected responsivity

The expected responsivity as a function of wavelength was calculated at the wavelength range of interest (580 nm to 980 nm). The responsivity, R', defined as the ratio of the photocurrent to the optical power, was computed based on the calculated external quantum detection efficiency, $QE_{external}$ (Equation 2.13). The external quantum detection efficiency was calculated (see **Section 2.3.2**) using the reflectance, r, at each photon wavelength at the air-photodiode interface and the internal quantum detection efficiency, $QE_{internal}$ (Equation 2.12). The internal quantum detection efficiency was calculated using Equation 2.11b, which accounts for the absorption of photons before reaching the depletion region (first term of Equation 2.11b) as well as the absorption in the active depletion and diffusion region (second term of Equation 2.11b).

In the detectors' geometry, there are two absorbing layers in front of the active region of the device. These are: 1) the metallization layer (primarily 200 nm of Au) on top of the p^+ layer as the form of the p^+ contact and 2) the dead layer in the p^+ layer, close to the surface of the detector. Starting with 1), the Au layer covered 45 % of each diode's face. Consequently, the first term of Equation 2.11b, for $m = 1$ becomes $\left[\left(1 - f_{geo}\right) \mathrm{e}^{(-\mu_1 x_1)} + f_{geo}\right]$, where f_{geo} is the geometrical fill factor of the devices which equals the area directly exposed to the incoming beam (= 55 % for these devices) and μ_1 and x_1 are the linear attenuation coefficient of Au and the thickness of the Au layer, respectively (Fraser, 1989). In the wavelength of interest, the term $e^{(-\mu_1 x_1)}$ was computed to be in the range $10^{-6} \sim 10^{-8}$, hence almost all photons falling on this are of the diode's face are absorbed at the Au layer. Consequently, the first term of Equation 2.11b, for $m = 1$, is simplified to f_{geo}.

Concerning layer 2), the total thickness of the p^+ layer was 0.5 μm. While in the ideal case the whole p^+ layer can be considered to be active, depending on material growth, there can be a dead layer, where surface recombination takes place (Saleh & Teich, 1991). For x_{dl} being the thickness of the dead layer at the p^+ side with a linear attenuation coefficient μ_{GaAs}, the first term of Equation 2.11b, for $m = 2$ becomes $e^{(-\mu_{GaAs} x_{dl})}$.

The second term of Equation 2.11b includes the carriers generated inside the depletion region from the absorption of photons as well as the carriers generated outside the depletion region which diffused into the reverse biased junction (Sze & Ng, 2007). The hole diffusion length, L_p, equals 1.2 μm in n-type GaAs with a dopant concentration of 2×10^{18} cm^{-3} (Hwang, 1969). Because the diffusion length of electrons is greater than the thickness of the p^+ layer (Wight et al., 1981), if there is no recombination region, the whole of the p^+ layer could be said to be active along with the i layer and the fraction of the n^+ layer determined by one hole diffusion length. The linear

attenuation coefficient of the active GaAs layer, μ_a, is related to the extinction coefficient (also known as attenuation index), κ, and using the values reported by Palik (1997), it was computed as a function of wavelength.

The expected responsivity was computed as a function of wavelength, assuming there was no dead layer at the p^+ side, and can be seen in **Figure 6.10**. When no dead layer close to the surface of the detector was taken into account, agreement between the calculated expected and the measured photoresponsivity was poor. **Figure 6.10** suggests that the difference between the measured responsivity at 580 nm (minimum) and 870 nm (maximum) was higher than the corresponding difference for the calculated expected responsivity, meaning that the experimental responsivity at short wavelengths (penetration depth < 1 μm) was lower than the expected responsivity. One explanation for this would be the presence of a non-active (dead) layer at the p^+ side, where the photogenerated carriers do not contribute to the photocurrent, possibly due to surface recombination. Including the presence of a 0.16 μm thick dead layer in the model resulted in agreement between the calculated expected and measured responsivity (**Figure 6.10**). The maximum value of the expected responsivity was found to be at 870 nm, reaching a value of 0.23 A/W for x_{dl} = 0.16 μm, in contrast with 0.26 A/W for x_{dl} = 0 μm, assuming any additional inefficiencies in detection in photons and charge transport losses were minimal. Overall, the apparent dead layer close to the surface of the detector resulted in a reduced responsivity, mainly at short wavelengths, where the penetration length was comparable to the thickness of the dead layer. The surface recombination of the photo-generated carriers may be reduced by surface passivation (Aberle, 2000) (Balaji, 2015), which can lead to increased responsivity.

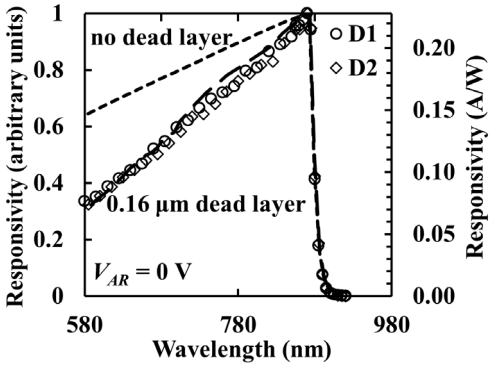

Figure 6.10. Calculated expected responsivity as a function of wavelength for dead layer thickness, x_{dl} = 0 μm (short dashes) and x_{dl} = 0.16 μm (long dashes), along with the measured responsivity of the GaAs p^+-i-n^+ mesa photodiode D1 (open circles) and D2 (open diamonds), all in arbitrary units. The calculated expected responsivity for dead layer thickness, x_{dl} = 0.16 μm is also shown in A/W. Although the responsivity of D1 and D2 was measured with 5 nm intervals, a subset (15 nm intervals) of the experimental points is shown in this figure to improve clarity.

6.5 Room temperature X-ray spectroscopy

6.5.1 Measurements with an ^{55}Fe radioisotope X-ray source

To characterise the X-ray detection performance of the devices, X-ray spectra were obtained using the GaAs p^+-i-n^+ mesa photodiode D1. An ^{55}Fe radioisotope X-ray source, with characteristic Mn Kα (5.9 keV) and Mn Kβ (6.49 keV) lines (Schötzig, 2000), was positioned 3 mm above the top of the diode. The diode was connected to a custom-made single-channel charge sensitive preamplifier (see **Section 2.3.3**). The diode and the preamplifier were kept at room temperature throughout the measurements. The signal of the preamplifier output was further shaped using an Ortec 572A shaping amplifier. The shaping amplifier was then connected to a multi-channel analyser (MCA). The live time limit for each accumulated spectrum was 120 s.

The diode was reverse biased at 0 V, -5 V, -10 V, and -15 V, in turn. At each reverse bias, X-ray spectra were obtained with varied shaping time, τ (= 0.5 μs, 1 μs, 2 μs, 3 μs, 6 μs, and 10 μs). **Figure 6.11** shows the obtained ^{55}Fe X-ray spectrum at 2 μs shaping time and -15 V reverse bias. The dashed lines in **Figure 6.11** represent the fitted Gaussians to the peak in the ratio appropriate for ^{55}Fe (Schötzig, 2000) and taking account of the relative difference in efficiency of the detector for 5.9 keV and 6.49 keV X-rays. The detected ^{55}Fe photopeak is the combination of the Mn Kα and Mn Kβ lines, at 5.9 keV and 6.49 keV respectively (Schötzig, 2000), due to the energy resolution being insufficient to resolve the individual lines. The position of the zero energy noise peak and the position of the fitted Mn Kα peak were used for energy calibration for each spectrum. In **Figure 6.11**, the counts of the zero energy noise peak of the preamplifier were limited by

setting the MCA low energy cut-off at 1.3 keV, but a small portion of the right hand side of the tail can still be seen in **Figure 6.11**.

The low energy tailing of the combined Mn Kα and Mn Kβ peaks, which can be seen in **Figure 6.11**, may be attributed to partial charge collection of charge created in the non-active layers (Barnett et al., 2015). The amount of low energy tailing can be quantified by the valley-to-peak (*V*/*P*) ratio. The *V*/*P* ratio was measured for all obtained spectra from the ratio between the number of counts at 3 keV and the number of counts at 5.9 keV; a mean value of 0.05 was found. This is comparable to the *V*/*P* ratio reported by Barnett at al. (2011) for a typical ^{55}Fe spectrum accumulated at 20 °C using a GaAs mesa p^+-i-n^+ photodiode with 2 µm i layer thickness, suggesting similar partial charge collection of charge created in the non-active layers between the 7 µm (reported here) and 2 µm (Barnett et al., 2011) i layer GaAs mesa p^+-i-n^+ photodiodes. The *FWHM* at 5.9 keV was measured for all obtained spectra and is presented in **Figure 6.12a – 6.12d** as a function of shaping time at 0 V, -5 V, -10 V and -15 V reverse bias, respectively. The uncertainty of the *FWHM* associated with fitting a Gaussian to the photopeak was estimated to be ± 10 eV for the GaAs p^+-i-n^+ mesa photodiode D1 reported in this section.

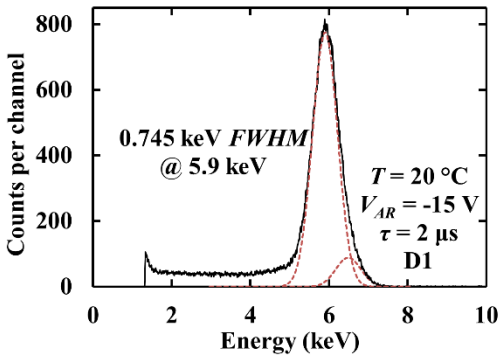

Figure 6.11. ^{55}Fe spectrum accumulated with the GaAs p^+-i-n^+ mesa photodiodes D1 at -15 V reverse bias (τ = 2 µs) along with the fitted Mn Kα and Kβ peaks (dashed lines).

The best energy resolution (*FWHM*) achieved was 745 eV at 2 µs shaping time and -15 V reverse bias. The form of the plots in **Figure 6.12** indicates that the optimum shaping time, τ_{opt}, for all reverse voltages was 1 µs $\leq \tau_{opt} \leq$ 2 µs.

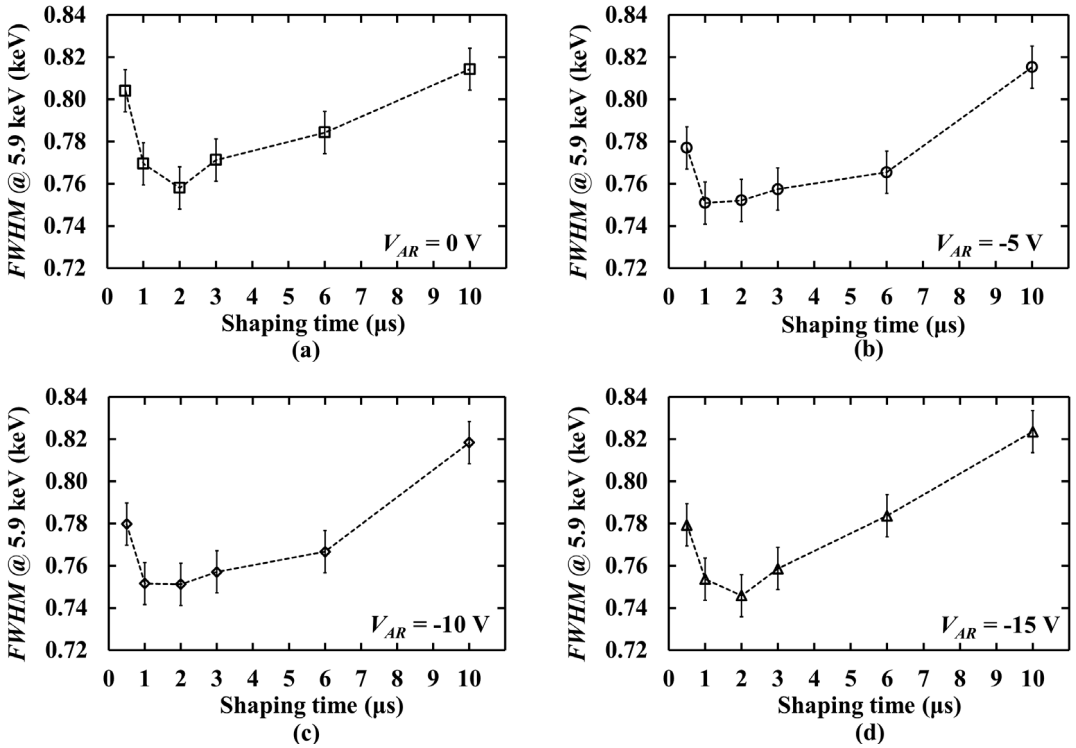

Figure 6.12. Measured *FWHM* at 5.9 keV for the GaAs p^+-i-n^+ mesa photodiode D1 as a function of shaping time at, a) 0 V (squares); b) -5 V (circles); c) -10 V (diamonds); and d) -15 V (triangles), reverse bias. Lines are guides for the eyes only.

At short shaping times, $\tau \leq 3$ μs, as the reverse bias increased from 0 V to -15 V, better *FWHM* at 5.9 keV was achieved. This was attributed to reduced charge trapping at high electric field strengths. However, at long shaping times, $\tau \geq 6$ μs, the *FWHM* of the photopeak at -15 V was equal (at 6 μs) or higher (at 10 μs) than photopeak at 0 V. The increase in leakage current, from 0.04 pA at 0 V to 3.86 pA at -15 V, resulted in larger parallel white noise at long shaping times, which outweighed the reduced incomplete charge collection noise from the greater electric field strength generated by the applied reverse bias. The noise sources contributing to the energy resolution are discussed in the next section.

6.5.2 Noise analysis

The energy resolution of a non-avalanche semiconductor detector coupled to a charge sensitive preamplifier, as measured by the *FWHM* of the photopeak, is defined by three mechanisms (sources of noise), which all degrade its resolution (see Equation 3.1). These are the Fano noise, incomplete charge collection noise and electronic noise. Given that the Fano noise, expected to be 128 eV at 5.9 keV in GaAs (assuming $F = 0.12$, and $\omega = 4.184$ eV), was much smaller than the measured energy resolution, there were clearly significant noise contributions beyond the statistical generation of charge carriers as quantified by the Fano noise.

The electronic noise, due to the detector itself and the preamplifier, comprises white parallel noise, *WP*, white series noise (including the induced gate current noise), *WS*, 1/*f* noise, and dielectric noise, *DN*. The first three noise components were calculated as described in **Section 3.2**. The leakage current of the detector (**Figure 6.4**) and the leakage current of the input JFET (5 pA) of the preamplifier (Siliconix, 2001), gave rise to the parallel white noise. The capacitance of the detector (including the capacitance of its packaging) and the capacitance of the input JFET (1.5 pF) of the preamplifier gave rise to the series white noise. The noise sources that cannot be directly calculated were the dielectric noise, *DN*, and the incomplete charge collection noise, *R*. However, by subtracting the calculated white series noise, white parallel noise, 1/*f* noise and the Fano noise in quadrature from the total *FWHM* of the photopeak, the rest can be attributed to the quadratic sum of the dielectric noise and the incomplete charge collection noise, $(DN^2 + R^2)^{1/2}$, both of which would normally be expected to be shaping time invariant for 0.5 μs ≤ τ ≤ 10 μs and this detector. The total noise along with the calculated contributions of the above noise sources as a function of shaping time, at -15 V reverse bias, can be seen in **Figure 6.13**.

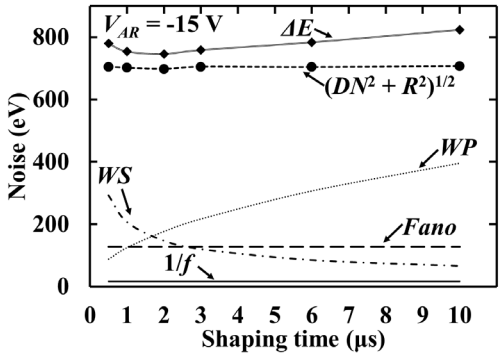

Figure 6.13. Total *FWHM* of the 5.9 keV peak (diamonds) with the quadratic sum of dielectric noise and incomplete charge collection noise (circles), series white noise (dash dot line), parallel white noise (round dot line), Fano noise (long dashes) and 1/*f* noise (solid line) for the GaAs p^+-i-n^+ mesa photodiode D1 at -15 V reverse bias, as a function of shaping time. Lines for total *FWHM* and quadratic sum of dielectric noise and incomplete charge collection noise are guides for the eyes only.

The series white noise contribution decreased with increasing shaping time, whereas the opposite was true for parallel white noise. The 1/*f* noise contribution was independent of shaping time (see **Section 3.2**). **Figure 6.13** indicates that the quadratic sum of dielectric noise and incomplete charge collection noise was the dominant noise contribution in the reported system. This combination was found to be independent of shaping time, as it was expected for both the dielectric noise and incomplete charge collection noise, and had a mean value of 704 eV ± 3 eV (rms deviance). Since the dielectric and incomplete charge collection noises cannot be

individually detangled from the present measurements, it can only be said that one of them or both are the most significant noise sources at all shaping times at -15 V, and indeed at all reverse applied biases. This is in agreement with previous reports of systems using comparable detectors and preamplifier electronics (Barnett et al., 2012a) (Barnett et al., 2015). The total measured noise and the computed quadratic sum of dielectric noise and incomplete charge collection noise as a function of applied reverse bias, at an indicative shaping time of 10 µs, are shown in **Figure 6.14**.

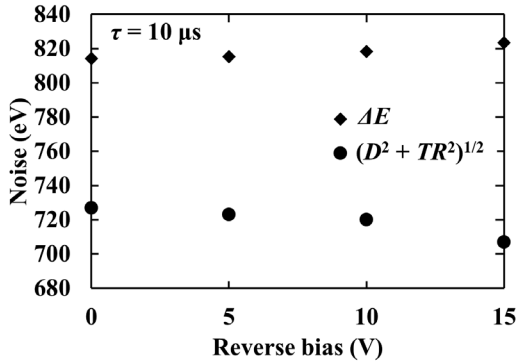

Figure 6.14. Total *FWHM* of the 5.9 keV peak (diamonds) with the calculated quadratic sum of dielectric and incomplete charge collection noise (circles), for the GaAs p^+-i-n^+ mesa photodiode D1 at 10 µs shaping time as a function of applied reverse bias.

Although there was an increase in the total noise as the reverse bias was increased from 0 V to -15 V, the corresponding contribution of the dielectric and incomplete charge collection noise decreased (see **Figure 6.14**). The increase in the total noise was attributed to the larger parallel white noise at -15 V compared to 0 V. Although the dielectric noise does not vary with detector reverse bias, this is not the case for the incomplete charge collection noise. Increased reverse bias (greater electric field strengths) can result in improved charge transport and less trapping noise (see **Section 3.5**). The same trend of the quadratic sum of the dielectric and incomplete charge collection noise with reverse bias, as shown in **Figure 6.14** for 10 µs shaping time, was observed for all investigated shaping times. From these measurements, it was therefore possible to estimate the additional incomplete charge collection noise present when the detector was operated at 0 V compared to -15 V. A comparison between the contribution of both the dielectric noise and the incomplete charge collection noise at 0 V and at -15 V, as a function of shaping time can be seen in **Figure 6.15**.

The quadratic sum of dielectric and incomplete charge collection noise was found to be 723 eV ± 5 eV at 0 V and 704 eV ± 3 eV at -15 V (see **Figure 6.15a**). Thus, it was calculated that the additional incomplete charge collection noise present when the detector was reverse biased at 0 V

compared to -15 V was 165 eV ± 24 eV (with the increase in uncertainty being due to combining errors). Consequently, from **Figure 6.15a** it can be said that the lower limit of incomplete charge collection noise at 0 V reverse bias was 165 eV ± 24 eV (see **Figure 6.15b**) and that the upper limit of the dielectric noise was 704 eV ± 3 eV at all reverse biases and at all shaping times.

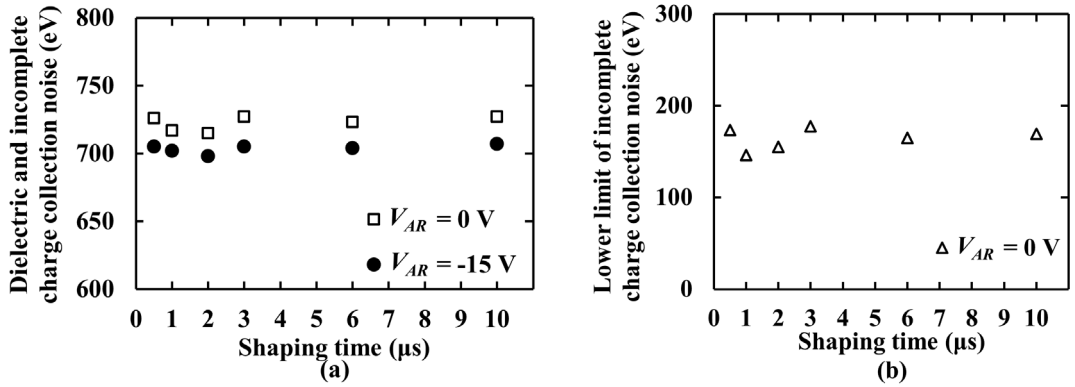

Figure 6.15. a) The calculated quadratic sum of dielectric and incomplete charge collection noise at 0 V (open squares) and -15 V (filled circles) for the GaAs p^+-i-n^+ mesa photodiode D1 as a function of shaping time and b) the corresponding lower limit of incomplete charge collection noise at 0 V.

The energy resolution (745 eV *FWHM* at 5.9 keV at -15 V reverse bias, corresponding to 76 e^- rms) of the detector reported here is better than previously reported for other 7 µm GaAs devices (1 keV (Ng et al., 2014)), and slightly better than thinner (2 µm and 3 µm) GaAs p^+-i-n^+ mesa photodiodes (≈ 800 eV (Barnett at al., 2011) (Barnett, 2014)), coupled to similar front-end electronics as used for the currently reported devices. However, it is far from the best experimental reports of GaAs detectors at room temperature (300 eV (Erd et al., 2002) and 266 eV (Owens et al., 2001) *FWHM* at 5.9 keV). The very good performance reported by Erd et al. (2002) and Owens at al. (2001) have yet to be replicated by independent researchers; they were probably due to exceptionally good epilayer quality and the low electronic noise of the system (242 eV (Owens et al., 2001)). Even though the electronic noise present in the system reported here is significant, making the *FWHM* significantly greater than the Fano limited energy resolution, the preamplifier used is specialist for the specific application, low noise (~ 40 e^- rms without detector), and has better performance than commercially available preamplifiers for detectors made from wide bandgap materials such as GaAs.

The energy resolution of the X-ray spectrometer employing the 7 µm GaAs p^+-i-n^+ mesa photodiode (745 eV at 5.9 keV) reported here is also better (lower) than the X-ray spectrometer employing the 4H-SiC Schottky diodes (1.36 keV at 17.4 keV) (reported in **Chapter 5**), even though similar front-end electronics were used for both spectrometers and they both had similar

equivalent noise charge (74 e^- rms the 4H-SiC spectrometer and 76 e^- rms the GaAs spectrometer). This better characteristic was attributed to the larger number of charge carriers generated in GaAs compared to the number of charge carriers generated in 4H-SiC for a given X-ray photon, resulting in better statistics, due to the lower electron hole pair creation energy of GaAs (4.184 eV (Bertuccio & Maiocchi, 2002)) c.f. 4H-SiC (7.8 eV (Bertuccio & Casiraghi, 2003)).

Similarly, low noise readout electronics are even more critical for wide bandgap detectors than they are for Si and narrow bandgap materials due to the typically greater electron hole pair creation energies of wide bandgap materials (see **Section 2.3.2**). The dielectric noise, arising from the dielectrics around the input of the preamplifier, such as the package of the JFET (Bertuccio et al., 1996), may have been the dominant source of noise limiting the energy resolution of the spectrometer reported here. It was estimated that if the dielectric noise could be eliminated, the energy resolution (*FWHM* at 5.9 keV) would be reduced to 264 eV, which is similar to the energy resolution of the best reported system with the GaAs detector spectrometer of Owens et al. (2001) and Erd et al. (2002). The dielectric noise computed for the current used preamplifier, which had an upper limit of 704 eV ± 3 eV (72 e^- rms), is comparable with previously reported results for similar front-end electronics (~ 700 eV (Barnett et al., 2012a)). Redesigning the preamplifier's front-end and eliminating the packaging of both the detector and the input JFET, ideally by integrating the JFET on the detector, would reduce the dielectric noise contribution, as it was reported by Bertuccio and Pullia (1993).

6.6 High temperature electrical characterisation

6.6.1 Current measurements as a function of bias

The temperature dependence of the current as a function of applied forward and reverse bias of both diodes were measured using a Keithley 6487 Picoammeter/Voltage Source (see **Section 2.5.1**). The diodes were installed inside a TAS Micro MT climatic cabinet for temperature control. The temperature was initially set to 120 °C and decreased to 0 °C, in 20 °C steps. To ensure thermal equilibrium, the diodes were left to stabilize at each temperature for 30 minutes before the measurements were started at each temperature. The measured dark current as a function of applied forward bias and temperature for both diodes D1 and D2 can be seen in **Figure 6.16**.

The current, I_F, as a function of forward applied biases can be approximated to the sum of the diffusion current, I_{diff}, and recombination current, I_{rec} (Equation 2.33). Their temperature dependences are

$$I_{diff} \propto n_i^2 e^{qV_D/kT}, \tag{6.1}$$

and

$$I_{rec} \propto n_i e^{qV_D/2kT}, \tag{6.2}$$

respectively.

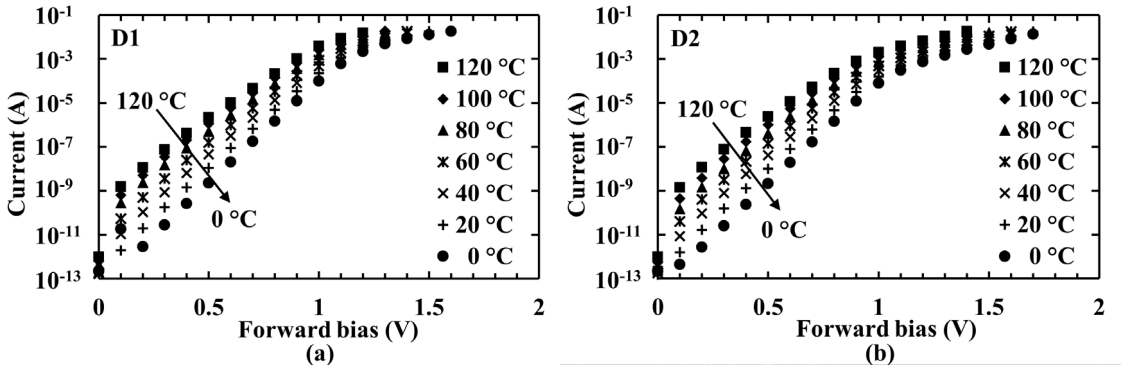

Figure 6.16. Current as a function of applied forward bias for the GaAs p⁺-i-n⁺ mesa photodiode (a) D1 and (b) D2 in the temperature range 0 °C to 120 °C. 120 °C (filled squares); 100 °C (filled diamonds); 80 °C (filled triangles); 60 °C (stars); 40 °C (× symbols); 20 °C (+ symbols); 0 °C (filled circles).

The data presented in **Figure 6.16** was found to be better described by Equation 6.2 rather than Equation 6.1 suggesting that the forward current was defined by the recombination current rather than the diffusion current. More specifically, the same proportionality factor was calculated between the measured current, I_F, and $n_i e^{qV_D/2kT}$ (Equation 6.2) over the investigated temperature range, for each forward bias and for each diode, unlike between the measured current, I_F, and $n_i^2 e^{qV_D/kT}$ (Equation 6.2). The saturation current and ideality factor can be extracted from the semi logarithmic current, I_F, as a function of applied forward bias, V_{AF}, plot (**Figure 6.16**), using Equation 2.33. The saturation current was found to vary from 440 pA ± 70 pA at 120 °C to 0.040 pA ± 0.002 pA at 0 °C for D1 and from 400 pA ± 100 pA at 120 °C to 0.036 pA ± 0.002 pA at 0 °C for D2. The uncertainties in the saturation current and the ideality factor were related to the standard deviation of the gradient and the *y* axis intercept point of the line of best fit calculated for the semi logarithmic current, I_F, as a function of applied forward bias, V_{AF}, plot using linear least squares fitting. The calculated ideality factor as a function of temperature can be seen in **Figure 6.17**.

The ideality factor improved from (1.94 ± 0.01) at 0 °C for both devices to (1.78 ± 0.03) and (1.79 ± 0.05) at 120 °C for D1 and D2 respectively. This improvement was attributed to the reduction of the recombination current and the increase of the diffusion current as the temperature increased (Sze & Ng, 2007). Although the ideality factor, *n*, was temperature dependent, the small decrease of *n* as the temperature increased was not sufficient to indicate significant contribution of tunnelling in the conduction process (Sellai, 2008). The semi-logarithmic current, I_F, as a function of applied forward bias, V_{AF}, plot of the devices (**Figure 6.16**) showed a non-linear region for $V_{AF} \geq 1$ V which originated from the effect of the series resistance (Sze & Ng, 2007).

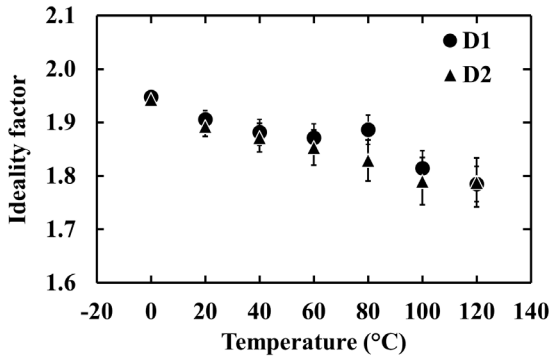

Figure 6.17. Ideality factor extracted from the measured current as a function of applied forward bias for the GaAs p^+-i-n^+ mesa photodiode D1 (circles) and D2 (triangles) in the temperature range 0 °C to 120 ° C. The error bars were calculated propagating the standard deviation of the gradient of the line of best fit of the measured current as a function of applied forward bias.

The leakage current, I_R, as a function of reverse applied bias of the two GaAs p^+-i-n^+ mesa photodiodes is shown in **Figure 6.18**. The leakage current was decreased with decreased temperature for all investigated reverse biases. More specifically, the leakage current of D1 at -15 V reverse bias decreased from 7.65 nA ± 0.01 nA at 120 °C to 0.9 pA ± 0.4 pA at 0 °C, whereas D2 showed lower dark current which decreased from 2.950 nA ± 0.007 nA at 120 °C to a current smaller than the uncertainty of the measurement 0.08 pA ± 0.40 pA at 0 °C, at the same applied reverse bias. The difference in the measured leakage current of the two devices was attributed to small variations arising from fabrication process and possibly variations in wafer quality. The leakage current density, J_R, at -15 V reverse bias (21.4 kV/cm) of both devices as a function of temperature can be seen in **Figure 6.19**. The leakage current density of both devices showed an exponential decrease with a constant factor, 3.229×10^{-9} for D1 and 2.701×10^{-10} for D2, as the temperature decreased from 100 °C to 0 °C. However, as explained below, the leakage

current mechanism at the temperature range 120 °C to 100 °C was different compared to lower temperatures.

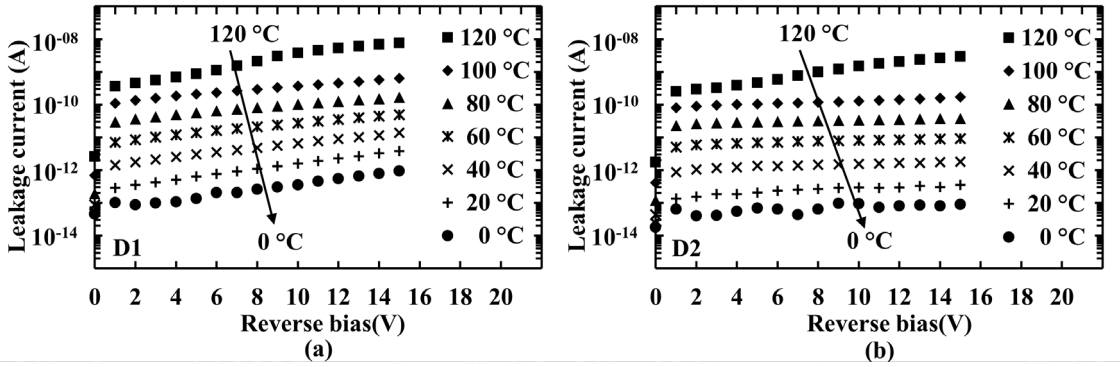

Figure 6.18. Leakage current as a function of applied reverse bias for the GaAs p^+-i-n^+ mesa photodiode (a) D1 and (b) D2 in the temperature range 0 °C to 120 °C. 120 °C (filled squares); 100 °C (filled diamonds); 80 °C (filled triangles); 60 °C (stars); 40 °C (× symbols); 20 °C (+ symbols); 0 °C (filled circles).

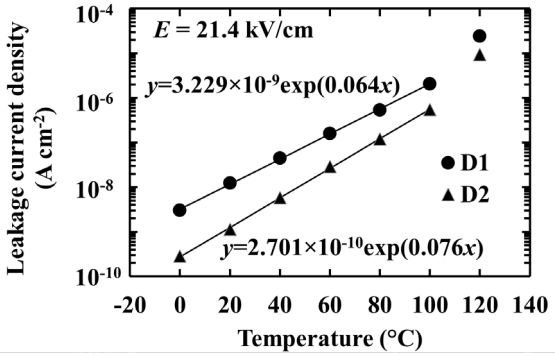

Figure 6.19. Measured leakage current density as a function of temperature at 21.4 kV/cm internal electric field for the GaAs p^+-i-n^+ mesa photodiode D1 (circles) and D2 (triangles). The line of best fit at the temperature range 0 °C to 100 °C can also be seen.

The current, I_R, as a function of reverse applied biases can be approximated to the sum of the diffusion current, I_{diff}, and generation current, I_{gen} (Equation 2.34). Since the diffusion current scales with n_i^2 and the generation current scales with n_i, a plot of $\ln(I_R)$, or equally of $\ln(J_R)$, as a function of $1/kT$ should yield a straight line whose gradient determines whether the generation or the diffusion current dominates (see **Section 2.4.2**). The logarithmic of leakage current density, $\ln(J_R)$, as a function of $1/kT$ graph was plotted for diode D1, and can be seen in **Figure 6.20**. Two linear regions can be seen in **Figure 6.20**, where the lines of best fit were calculated using linear least squares fitting. The prevailing conduction process at the temperature range 0 °C to 100 °C was found to be generation given that the gradient of the $\ln(J_R)$, as a function of $1/kT$ plot is

approximately -*Eg*/2, and the diffusion current dominated for temperatures higher than 100 °C given that the gradient of the ln(J_R), as a function of 1/k*T* plot is approximately -*Eg*.

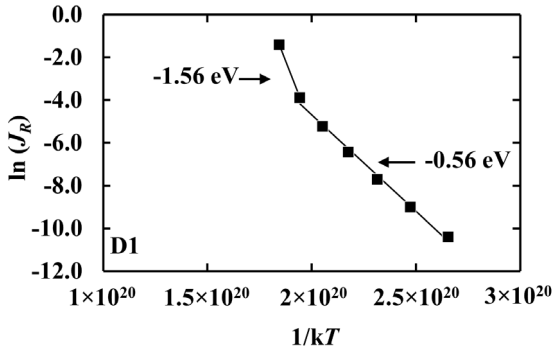

Figure 6.20. Ln(J_R) as a function of 1/k*T* for the GaAs p^+-i-n^+ mesa photodiode D1. The lines of best fit, as determined by linear least squares fitting, across the temperature ranges 0 °C to 100 °C, and 100 °C to 120 °C, and the gradients of the lines (-0.56 eV for 0 °C to 100 °C; -1.56 eV for 100 °C to 120 °C) can also be seen.

Both GaAs p^+-i-n^+ diodes showed comparable leakage current densities to other high quality GaAs p^+-i-n^+ diodes at temperatures close to room temperature. More specifically, diode D1 had a leakage current density of 22.3 nA/cm^2 ± 0.9 nA/cm^2 and D2 had a leakage current density of 2.6 nA/cm^2 ± 0.1 nA/cm^2 at 30 °C and at 21.4 kV/cm internal electric field (calculated based on **Figure 6.19**). Other high quality GaAs p^+-i-n^+ diodes had leakage current densities of ~ 10 nA/cm^2 at the same temperature and internal electric field (Bertuccio et al., 2003).

6.6.2 Capacitance measurements as a function of bias

The depletion width and the doping concentration in the i layer were calculated for both devices as functions of temperature, based on temperature dependence capacitance measurements over the temperature range 0 °C to 120 °C, as per the measurements of the devices' currents as functions of applied forward and reverse bias reported in **Section 6.6.1**. The capacitance measurements were performed using an HP 4275A Multi Frequency LCR meter (see **Section 2.5.2**), with its test signal having a 50 mV rms magnitude and a 1 MHz frequency, as per the room temperature measurements reported in **Section 6.3.2**. The capacitance of the empty packages, C_{pack}, which was measured to temperature invariant and equal to 0.6 pF based on capacitance measurements on empty packages, was subtracted from the measured total capacitance. The resulting capacitance (i.e. the junction capacitance) as a function of applied forward bias at the temperature range 0 °C to 120 °C can be seen in **Figure 6.21**.

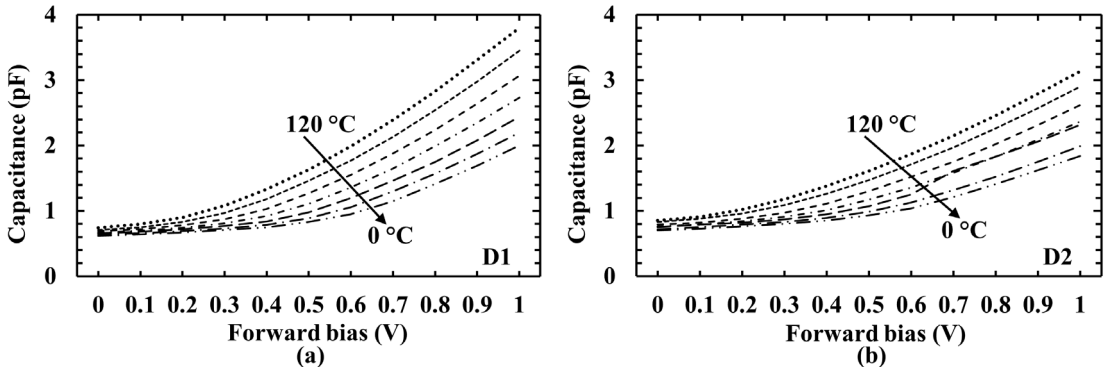

Figure 6.21. Capacitance as a function of applied forward bias for the GaAs p^+-i-n^+ mesa photodiodes (a) D1 and (b) D2 in the temperature range 0 °C to 120 °C. The data points have been replaced by lines for clarity.

As the temperature decreased from 120 °C to 0 °C, the capacitance of both devices decreased at each applied forward bias. There is a significant contribution of the diffusion capacitance, C_{Diff}, to the junction capacitance at forward applied biases due to the rearrangement of the minority carrier density (see **Section 2.4.2**). Bearing in mind that the diffusion capacitance is directly proportional to the forward current, I_F, the temperature dependency of the forward biased capacitance (**Figure 6.21**) was attributed to the temperature dependency of the forward current shown in **Figure 6.16**.

The measured capacitance as a function of temperature at different applied reverse biases (0 V, -1V, -10 V and -15 V) for both devices can be seen in **Figure 6.22**. When reverse biased, the junction capacitance was mostly defined by the depletion layer capacitance, C_{DL}, rather than the diffusion capacitance (see **Section 2.4.2**). A temperature invariant depletion layer capacitance was measured for reverse biases $|V_{AR}| > 1$ V. However, a capacitance increase with temperature was recorded for low reverse biases $|V_{AR}| \leq 1$ V.

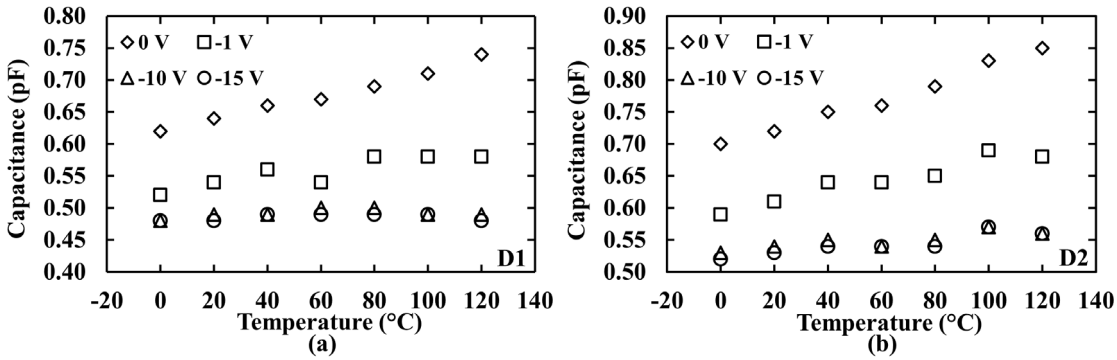

Figure 6.22. Capacitance as a function of temperature for the GaAs p^+-i-n^+ mesa photodiodes (a) D1 and (b) D2 in the range 0 °C to 120 °C at four reverse biases values.

In order to explain this capacitance variation with temperature, the depletion width was plotted as a function of applied reverse bias for diode D1 at 0 °C and 120 °C. The depletion layer width, W_D, was computed using the measured depletion layer capacitance and Equation 2.37. The calculated depletion widths of diode D1 as functions of applied reverse bias at temperatures of 0 °C and 120 °C can be seen in **Figure 6.23**. The depletion width increased with applied reverse bias at both the lowest and highest investigated temperature, as was expected. The depletion width was found to decrease from 5.8 μm ± 0.3 μm at 0 °C, to 4.8 μm ± 0.2 μm at 120 °C, when no bias was applied. However, it was found to be 7.5 μm ± 0.5 μm for both temperatures at -15 V reverse bias. Considering that the doping concentrations of the p^+ and n^+ layers were high (2×10^{18} cm^{-3}), compared to the i layer (10^{14} cm^{-3}), the extension of the depletion region to the p^+ and n^+ layers was negligible, and hence the i layer thickness of D1 was found to be 7.5 μm ± 0.5 μm. Another important observation, based on **Figure 6.23**, is that the diode D1 was fully depleted at -5 V reverse bias when the temperature was 0 °C. Although the diode was almost fully depleted at -6 V, full depletion was achieved at -14 V, when the temperature was 120 °C. This may be explained by the presence of a thin region around the depletion layer with non-ionised dopants at low temperatures, similarly to as was found by Mazzillo et al. (2012) for 4H-SiC Schottky photodiodes. These dopants were progressively ionised with temperature, and limited the extension of the depletion layer preventing the diode to be fully depleted at low reverse biases. The ratio between the thickness of this region and the depletion layer was to be lower for high reverse biases compared to low reverse biases resulting in an invariant capacitance with temperature at high reverse biases.

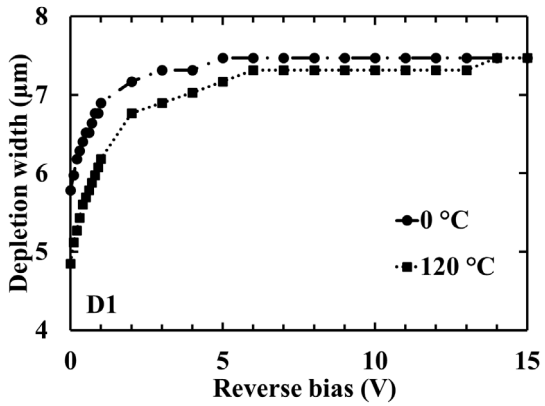

Figure 6.23. Calculated depletion width for the GaAs p^+-i-n^+ mesa photodiode D1 calculated from capacitance measurements as a function of applied reverse bias at 0 °C and 120 °C.

The i layer thickness of diode D2 was found to be 6.7 μm ± 0.4 μm, which was the same with the i layer thickness of diode D1 (7.5 μm ± 0.5 μm) within the uncertainties. The uncertainties of the

calculated depletion widths were related to the uncertainty in the capacitance measurements (± 0.03 pF).

The relationship between $1/C_{DL}^2$ and applied bias was found to be linear at the bias range -0.4 V to 0.4 V. A line of best fit was calculated for the $1/C_{DL}^2$ (V_{AB}) data for both diodes at all investigated temperatures. The value of the built in voltage, V_{bi}, was extracted from the voltage axis intercept point (see **Section 2.4.2**). The built in voltage was found to be temperature dependent and to decrease with increasing temperature from 1.47 V ± 0.06 V at 0 °C to 0.77 V ± 0.05 V at 120 °C, for D1, and 1.47 V ± 0.05 V at 0 °C to 0.86 V ± 0.06 V at 120 °C, for D2. The build in voltage is inversely proportional to the intrinsic carrier density, n_i, of the semiconductor material (Sze & Ng, 2007). Also, the intrinsic carrier density is directly proportional to temperature. Hence, the build in voltage was expected to decrease with increasing temperature, as was also reported for a Si p^+-i-n^+ diode by Sellai (2008).

The effective doping concentration as a function of depletion layer width, $N_{eff}(W_D)$, was calculated using the differential capacitance method, based on Equation 2.38; the results are shown in **Figure 6.24**. It was found that the doping concentration increased from 0.6×10^{14} cm^{-3} ± 0.1×10^{14} cm^{-3} at 5 µm below the p^+-i junction to 12.7×10^{14} cm^{-3} ± 0.7×10^{14} cm^{-3} at the i-n^+ interface for both temperatures. However, the doping profile of the i layer of D1 (**Figure 6.24**) suggested the presence of a layer close to i-n^+ junction with non-ionised dopants at 0 °C which were ionised at 120 °C. This is in accordance with the findings presented in **Figure 6.22**, which showed that the measured capacitance was temperature dependent in the temperature range 0 °C to 120 °C for low reverse biases $|V_{AR}| \leq 1$ V. The carrier concentration of D2 was found to be slightly higher than the carrier concentration of D1, varying as it did from 0.87×10^{14} cm^{-3} ± 0.02×10^{14} cm^{-3} at 5 µm below the p^+-i junction to 16×10^{14} cm^{-3} ± 9×10^{14} cm^{-3} at the i-n^+ interface at 0 °C.

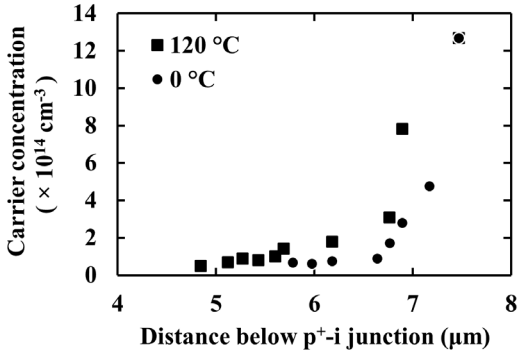

Figure 6.24. Calculated effective doping concentration as a function of depletion layer width of the GaAs p^+-i-n^+ mesa photodiode D1 at 0 °C and 120 °C.

6.7 High temperature X-ray spectroscopy

6.7.1 Measurements with an ^{55}Fe radioisotope X-ray source

X-ray spectra were obtained using GaAs p^+-i-n^+ photodiode D1 to characterise its X-ray detection performance as a function of temperature. An ^{55}Fe radioisotope X-ray source was positioned 3 mm above the top of the device. The diode was connected to a custom-made, single-channel, charge sensitive preamplifier without feedback resistor (see **Section 2.3.3**). The detector along with the preamplifier were installed inside a TAS Micro MT climatic cabinet throughout the measurements for temperature control. The output signal of the preamplifier was shaped using an Ortec 572A shaping amplifier which was further connected to a multi-channel analyser (MCA) for digitisation.

The temperature was initially set to 60 °C and it was decreased to 0 °C with a 20 °C step. Spectra were accumulated at each temperature for different reverse bias conditions (0 V, -5 V, -10 V, and -15 V). The shaping time, τ, was varied; spectra were accumulated for τ = 0.5 μs, 1 μs, 2 μs, 3 μs, 6 μs, and 10 μs at each applied reverse bias. The live time limit of each spectrum was set to be 60 s. The accumulated spectra with the best energy resolution (smallest *FWHM*) of the ^{55}Fe radioisotope X-ray source obtained with the spectrometer at temperatures of 0 °C and 60 °C, can be seen in **Figure 6.25**. The detected ^{55}Fe X-ray photopeak is the combination of the characteristic Mn Kα (5.9 keV) and Mn Kβ at (6.49 keV) lines of the ^{55}Fe radioisotope X-ray source (Schötzig, 2000). Gaussians were fitted to the peak taking into account the relative emission ratio (Schötzig, 2000) and the relative efficiency of the detector for the 5.9 keV and 6.49 keV peak. The spectra were energy calibrated based on the positions of the zero energy noise peak and the Mn Kα peak. The uncertainty of the *FWHM* associated with fitting a Gaussian to the photopeak was estimated to be ± 10 eV for the GaAs p^+-i-n^+ mesa photodiode D1 reported in this section.

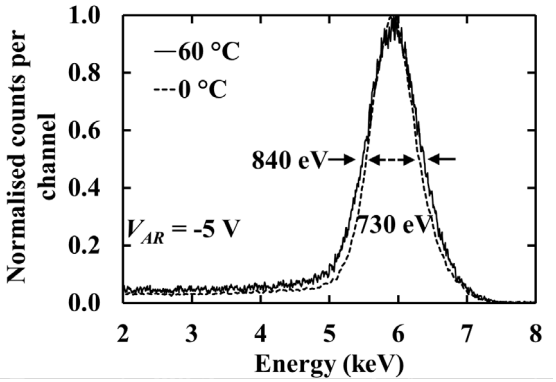

Figure 6.25. ^{55}Fe spectra accumulated with the GaAs p^+-i-n^+ mesa photodiode D1 at -5 V reverse bias at two different temperatures; 60 °C (solid line) and 0 °C (square dots).

Partial charge collection of charge created in the non-active layers of the device resulted in the low energy tailing of the photopeak seen in **Figure 6.25**, similarly to as reported by Barnett et al. (2015). The *FWHM* was measured for all obtained spectra. **Figure 6.26** shows the *FWHM* of the 5.9 keV peak as measured at -5 V and -10 V reverse bias, as a function of temperature, for the optimum shaping time, τ_{opt}. The *FWHM* increased as the temperature increased from 730 eV at 0 °C (τ = 6 μs) to 840 eV at 60 °C (τ = 2 μs) at -5 V reverse bias, and from 740 eV at 0 °C (τ = 10 μs) to 910 eV at 60 °C (τ = 2 μs) at -10 V reverse bias. The noise of the system is analysed in the following section.

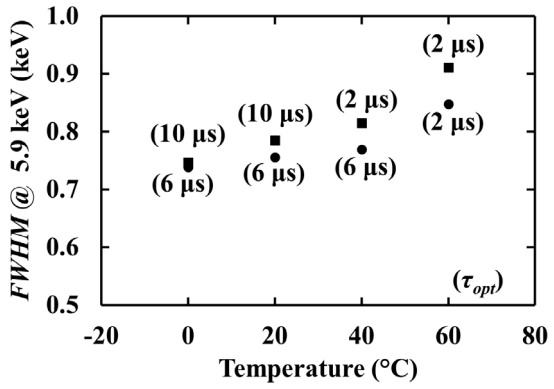

Figure 6.26. *FWHM* of 5.9 keV peak as a function of temperature at -5 V (circles) -10 V (squares) reverse bias, at the optimum shaping time for the GaAs p^+-i-n^+ mesa photodiode D1.

6.7.2 Noise analysis

The energy resolution of a non-avalanche semiconductor detector coupled to a charge sensitive preamplifier is degraded due to three independent sources of noise (Equation 3.1), as it has already been discusses in **Section 3.1**. These are the Fano noise, the incomplete charge collection noise and the electronic noise. The expected Fano limited resolution of the GaAs device at 5.9 keV was calculated to be 128 eV, assuming a Fano factor of 0.12 (Bertuccio et al., 1997) and an electron hole pair creation energy of 4.184 eV (Bertuccio & Maiocchi, 2002). Since the measured energy resolution was greater than the Fano noise, it can be said that there was a significant contribution from either the incomplete charge collection noise or electronic noise.

The electronic noise, arising from the detector and the preamplifier consists of the white parallel noise, white series noise, 1/*f* noise and dielectric noise. The first three noise sources were calculated as described in **Section 3.2**, where a more detailed explanation of the noise components is given. The white parallel noise, due to the leakage current of the detector and of the input JFET, was directly proportional to the shaping time. It was calculated based on the measured leakage current of the detector at different temperatures (**Figure 6.18**) and on the estimated

leakage current of the input JFET as a function of temperature (Siliconix, 2001). The white series noise, due to the capacitance of the detector and of the input JFET, was inversely proportional to the shaping time. It was calculated based on the measured capacitance of the detector at different temperatures (**Figure 6.22**) and on the estimated input capacitance of the input JFET of the preamplifier (Siliconix, 2001). The $1/f$ noise was shaping time invariant. Although the dielectric noise and the incomplete charge collection noises cannot be directly calculated, the difference between the total *FWHM* of the peak and the quadratic sum of the rest noise components (white series noise, white parallel noise, $1/f$ noise and Fano noise) was attributed to the quadratic sum of the dielectric and the incomplete charge collection noises.

The *FWHM* increase shown in **Figure 6.26**, which occurred as the temperature increased, was attributed to the white parallel noise and the quadratic sum of the dielectric and incomplete charge collection noises increasing with temperature. At -10 V reverse bias, the best energy resolution was achieved at short shaping times (τ = 2 μs) at 60 °C and 40 °C, and at long shaping times (τ = 10 μs) at 20 °C and 0 °C. This was attributed to the fact that the parallel white noise increased with shaping time, the series white noise decreased with shaping time, and the quadratic sum of the dielectric and incomplete charge collection noises was expected to be shaping time invariant. Hence, the energy resolution was found to be limited by the leakage current of the detector and/or the input JFET rather than their capacitances at $T \geq 40$ °C, whereas the opposite was true at $T \leq 20$ °C, over the investigated temperature range. To make this clearer, the total noise along with the calculated noise contributions at 60 °C and -10 V reserve bias are presented in **Figure 6.27** as a function of shaping time.

The dominant source of noise at shaping times ≤ 3 μs was found to be the quadratic sum of the dielectric noise and incomplete charge collection noise with a mean value of 775 eV ± 30 eV. However, the white parallel noise was the limiting factor for the energy resolution for 6 μs and 10 μs shaping times, at 60 °C and -10 V reverse bias (**Figure 6.27**). The parallel noise was found to be the dominant noise at long shaping times (6 μs and 10 μs) for -5 V and -15 V reverse bias, whereas the sum of the dielectric noise and incomplete charge collection noise was found to dominate at all shaping times, at 0 V and 60 °C.

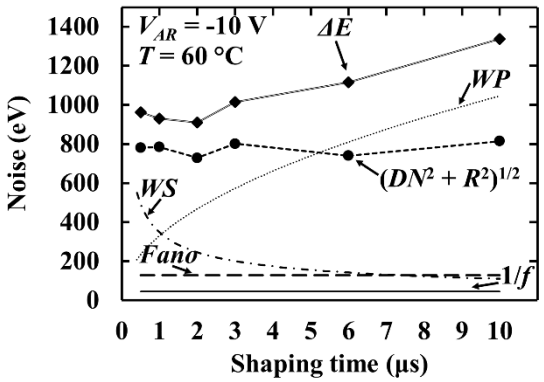

Figure 6.27. Total measured *FWHM* of 5.9 keV peak (diamonds) as a function of shaping time at 60 °C and -10 V reverse bias with the calculated noise components: quadratic sum of dielectric noise and incomplete charge collection noise (circles), series white noise (dash dot line), parallel white noise (round dot line), Fano noise (long dashes) and 1/*f* noise (solid line) with the GaAs p^+-i-n^+ mesa photodiode D1. Lines for total *FWHM* and quadratic sum of dielectric noise and incomplete charge collection noise are guides for the eyes only.

The dielectric noise, as a function of temperature was estimated assuming that incomplete charge collection noise at -15 V reverse bias was insignificant. This assumption was made due to the improved charge transport with increased reverse bias resulting in less trapping noise. The measured energy resolution at -15 V reverse bias and at each temperature was plotted as a function of shaping time and can be seen in **Figure 6.28**. Following this, the *FWHM* was calculated based on the known noise sources (white series noise, white parallel noise, 1/f noise and Fano noise) and was subtracted in quadrature from the total measured *FWHM*. The result was attributed to the dielectric noise. Since the dielectric noise was expected to be shaping time invariant, the mean value and the rms error was calculated for the dielectric noise as a function of shaping time at each temperature, at -15 V reverse bias. The total calculated *FWHM* at 5.9 keV, including the dielectric noise can be seen in **Figure 6.28**.

The dielectric noise was expected to vary with temperature (Equation 3.14). The estimated dielectric noise as a function of temperature can be seen in **Figure 6.29**. It was found to increase from 716 eV ± 29 eV at 0 °C to 872 eV ± 74 eV at 60 °C. The larger uncertainty in the dielectric noise at 60 °C compared to lower temperatures was attributed to possible leakage current instabilities at high temperatures and -15 V reverse bias.

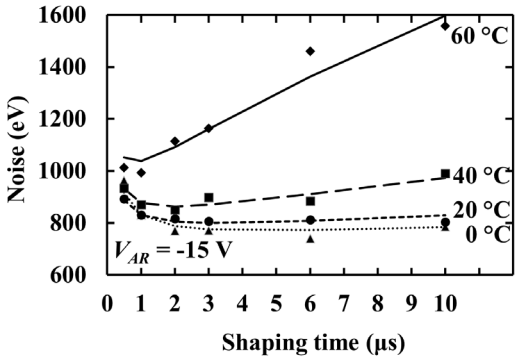

Figure 6.28. Total measured (60 °C (diamonds); 40 °C (squares); 20 °C (circles); 0 °C (triangles)) and calculated (60 °C (solid line); 40 °C (long dashes); 20 °C (square dots); 0 °C (round dots)) *FWHM* of 5.9 keV peak as a function of shaping time at -15 V reverse bias with the GaAs p^+-i-n^+ mesa photodiode D1.

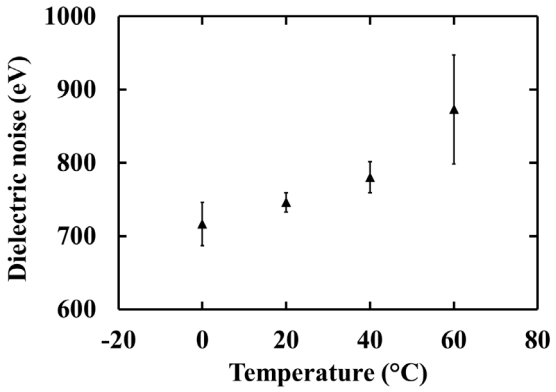

Figure 6.29. Estimated dielectric noise as a function of temperature.

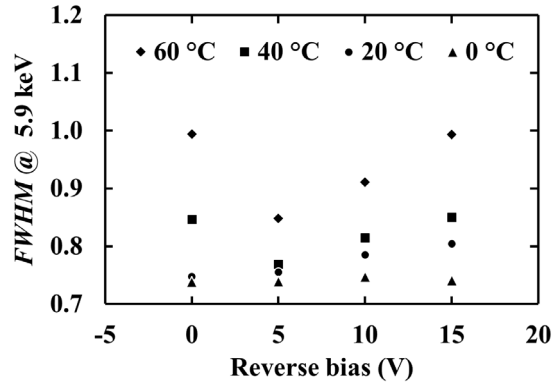

Figure 6.30. Measured *FWHM* of 5.9 keV as a function of reverse bias at the temperature range 0 °C to 60 °C (60 °C (diamonds); 40 °C (squares); 20 °C (circles); 0 °C (triangles)) at τ_{opt} with the GaAs p^+-i-n^+ mesa photodiode D1.

The measured *FWHM* at 5.9 keV over the temperature range 0 °C to 60 °C as a function of reverse bias can be seen in **Figure 6.30**. The best energy resolution (*FWHM* at 5.9 keV) was achieved at -5 V reverse bias at each investigated temperature. It was measured to be 730 eV at 0 °C, 750 eV at 20 °C, 770 eV at 40 °C, and 840 eV at 60 °C. Previously reported other 7 μm GaAs devices had an energy resolution (the combined 5.9 keV and 6.5 keV peak) of 1 keV at room temperature (Ng et al., 2014) and thinner GaAs p^+-i-n^+ mesa photodiodes (2 μm) had 1.07 keV *FWHM* at 60 °C (Barnett at al., 2011), coupled to similar front-end electronics. The improving of the energy resolution was attributed to slightly lower electronic noise arising from the preamplifier in addition to better electrical characteristics (leakage current and capacitance) of the detector compared to those previously reported (Barnett at al., 2011) (Ng et al., 2014). However, the best energy resolutions of Schottky GaAs detector X-ray spectrometers, where the GaAs diodes were coupled to ultra-low-noise front-end electronics (300 eV *FWHM* at 5.9 keV (Erd et al., 2002)) and (266 eV *FWHM* at 5.9 keV (Owens et al., 2001)) are far better than the spectrometer currently reported mesa p^+-i-n^+ device with Ohmic contacts. The dominant source of noise in the system reported here, dielectric noise, arose from lossy dielectrics at the input of the preamplifier. These likely include the materials used in the packaging of the input JFET, as well as the detector's package. A 40 % reduction in dielectric noise has been reported when the encapsulated input JFET was replaced by a decanned JFET (Bertuccio & Pullia, 1993). The GaAs detector chip along with the input JFET die were mounted on a low loss ceramic substrate to ensure low dielectric noise, at both the best experimental reports for GaAs detector X-ray spectrometers (Owens et al., 2001) (Erd et al., 2002). It was estimated that if the dielectric noise could be eliminated, the energy resolution (*FWHM* at 5.9 keV) would be reduced to 276 eV at 20 °C, and 470 eV at 60 °C, which is similar to the energy resolution of the best reported system with the GaAs detector spectrometer of Owens et al. (2001) and Erd et al. (2002).

6.8 Conclusion

The performances of two randomly selected 200 μm diameter GaAs mesa p^+-i-n^+ photodiodes (D1 and D2) with 7 μm i layers have been characterised at room temperature (20 °C) and as a function of temperature. More specifically, these detectors have been electrically characterised at room temperature and their responsivity in the wavelength range 580 nm to 980 nm investigated, as well as the performance of one of them as detector for photon counting X-ray spectroscopy studied. Following this, the detectors were both electrically characterised over the temperature range 0 °C to 120 °C and one of the diodes was characterised as detector for photon counting X-ray spectroscopy at the temperature range 0 °C to 60 °C.

The dominant current mechanism of the devices at room temperature was found to be recombination. Low leakage current densities were measured for both devices (17.4 nA/cm^2 for

D1 and 1.08 nA/cm^2 for D2) at room temperature, at an internal electric field of 22 kV/cm. The leakage currents of the devices as functions of time were found to stabilise after annealing the detectors at 120 °C. The i layer thickness and doping concentration of the devices were deduced from capacitance measurements. It was found that D1 had a 7.3 μm ± 0.4 μm thick i layer with a carrier concentration of 6×10^{13} cm^{-3} ± 1×10^{13} cm^{-3} and D2 had a 6.6 μm ± 0.4 μm thick i layer with a carrier concentration of 8×10^{13} cm^{-3} ± 1×10^{13} cm^{-3}, suggesting that the devices had the same i layer thickness within the uncertainty, and D1 slightly less carrier concentration compared to D2.

Visible and near infrared responsivity measurements at room temperature suggested the presence of a dead layer at the face of the devices with a thickness of 0.16 μm, in which the generated carriers from photon absorption did not contribute to the photocurrent. The maximum expected responsivity of the devices was calculated to be 0.23 A/W at 870 nm.

Results characterising one device (D1) at room temperature for X-ray spectroscopy with an ^{55}Fe radioisotope X-ray source were reported as functions of applied reverse bias and shaping time. The best energy resolution (*FWHM* at 5.9 keV = 745 eV) was achieved at 2 μs, at -15 V reverse bias. Subsequent noise analysis showed that there was at least 165 eV ± 24 eV incomplete charge collection noise at 0 V and that the dominant source of noise was the dielectric noise, which was determined to have an upper limit of noise contribution of 704 eV ± 3 eV.

The ideality factor of the devices as functions of temperature was calculated based on the measured currents as functions of applied forward bias. The ideality factor, which was found to improve from (1.94 ± 0.01) at 0 °C for both devices, to (1.78 ± 0.03) and (1.79 ± 0.05) at 120 °C for D1 and D2 respectively, indicated that the recombination current defined the forward current and its small temperature dependence excluded tunnelling from significant contribution to the forward current. The leakage current decreased with decreasing temperature from 7.65 nA ± 0.01 nA (24.36 μA/cm^2 ± 0.05 μA/cm^2) at 120 °C, to 0.9 pA ± 0.4 pA (3 nA/cm^2 ± 1 nA/cm^2) at 0 °C, and from 2.950 nA ± 0.007 nA (9.39 μA/cm^2 ± 0.02 μA/cm^2) at 120 °C to a current which was smaller than the uncertainty of the measurement, 0.08 pA ± 0.40 pA (0.2 nA/cm^2 ± 1.2 nA/cm^2) at 0 °C for D1 and D2 respectively, at -15 V reserve bias. The leakage current density of the devices was found to exponentially increase with temperature with a constant factor, up to 100 °C. However, the leakage current density over the temperature range 100 °C to 120 °C was found to be different compared to the exponentially increase with temperature with a constant factor over the temperature range 0 °C to 100 °C, for both devices. This was attributed to the diffusion current being the prevailing conduction process for

temperatures higher than 100 °C, in contrast to the generation current being dominant at lower temperatures.

The diffusion capacitance, at forward applied biases, decreased as the temperature decreased from 120 °C to 0 °C, due to the diffusion capacitance being directly proportional to the forward current. Measurements of the depletion layer capacitance as well as computation of the depletion layer width of the devices as a function of temperature suggested the presence of a thin region around the depletion layer with non-ionised dopants at low temperatures, which were progressively ionised with temperature. As a result, the depletion layer width was limited at high temperatures and low reverse biases from the ionised dopants and a temperature dependent depletion layer capacitance was measured for reverse biases $|V_{AR}| \leq 1$ V. The i layer thickness was found to be 7.5 μm ± 0.5 μm for D1, and 6.7 μm ± 0.4 μm for D2. The carrier concentration was found to increase from 0.6×10^{14} cm^{-3} ± 0.1×10^{14} cm^{-3} at 5 μm below the p^+-i junction to 12.7×10^{14} cm^{-3} ± 0.7×10^{14} cm^{-3} at the i-n^+ interface for D1 and from 0.87×10^{14} cm^{-3} ± 0.02×10^{14} cm^{-3} at 5 μm below the p^+-i junction to 16×10^{14} cm^{-3} ± 9×10^{14} cm^{-3} at the i-n^+ interface for D2.

The X-ray detection performance of D1 was characterised as a function of temperature from 0 °C to 60 °C. ^{55}Fe spectra were accumulated at different detector reverse bias conditions (0 V, -5 V, -10 V and -15 V) and varied shaping time (0.5 μs, 1 μs, 2 μs, 3 μs, 6 μs and 10 μs). The lowest *FWHM* at each temperature was measured at -5 V reverse bias; 730 eV at 0 °C, 750 eV at 20 °C, 770 eV at 40 °C, 840 eV at 60 °C. The *FWHM* increase with temperature was attributed to the white parallel noise, and the quadratic sum of the dielectric and incomplete charge collection noises which increased as the temperature increased. Subsequent noise analysis at 60 °C revealed that the sum of the dielectric and incomplete charge collection noises was the dominant source of noise at all shaping times at 0 V reverse bias and at short shaping time ($\tau \leq 3$ μs) at high reverse biases (-5 V, -10 V and -15 V), whereas the white parallel noise was the main source of noise at long shaping times (6 μs and 10 μs) at high reverse biases. An estimation of the dielectric noise, arising from lossy dielectrics at the input of the preamplifier, at each temperature was made under the assumption that the incomplete charge collection noise at -15 V was negligible. It was found to increase from 716 eV ± 29 eV at 0 °C to 872 eV ± 74 eV at 60 °C.

The energy resolution (*FWHM* at 5.9 keV) of the GaAs p^+-i-n^+ mesa photodiode, D1, reported here is better than previously reported thinner mesa X-ray photodiodes, coupled to similar front-end electronics; 1 keV *FWHM* at 5.9 keV, at 60 °C, having a 2 μm i layer thickness (Barnett at al., 2011) and ≈ 800 eV *FWHM* at 5.6 keV, at room temperature, having a 3 μm i layer thickness (Barnett, 2014). This improvement was attributed to the lower capacitance of the 7 μm i layer thick GaAs p^+-i-n^+ mesa photodiode, D1, compared to those previously reported which

resulted in less *WS*, 1/*f*, and dielectric noise contributions and possibly improved GaAs material quality. Also, the energy resolution of the GaAs p^+-i-n^+ mesa photodiode reported here is better than previously reported similar (same i layer thickness) mesa X-ray photodiodes (1 keV *FWHM* at 5.9 keV, at room temperature, (Ng et al., 2014)) due to the low noise of the associated readout electronics used in this work. However, the results presented here are modest compared to the best reported results for GaAs Schottky photodiode detectors coupled to ultra-low-noise readout electronics (300 eV by Erd et al. (2002) and 266 eV by Owens et al. (2001)). These best reported results were achieved with both the GaAs detector chip and the input JFET die mounted on a low loss ceramic substrate in close proximity to each other, to ensure negligible dielectric noise. It was predicted that the energy resolution of the GaAs p^+-i-n^+ mesa photodiode detectors reported here would become similar to those reported by Erd et al. (2002) and Owens et al. (2001), if the noise of the dielectrics could be eliminated.

Chapter 7 10 μm i Layer GaAs Mesa p^+-i-n^+ Photodiodes

7.1 Introduction and background

The higher quantum detection efficiency and the improved energy resolution (*FWHM* at 5.9 keV) of the 7 μm i layer thick GaAs mesa p^+-i-n^+ photodiodes (reported in **Chapter 6**), compared to previously reported thinner GaAs mesa X-ray photodiodes, enabled the research on thicker devices (i layer > 7 μm) and their performance as X-ray detectors at room and elevated temperatures.

Chapter 7 is divided into two parts. The first part (**Section 7.3** to **Section 7.5)** reports results characterising GaAs p^+-i-n^+ mesa photodiodes with a 10 μm i layer for their spectral response under illumination of X-rays and β^- particles. A total of 22 devices, having diameters of 200 μm and 400 μm, were electrically characterised at room temperature. ^{55}Fe X-ray spectra were obtained using one 200 μm diameter GaAs p^+-i-n^+ mesa photodiode (D1) and one 400 μm diameter GaAs p^+-i-n^+ mesa photodiode (D2). Noise analysis is presented and the limiting factors for the energy resolution of the system are discussed. The potential utility of these detectors for electron and β^- particle detection is examined with ^{63}Ni β^- particle spectra obtained using the 200 μm diameter GaAs p^+-i-n^+ mesa photodiode, D1.

The second part, **Section 7.6**, reports an X-ray fluorescence spectrometer for in situ characterisation of deep seabed minerals using the 200 μm diameter GaAs p^+-i-n^+ mesa photodiode, D1. The importance of the in situ elemental analysis of deep seabed minerals, for providing an insight into hydrothermal and other processes in the ocean, deep sea mining and exploration of the oceans of icy moons is introduced. The GaAs photodiode was initially electrically characterised at 4 °C (the ambient temperature of the deep ocean) and 33 °C (the temperature at which multi-energy X-ray spectra are subsequently accumulated). Spectra obtained using an ^{55}Fe radioisotope X-ray source are used to characterise the detector and the spectrometer, and compare their performance to other devices and instruments. The performance of the spectrometer was also characterised across the energy range 4.95 keV to 21.17 keV, at 33 °C, using high-purity X-ray fluorescence calibration samples excited by a Mo target X-ray tube. The same Mo target X-ray tube was used to excite the two deep seabed geological samples (a manganese nodule and a black smoker), X-ray fluorescence spectra obtained using the 200 μm diameter GaAs p^+-i-n^+ mesa photodiode, D1, and the associated readout electronics, are presented and discussed.

7.2 Device structure

The GaAs p^+-i-n^+ mesa photodiodes were grown and fabricated at the EPSRC National Centre for III-V Technologies, Sheffield, UK. GaAs epilayers were grown on a commercial GaAs n^+ substrate by metalorganic vapour phase epitaxy (MOVPE). The unintentionally doped i layer had a thickness of 10 μm. The thickness of the i layer was chosen in order to enable the research on thicker devices compared to those reported in **Chapter 6** (i layer = 7 μm). The resulting wafer structure is summarized in **Table 7.1**. Mesa diodes with diameters of 200 μm and 400 μm were chemically etched using a 1:1:1 H_3PO_4:H_2O_2:H_2O solution followed by 10 s in a 1:8:80 H_2SO_4:H_2O_2:H_2O solution. The top Ohmic contact consisted of 20 nm of Ti and 200 nm of Au. It covered 45 % of the surface of the 200 μm diameter devices and the 33 % of the 400 μm diameter devices. The rear Ohmic contact consisted of 20 nm of InGe and 200 nm of Au. The GaAs devices were unpassivated.

Material	Type	Thickness (nm)	Doping density (cm^{-3})
Ti		20	
Au		200	
GaAs	p^+	500	2×10^{18}
GaAs	i	10000	undoped
GaAs	n^+	1000	2×10^{18}
GaAs	n^+ (substrate)	-	-
Au		200	
InGe		20	

Table 7.1. Layers structure of the GaAs p^+-i-n^+ wafer.

The internal quantum detection efficiency of the devices was calculated for photon energies up to 30 keV using Equation 2.11a (see **Section 2.3.2**) and is presented in **Figure 7.1**. As a cautious assumption, to prevent over estimation of the quantum detection efficiency, the whole of the p^+ layer was assumed to be a dead region and only the i layer was assumed to be the active region of the devices. The internal quantum detection efficiency of the devices reported here (10 μm i layer) compared to the internal quantum detection efficiency of the 7 μm i layer thick GaAs p^+-i-n^+ mesa photodiodes (**Figure 6.2**), was calculated to be higher at the energy range 3.9 keV to 30 keV, due to the thickness of the active layer, but lower at the energy range 0.01 keV to 3.89 keV. The latter was the result of the assumption that the whole of the p^+ layer was dead (0.5 μm), compared to the 7 μm i layer thick GaAs p^+-i-n^+ mesa photodiodes having an implied from visible and near infrared responsivity measurements (**Section 6.4**) top dead layer of 0.16 μm.

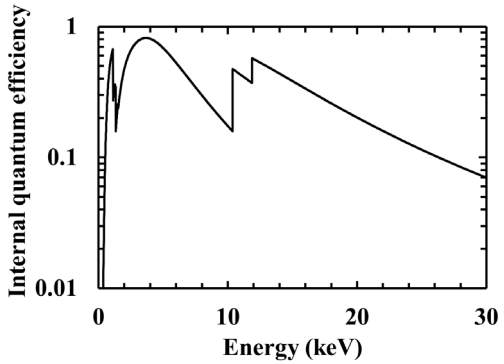

Figure 7.1. Calculated X-ray quantum detection efficiency of the GaAs p^+-i-n^+ mesa photodiodes as a function of X-ray photon energy.

7.3 Room temperature electrical characterisation

7.3.1 Current measurements as a function of bias

Dark current measurements as functions of both forward and reverse applied bias were performed using a Keithley 6487 Picoammeter/Voltage Source (see **Section 2.5.1**). The dark current was measured as a function of forward bias from 0 V to 1 V and as a function of reverse bias from 0 V to -50 V at room temperature. **Figure 7.2** shows the measured currents, I_F, as a function of applied forward bias, V_{AF}, of representative 200 μm and 400 μm diameter devices.

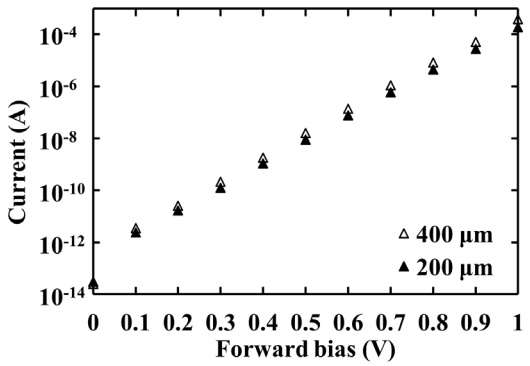

Figure 7.2. Current as a function of applied forward bias for a representative 200 μm (filled triangles) and 400 μm (open triangles) diameter GaAs p^+-i-n^+ photodiode, measured at room temperature.

The ideality factor, n, and the saturation current, I_{sat}, were both calculated from the measured semi-logarithmic forward current, I_F, as a function of applied forward bias, V_{AF}, of the 22 devices (see Equation 2.33). The saturation current, I_{sat}, was found to vary from 0.3 pA to 0.7 pA among different devices at room temperature with a mean of 0.5 pA ± 0.1 pA (rms deviance). The ideality factor, n, was found to vary from 1.89 to 1.99 among different devices with a mean of 1.95 ± 0.02. The calculated ideality factor values (≈ 2) suggest that the recombination current dominated (Sze & Ng, 2007). Dark current measurements as functions of applied forward bias

and temperature would help to identify the contribution of tunnelling on the conduction process as well as the conduction mechanism at high temperatures, but are not reported here. Although the area of the 400 μm diameter devices is four times larger than the area of the 200 μm diameter devices, the 400 μm diameter devices' dark currents at 1 V forward bias were found to be only two times greater than the dark current of the 200 μm devices. The dark current at 1 V applied forward bias was measured to be 0.20 mA ± 0.01 mA for the 200 μm diameter devices and 0.40 mA ± 0.02 mA for the 400 μm diameter devices. The dark forward current scaled with perimeter of the devices, rather than their area which suggested that the surface leakage component was not negligible, but dominated over the bulk leakage current, and that future devices may benefit from surface passivation (Carpenter et al., 1988a). The passivation of GaAs, and the removal of its perimeter surface states have been studied with different materials such as sulphides (e.g. Na_2S and $(NH_4)_2S$ (Carpenter et al., 1988a) (Carpenter et al., 1988b), P_2S_5/NH_4OH (Lee et al., 1989), $P_2S_5/(NH_4)_2S$ (Hwang & Li, 1990), and trioctylphosphine sulfide (Sheldon et al., 2012)), S (Szűcs et al., 2003) (Wang et al., 2010), gadolinium oxides (e.g. Gd_2O_3 (Hong et al., 1999)) as well as H, Cl, F and GaO (Wang et al., 2010). The reduction of the exposed mesa edges, giving rise to surface recombination current (forward bias), due to surface passivation may also reduce the surface generation current (reverse bias) (Carpenter et al., 1988a).

The measured dark currents, I_R, as a function of applied reverse bias, V_{AR}, of one representative 200 μm and one representative 400 μm diameter device are shown in **Figure 7.3**. All GaAs p^+-i-n^+ photodiodes showed low leakage current densities at a mean electric field of 50 kV/cm across the i region (-50 V reverse bias) at room temperature: the measured leakage current density was found to vary from 13 nA/cm^2 to 67 nA/cm^2 with a mean of 40 nA/cm^2 ± 16 nA/cm^2 among the 200 μm diameter devices, and from 4 nA/cm^2 to 21 nA/cm^2 with a mean of 13 nA/cm^2 ± 6 nA/cm^2 among the 400 μm diameter devices, at 50 kV/cm. For comparison purposes, the leakage current densities at an electric field of 22 kV/cm are also presented: they were found to vary from 10 nA/cm^2 to 40 nA/cm^2 with a mean of 24 nA/cm^2 ± 7 nA/cm^2 among the 200 μm and from 4 nA/cm^2 to 9 nA/cm^2 with a mean of 7 nA/cm^2 ± 2 nA/cm^2 among the 400 μm diameter devices. These values are comparable with other high quality GaAs p^+-i-n^+ photodiodes previously reported e.g. ~10 nA/cm^2 (Bertuccio et al., 2003), from 20 nA/cm^2 to 100 nA/cm^2 (Ng et al., 2014), and 17.4 nA/cm^2 and 1.08 nA/cm^2 for the 7 μm i layer GaAs p^+-i-n^+ mesa photodiode D1 and D2 respectively, reported in **Section 6.3**, all at room temperature and at an electric field of 22 kV/cm.

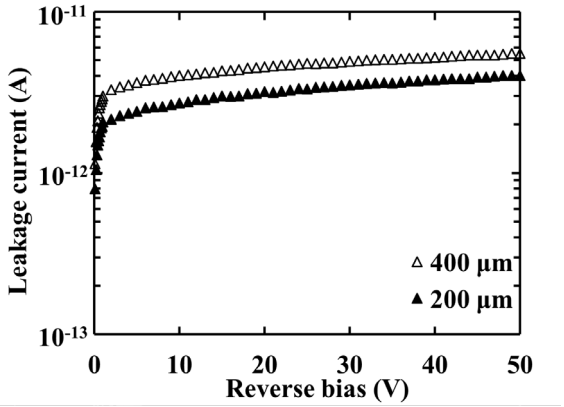

Figure 7.3. Leakage current as a function of applied reverse bias for representative 400 μm (open triangles) and 200 μm (filled triangles) diameter GaAs p^+-i-n^+ photodiodes at room temperature.

The leakage current density, J_R, at an electric field of 50 kV/cm and at room temperature, for all devices can be seen in **Figure 7.4**. The 400 μm diameter devices showed lower leakage current densities than the 200 μm diameter devices at 50 kV/cm, suggesting that the leakage current did not scale with the junction area. This was attributed to the surface leakage current not being negligible similarly to Takenaka et al. (2012), due to the devices being unpassivated, and in accordance with the current measurements as a function of forward applied bias. The perimeter surface states formed by segregated arsenic atoms via oxidation reaction, resulting in deep level traps, may be the main cause of surface generation current (Lee et al., 1989). The separation of the bulk and surface components of the leakage current could be achieved with dark current measurements on different diameter devices, and the effects of the passivation on surface leakage current could be investigated with measurements on devices with different passivation materials.

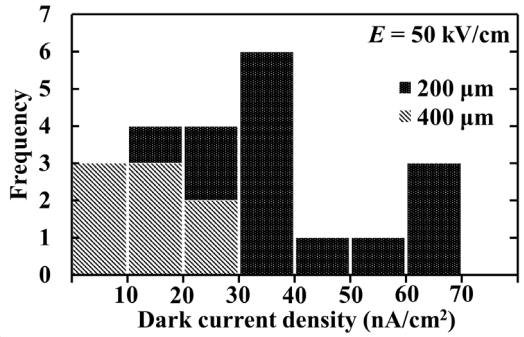

Figure 7.4. Histogram of the dark current density of the 200 μm (black) and 400 μm (grey) diameter GaAs p^+-i-n^+ photodiodes at an electric field of 50 kV/cm.

7.3.2 Capacitance measurements as a function of bias

To determine the depletion width, W_D, and the effective doping concentration, N_{eff}, in the intrinsic layer of the GaAs p^+-i-n^+ devices, the 22 devices' capacitances were measured as functions of applied forward and reverse bias, at room temperature. The capacitances were measured using an HP 4275A Multi Frequency LCR meter (see **Section 2.5.2**), whose test signal was sinusoidal with a 50 mV rms magnitude and 1 MHz frequency. The capacitance of the empty packages was determined by measuring the capacitance between the common pin (GND) and 17 pins with no diode connected across four packages. It was found to vary from 0.71 pF to 0.81 pF, with a mean value of 0.78 pF ± 0.02 pF, being subtracted from the total measured capacitance. The resulting capacitance, the p^+-i-n^+ junction capacitance, as a function of applied forward bias of representative 200 μm and 400 μm diameter devices is presented in **Figure 7.5**.

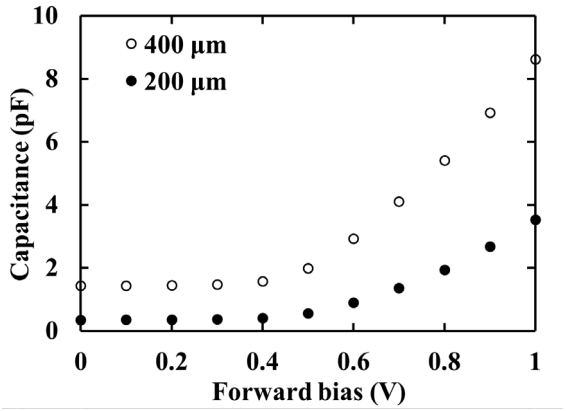

Figure 7.5. Capacitance as a function of applied forward bias for a representative 200 μm (filled circles) and 400 μm (open circles) diameter GaAs p^+-i-n^+ photodiode at room temperature.

The junction capacitance was mostly defined by the diffusion capacitance, $C_{Diff}(V_{AF})$, at forward applied biases. The junction capacitance was found to increase by 7.7 pF ± 0.8 pF for the 400 μm diameter devices and by 3.5 pF ± 0.7 pF for the 200 μm diameter devices, as the applied forward bias increased from 0 V to 1 V. Assuming there was zero diffusion capacitance at 0 V, it may be said that there was 7.7 pF ± 0.8 pF diffusion capacitance for the 400 μm diameter devices and 3.5 pF ± 0.7 pF diffusion capacitance for the 200 μm diameter devices, at 1 V forward applied bias. The ratio of the diffusion capacitance of the 400 μm devices over the diffusion capacitance of the 200 μm diameter devices (= 2.1 ± 0.5), at 1 V is in accordance with the ratio of the forward dark current of the 400 μm diameter devices over the forward dark current of the 200 μm diameter devices (= 2) (see **Figure 7.2**), at 1 V, which was expected since the diffusion capacitance is directly proportional to the forward dark current (see **Section 2.4.2**).

The measured capacitance as a function of applied reverse bias of representative 200 μm and 400 μm diameter devices can be seen in **Figure 7.6**. The junction capacitance was mostly defined by the depletion layer capacitance, $C_{DL}(V_R)$, at reverse biases (see **Section 2.4.2**). The depletion layer capacitance was found to decrease from 1.45 pF ± 0.03 pF at 0 V to 1.36 pF ± 0.03 pF at -50 V for the 400 μm diameter devices and from 0.35 pF ± 0.03 pF at 0 V to 0.32 pF ± 0.03 pF at -50 V for the 200 μm diameter devices. The apparent variation of the capacitance (± 0.03 pF) among different devices at the same applied bias is in agreement with the total uncertainty in the capacitance measurements (± 0.03 pF).

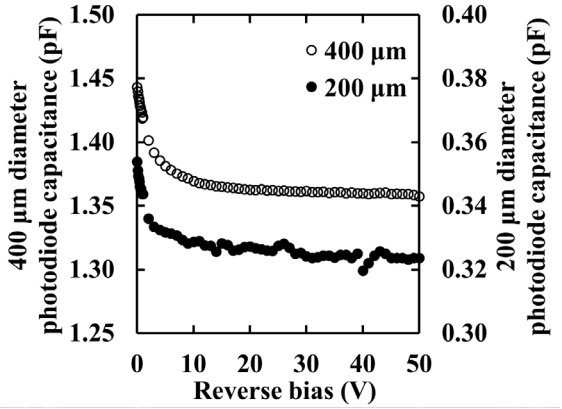

Figure 7.6. Capacitance as a function of applied reverse bias for representative 200 μm (filled circles) and 400 μm (open circles) diameter GaAs p^+-i-n^+ photodiodes at room temperature.

The depletion layer width of the diodes as a function of applied reverse voltage was calculated using Equation 2.37 and is presented in **Figure 7.7**. Once the lightly doped intrinsic layer was fully depleted, the capacitance was independent of the applied reverse bias. All the diodes were almost fully depleted at 0 V. More specifically, the depletion widths of the 400 μm diameter devices were found to increase by a mean of 0.68 μm ± 0.04 μm; from 9.9 μm ± 0.2 μm at 0 V to 10.6 μm ± 0.2 μm at -50 V. The depletion widths of 13 out of 14 200 μm diameter devices were found to increase by 1.0 μm ± 0.2 μm; from a mean of 10 μm ± 1 μm at 0 V to 11 μm ± 1 μm at -50 V. The standard deviation (rms deviance) of the depletion widths of the 400 μm and 200 μm diameter devices were in agreement with the uncertainty of the depletion width for each diode calculated based on the total uncertainty in the capacitance measurements (± 0.03 pF). One of the 200 μm diameter devices had an apparent depletion width of 11 μm ± 1 μm at 0 V increasing to an apparent width of 14 μm ± 2 μm at -50 V. This result was unlikely to have been due to variations in the i layer thickness; instead it was more likely to have been a consequence of this device having a packaging capacitance of 0.7 pF rather than the mean value of 0.78 pF. With the assumption of a 0.7 pF packaging capacitance, this device's depletion width became identical to all other devices.

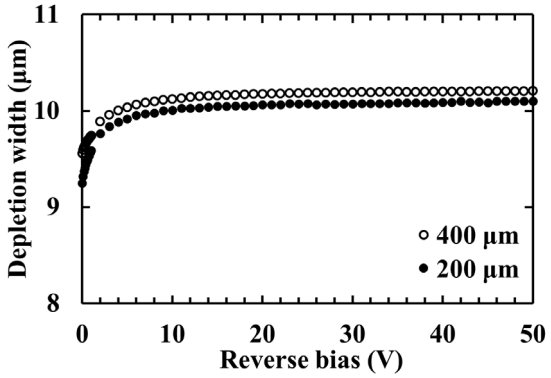

Figure 7.7. Calculated depletion width for representative 200 μm (filled circles) and 400 μm (open circles) diameter GaAs p^+-i-n^+ photodiode calculated from capacitance measurements as a function of applied reverse bias at room temperature.

The effective doping concentration as a function of depletion layer width, $N_{eff}(W_D)$, was calculated using the differential capacitance method, based on Equation 2.38. **Figure 7.8** shows the calculated effective doping concentration of a representative 200 μm and 400 μm diameter device based on the data of **Figure 7.7**.

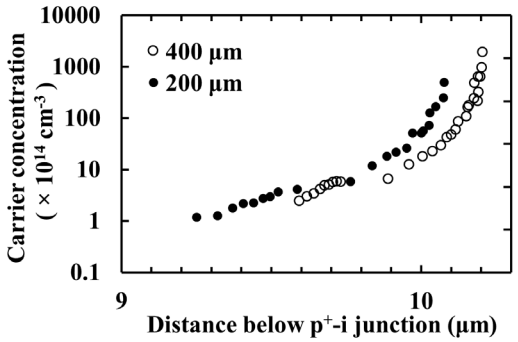

Figure 7.8. Calculated effective doping concentration as a function of depletion layer width of a representative 200 μm (filled circles) and 400 μm (open circles) diameter GaAs p^+-i-n^+ mesa photodiode at room temperature.

Since the calculated carrier concentration was based on the measurements of capacitance as function of reverse bias (depletion layer capacitance), carrier concentration calculations could only be computed accurately at deep distances (close to the i-n^+ junction). The doping density of the i layer increased from 2.8×10^{14} cm^{-3} $\pm$ 0.9×10^{14} cm^{-3} (rms deviance) to 13×10^{16} cm^{-3} $\pm$ 5×10^{16} cm^{-3} among the 400 μm diameter devices and from 0.8×10^{14} cm^{-3} $\pm$ 0.4×10^{14} cm^{-3} to 3×10^{16} cm^{-3} $\pm$ 2×10^{16} cm^{-3} among the 200 μm diameter devices as the i layer reached the i-n^+ junction, at room temperature. The difference between the doping density of the 400 μm and 200 μm diameter devices was attributed to the uncertainty of the capacitance measurements

(± 0.03 pF), which was not negligible considering the capacitances of the devices (**Figure 7.6**) and which, propagating, gave rise to uncertainty in both the implied distance below the p^+-i junction and the carrier concentration. Uncertainties in the diameters of the two photodiodes could also result in differences between their calculated effective doping concentrations.

7.4 Room temperature X-ray spectroscopy

7.4.1 Measurements with an ^{55}Fe radioisotope X-ray source

X-ray spectra were accumulated using representative 200 μm and 400 μm diameter GaAs p^+-i-n^+ mesa photodiodes, D1 and D2 respectively, to characterise their X-ray detection performance. Each device was connected in turn to a custom-made, single-channel, charge sensitive preamplifier (see **Section 2.3.3**). The output signal of the preamplifier was shaped and amplified using an Ortec 572A shaping amplifier. Digitization was achieved using an Ortec EASYMCA multi-channel analyser (MCA). An ^{55}Fe radioisotope X-ray source was positioned 5 mm above the top of each device in turn. The live time for each obtained spectrum was 180 s.

X-ray spectra were obtained for both devices at the optimum shaping time (10 μs) for the currently reported GaAs detector spectrometer, at a range of applied reverse biases, from -5 V to -30 V in 5 V steps. The detected ^{55}Fe X-ray photopeak was the combination of the characteristic Mn Kα at 5.9 keV and Mn Kβ at 6.49 keV lines of the ^{55}Fe radioisotope X-ray source (Schötzig, 2000). Gaussians were fitted to the detected photopeak taking into account the relative emission ratio (Schötzig, 2000) and the relative efficiency of the detectors for the 5.9 keV and the 6.49 keV peaks. The position of the zero energy noise peak and the position of the fitted Mn Kα peak were used for the energy calibration of each spectrum. The uncertainty of the *FWHM* associated with fitting a Gaussian to the photopeak was estimated to be ± 10 eV for both the 200 μm and the 400 μm diameter GaAs p^+-i-n^+ mesa photodiodes reported in this section. The best energy resolutions (*FWHM* at 5.9 keV) with each device were achieved at -5 V reverse bias: 625 eV and 740 eV for the 200 μm and the 400 μm diameter device, respectively.

Figure 7.9 shows ^{55}Fe X-ray spectra obtained with the 200 μm (D1) and 400 μm (D2) diameter devices at -5 V reverse bias, 10 μs shaping time, and room temperature. The counts of the zero energy noise peak were limited by setting the MCA low energy cut-off at 0.8 keV and at 1.0 keV for the 200 μm (**Figure 7.9a**) and the 400 μm (**Figure 7.9b**) diameter devices, respectively. However, a small portion of the right hand side of the zero energy noise peak of the preamplifier can be seen in **Figure 7.9a**. The low energy tailing of the photopeak was attributed to possible partial charge collection of charge created in the non-active layers of the devices, as it was for the low energy tailing of the photopeaks of the spectra presented in **Section 6.51** and **Section 6.7.1**

(Barnett et al., 2015). The valley-to-peak (*V*/*P*) ratios were 0.030 and 0.034, for the 200 µm (**Figure 7.9a**) and the 400 µm (**Figure 7.9b**) diameter devices respectively.

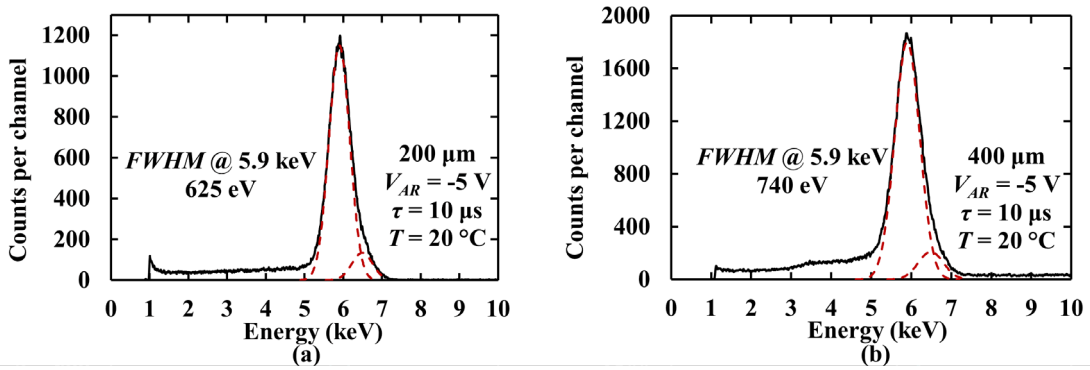

Figure 7.9. ^{55}Fe spectra accumulated with a) the 200 µm GaAs p⁺-i-n⁺ mesa photodiode, D1 and b) the 400 µm diameter GaAs p⁺-i-n⁺ mesa photodiode, D2 at -5 V reverse bias (τ = 10 µs) along with the fitted Mn Kα and Kβ peaks (dashed lines).

7.4.2 Noise analysis

The *FWHM* of the 5.9 keV peak was measured for all obtained spectra and can be seen in **Figure 7.10** as a function of applied reverse bias, for both devices at 10 µs and room temperature. The *FWHM* of the 5.9 keV peak was found to increase from 625 eV at -5 V reverse bias to 665 eV at -30 V reverse bias for the 200 µm diameter device. Similarly, the *FWHM* of the 5.9 keV peak was found to increase from 740 eV at -5 V reverse bias to 780 eV at -30 V reverse bias for the 400 µm diameter device. Explanation of this increase in *FWHM* at greater reverse biases requires discussion of the noise sources affecting the resolution of the photopeak.

There are three noise components which affect the energy resolution of a non-avalanche semiconductor detector coupled to a charge sensitive preamplifier (see Equation 3.1). These are the Fano noise, the incomplete charge collection noise and the electronic noise (see **Chapter 3** for more details). Given a Fano factor of 0.12 (Bertuccio et al., 1997) and an electron hole pair creation energy of 4.184 eV (Bertuccio & Maiocchi, 2002) for GaAs, the Fano noise was calculated to be 128 eV at 5.9 keV. Along with the Fano noise, the white parallel noise, the white series noise and the 1/*f* noise can be directly calculated, as described in **Section 3.2**. The white series noise, due to the capacitance of the detector and input JFET, is inversely proportional to the shaping time, the white series noise, due to the leakage current of the detector and the input JFET, is directly proportional to the shaping time and lastly, the 1/*f* noise is independent of shaping time. The quadratic sum of the Fano noise and the readily calculated electronic noise components (*WP*, *WS* and 1/*f*) was calculated for both the 200 µm (D1) and the 400 µm (D2) diameter device as functions of applied reverse bias at 10 µs shaping time and room temperature,

and can be seen in **Figure 7.10**. It was found to increase slightly from 254 eV at -5 V reverse bias to 293 eV at -30 V reverse bias for the 200 μm diameter device and from 257 eV at -5 V reverse bias to 284 eV at -30 V reverse bias for the 400 μm diameter device, all at 10 μs.

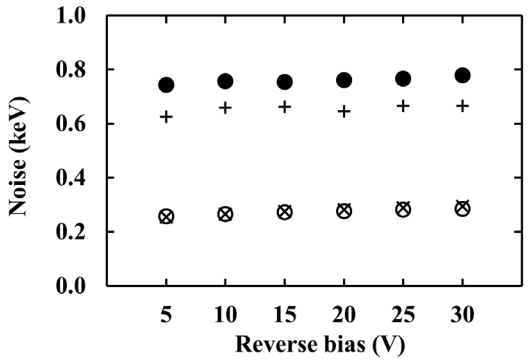

Figure 7.10. Total *FWHM* at 5.9 keV for the 200 μm diameter GaAs p^+-i-n^+ mesa photodiode, D1 (+ symbol) and 400 μm diameter GaAs p^+-i-n^+ mesa photodiode, D2 (filled circles) as a function of applied reverse bias. The calculated Fano noise, white parallel noise, white series noise, and 1/*f* noise (i.e. the readily calculated electronic noise components) for the same 200 μm (× symbol) and 400 μm (open circles) photodiodes are also shown. All values are at room temperature, and for a shaping time of 10 μs.

Since the white parallel noise is dominant over the white series noise contribution at long shaping times, the increase in the total measured *FWHM* of the 5.9 keV peak as the reverse bias increased from -5 V to -30 V, shown in **Figure 7.10**, was expected and was in agreement with the increase of the quadratic sum of the Fano noise and the readily calculated electronic noise components as the reverse bias increased. Although the 400 μm diameter device capacitance (2.1 pF for $|V_R| \geq$ 5 V) was greater than that for the 200 μm device (1.1 pF for $|V_R| \geq 5$ V), the contribution of the white series noise was less significant at 10 μs compared to the contribution of the white parallel noise (4.9 pA and 5.8 pA at -30 V reverse bias for the 400 μm and 200 μm diameter devices, respectively) resulting in similar quadratic sums of Fano, white parallel, white series, and 1/*f* noise at all reverse biases for both devices.

The difference between the measured *FWHM* at 5.9 keV and the calculated quadratic sum of the Fano and the readily calculated electronic noise components (*WS*, *WP* and 1/*f*) was attributed to dielectric noise, *DN*, (due to lossy dielectrics at the proximity of the input of the preamplifier (Bertuccio et al., 1996)) and incomplete charge collection noise, *R*. The quadratic sum of the dielectric and incomplete charge collection noise was calculated for both the 200 μm and the 400 μm diameter device as functions of applied reverse bias at 10 μs shaping time and room temperature, and can be seen in **Figure 7.11**. It was found to be independent of shaping time with

a mean of 590 eV ± 20 eV for the 200 μm and of 710 eV ± 20 eV for the 400 μm diameter device, respectively.

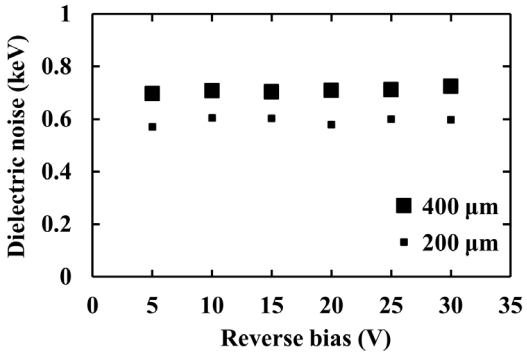

Figure 7.11. Calculated quadratic sum of the dielectric and incomplete charge collection noise for the 200 μm (small filled squares) and the 400 μm (large filled squares) diameter GaAs p^+-i-n^+ mesa photodiode as a function of applied reverse bias at 10 μs and at room temperature.

The non-dependence of the quadratic sum of the dielectric and incomplete charge collection noise with the applied reverse bias suggested that the contribution of the incomplete charge collection noise was insignificant. The dielectric noise was expected to be independent of the applied reverse bias for $|V_{AR}| \geq 5$ V, since the dielectric noise is proportional to the capacitance of the lossy dielectrics (Bertuccio et al., 1996) and the capacitances of both devices are independent of the reverse bias for the same range. The incomplete charge collection noise was expected to vary with detector reverse bias. Increased reverse bias can result in less trapping noise due to improved charge transport. Hence, it may be assumed that even at -5 V reverse bias, there was no significant incomplete charge collection noise. Consequently, it can be said that there was 590 eV ± 20 eV and 710 eV ± 20 eV dielectric noise when the 200 μm and the 400 μm diameter devices were used, respectively. The greater dielectric noise of the 400 μm diameter device-preamplifier system compared to the 200 μm diameter device-preamplifier system was attributed to the higher capacitance of the 400 μm diameter device.

Assuming only the contribution of the detector to the dielectric noise was different between the 200 μm diameter device-preamplifier system and the 400 μm diameter device-preamplifier system, a dielectric noise contribution of 409 eV and 568 eV was calculated for the 200 μm diameter and the 400 μm diameter device, respectively. The contribution of the rest of the lossy dielectrics of the device-preamplifier system to the dielectric noise was computed to be 426 eV. An apparent dissipation factor, D, (Equation 3.14) of 4×10^{-3} was calculated for the currently reported GaAs p^+-i-n^+ mesa photodiodes, at room temperature. It should be noted that, although the calculated apparent dissipation factor of GaAs was one order of magnitude higher than

previous reported measurements of the dissipation factor of GaAs (2×10^{-4} at 2.5 GHz (Courtney, 1977) and 2×10^{-4} at 12.4 GHz (Krupka et al., 2008), both at 26 °C), this apparent dissipation factor was believed to be an upper limit (overestimation) of the actual dissipation factor due to other sources of noise being possible included in the dielectric noise presented in **Figure 7.11**. Future measurements which would enable the direct determination, rather than calculation, of the different noise contributions could result in the estimation of the actual dissipation factor of GaAs.

To conclude, both devices had similar quadratic sums of Fano, white parallel, white series, and 1/*f* noise at all reverse biases at 10 μs, as can be seen in **Figure 7.10**, but the greater capacitance of the 400 μm diameter device compared with that of the 200 μm diameter device resulted in larger dielectric noise for the spectrometer with 400 μm diameter photodiode compared with the spectrometer with the 200 μm diameter photodiode. Overall, a better energy resolution (*FWHM* at 5.9 keV) was obtained using the 200 μm diameter device in comparison with the 400 μm device, while compromising the count rate.

The energy resolution of the 200 μm p^+-i-n^+ mesa photodiode (D1) reported here (625 eV) is the best reported for this type of device. This improvement of the energy resolution compared to previously reported results for same diameter, thinner devices (≈ 800 eV *FWHM* at 5.6 keV for 3 μm i layer (Barnett, 2014) and 745 eV *FWHM* at 5.9 keV for a 7 μm i layer reported in **Chapter 6**), coupled to similar front-end electronics, was attributed to the lower capacitance of the 200 μm diameter device compared to those previously reported which resulted in less white series, 1/*f*, and dielectric noise contributions and improved GaAs material quality. The GaAs p^+-i-n^+ device's (D1) low capacitance (1.1 pF) and leakage current (3.8 pA) resulted in a total Fano noise, white parallel noise, white series noise and 1/*f* noise contribution of 254 eV at 5.9 keV (1 μs shaping time and -5 V reverse bias). However, the dielectric noise (590 eV ± 20 eV) limited the spectral resolution of the currently reported system, resulting in an energy resolution not as good as the best experimental reports of GaAs p^+-i-n^+ structures grown on a semi-insulating substrates with Schottky contacts at room temperature; 266 eV *FWHM* at 5.9 keV (Owens et al., 2001) and 300 eV *FWHM* at 5.9 keV (Erd et al., 2002). In both cases, the input of the preamplifier was optimised for reduced dielectric noise; the detector and the input JFET of the preamplifier were mounted in close proximity on the same low-loss substrate (Erd et al., 2002) (Bertuccio et al., 2003).

7.5 ^{63}Ni β^- particle spectroscopy

Previously, β^- particle (electron) spectrometers have been developed using microchannel plate (MCP) detectors, which have been proven to be useful devices in space applications (e.g. the Electron Spectrometer in the Cassini Plasma Spectrometer for the exploration of the Saturn

system (Linder et al., 1998)). Langmuir probes are also used for electron detection (e.g. in measuring the electron energy distribution functions in plasmas (Gruenwald et al., 2013)). Although scintillators, along with photomultiplier tubes (Tatsuhiko et al., 2010) or photodiode detectors (Kriss & Hamby, 2004) used to convert the scintillation light into an electrical pulse, can be used for electron spectroscopy (Knoll, 2010) (Celiktas, 2012), direct detection with semiconductor detectors are of a great advantage in many electron detection applications (see **Section 1.4.1**). Poorer energy resolution is achieved using scintillators than using direct semiconductor detectors (Tsoulfanidis, 1995) (Knoll, 2010). The smaller amount of energy needed to produce an electron–hole pair in a semiconductor (e.g. 4.184 eV for GaAs (Bertuccio & Maiocchi, 2002)) than the energy needed to produce one information carrier (photoelectron) in a scintillation/photomultiplier tube (of the order of 100 eV, considering the inefficient steps involved in the conversion of incident radiation to light and the subsequent generation of electrical signal (Knoll, 2010)) results in better statistics (greater number of charge carriers produced from the primary ionisation effect) and hence in better energy resolution in semiconductor detectors (Grupen & Buvat, 2012).

Work has been reported on the direct detection of electrons with semiconductor detectors including CCDs, DEPFETs, pixel detectors and p^+-i-n^+ photodiodes. CCDs have been studied for their use in direct detection of β^- particles (electrons) (Daud et al., 1987) (Stearns & Wiedwald, 1989) (Ellilä & Pollari, 1990), and as alternatives to MCP detectors without the need of high voltages and high vacuums required in MCP detectors, in a collimator – electrostatic analyzer head configuration (Bedington et al., 2012). However, CCDs have been proven to be prone to radiation damage from high fluxes of energetic electrons (Ellilä & Pollari, 1990) (Bedington et al., 2012). Detection of β^- particles from ^3H and ^{14}C β^- particle source has been demonstrated using DEPFET pixels, due to their thin backside entrance window and their low noise performance (Ulrici et al., 2005). Si and GaAs hybrid pixel detectors (Bertolucci et al., 1997) (Abate et al., 2001) (Mettivier et al., 2004) (Moldovan et al., 2012) and monolithic active pixel detector (Deptuch, 2005) have been proposed for electron detection to achieve good spatial resolution, high detection efficiency, and real-time capabilities. Since the first report on p^+-i-n^+ photodiodes for electron detection (Schmidt-Ott et al., 1989), work has been conducted on Si (Vapirev et al., 1994), GaAs (Barnett et al., 2012b), and AlGaAs (Barnett et al., 2013) p^+-i-n^+ photodiodes for direct detection of electrons.

A potential application of GaAs p^+-i-n^+ mesa photodiodes is in situ low energy (1 keV to 100 keV) electron spectroscopy at Europa, which when paired with contemporaneous UV imaging from either an orbiter or the Hubble Space Telescope (HST), would allow direct observational data gathering to test predictions that electron impact excitation of water vapor plumes explains recent

auroral observations at Europa's polar regions (Roth et al., 2014) (Sparks et al., 2016). Electrons of energy < 100 keV have been poorly sampled at Europa in the past, but using the Divine and Garett Jupiter radiation belt model (Divine & Garrett, 1983), Paranicas et al. (2009) have estimated that the electron flux ranges from 3×10^9 e^-/cm^2 s at 1 keV to 3×10^8 e^-/cm^2 s at 100 keV, at a radial distance of 9.50 R_J (Jupiter's equatorial radius); Europa's mean orbital radius is 9.39 R_J.

Scattering of electrons incident on the detector's surface and interaction of electrons with the detector material before and after the active region (dead layers) reduces the detected energy and hence results in reduced intrinsic quantum detection efficiency and a distorted energy spectrum. The material of the detector as well as its geometry should carefully be selected and designed to maximise the intrinsic quantum detection efficiency. A detector which could withstand the intense radiation environment of Europa, and hence increase mission duration, would also be advantageous.

In this section, experimental and computer modelling results characterising the 200 μm diameter GaAs p^+-i-n^+ mesa photodiode, D1, for its suitability for β^- particle (electron) spectroscopy are reported. A ^{63}Ni (endpoint energy = 66 keV) β^- particle spectrum was acquired using the 200 μm diameter GaAs p^+-i-n^+ mesa photodiode, D1, coupled to the same low-noise readout electronics as used above, to characterise this prototype spectrometer's performance for β^- particle and electron counting spectroscopy. The accumulated ^{63}Ni spectrum is shown and the results are discussed based on the accepted shape of the ^{63}Ni β^- spectrum. Computer modelling results of the electron absorption in the measurement system, using the computer program CASINO (Hovington et al., 1997) (Drouin et al., 1997), are also used to interpret the experimental results.

7.5.1 Internal quantum detection efficiency of the detector

To characterise the GaAs detector for its intrinsic internal quantum detection efficiency, $QE_{internal}$, defined as the ratio of the total electron energy deposited in the active layer by the total electron energy incident on detector face (excluding scattering of electrons at the air-photodiode interface, see **Section 2.3.2**) at electron energies ≤ 100 keV, the computer program CASINO was used. The computer program CASINO allows Monte Carlo simulations of electrons interacting with solids (Hovington et al., 1997) (Drouin et al., 1997). The electron absorption in the detector was modelled taking into account the p^+-i-n^+ structure of the detector (10 μm i layer) and hence losses introduced by the absorption of electrons (β^- particles) in the dead layers of the detector (p^+ layer, n^+ layer, and substrate). The internal quantum detection efficiency of the 200 μm diameter GaAs p^+-i-n^+ mesa photodiode, D1, for electron (β^- particles) energies up to 100 keV is presented in **Figure 7.12**. The internal quantum detection efficiency of the detector at low electron energies

(9 keV to 55 keV) increased with increasing electron energy, reaching a value of 78 % at 55 keV (and 60 keV), and was believed to be limited by the absorption of electrons at the top dead layer (p^+ layer). The internal quantum detection efficiency of the detector at high electron energies (60 keV to 100 keV) decreased with increasing electron energy reaching a value of 48 % at 100 keV, and was believed to be limited by the absorption of electrons at the n^+ layer/substrate. A 77 % internal quantum detection efficiency was calculated at 66 keV.

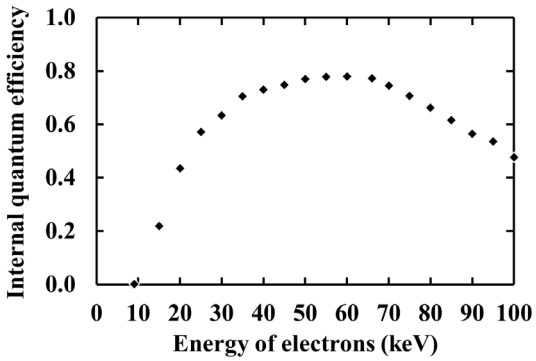

Figure 7.12. Internal quantum detection efficiency of the GaAs p^+-i-n^+ mesa photodiode as a function of electron energy.

7.5.2 ^{63}Ni β^- particle spectra and discussion

The ^{63}Ni radioisotope β^- particle source was positioned 5 mm above the top of the 200 μm diameter GaAs p^+-i-n^+ mesa photodiode, D1. Due to a different front-end configuration of the preamplifier to accommodate the ^{63}Ni source, the optimum shaping time for the system shortened to 2 μs. The detector was reverse biased at -10 V throughout the accumulation (live time limit = 400 s). A low energy threshold of 2 keV was set to minimize counts from the zero energy noise peak. The accumulated ^{63}Ni β^- spectrum is presented in **Figure 7.13**. The spectrum was energy calibrated using the energy calibration derived from ^{55}Fe radioisotope X-ray source (Mn Kα = 5.9 keV; Mn Kβ = 6.49 keV) measurements under the same conditions (shaping time, reverse bias, and temperature).

The events which comprise the spectrum shown in **Figure 7.13** have detected energies equal to those deposited in the active layer of the device. The energy deposited by each β^- particle in the active layer of the device is different form its initial energy and dependent upon its initial energy and track through the inactive Nickel overlayer (~1 μm) covering the ^{63}Ni radioisotope β^- particle source, the air layer (5 mm) between the ^{63}Ni radioisotope β^- particle source and the top of the detector, as well as the detector. The apparent endpoint energy measured with the device was 50 keV, which is lower than the accepted endpoint energy of the ^{63}Ni β^- spectrum (Preiss et al., 1957). It suggested that 75 % of the 66 keV particle energy was deposited at the active i layer

whilst the rest was deposited at the top dead layers (Ni overlayer, air, Ti/Au contacts, and p^+ layer) and n^+ layer/substrate. CASINO simulations, presented in **Section 7.5.3**, explained the accumulated ^{63}Ni β^- spectrum.

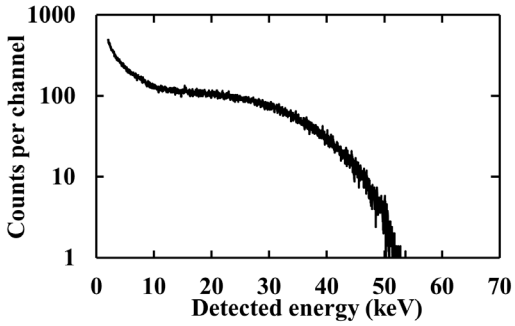

Figure 7.13. ^{63}Ni β^- spectrum obtained with the 200 μm diameter GaAs p^+-i-n^+ mesa photodiode, D1 at 2 μs shaping time, -10 V reverse bias and at room temperature.

Although the GaAs devices reported here were not specifically designed for β^- particle or electron spectroscopy, **Figure 7.13** shows that they can be used for counting β^- particles and measuring the total energy being deposited in the active region of the detectors. **Figure 7.14** shows the accepted shape of the ^{63}Ni β^- spectrum as reported by Preiss et al. (1957) along with the accumulated ^{63}Ni β^- spectrum using the 200 μm diameter GaAs photodiode. Preiss et al.'s data (1957) have been normalized to the accumulated spectrum to reflect the different count rates and accumulation times.

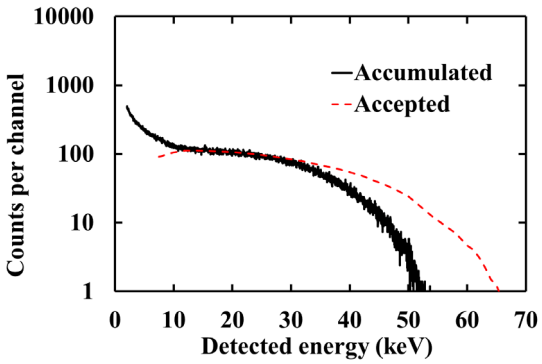

Figure 7.14. Accumulated ^{63}Ni β^- spectrum (solid line) and accepted shape of the ^{63}Ni β^- spectrum (dashes) as reported by Preiss et al. (1957).

7.5.3 CASINO simulations

The computer program CASINO (Hovington et al., 1997) (Drouin et al., 1997) was used for the simulations of the electron absorption in the reported system. Such simulations give an indication

of how the structure of the photodiode (thickness of dead layers and active layers) affects the total energy detected (deposited in the active layer) at the device. The geometry of the detector was defined in CASINO with the structure shown in **Table 7.1**. Since the top Ohmic contact covered 45 % of the face of the 200 μm diameter device (55 % of the face being open to illumination), simulations were carried out for situations without and with the contact to cover both cases. The inactive Nickel overlayer (~1 μm) covering the ^{63}Ni radioisotope β^- particle source was also included in the simulations as was the air layer (5 mm, assumed to be composed entirely of N_2) between the ^{63}Ni radioisotope β^- particle source and the top of the detector.

The simulated electrons, 4000 electrons at each energy, had energies from 1 keV to 66 keV (the ^{63}Ni endpoint energy), with a step of 1 keV. The maximum depths to which electrons of each energy could penetrate before being completely absorbed in the device, both when they were incident on the optical window of the detector (55 % of the area of the face of the 200 μm diameter device) and when they were incident on the top Ti/Au contact (45 % of the area of the face of the 200 μm diameter device), were calculated using CASINO. The results of the simulations are presented in **Figure 7.15** as a function of electron energy. To explore the attenuating effects of the inactive Nickel overlayer of the source in addition to the air and contacts, the final absorption depth of the simulated electrons as a function of their energy when only the p^+-i-n^+ structure was taken into account (i.e. no inactive Nickel overlayer, air or Ti/Au contacts, and thus p^+ layer being the only dead layer), is also presented in **Figure 7.15**.

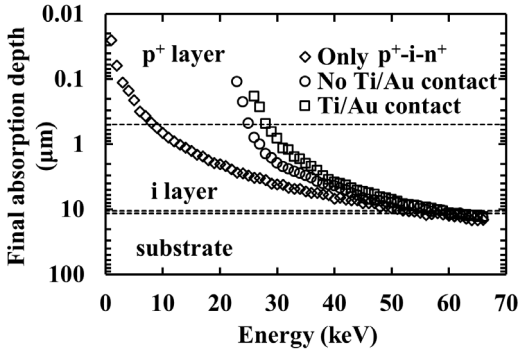

Figure 7.15. Calculated final absorption depth of electrons in the 200 μm diameter GaAs p^+-i-n^+ mesa photodiode, D1, as a function of their energy. All layers of the GaAs p^+-i-n^+ device (p^+, i, n^+, and substrate) are also included. n^+ layer, between i layer and substrate is not labelled on the figure for clarity.

The electrons lost their energy along their path through matter. A percentage of the particle energy incident on the device was deposited in the dead layers reducing the total particle energy deposited in the active i layer, therefore reducing the energy detected. For simulated electrons (β^-

particles) impinging directly on top of the p^+-i-n^+ photodiode (i.e. no attenuation from the inactive Ni overlayer, air, or Ti/Au contacts), it was found that only particles of energy ≤ 8 keV did not reach the detector's i layer (**Figure 7.15**). Particles of energy ≥ 53 keV lost part of their energy in the n^+ layer / substrate, with the 66 keV β^- particles reaching a maximum depth of 14.5 μm.

For simulated electrons (β^- particles) emitted from the ^{63}Ni radioisotope β^- particle source (i.e. attenuation from the inactive Ni overlayer, air, Ti/Au contacts, p^+ layer, n^+ layer, and substrate included), particles of energy ≤ 25 keV, when incident on the optical window of the detector, and particles of energy ≤ 28 keV, when incident on the Au/Ti top Ohmic contact were completely absorbed within the top dead layers (i.e. the source's inactive Ni overlayer, air, detector contacts, and detector p^+ layer). A percentage of the electrons with energies ≥ 60 keV (when both incident on and not incident on the Au/Ti top Ohmic contact) were also absorbed in the n^+ layer / substrate reducing the available particle energy being deposited at the active layer. It was found that 0.1 % (for 60 keV) to 1.4 % (for 66 keV) of electrons, when incident on the top Ohmic contact, deposited part of their energy in the n^+ layer / substrate. Similarly, it was found that 0.2 % (for 60 keV) to 1.7 % (for 66 keV) of electrons, when they were incident on the optical window of the detector, deposited part of their energy in the n^+ layer / substrate. The maximum depth of the 66 keV electrons (^{63}Ni endpoint energy) was found to be 13.5 μm and 13 μm when they were not incident on and incident on the Au/Ti top Ohmic contact, respectively. It should be noted here that the inactive Ni overlayer of the ^{63}Ni radioisotope β^- particle source also attenuated a portion of the energy of all β^- particles emitted.

The simulations showed that the elimination of the inactive nickel overlayer of the ^{63}Ni radioisotope β^- particle source and the air gap between the source and the top of the device along with a reduction of the thickness of the p^+ layer, from 0.5 μm to ideally 0 nm (assuming the entire p^+ layer were inactive, which is pessimistic) and an increase in the thickness of the i layer, from 10 μm to 14.5 μm, would result in the deposition of the total β^- particle energy in the active layer and hence to the detection of all β^- particles emitted from the ^{63}Ni radioisotope β^- particle source. The fact that these criteria were not fulfilled, together with the simulation results discussed below, explained the apparent endpoint energy observed in the experimental measurements presented in **Section 7.5.2**.

The computed trajectories of 4000 electrons each having an energy of 66 keV were also used to calculate the energy deposited in the i layer. Similarly to the previous CASINO simulations, electrons were simulated for situations where the electrons were incident on the top Ohmic contact and where the electrons were incident on the optical window of the detector (the inactive Ni

overlayer and air were also included). For both cases, the distribution of particle energy deposited in the i layer for 4000 electrons each of energy 66 keV, is presented in **Figure 7.16**.

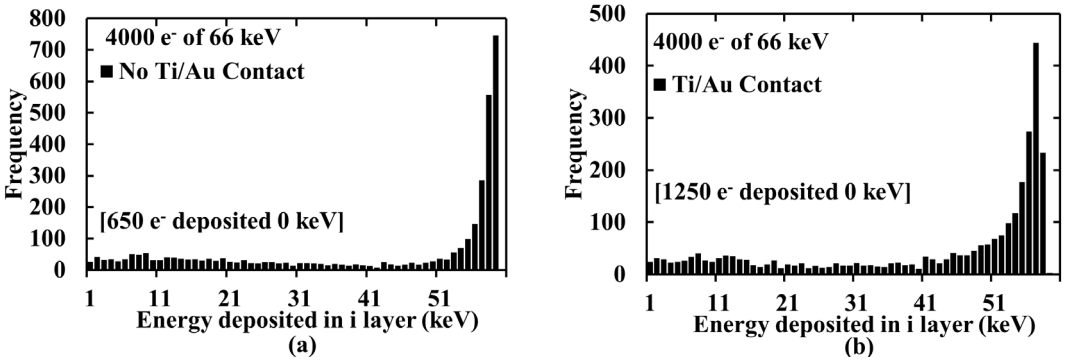

Figure 7.16. Calculated distribution of total energy deposited in i layer of 4000 66 keV electrons when a) not interacting and b) interacting with the Ti/Au top Ohmic contact which covered 45 % of the face of the 200 μm GaAs p^+-i-n^+ mesa photodiode, D1.

CASINO simulations showed that the most probable (18.6 % of electrons simulated) amount of energy deposited in the i layer by 66 keV electrons incident on the optical window of the detector was 59 keV (**Figure 7.16a**), with the maximum energy being 60 keV (0.05 %). It was also found that a total of 16.2 % (650 out of 4000) of the electrons were fully absorbed before reaching the i layer and thus not detected at all. When the same electrons were simulated as incident upon the top Ohmic contact, it was found that the maximum energy deposited in the i layer was reduced to 59 keV, with the most probable energy (31.2 %) deposited becoming 0 keV, followed by 57 keV (11.1 %) (**Figure 7.16b**). Hence, a 66 keV β^- particle emitted from the ^{63}Ni radioisotope β^- particle source could deposit in the i layer of the GaAs p^+-i-n^+ photodiode energy totalling between 0 keV and 60 keV, depending on its three dimensional trajectory. This was in accordance with the apparent endpoint energy (= 50 keV) of the accumulated ^{63}Ni β^- spectrum (**Figure 7.13**).

7.5.4 Conclusions

The reported spectrometer, including a prototype GaAs p^+-i-n^+ detector and a custom-made charge sensitive preamplifier, has been demonstrated as an electron spectrometer with a potential application for in situ low energy (1 keV to 100 keV) electron spectroscopy at Europa. The benefit of the radiation resistance of GaAs compared with materials which are more prone to radiation damage (such as Si) becomes increasingly significant at environments of intense radiation (such as Jupiter and the Galilean moons). The geometry of future photodiode detectors should be improved to accommodate better the requirement of high intrinsic quantum detection efficiency across the electron range of interest (1 keV to 100 keV). Reducing the thickness of the p^+ layer to be as thin possible, within practicalities, would increase the intrinsic quantum detection

efficiency at low electron energies. Similarly, increasing the thickness of the active i layer to ~30 μm would increases the intrinsic quantum detection efficiency at high electron energies. A careful design of the instrument's optics (e.g. electron collimator), to eliminate lossy interactions of the electrons before they reach the detector, and the above modifications of the detector's geometry, would provide instrumentation which would allow direct detection of low energy electrons at Europa with a potential verification (or refutation) of the hypothesis that the Europan auroral observations of Roth et al. (2014) and Sparks et al. (2016) are due to electron impact excitation of water vapour plumes, with the potential implication that the Europan ocean and surface are linked.

7.6 Elemental analysis of deep seabed minerals using a prototype GaAs photodiode X-ray fluorescence spectrometer

7.6.1 Introduction

Deep seabed minerals are present in three forms: polymetallic nodules, polymetallic sulphides, and cobalt-rich crusts (Park, 2012). Polymetallic nodules are created via the precipitation of seawater dissolved metallic components and the subsequent formation of rock concentrations (Park, 2012). Polymetallic sulphides are found in deep-sea hydrothermal vents (Kohler et al., 1994). The hydrothermal vents are the result of metallic elements dissolved into the seawater being risen and erupted in reaction to high temperatures and pressures by volcanic rocks (Park, 2012). The hydrothermal vent solution gives rise to precipitates that form chimneys, called black smokers and white smokers. Black smokers originate from the precipitation of Fe, Cu, Zn, and Pb sulphides, when hydrothermal fluids of temperatures up to 400 °C mix with seawater, whereas white smokers originate from the precipitation of silica and Ba or Ca sulphates when alkaline hydrothermal solutions of temperatures from 260 °C to 300 °C interact with seawater (Gargaud et al., 2011). Lastly, cobalt-rich crusts are formed by the absorption of seawater metals in the rocky beds of seamount slopes (Park, 2012). The knowledge of the elemental composition of these minerals can provide an insight into hydrothermal processes and general information on physical, chemical and biological processes in the ocean (Puri et al., 1998) (Tivey, 1998). Also, the high concentration of valuable minerals (including Mn, Cu, Co, and Ni) in such deposits in these formations makes them attractive for deep sea mining (Park, 2012). The in situ characterisation of deep ocean geology could revolutionise this activity.

Ocean mining offers many benefits over land-based mining. Mining of selected marine deposits with high diversity (more than one minerals can be recovered from a single mine site) and high concentrations of valuable minerals is possible, since the mining platform (surface vessel) could be moved to new locations (Hein et al., 2013). Additionally, little infrastructure is required for ocean mining, and hence a smaller footprint should be left compared to land-based mining

needing roads, buildings, and open pits. Also, a lower quantity of CO_2 should be produced per tonne of metal delivered by ocean mining due to less or no overburden (loose or consolidated material lying over a mineral deposit) being required to be removed compared to land-based mining, where an increased amount of overburden must be removed to reach the selected ores. Furthermore, ocean mining does not require displacement of indigenous people and according to Agarwal et al. (2012) a less populated ecosystem would be affected compared to land-based mining. A potential disadvantage of ocean mining is the disturbance of the ocean biota. However, according to Scott (2001), the affected areas would be expected to be repopulated eventually, as the species concerned are widespread.

The characterisation of deep seabed minerals currently requires samples to be retrieved from the ocean and transported to the surface vessel or back to land for analysis. Sampling methods include wax sampling, push core sampling, and box sampling, as well as retrieval of material by remotely operated vehicle. However, characterisation of the seafloor material using a sampling method can be conducted after the samples have been retrieved and transferred to the surface. This imposes time delays and inefficiencies in the mining process. Additionally, the limited amount of randomly selected samples analysed during sampling would prevent selected mining of targeted marine deposits with high diversity and high concentrations of valuable minerals. A technique for deep seabed minerals characterisation using a remotely operated vehicle to overcome the above limitations of the sampling methods has been proposed (Smith & Leach, 2015). Such a remotely operated vehicle may be equipped with an X-ray fluorescence or a neutron activation analysis detector mounted in a pressure rated housing which can provide in situ estimates on the composition and concentration of valuable minerals within the seafloor material.

One of the major challenges of the in situ characterisation of geological deposits on the seabed is the high pressure encountered at the ocean seafloor, which imposes the need for the development of pressure tolerance instrumentation. Additionally, in situ characterisation of deep ocean geology requires operation at extreme environments mainly because of the high temperatures (from just few degrees above that of the ambient seawater, ~4 °C, to ≥ 350 °C) encountered at high depths at the seafloor hydrothermal systems (Von Damm, 1990). The use of wide bandgap semiconductor detectors for such activities may be beneficial, as it has already been discussed in **Section 1.5**. The detector is also required to resolve X-ray lines for the identification of the elements of deep seabed minerals with in situ X-ray fluorescence analysis. The necessary X-ray energy range spans from Si (Kα at 1.74 keV (Thompson et al., 2009)) and an upper limit of Mo

(Kβ at 19.6 keV (Thompson et al., 2009)). Within the energy range of interest, a high intrinsic quantum detection efficiency and a sufficiently good energy resolution are desirable.

In addition to the characterisation of deep seabed minerals formed by hydrothermal vents on Earth with in situ X-ray fluorescence analysis, there is a potential interest in exploring the oceans of icy moons, such as Europa. Detailed images from Europa showed a surface of ice and magnetometer measurements indicated the existence of an ocean under Europa's ice sheet believed to be formed from Europa's internal heating due to Jupiter's tidal pull (Powell et al., 2005). The tidal forces generated by Jupiter could also result in the formation of a network of hydrothermal vents on Europa's ocean floor. Submarines designs for future icy moon ocean exploration have already been reported (Powell et al., 2005) (Fernandez & Sanchez-Torres, 2015), to investigate Europa's potentially habitable environment. Employing an X-ray fluorescence spectrometer in such a submarine for in situ characterisation would eliminate the need to return collected samples back to the surface of Europa or bring them inside the submarine. The requirement of radiation hard electronics in the intense radiation environment of Europa could be accommodated using a GaAs photodiode detector, as has already been discussed in **Section 1.5**.

In this section, a prototype GaAs photodiode X-ray fluorescence spectrometer is developed for in situ characterisation of deep seabed minerals. The detector used was the 200 μm diameter GaAs p^+-i-n^+ mesa photodiode, D1, with a 10 μm i layer thickness. Initially, the photodiode was electrically characterised at 4 °C, which is the ambient seawater temperature in the deep ocean. Because the subsequent energy calibration of the system and the elemental analysis of two representative geological samples were performed at 33 °C (the ambient Mo target X-ray tube temperature), electrical characterisation at 33 °C was also included. The noise analysis of the X-ray fluorescence spectrometer was performed with an ^{55}Fe radioisotope X-ray source. ^{55}Fe X-ray spectra were accumulated at 4 °C and the different noise contributions were detangled. In addition, ^{55}Fe spectra were accumulated at 33 °C to investigate the change in noise contributions at this elevated temperature. Following this, the energy calibration of the system over the energy range 4.95 keV to 21.17 keV at 33 °C, using known fluorescence calibration samples is presented. The linearity of the detector with varying X-ray intensity at the energies 8.63 keV and 16.6 keV at 33 °C is also reported. Then, two samples of deep seabed minerals were analysed for their elemental composition with XRF spectroscopy. The deep seabed minerals tested in this study were a manganese nodule, from the Clarion-Clipperton Fracture Zone, Pacific Ocean, and a black smoker, from Rodriquez Triple Junction, Indian Ocean.

7.6.2 Electrical characterisation

The dark current of the photodiode as a function of both forward and reverse applied bias was measured using a Keithley 6487 Picoammeter/Voltage Source (see **Section 2.5.1**). The photodiode was installed inside a TAS Micro MT climatic cabinet for temperature control. Temperatures of 4 °C – the ambient water temperature in the deep ocean, and 33 °C – the temperature at which the energy-charge (**Section 7.6.4**) and count rate-X-ray intensity (**Section 7.6.5**) linearity response was characterised, and X-ray fluorescence spectra of representative geological samples were accumulated in the laboratory (**Section 7.6.6**). The dark current was measured as a function of forward bias from 0 V to 1 V, and as a function of reverse bias from 0 V to -50 V. **Figure 7.17** shows the measured currents of the photodiode at both temperatures.

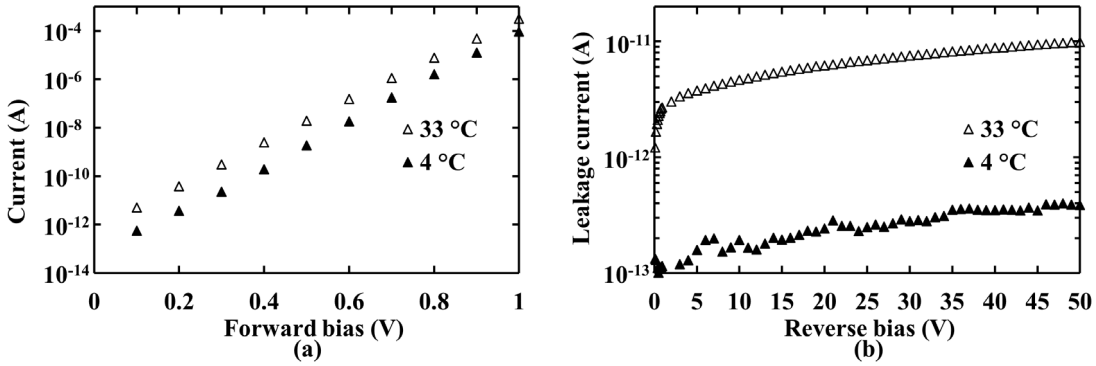

Figure 7.17. Dark current at 4 °C (filled triangles) and 33 °C (empty triangles) as a function of applied (a) forward and (b) reverse bias for the 200 μm diameter GaAs p^+-i-n^+ mesa photodiode, D1.

The saturation current, I_{sat}, and the ideality factor, n, of the photodiode were extracted based on the linear region of the semi-logarithm dark current as a function of forward bias, using Equation 2.33. The saturation current was found to increase with increased temperature, as expected, from 0.046 pA ± 0.007 pA at 4 °C to 0.72 pA ± 0.06 pA at 33 °C. Although the 7 μm i layer thick GaAs mesa p^+-i-n^+ photodiodes, D1 and D2, reported in **Chapter 6** showed an improved ideality factor with increased temperature (**Figure 6.18**), attributed to the reduction of the recombination current and the increase of the diffusion current as the temperature increased (Sze & Ng, 2007), a different behaviour was observed with the 10 μm i layer thick GaAs mesa p^+-i-n^+ photodiode, D1. The ideality factor was found to be improved at 4 °C (= 1.84 ± 0.02) compared with 33 °C (= 1.96 ± 0.01). Ideality factor values close to 2 suggest that the recombination current dominated over the diffusion current (see **Section 2.4.2**). The deterioration of the ideality factor at 33 °C was attributed to more thermally stimulated crystal lattice defects compared to 4 °C, being the main cause of the non-ideal behaviour of the device. The leakage current, I_R, of the device was found to increase with increased temperature from 0.4 pA (1.2 nA/cm^2) at 4 °C to 9.9 pA

(31.6 nA/cm^2) at 33 °C, both at the highest investigated reverse bias, -50 V (~ 50 kV/cm internal electric field). The reported photodiode had comparable leakage current density with other high quality GaAs p^+-i-n^+ diodes, and as an example a leakage current density of 23 nA/cm^2 at 33 °C was measured for the currently reported photodiode compared to 92 nA/cm^2 at 30 °C (Bertuccio & Casiraghi, 2003) both at an internal electric field of ~ 30 kV/cm.

The X-ray spectra to characterise the charge linearity response (**Section 7.6.4**) and the linearity with X-ray intensity (**Section 7.6.5**) of the spectrometer, as well as the X-ray fluorescent spectra of representative geological samples (**Section 7.6.6**) were all accumulated in the laboratory, at a temperature of 33 °C with the photodiode detector reverse biased at -15 V and at 1 μs shaping time. The stability of the leakage current with time and its effect to the white parallel noise (**Section 3.2**) of the spectroscopic system was investigated and the results are presented below. The photodiode was left reverse biased at -15 V, and its leakage current was measured over a period of 8 hours, every 1 minute, at 33 °C. The leakage current time stability of the photodiode at -15 V reverse bias and 33 °C can be seen in **Figure 7.18** along with the calculated white parallel noise contribution at 1 μs, as described in **Section 3.2**.

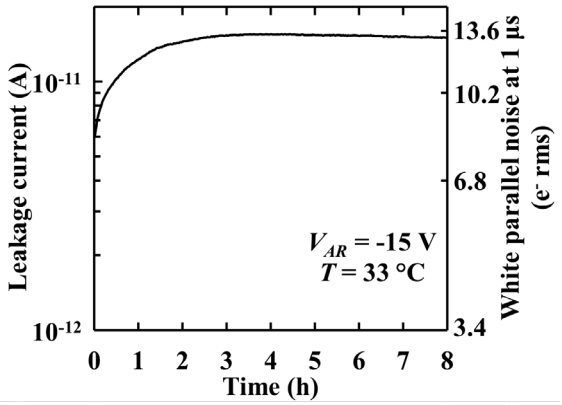

Figure 7.18. Leakage current of the 200 μm GaAs p^+-i-n^+ mesa photodiode, D1, measured at 33 °C and -15 V reverse bias as a function of time. The right y-axis shows the corresponding white parallel noise contribution of the measured dark current at 1 μs shaping time.

The leakage current increased from 5.8 pA (corresponding to 8 e^- rms) to 15 pA (corresponding to 13 e^- rms) after 2.5 hours and remained stable thereinafter. The source of leakage current time instability is related to the mechanism of conduction (Street, 2000). Comparing **Figure 7.18** with **Figure 6.5**, it can be said that there was a different cause of the leakage current instability of the 10 μm i layer thick GaAs p^+-i-n^+ photodiode D1 at 33 °C and -15 V reverse bias compared to the leakage current instability of the two 7 μm i layer thick GaAs p^+-i-n^+ photodiodes, D1 and D2, at 20 °C and -15 V reverse bias. The exponential increase of the leakage current with time of the

two 7 μm i layer thick GaAs p^+-i-n^+ photodiodes, D1 and D2, at 20 °C and -15 V reverse bias (**Figure 6.5**) was attributed to trap assisted generation current due to possible defects which were annealed at 120 °C and/or to surface leakage current reduction due to the breaking of possible bonds between the atoms at the surface of the semiconductor and atoms in the atmosphere at this elevated temperature. The slow and logarithmic increase of leakage current of the 10 μm i layer thick GaAs p^+-i-n^+ photodiode D1 at 33 °C and -15 V reverse bias over the first 2.5 hours is currently unknown.

The depletion layer width, W_D, and the effective doping concentration, N_{eff}, of the i layer, as well as the white series noise contribution (see **Section 7.6.3**) of the photodiode were all determined from capacitance measurements. The capacitance measurements were performed using an HP 4275A Multi Frequency LCR meter (see **Section 2.5.2**) with 50 mV rms magnitude and 1 MHz frequency test signal. The photodiode was installed inside a TAS Micro MT climatic cabinet for temperature control. **Figure 7.19** shows the measured junction capacitance as a function of forward and reverse bias at 4 °C and 33 °C. The capacitance of the package (0.76 pF at 4 °C and 0.95 pF at 33 °C) was subtracted from the total measured capacitance to give the junction capacitance shown in **Figure 7.19**. The total error in the capacitance measurements, including the error in LCR meter, in packaging capacitance and rms error was estimated to be ± 0.03 pF.

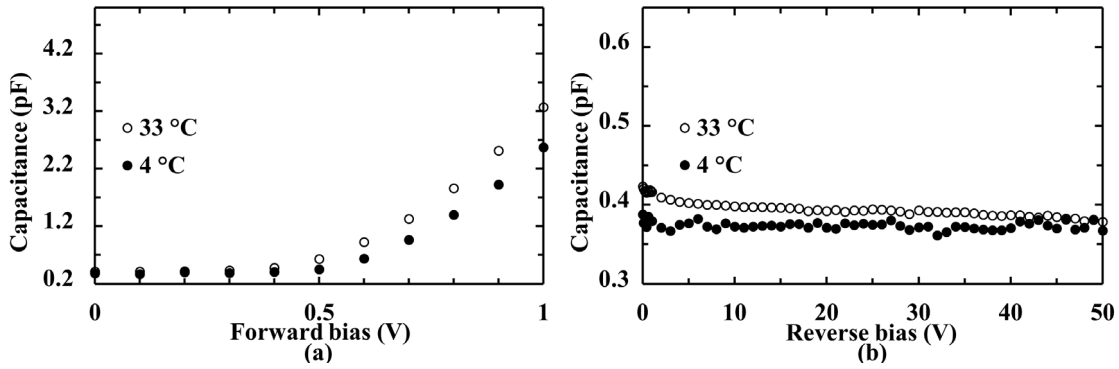

Figure 7.19. Capacitance as a function of (a) forward and (b) reverse bias of the 200 μm GaAs p^+-i-n^+ mesa photodiode, D1, measured at 4 °C (filled circles) and 33 °C (empty circles).

The forward biased junction capacitance at 1 V was measured to increase with increased temperature, from 2.58 pF at 4 °C to 3.27 pF at 33 °C. There is a significant contribution of the diffusion capacitance to the junction capacitance at forward applied biases due to the rearrangement of the minority carrier density (see **Section 2.4.2**). The increase of the forward biased junction capacitance with increased temperature was attributed to the higher forward current, I_F, at 33 °C compared to that at 4 °C (**Figure 7.17a**), since the diffusion capacitance is directly proportional to the forward current.

The depletion layer capacitance, defining the junction capacitance at applied reverse biases, was found to be temperature invariant for reverse biases greater than -3 V, at the investigated temperatures within the measurement error. It was measured to be 0.38 pF at -50 V reverse bias both at 4 °C and 33 °C. However, a temperature dependent depletion layer capacitance was measured for applied reverse biases ranging from 0 V to -3 V. The depletion layer width, W_D, of the photodiode was calculated using the measured depletion layer capacitance, C_{DL} and Equation 2.37 as a function of applied reverse bias for both temperatures, and can be seen in **Figure 7.20**.

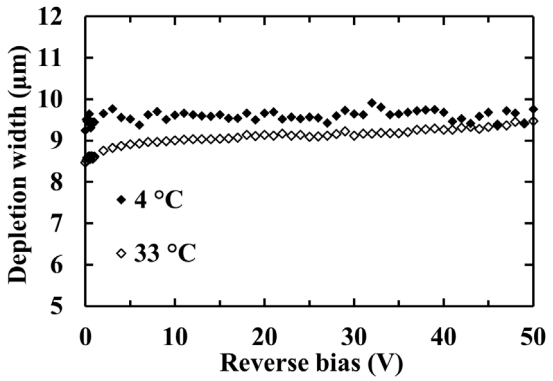

Figure 7.20. Calculated depletion width for the 200 μm GaAs p^+-i-n^+ mesa photodiode, D1, calculated from capacitance measurements as a function of applied reverse bias at 4 °C (filled diamonds) and 33 °C (empty diamonds).

The depletion layer width of the photodiode was determined to only slightly increase with increased reverse bias. More specifically, it was found to increase from 9.2 μm ± 0.7 μm at 0 V to 9.8 μm ± 0.8 μm at -50 V reverse bias and 4 °C and from 8.5 μm ± 0.5 μm at 0 V to 9.5 μm ± 0.7 μm at -50 V reverse bias and 33 °C. Another observation based on **Figure 7.20** is that the photodiode is almost fully depleted at -1 V reverse bias, when operating at 4 °C whereas the same occurs at ~ -40 V reverse bias, when operating at 33 °C. This might be explained, similarly to the same observation for the 7 μm i layer GaAs p^+-i-n^+ mesa photodiode D1 (**Figure 6.23**), with a presence of a thin region around the depletion region with non-ionised dopants at 4 °C which were ionised at 33 °C and limited the extension of the depletion layer at low reverse biases. (Mazzillo et al., 2012).

The majority carrier concentration, approximated to the effective i layer doping concentration, N_{eff}, of the i layer, as a function of distance below the p^+-i junction was calculated using the differential capacitance method, based on Equation 2.38 and is shown in **Figure 7.21**. It was found to increase from 0.2×10^{14} cm^{-3} at 9.2 μm ± 0.7 μm below the p^+-i junction to 43×10^{14} cm^{-3}

at the i-n^+ interface at 4 °C. Similarly, the effective doping density was found to increase from 1 × 10^{14} cm^{-3} at 8.5 μm ± 0.5 μm below the p^+-i junction to 86 × 10^{14} cm^{-3} at the i-n^+ interface at 33 °C. Although the photodiode was found to be fully depleted (i.e. its depletion region was equal to the i layer thickness) at both temperatures, the doping profile of the i layer suggested that there might be a layer close to i^+-n junction with non ionised dopants at 4 °C which were ionised at 33 °C. The uncertainties of the depletion layer widths were calculated propagating the uncertainty in the capacitance measurements (± 0.03 pF). The arbitrary doping profile of the i layer (**Figure 7.21**) determined using the differential capacitance method had a spatial resolution of the order of a Debye length, which has been calculated for GaAs with a doping concentration of 10^{14} cm^{-3} at the temperature range 4 °C to 33 °C to be 0.4 μm (Sze & Ng, 2007).

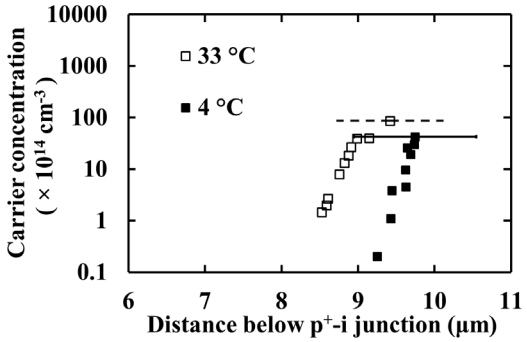

Figure 7.21. Calculated effective doping concentration as a function of distance below p^+-i junction of the 200 μm GaAs p^+-i-n^+ mesa photodiode D1, at 4 °C (filled squares) and 33 °C (empty squares). The uncertainty of the i layer thickness (highest depletion layer width) of the 200 μm GaAs p^+-i-n^+ mesa photodiode D1, at 4 °C and 33 °C, as calculated by propagating the error in the capacitance measurement (± 0.03 pF), can also be seen.

7.6.3 Measurements with an ^{55}Fe radioisotope X-ray source

The performance of the X-ray fluorescence spectrometer was initially characterised with ^{55}Fe X-ray measurements at 4 °C. In this section, the different noise contributions of the system at 4 °C are concerned. The relative performance of the instrument at 33 °C, which is the temperature of the subsequent measurements using the Mo target X-ray tube, is also shown.

The 200 μm GaAs p^+-i-n^+ mesa photodiode, D1, was connected to the input of a custom-made, single-channel charge sensitive preamplifier without the feedback resistor (see **Section 2.3.3**). An ^{55}Fe radioisotope X-ray source was positioned 3 mm above the top of the device. The detector along with the preamplifier were installed inside a TAS Micro MT climatic cabinet throughout the measurements for temperature control. The signal of the preamplifier was shaped using an

Ortec 572A shaping amplifier and was further connected to a multi-channel analyser (MCA) for digitisation. The live time limit for each accumulated spectrum was 60 s.

The temperature was initially set to 4 °C, the detector was kept reverse biased at -15 V and spectra were accumulated for τ = 0.5 µs, 1 µs, 2 µs, 3 µs, 6 µs and 10 µs. Then, the temperature was increased to 33 °C and ^{55}Fe were obtained for the same shaping times. The accumulated spectra of the ^{55}Fe radioisotope X-ray source at 4 °C and 33 °C with the best energy resolution (lowest *FWHM*) can be seen in **Figure 7.22**. The detected ^{55}Fe photopeak is the combination of the characteristic Mn Kα (5.9 keV) and Mn Kβ at (6.49 keV) lines of the ^{55}Fe radioisotope X-ray source (Schötzig, 2000). Gaussians were fitted to the peak taking into account the relative emission ratio (Schötzig, 2000) and the relative efficiency of the detector for the 5.9 keV and 6.49 keV peak. The spectra were energy calibrated based on the positions of the zero energy noise peak and the Mn Kα peak. The uncertainty of the *FWHM* associated with fitting a Gaussian to the photopeak was estimated to be ≤ ± 10 eV for the GaAs p^+-i-n^+ mesa photodiode D1 reported in this section. The energy resolution degraded from 580 eV at 4 °C to 680 eV at 33 °C, both at -15 V reverse bias and 2 µs shaping time.

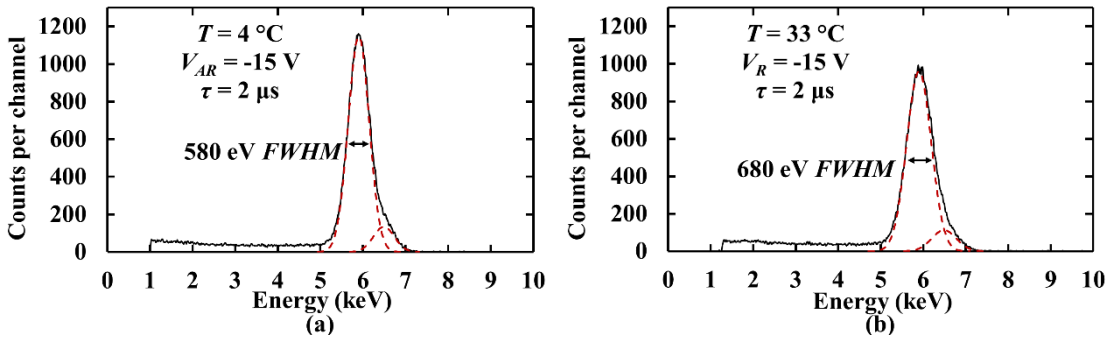

Figure 7.22. ^{55}Fe spectra accumulated with the 200 µm GaAs p^+-i-n^+ mesa photodiode, D1, at -15 V reverse bias and 2 µs shaping time at (a) 4 °C and (b) 33 °C, along with the fitted Mn Kα and Kβ peaks (dashed lines).

The *FWHM* was measured for all obtained spectra and can be seen in **Figure 7.23**. The optimum shaping time was found to be 2 µs for both temperatures. The energy resolution of a non-avalanche semiconductor detector coupled to a charge sensitive preamplifier assuming the incomplete charge collection noise is negligible, is degraded due to two independent sources of noise: Fano noise and electronic noise (see **Section 3.1**). The Fano noise was calculated to be 128 eV at 5.9 keV assuming an electron hole pair creation energy of 4.184 eV (Bertuccio & Maiocchi, 2002) and a Fano factor of 0.12 (Bertuccio et al., 1997). The electronic noise, due to the detector itself and the preamplifier comprises white parallel noise, white series noise

(including the induced gate current noise contribution), 1/*f* noise and dielectric noise (see **Section 3.2**). The white parallel noise, due to the leakage current of the detector and of the input Junction Field-Effect Transistor (JFET), is directly proportional to the shaping time. The white series noise, due to the capacitance of the detector and of the input JFET, is inversely proportional to the shaping time. The 1/*f* and dielectric noise are both shaping time invariant. Hence, the experimental values of *FWHM* as a function of shaping time can be fitted through a multidimensional least squares estimation method to find the three parameters each of which has a different relationship with τ (Bertuccio & Pullia, 1993).

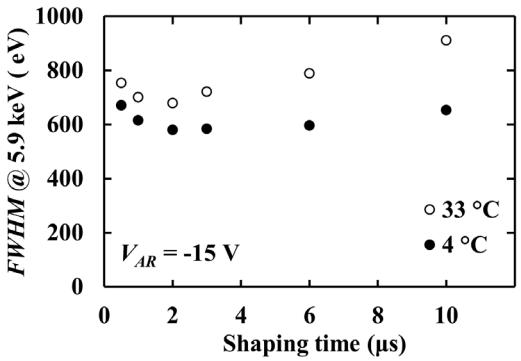

Figure 7.23. *FWHM* at 5.9 keV at 4 °C (filled circles) and 33 °C (empty circles) as a function of shaping time at -15 V reverse bias for the 200 μm GaAs p^+-i-n^+ mesa photodiode D1.

A multidimensional unconstrained nonlinear minimization was applied to the *FWHM* as a function of shaping time (**Figure 7.23**) for both temperatures and the fitting can be seen in **Figure 7.24**.

The equivalent total capacitance and leakage current of the system were estimated from the $1/\tau$ and τ proportional contributions respectively. A total input capacitance including the detector capacitance, C_{det}, the feedback capacitance, C_f, the stray capacitance, C_s and the input JFET capacitance, C_i, of 3.90 pF and 4.12 pF was estimated for 4 °C and 33 °C respectively. This capacitance was attributed to the capacitance C_{det} of the packaged detector at -15 V reverse bias, which was measured to be 1.13 pF and 1.35 pF at 4 °C and 33 °C respectively, to the capacitance C_i of the input JFET of the preamplifier (2 pF (Siliconix, 2001)), to the feedback capacitance C_f of the preamplifier and to the stray capacitance, C_s. A total noisy leakage current (see **Section 3.4.3**), including twice the contribution of the detector leakage current, I_{LD}, and the input JFET drain to gate leakage current, I_{DG}, (i.e. $2(I_{LD} + I_{DG})$), of 13.35 pA and 44.07 pA was estimated for 4 °C and 33 °C respectively. Hence, the measured *FWHM* as a function of shaping time suggests that the sum of detector and input JFET leakage current was 6.67 pA and 22.03 pA at 4 °C and 33 °C respectively. The input JFET drain to gate leakage current is regarded

negligible (< 1 pA) at the investigated temperatures, and thus the contributed leakage current was attributed to the detector being reverse biased at -15 V.

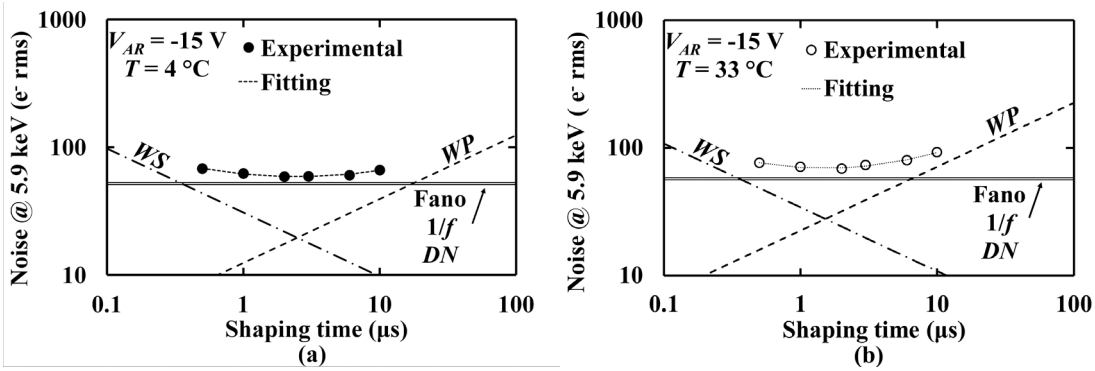

Figure 7.24. Equivalent noise charge at (a) 4 °C and (b) 33 °C as a function of shaping time. The three noise contributions, inversely proportional to shaping time (white series), directly proportional to shaping time (white parallel) and shaping time invariant (Fano, 1/*f* and dielectric) have been determined with a multidimensional least squares fitting of the experimental points.

The shaping time invariant noise contribution, consisting the Fano, 1/*f* and dielectric noise was estimated to be 512 eV and 565 eV at 4 °C and 33 °C respectively. Subtracting in quadrature the calculated Fano noise at 5.9 keV and 1/*f* noise from the total shaping time invariant noise contribution, the dielectric noise of the system can be calculated. It was found to be 495 eV (corresponding to 50 e^- rms equivalent noise charge contribution) and 550 eV (corresponding to 56 e^- rms equivalent noise charge contribution) at 4 °C and 33 °C respectively. The dielectric noise, attributed to lossy dielectrics at the input of the preamplifier, such as the feedback capacitance, the passivation of the input JFET surface as well as the detector itself and the packaging of the detector and input JFET, was found to be the dominant source of noise at all investigated shaping times and both temperatures, at -15 V reverse bias except at long shaping times at 33 °C. At shaping times > 6 μs, the leakage current of the detector being reverse biased at -15 V and operating at 33 °C was found to give rise to the most significant noise contribution, the parallel white noise. The increase of the dielectric noise at 33 °C compared to 4 °C is in accordance with the expected change in dielectric noise considering its relationship with the temperature and the capacitance (Equation 3.14). Overall, the degradation of the energy resolution at 33 °C compared to 4 °C was attributed to both the leakage current and dielectric noise increase.

7.6.4 Energy calibration of the system

The 200 μm GaAs p^+-i-n^+ mesa photodiode, D1, was connected to the input of the same custom-made, single-channel charge sensitive preamplifier used for the obtained spectra of an ^{55}Fe radioisotope X-ray source (**Section 7.6.3**). The photodiode along with the preamplifier were housed in a metal box which had a 4 μm thick Al foil window. The preamplifier housing was installed within an LD Didactic GmbH X-ray apparatus (part number 554 801) with a Mo target X-ray tube. A custom-made Al collimator with internal PTFE was collimating X-rays from the Mo target X-ray tube. The preamplifier and the photodiode were attached to the goniometer of the apparatus for precise positioning. The output of the preamplifier was connected to an Ortec 572A shaping amplifier. The output of the shaping amplifier was then connected to an Ortec EASYMCA multi-channel analyser (MCA) for digitisation.

The energy-charge response linearity of the system was performed using high purity metal X-ray fluorescence calibration targets of known composition. A total of 9 metal targets were positioned in turn on the sample stand. **Table 7.2** shows the 9 metal targets used along with their primary line energy.

Material (Primary line)	**Line Energy (keV)**
V (Kα)	4.95
Cr (Kα)	5.41
Mn (Kα)	5.89
Cu (Kα)	8.04
Zn (Kα)	8.63
Au (Lα)	9.71
Ge (Kα)	9.88
Au (Lβ)	11.44
Nb (Kα)	16.61
Pd (Kα)	21.17

Table 7.2. Fluorescence calibration samples used in this work with the corresponding X-ray emission line energies (Thompson et al., 2009).

The calibration samples and the detector were positioned 45 ° and 135 ° to the collimator, respectively. A diagram of the experimental set up can be seen in **Figure 7.25**. A spectrum from each target was accumulated for 3 hours. The X-ray tube voltage and current was set to 35 kV

and 1 mA respectively. The X-ray tube was powered for 3 hours prior to any measurements in order for the temperature of the system to stabilize at 33 °C. The detector was reverse biased at -15 V throughout the measurements and the shaping time of the shaping amplifier was set to 1 μs.

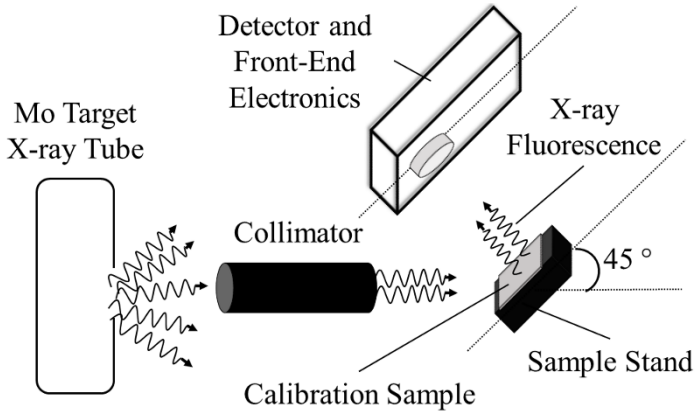

Figure 7.25. Diagram shown the experimental set up of the energy-charge response linearity characterisation of the spectrometer.

Gaussians were fitted to the peaks of each accumulated spectra. The centroid channel number of each fitted peak from each fluorescence calibration sample along with the accepted energies of those peaks were used to energy calibrate the system. The plot of the MCA channel number as a function of energy can be seen in **Figure 7.26**. The charge outputs had a linear relationship with photon energy, and the line of best fit was calculated using linear least squares fitting.

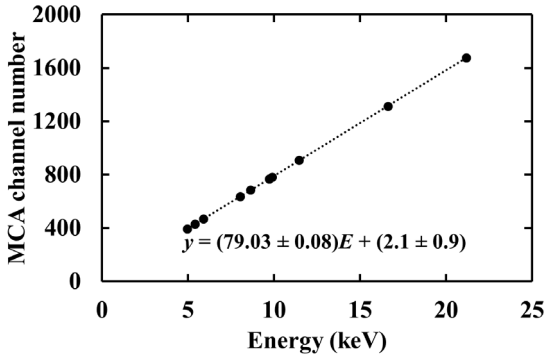

Figure 7.26. Centroid MCA channel number as a function of energy for the 200 μm GaAs p^+-i-n^+ mesa photodiode, D1. The line of best fit, as calculated using linear least squares fitting, can also be seen.

The energy resolution (*FWHM*) of each fitted photopeak was measured and can be seen in **Figure 7.27**. It was found to increase from 695 eV at 4.95 keV to 735 eV at 21.17 keV. The *FWHM* was attributed to the Fano noise and to the electronic noise, since it was found that the contribution of the incomplete charge collection noise was insignificant for these devices even at -5 V reverse

bias (**Section 7.4**). Electronic noise was expected to be energy invariant. However, the Fano noise was expected to increase with increasing photon energy (Equation 2.5); it was calculated to increase from 117 eV at 4.95 keV to 242 eV at 21.17 keV, assuming an electron hole pair creation energy of 4.184 eV (Bertuccio & Maiocchi, 2002) and a Fano factor of 0.12 (Bertuccio et al., 1997). The electronic noise was calculated by subtracting the Fano noise at each energy from the total measured *FWHM*. It was found to be energy invariant with a mean of 680 eV ± 30 eV. Its rms deviance was attributed to the error in fitting the photopeaks (±10 eV) and to possible leakage current instabilities of the detector throughout the measurements resulting in variations of the white parallel noise contribution. The predicted *FWHM* can also be seen in **Figure 7.27**. It was calculated assuming that the total *FWHM* comprised the electronic noise (= 680 eV) and the Fano noise calculated at each energy, and it was in good agreement with the measured *FWHM*.

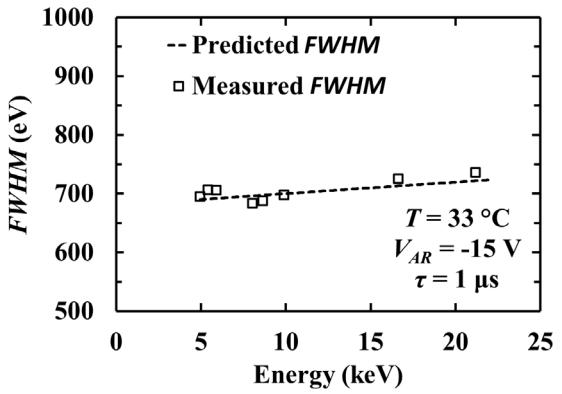

Figure 7.27. *FWHM* across the measured energy range. The Au Lα and Lβ peaks were excluded from this graph due to difficulty of deconvolving them.

7.6.5 Detector linearity with X-ray intensity

The X-ray flux for the energy calibration of the system was kept at its maximum by setting the X-ray tube current at 1 mA. In this section, the linearity of the photodiode detector response with varied X-ray intensity was investigated. This was achieved by measuring the detected count rate (counts per second) as a function of X-ray tube current. The same spectrum accumulation procedure was followed as it was for the energy calibration of the system, for two fluorescence calibration samples, Zn (Kα at 8.63 keV) and Nb (Kα at 16.6 keV). The only difference was that the X-ray tube current was varied from 0.2 mA to 1 mA with a 0.2 mA step. The count rate (counts per second) at each Kα peak, at both 8.63 keV and 16.6 keV, was determined as a function of X-ray tube current, and can be seen in **Figure 7.28**. In order to remove any non-linearity of the X-ray tube's output, a commercial LD Didactic GmbH Si p^+-i-n^+ photodiode detector (part number 559 938) was also used, and suggested a linear output of the X-ray tube with X-ray tube current.

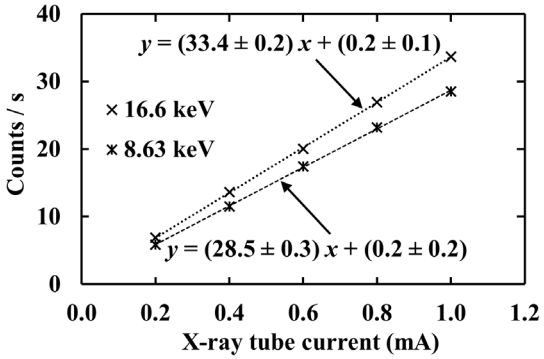

Figure 7.28. Count rate at Nb Kα peak (16.6 keV) (× symbols) and Zn Kα peak (8.63 keV) (stars) as a function of X-ray tube current using the present 200 μm GaAs p^+-i-n^+ mesa photodiode. The lines of best fit, as calculated using linear least squares fitting, can also be seen.

A linear relationship was found for the 200 μm GaAs p^+-i-n^+ mesa photodiode response with varying X-ray tube current. The line of best fit was calculated using linear least squares fitting and can be seen in **Figure 7.28**.

7.6.6 Elemental analysis of deep seabed minerals

A circular mesa GaAs p^+-i-n^+ photodiode for photon counting X-ray spectroscopy of 200 μm diameter having an i layer thickness of 10 μm have been characterised over the energy range 4.95 keV to 21.17 keV at 33 °C. The charge outputs as function of input photon energy was found to be linear. Also, its response as a function of X-ray flux was found to be linear. The spectra of two different samples (a manganese nodule and a black smoker) were obtained for elemental analysis.

The procedure followed for obtaining spectra of the samples was the same as for the calibration targets. Each sample was placed inside the LD Didactic GmbH X-ray apparatus on the sample stand. The sample stand and the detector were positioned 45 ° and 135 ° to the collimator, respectively. The temperature in the proximity of the X-ray tube was 33 °C. The detector was reverse biased at -15 V throughout the measurements and the shaping time of the shaping amplifier was set to 1 μs. Each spectrum was accumulated for 8 hours. The background spectrum was also accumulated for the same period of time and subtracted from the obtained spectra. The resulting spectra for the manganese nodule and the black smoker can be seen in **Figure 7.29** and **Figure 7.30** respectively.

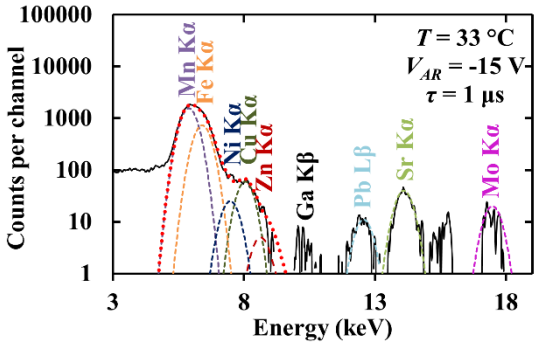

Figure 7.29. Accumulated XRF spectrum of a manganese nodule using the 200 µm GaAs p^+-i-n^+ mesa photodiode, D1. The fitted Mn Kα (purple), Fe Kα (orange), Ni Kα (blue), Cu Kα (green), Zn Kα (dark red), Pb Lβ (light blue), Sr Kα (light green), and Mo Kα (pink) can be seen. The red dotted line corresponds to the sum of Mn, Fe, Ni, Cu and Zn Kα and Kβ peaks.

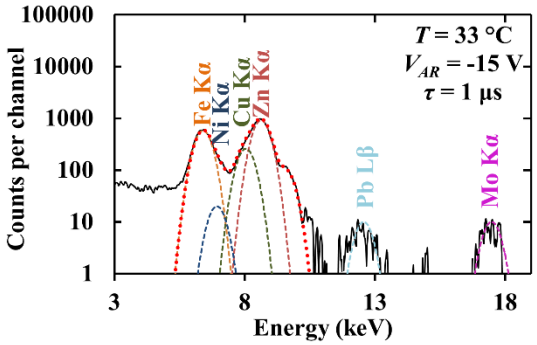

Figure 7.30. Accumulated XRF spectrum of a black smoker using the 200 µm GaAs p^+-i-n^+ mesa photodiode, D1. The fitted Fe Kα (orange), Ni Kα (blue), Cu Kα (green), Zn Kα (dark red), Pb Lβ (light blue), and Mo Kα (pink) can be seen. The red dotted line corresponds to the sum of Fe, Ni, Cu and Zn Kα and Kβ peaks.

For each spectrum, the energy of the main photopeaks was found and the elements of the deep seabed minerals were identified. This was achieved with the aid of the energy calibration equation found for this system. The elements being present in each sample were identified by the energies of their X-ray emission lines (Thompson et al., 2009). The predicted *FWHM* defined previously was used to fit the main photopeaks of each spectrum. A multi-peak fit, for peaks not being able to be resolved, was achieved adjusting the height of the emission lines of the potential elements using the energies of their X-ray emission lines (Thompson et al., 2009), the predicted *FWHM* of the system at each energy and the relative emission ratio (Sánchez del Rio et al., 2003) and the relative efficiency of the detector for their Kα and the Kβ peaks.

The major and trace elements found in the manganese nodule was Mn, Fe, Ni, Cu, Zn, Pb, Sr, and Mo (**Figure 7.29**). This is in agreement with the elements found in previously reported elemental

analysis of polymetallic nodules from the Central Indian Basin (Puri et al., 1998). Also, manganese nodules from the Clarion-Clipperton Fracture Zone region were previously found to be enriched in Mn, Fe, Ni, Cu, Zn, Pb, and Mo (Glasby, 2006). Although the tops of these nodules were also found to consist Co (Kα at 6.9 keV (Thompson et al., 2009)) at an average composition of 0.23 %, such a finding cannot be concluded for the presently reported manganese nodule.

The major elements identified in the black smoker were Fe, Ni, Cu, Zn, Pb, and Mo (**Figure 7.30**). The most commonly observed minerals in previously studied black smokers were Fe, Cu, and Zn sulphides (Von Damm, 1990). Mineralogical studies of sulfide chimneys from the Central Indian Ridge (north of the Rodriguez Triple Junction), Indian Ocean, showed a high cumulative Cu, Fe and Zn concentrations close to 50-60 wt. % (Münch et al., 1999). They also showed high Co (Kα at 6.9 keV (Thompson et al., 2009)), Mo, and As (Kα at 10.5 keV (Thompson et al., 2009)) contents.

The reported spectrometer, including a prototype GaAs p^+-i-n^+ mesa X-ray photodiode and a custom-made charge sensitive preamplifier, has been demonstrated as an X-ray spectrometer in the laboratory environment at 33 °C with a potential application in elemental analysis of deep seabed minerals. The density and effective atomic number of GaAs directly affects the intrinsic quantum detection efficiency and hence, the accumulation time, over the X-ray energy range of interest (1 keV to 20 keV). Thus, the choice of GaAs as the detector material results in minimised accumulation time compared to when a material with lower density and atomic number, such as Si, is used as the detector material. Additionally, the high temperature tolerance of a spectrometer employing a GaAs p^+-i-n^+ photodiode detector (see **Section 1.5**) may be advantageous for such an application, where the detector might be required to operate at temperatures higher than the ambient seawater temperature (> 4 °C) in the vicinity of active hydrothermal vents. Although the identification of major elements in the deep seabed minerals achieved with the currently reported spectrometer, having an energy resolution (*FWHM* at 5.9 keV) of 700 eV at 33 °C (1 μs), for minor and trace elements identification, a better energy resolution is required. An improvement of the energy resolution of the system is expected when operating at 4 °C (temperature of the ambient seawater) at the optimum shaping time (2 μs) compared to 33 °C. The energy resolution (*FWHM*) of the spectrometer at 5.9 keV was found to improve by 390 eV, reaching a value of 580 eV at 4 °C (2 μs) (see **Section 7.6.3**). The dielectric noise was found to be the dominant source of noise at 4 °C (see **Section 7.6.3**). An improved design of the preamplifier's front-end and the elimination of the packaging of both the detector and the input JFET would lead to better energy resolution compared to the currently reported spectrometer.

7.7 Conclusion

A total of 22 randomly selected GaAs p^+-i-n^+ mesa X-ray photodiodes have been electrically characterised at room temperature with two representative diodes being further characterised as detectors for photon counting X-ray spectroscopy and one of the diodes for β^- particle counting spectroscopy and elemental analysis of deep seabed minerals with X-ray fluorescence spectroscopy. The devices had a 10 μm thick i layer. There were 14 diodes with 200 μm diameters and 8 diodes with 400 μm diameters.

The ideality factor, which was found to vary from 1.89 to 1.99 among different devices with a mean of 1.95 ± 0.02, indicated that the recombination current defined the forward current. Low leakage current densities were measured for all devices at room temperature, at an applied electric field of 50 kV/cm: it was found to vary from 4 nA/cm^2 to 67 nA/cm^2 among all diodes (both 200 μm and 400 μm diameter devices) with a mean of 30 nA/cm^2 ± 20 nA/cm^2. The 400 μm diameter devices showed lower leakage current densities than the 200 μm diameter devices at 50 kV/cm, suggesting that the surface leakage current was not negligible, possibly due to the devices being unpassivated.

The i layer thickness and doping concentration of the devices were deduced from capacitance measurements. All the diodes were almost fully depleted at 0 V. The depletion width of the 400 μm diameter devices was found to increase from 9.9 μm ± 0.2 μm at 0 V to 10.6 μm ± 0.2 μm at -50 V reverse bias. The depletion width the 200 μm diameter devices was determined to be 10 μm ± 1 μm at 0 V and 11 μm ± 1 μm at -50 V reverse bias. The minimum unintentional doping density of the i layer, at the minimum distance below the p^+-i junction, was found to be 2.8×10^{14} cm^{-3} ± 0.9×10^{14} cm^{-3} for the 400 μm diameter devices and 0.8×10^{14} cm^{-3} ± 0.4×10^{14} cm^{-3} for the 200 μm diameter devices.

Results demonstrating the devices' performance as room temperature X-ray spectrometers with an ^{55}Fe radioisotope X-ray source were reported for the 200 μm diameter GaAs p^+-i-n^+ mesa photodiode, D1 and the 400 μm diameter GaAs p^+-i-n^+ mesa photodiode, D2, as functions of applied reverse bias at 10 μs shaping time. The best energy resolution (*FWHM* at 5.9 keV) was achieved at -5 V reverse bias for both the 200 μm and a 400 μm diameter devices. The *FWHM* was found to increase from 625 eV at -5 V reverse bias to 665 eV at -30 V reverse bias for the 200 μm diameter detector. Similarly, the *FWHM* of the 5.9 keV peak was found to increase from 740 eV at -5 V reverse bias to 780 eV at -30 V reverse bias for the 400 μm diameter detector. Noise analysis showed that the dominant source of noise of the currently reported system was the dielectric noise. It was calculated to be 590 eV ± 20 eV and 710 eV ± 20 eV when the 200 μm and the 400 μm diameter GaAs p^+-i-n^+ mesa photodiode, respectively, were used. The ^{55}Fe X-ray

spectra obtained with the two different diameters GaAs p^+-i-n^+ mesa photodiodes enabled the determination of the apparent dissipation factor of GaAs, assuming only the contribution of the detector to the dielectric noise was different between the 200 μm diameter device-preamplifier system and the 400 μm diameter device-preamplifier system; a value of 4×10^{-3} at room temperature was determined.

A ^{63}Ni (endpoint energy = 66 keV) β^- spectrum was obtained with the 200 μm diameter GaAs p^+-i-n^+ mesa photodiode, D1, to characterise the GaAs photodiodes as electron detectors. An internal quantum detection efficiency, $QE_{internal}$, of 77 % at 66 keV was calculated for the reported detector. The accumulated spectrum had an apparent endpoint energy of 50 keV which suggested that 75 % of the 66 keV particle energy was deposited at the active i layer. CASINO simulations showed that the layers between the active ^{63}Ni and detector (i.e. inactive Nickel overlayer of the ^{63}Ni radioisotope β^- particle source and 5 mm of air) and the inactive layers at the front of the detector (annular Ti/Au contact and p^+ layer) limited the total energy being deposited at the active layer of the device. Simulations showed that β^- particles with an energy of 25 keV impinging on the optical window of the detector (28 keV when impinging on the top Ohmic contact) were all absorbed before reaching the active i layer. Also, a percentage of β^- particles with an energy higher than 60 keV was absorbed in the n^+ layer/substrate. CASINO simulations at the endpoint energy of the ^{63}Ni radioisotope β^- particle source revealed that the detected energy of 66 keV β^- particles can range from 0 keV to 60 keV, depending on their track. Although the GaAs devices reported here were not specifically designed for β^- or electron spectroscopy, it can be concluded that they can be used for counting β^- particles (electrons) and measuring the total energy being deposited in their active region.

The 200 μm diameter GaAs p^+-i-n^+ mesa X-ray photodiode, D1, has been studied for its suitability for in situ elemental analysis of deep seabed minerals using XRF. Initially, the photodiode detector was electrically characterised at 4 °C. Due to the temperature, 33 °C, set by the Mo target X-ray tube used to excite the X-ray fluorescence calibration samples and the deep seabed minerals, electrical characterisation at this elevated temperature was also included. An increase of the saturation current from 0.046 pA ± 0.007 pA at 4 °C to 0.72 pA ± 0.06 pA at 33 °C was measured. Also, a deterioration of the ideality factor from 1.84 ± 0.02 at 4 °C to 1.96 ± 0.01 at 33 °C was identified and was attributed to more thermally stimulated crystal lattice defects at 33 °C compared to 4 °C, being the main cause of the non-ideal behaviour of the device. A leakage current increase from 0.4 pA (1.2 nA/cm^2) at 4 °C to 9.9 pA (31.6 nA/cm^2) at 33 °C, both at the highest investigated reverse bias, -50 V (~ 50 kV/cm internal electric field) was also measured. The leakage current was found to increase from 5.8 pA (corresponding to 8 e- rms) to 15 pA

(corresponding to 13 e- rms) after 2.5 hours and remained stable thereinafter, when reverse biased at -15 V and operating at 33 °C.

Capacitance measurements showed that although the forward biased junction capacitance, contributed by the diffusion capacitance, was temperature dependent, increasing from 2.58 pF at 4 °C to 3.27 pF at 33 °C at 1 V forward bias, the depletion layer capacitance was temperature invariant for reverse biases greater than -3 V, at the investigated temperatures within the measurement error. The depletion layer was determined to be 9.8 μm ± 0.8 μm and 9.5 μm ± 0.7 μm at 4 °C and 33 °C respectively, at -50 V reverse bias. However, the depletion layer capacitance was found to be temperature dependent at low reverse applied biases ($|V_{AR}| < 3$ V). This was explained with a presence of a thin region around the depletion region with non-ionised dopants at 4 °C which were ionised at 33 °C and limited the extension of the depletion layer at low reverse biases. The effective doping concentration of the i layer was determined to increase from 0.2×10^{14} cm^{-3} at 9.2 μm ± 0.7 μm below the p^+-i junction to 43×10^{14} cm^{-3} at the i-n^+ interface at 4 °C. Similarly, the effective doping concentration was found to increase from 1×10^{14} cm^{-3} at 8.5 μm ± 0.5 μm below the p^+-i junction to 86×10^{14} cm^{-3} at the i-n^+ interface at 33 °C.

The noise analysis of the system was performed at 4 °C and the effects of increasing the temperature at 33 °C was investigated. These were achieved with ^{55}Fe spectra obtained at both temperatures as functions of shaping time. The optimum shaping time at -15 V reverse bias was found to be 2 μs and a broadening of the 5.9 keV peak, quantified by the *FWHM*, from 580 eV at 4 °C to 680 eV at 33 °C was recorded. This was attributed to the leakage current and dielectric noise increase at 33 °C. The measured *FWHM* as a function of shaping time at 4 °C suggested the presence of 3.90 pF total capacitance and 13.35 pA total leakage current at the input of the preamplifier with additionally 50 e^- rms equivalent noise charge contribution of the dielectric noise. Similarly, the measured *FWHM* as a function of shaping time at 33 °C suggested the presence of 4.12 pF total capacitance and 44.07 pA total leakage current at the input of the preamplifier with additionally 56 e^- rms equivalent noise charge contribution of the dielectric noise.

The 200 μm GaAs p^+-i-n^+ mesa photodiode, D1, was then characterised over the energy range 4.95 keV to 21.17 keV at 33 °C. Initially, 9 known fluorescence calibration targets were used to energy calibrate the system. A Mo target X-ray tube was used for exciting the samples. The plot of the MCA channel number as a function of energy showed that the charge outputs had a linear relationship with photon energy. The line of best fit was calculated using linear least squares fitting. The *FWMH* of each photopeak of all calibration targets was measured. It was found to increase from 695 eV at 4.95 keV to 735 eV at 21.17 keV. The increase of the *FWHM* with

increased energy was attributed to the increase of the Fano noise from 117 eV at 4.95 keV to 242 eV at 21.17 keV. The electronic noise was found to be energy invariant having a mean value of 680 eV ± 30 eV over the measured energy range. Additionally, the relationship of the photodiode response was investigated as a function of varied X-ray intensity using two fluorescence calibration samples, Zn (Kα at 8.63 keV) and Nb (Kα at 16.6 keV), and found to be linear.

Two different deep seabed minerals, a manganese nodule from the Pacific Ocean and a black smoker from the Indian Ocean, were analysed for their elemental composition using the same Mo target X-ray tube and the 200 μm GaAs p^+-i-n^+ mesa photodiode, D1. The energy of the main photopeaks of the obtained spectra was calculated using the energy calibration of the system. Gaussian peaks were fitted to each photopeak using the predicted *FWHM* of the reported system at each energy. It was found that the manganese nodule consisted of Mn, Fe, Ni, Cu, Zn, Pb, Sr, and Mo. The black smoker was found to consist of Fe, Ni, Cu, Zn, Pb, and Mo. All are in agreement with previous studies of manganese nodules (Puri et al., 1998) (Glasby, 2006) and black smokers (Von Damm, 1990) (Münch et al., 1999).

The use of a GaAs p^+-i-n^+ mesa photodiode for elemental analysis of deep seabed minerals using XRF spectroscopy has been demonstrated in the laboratory environment at 33 °C. The XRF spectrometer can potentially provide insight into hydrothermal processes and revolutionize the seabed mining activities with in situ characterisation of the seabed minerals. Another potential application of the reported GaAs XRF spectrometer could be for future space missions to icy moons, such as Europa, and the exploration of their oceans.

Chapter 8 Conclusions and Future Work

8.1 Conclusions

4H-SiC and GaAs photodiode detectors have been investigated for their suitability as radiation detectors for harsh environment (high temperature and intense radiation) applications.

4H-SiC Schottky UV photodiode detectors (D1 to D4) with Ni_2Si interdigitated contacts were characterised for their response under UV illumination. The measurements conducted included dark current and capacitance measurements as functions of applied bias at temperatures from 20 °C to 120 °C as well as UV responsivity measurements as functions of wavelength at biases from 0 V to -15 V at room temperature. The electrical characterisation was completed with calculations of key parameters of the devices and the UV responsivity measurements were supported by calculated expected responsivity.

The ideality factor improvement and the zero band barrier height increase as the temperature increased from 20 °C to 120 °C suggested the presence of an inhomogeneous barrier. The high quality of the 4H-SiC epitaxial layer and the high barrier height of the Ni_2Si/4H-SiC Schottky contact was believed to result in the measured low leakage current densities, which were comparable with the lowest leakage current densities reported for 4H-SiC Schottky diodes. At the highest investigated temperature (120 °C) and applied reverse bias (-50 V, corresponding to an internal electric field of 83 kV/cm), the leakage current densities of D1, D2, D3, and D4 were measured to be 8.2 nA/cm^2, 8.3 nA/cm^2, 8.3 nA/cm^2 and 8.9 nA/cm^2, respectively. The better photoresponsivity, and equally the higher internal quantum detection efficiency, under UV illumination of the 4H-SiC Schottky UV photodiodes reported here compared to previously reported 4H-SiC UV Schottky diodes employing thin metal Schottky contacts was attributed to the interdigitated Schottky contacts. A peak UV photoresponsivity (at 270 nm) of 0.080 A/W, 0.100 A/W, 0.098 A/W, and 0.094 A/W was measured at room temperature and at -15 V reverse bias for D1, D2, D3, and D4, respectively. Comparisons of the measured UV photoresponsivity with the calculated expected photoresponsivity suggested trapping and charge loss at low internal electric fields which were improved with increased applied reverse bias. The low dark currents of the 4H-SiC Schottky diodes and the Ni_2Si interdigitated contacts, both resulting in almost four orders of magnitude UV photocurrent-to-dark current contrast (despite the relatively low illumination intensity used for the UV responsivity measurements), along with the inherent properties of 4H-SiC and the Schottky structure, resulting in high visible blindness (at least 10^{-3}), suggested that the reported devices could operate even at low UV light intensities and at high visible and IR backgrounds without the use of filters.

4H-SiC Schottky diode arrays were characterised for their high temperature X-ray spectral properties. Five 4H-SiC Schottky diodes (D1 to D5) with thin NiSi Schottky contacts, to improve the internal quantum detection efficiency, were in a combined 2 × 2 and 1 × 3 pixel configuration. Although the 4H-SiC Schottky diodes showed unexpected high leakage current at room temperature, double barrier heights and high ideality factors, they operated as detectors for photon counting X-ray spectroscopy at 33 °C, with modest energy resolution. The diodes were reverse biased at -60 V and the measured energy resolution (*FWHM* at 17.4 keV) achievable with each diode ranged from 1.36 keV (D4) to 1.68 keV (D1), at 33 °C and 1 μs shaping time. These results are not as good as the best experimental reports on single pixel 4H-SiC X-ray detectors (196 eV *FWHM* at 5.9 keV at 30 °C (Bertuccio et al., 2011)). However, the majority of the noise present in the 4H-SiC X-ray spectrometer reported here appeared to be from the non-optimised preamplifier input (dielectrics around the input of the preamplifier) giving rise to dielectric noise. The electrical characterisation over the temperature range 20 °C to 140 °C showed a slight increase in leakage current, as the temperature increased from 20 °C to 80 °C, and in capacitance as the temperature increased from 20 °C to 140 °C, which suggested that the presented 4H-SiC Schottky diodes are likely to operate well at high temperatures.

GaAs mesa p^+-i-n^+ X-ray photodiodes (D1 and D2) with 7 μm i layers and 200 μm diameters have also been investigated. At the maximum applied reverse bias (-15 V, corresponding to an internal electric field of 22 kV/cm), the leakage current densities of D1 and D2 were measured to be 17.4 nA/cm^2 and 1.08 nA/cm^2 at room temperature, increasing to 24.36 μA/cm^2 and 9.39 μA/cm^2 at 120 °C, respectively. These values, which resulted from generation for temperatures < 100 °C and from diffusion for temperatures ≥ 100 °C, were comparable with other high quality GaAs p^+-i-n^+ photodiodes (Bertuccio et al., 2003). The presence of a dead layer at the face of the devices with a thickness of 0.16 μm, in which the generated carriers from photon absorption did not contribute to the photocurrent, was deduced from visible and near infrared responsivity measurements at room temperature. The X-ray spectrometer, including one GaAs mesa p^+-i-n^+ photodiode with a 7 μm i layer and a custom-made charge sensitive preamplifier, had an energy resolution (*FWHM* at 5.9 keV) of 730 eV, at 0 °C, which increased to 840 eV at 60 °C. The dielectric noise was found to be the dominant source of noise of the X-ray spectrometer apart from the spectra obtained at 60 °C (and $|V_{AR}| > 0$ V, $\tau > 5$ μs), where the parallel white noise dominated. Although the energy resolution of the GaAs (7 μm i layer thick) X-ray spectrometer was better than previously reported thinner mesa X-ray photodiodes, the energy resolution could be further improved, towards the best reported results for GaAs photodiodes (300 eV by Erd et al. (2002) and 266 eV by Owens et al. (2001)), by some modifications. The elimination of the detector's and input JFET's packaging, and the integration of both on the same wafer is believed

to reduce the dielectric noise. A *FWHM* at 5.9 keV of 276 eV was estimated if the dielectric noise could be eliminated.

GaAs mesa p^+-i-n^+ photodiodes of similar design and thicker i layers (10 μm) have been characterised to investigate the performance improvements compared to thinner devices. A total of 22 devices, having diameters of 200 μm and 400 μm, were electrically characterised at room temperature. Dark current measurements showed that the generation-recombination current dominated, and they revealed the significant contribution of the surface leakage component, which may be reduced in future with surface passivation. An improvement of the *FWHM* at 5.9 keV of the X-ray spectrometer employing a 10 μm i layer thick GaAs mesa p^+-i-n^+ photodiode (625 eV, at room temperature) compared to the X-ray spectrometer employing a 7 μm i layer thick GaAs mesa p^+-i-n^+ photodiode (745 eV, at room temperature) was recorded, which was attributed to the lower capacitance of the 10 μm c.f. 7 μm i layer thick devices resulting in less *WS*, 1/*f*, and dielectric noise contributions.

One 10 μm i layer GaAs mesa p^+-i-n^+ photodiode has also been investigated for its suitability in β^- particle (electron) spectroscopy. Although the GaAs device was not specifically designed for β^- or electron spectroscopy, it was concluded that it can be used for counting β^- particles (electrons) and measuring the total energy from each particle deposited in its active region. The reported electron spectrometer had an internal quantum detection efficiency of 77 % at 66 keV. The accumulated ^{63}Ni β^- spectrum (endpoint energy = 66 keV) had an apparent endpoint energy of 50 keV which was attributed to the absorption of electrons (β^- particles) in the dead layers of the measurement system (Ni overlayer, air, Ti/Au contacts, p^+ layer, n^+ layer, and substrate), based on CASINO simulations. One potential application of such an electron spectrometer is in situ low energy (1 keV to 100 keV) electron spectroscopy at Europa towards verification of the auroral observations (Roth et al., 2014) (Sparks et al., 2016) being due to electron impact excitation of water vapor plumes. The use of GaAs detector in such an application would accommodate the requirement of radiation hard electronics in intense radiation environments, such as Europa. A reduced thickness of the p^+ layer (~ 0 μm) and an increased thickness of the active i layer (~30 μm) would increase the intrinsic internal quantum detection efficiency of the detector within the electron energy of interest (1 keV to 100 keV).

Preliminary work towards the development of an X-ray spectrometer for in situ analysis of deep seabed minerals was reported. The same 10 μm i layer GaAs mesa p^+-i-n^+ photodiode detector was characterised at temperatures of 4 °C (the ambient temperature of deep ocean water) and 33 °C. The GaAs X-ray fluorescence spectrometer had a *FWHM* at 5.9 keV of 580 eV, at 4 °C. It was found that the charge output of the X-ray spectrometer had a linear relationship with photon

energy over the energy range of 4.95 keV to 21.17 keV and that the response of the X-ray spectrometer (counts per second) had a linear relationship with X-ray intensity. Using the prototype spectrometer, X-ray fluorescence analysis of two deep seabed minerals (manganese nodule and black smoker) at 33 °C revealed the presence of Mn, Fe, Ni, Cu, Zn, Pb, Sr, and Mo, in the manganese nodule, and of Fe, Ni, Cu, Zn, Pb, and Mo, in the black smoker. The GaAs X-ray spectrometer had an energy resolution (*FWHM* at 5.9 keV) of 680 eV, at this elevated temperature (33 °C). The main source of noise was found to be the dielectric noise, and again, a reduction of the dielectric noise, believed to be achievable through the elimination of the detector's and input JFET's discrete packaging, and the integration of both on the same wafer, could further improve the energy resolution of the GaAs X-ray fluorescence spectrometer. In situ characterisation of deep seabed minerals with XRF, potentially advancing ocean mining activities, could be benefit from the use of a wide bandgap detector, such as GaAs, which can potentially withstand the high temperatures encountered at seafloor hydrothermal systems.

The work presented in this thesis, including extensive characterisation of the devices at different operating conditions (bias, temperature, and illumination), supported calculations, and accompanied comparisons of the results with previous published reports, advances the state of the art for 4H-SiC and GaAs photodiode radiation detectors for harsh environment applications. The results showed that both wide bandgap semiconductor materials are good candidates for high temperature and intense radiation environment applications (both extra-terrestrial and terrestrial) with restrictions in mass, volume, power consumption, and cost. Such applications include future space missions to high temperature (> 20 °C) environments (such as 482 °C at the surface of Venus (Kolawa et al., 2007)) and to intense radiation environments (such as Jupiter and the Galilean moons (Atzei et al., 2007) where doses as high as 6 MRad may be encountered). X-ray fluorescence spectroscopy for elemental analysis of deep seabed minerals may also be benefit from the use of wide bandgap semiconductor radiation detectors.

It should be noted that the selection of the most appropriate semiconductor detector (semiconductor material, type of detector, growth and fabrication techniques) for each application differs, and it is driven from the application's requirements (temperature of operation, energy range of detection, energy resolution, quantum efficiency). As in other cases, trade-offs usually occur in the selection of the suitable detector. One trade-off, underlined in the thesis, is between a semiconductor material with wide bandgap to reduce the thermally generated carriers and a material with a small electron hole pair creation energy to increase the number of charge carriers generated per energy of the incoming photon. A leakage current density of 8.2 nA/cm^2 (at 83 kV/cm internal electric field, **Section 4.3.1**) and 9.39 μA/cm^2 (at 22 kV/cm internal electric field, **Section 6.6.1**) at 120 °C was measured with a 4H-SiC and GaAs device, respectively, with

the lower leakage current density of 4H-SiC device attributed to its wider bandgap compared to GaAs. However, the lower electron hole pair creation energy of GaAs compared to 4H-SiC resulted in better (lower) energy resolution of the X-ray spectrometer employing a GaAs detector (745 eV *FWHM* at 5.9 keV) compared to the X-ray spectrometer employing a 4H-SiC detector (1.36 keV *FWHM* at 17.4 keV), even though both spectrometers had similar equivalent noise charge (76 e^- rms in the GaAs spectrometer and 74 e^- rms in the 4H-SiC spectrometer). A direct consequence of the relationship between the electron hole pair creation energy and the energy resolution of the spectrometer (Equation 3.1) is the importance of low noise readout electronics for wide bandgap detectors due to the typically greater electron hole pair creation energies of wide bandgap materials compared to Si and narrow bandgap materials.

8.2 Future work

Along with the results and the discussions, possible further measurements were proposed, as were different potential improvements for each detector/spectrometer presented in the thesis, which all could be considered for future work.

The importance of the use of a wide bandgap (6H-SiC) input transistor for the preamplifier in reducing the electronic noise of the wide bandgap spectrometer, especially at high temperatures (> 20 °C), has been suggested based on analytical theory. The calculations of the noise arising from a 6H-SiC input JFET need to be confirmed by experimentally determined values, at room and higher temperatures. This would allow verification/refutation of the predicted improvement that a wide bandgap input transistor would offer compared to a Si JFET. In addition to 6H-SiC JFETs, other wide bandgap JFETs, such as GaAs and GaN, should be investigated, both analytically and experimentally, for their performance as input JFET in a charge sensitive preamplifier to be used in X-ray and electron spectroscopy at high temperatures.

Thicker (> 6 μm) 4H-SiC UV Schottky diodes would result in increased UV photoresponsivity at the long wavelength range (280 nm to 380 nm) with the benefit of UV detection at low UV light intensities. To ensure operation at high temperatures and characterise the detectors' performance as high temperature UV detectors, the UV photoresponsivities of the existing 4H-SiC Schottky photodiodes should be investigated at temperatures up to 120 °C.

Studies on the growth and fabrication processes of the 4H-SiC Schottky arrays as well as the GaAs mesa p^+-i-n^+ photodiodes should be carried out to optimise these processes. Techniques to eliminate the presence of inhomogeneous barrier of the Schottky diodes, and to supress the peripheral leakage currents (such as passivation), which currently lead to non idealities, should also be investigated.

An immediate benefit would result from improving the energy resolution of the X-ray and electron spectrometers reported in this thesis. The dominant source of noise of the reported spectrometers, the dielectric noise, is believed to be supressed by redesigning the preamplifier's front-end and eliminating the discrete packaging of both the detector and the input JFET, ideally by integrating the JFET on the detector.

Although radiation hardness measurements have been previously reported for both 4H-SiC and GaAs with γ-rays, electrons, neutrons, protons, and α particles, characterisation of the radiation hardness of the reported wide bandgap photodiodes would be beneficial. Radiation hard measurements with the particles/photons, energy ranges, and fluxes of the specific radiation environments of the proposed applications (such as Europa) would be essential to verify the suitability of these wide bandgap materials to particular applications and accurately determine the likely lifetime of detector in such environments.

References

Abate, L., Bertolucci, E., Conti, M., Mettivier, G., Montesi, M.C., and Russo, P., 2001, *GaAs Pixel Arrays for β Imaging in Medicine and Biology*, Nuclear Instruments and Methods in Physics Research A, Vol. 460, pp. 97-106.

Abbey, A.F., Bennie, P.J., Turner, M.J.L., Altieri, B., and Rives, S., 2003, *Cooling out the Radiation Damage on the XMM-Newton EPIC MOS CCDs*, Nuclear Instruments and Methods in Physics Research A, Vol. 513, pp. 136-142.

Aberle, A.G., 2000, *Surface Passivation of Crystalline Silicon Solar Cells: A Review*, Progress in Photovoltaics: Research and Applications, Vol. 8, pp. 437-487.

Adamo, G., Agro, D., Stivala, S., Parisi, A., Curcio, L., Ando, A., Tomasino, A., Giaconia, C., Busacca, A.C., Mazzillo, M.C., Sanfilippo, D., and Fallica, G., 2014, *Responsivity Measurements of Silicon Carbide Schottky Photodiodes in the UV Range*, Proceedings of the IEEE Third Mediterranean Photonics Conference, 7-9 May, Italy.

Adler, I., Gerard, J., Trombka, J., Schmadebeck, R., Lowman, P., Blodget, H., Yin, L., Eller, E., Lamothe, R., and Gorenstein, P., 1972, *The Apollo 15 X-ray Fluorescence Experiment*, Lunar and Planetary Science Conference Proceedings, Vol. 3, p. 2157.

Adriani, O., Barbarino, G.C., Bazilevskaya, G.A., Bellotti, R., Boezio, M., Bogomolov, E.A., Bongi, M., Bonvicini, V., Borisov, S., Bottai, S., Bruno, A., Cafagna, F., Campana, D., Carbone, R., Carlson, P., Casolino, M., Castellini, G., Consiglio, L., De Pascale, M.P., De Santis, C., De Simone, N., Di Felice, V., Galper, A.M., Gillard, W., Grishantseva, L., Jerse, G., Karelin, A.V., Koldashov, S.V., Krutkov, S.Y., Kvashnin, A.N., Leonov, A., Malakhov, V., Malvezzi, V., Marcelli, L., Mayorov, A.G., Menn, W., Mikhailov, V.V., Mocchiutti, E., Monaco, A., Mori, N., Nikonov, N., Osteria, G., Palma, F., Papini, P., Pearce, M., Picozza, P., Pizzolotto, C., Ricci, M., Ricciarini, S.B., Rossetto, L., Sarkar, R., Simon, M., Sparvoli, R., Spillantini, P., Stochaj, S.J., Stockton, J.C., Stozhkov, Y.I., Vacchi, A., Vannuccini, E., Vasilyev, G., Voronov, S.A., Wu, J., Yurkin, Y.T., Zampa, G., Zampa, N., and Zverev, V.G., 2011, *Cosmic-Ray Electron Flux Measured by the PAMELA Experiment between 1 and 625 GeV*, Physical Review Letters, Vol. 106, Art. No. 201101.

Agarwal, B., Hu, P., Placidi, M., Santo, H., and Zhou, J.J., 2012, *Feasibility Study on Manganese Nodules Recovery in the Clarion-Clipperton Zone*, LRET Collegium 2012 Series, Vol. 2, University of Southampton, UK.

Ahmed, S.N., 2007, *Physics and Engineering of Radiation Detection*, Elsevier, UK.

Akimov, Yu.K., 2007, *Silicon Radiation Detectors (Review)*, Instruments and Experimental Techniques, Vol. 50, pp. 1-28.

Andrews, G.B., Zurbuchen, T.H., Mauk, B.H., Malcom, H., Fisk, L.A., Gloeckler, G., Ho, G.C., Kelley, J.S., Koehn, P.L., LeFevere, T.W., Livi, S.S., Lundgren, R.A., and Raines, J.M., 2007, *The Energetic Particle and Plasma Spectrometer Instrument on the MESSENGER Spacecraft*, Space Science Reviews, Vol. 131, pp. 523-556.

Angelo, J.A., 2007, *Spacecraft for Astronomy*, Infobase Publishing, New York, USA, p. 139.

Anon, *Broadband SiC based UV photodiode A = 0.50 mm², SG01D–18*, Rev. 6.0, SGlux SolGel Technologies GmbH, Berlin, Germany, N.D.

Anon, *Broadband SiC based UV photodiode A = 1.00 mm², SG01L–18*, Rev. 6.0, SGlux SolGel Technologies GmbH, Berlin, Germany, N.D.

Atzei, A., Wielders, A., Stankov, A., and Falkner, P., 2007, *Overview of the ESA Jovian Technology Reference Studies*, ESA/ESTEC Technical Note, Netherlands.

Auckloo, A., Cheong, J.S., Meng, X., Tan, C.H., Ng, J.S., Krysa, A., Tozer, R.C., and David, J.P.R., 2016, *$Al_{0.52}In_{0.48}P$ Avalanche Photodiodes for Soft X-ray Spectroscopy*, Journal of Instrumentation, Vol. 11, Art. No. P03021

Balaji, N., Hussain, S.Q., Park, C., Raja, J., Yi, J., and Jeyakumar, R., 2015, *Surface Passivation Schemes for High-Efficiency c-Si Solar Cells - A Review*, Transactions on Electrical and Electronic Materials, Vol. 16, pp. 227-233.

Ballabriga, R., Campbell, M., Heijne, E., Llopart, X., Tlustos, L., and Wong, W., 2011, *Medipix3: A 64 k Pixel Detector Readout Chip Working in Single Photon Counting Mode with Improved Spectrometric Performance*, Nuclear Instruments and Methods in Physics Research A, Vol. 633 Supplement 1, pp. S15-S18.

Bar-Lev, A., 1993, *Semiconductor and Electronic Devices*, 3rd ed., Prentice Hall, Hertfordshire, UK.

Barnett, A.M., 2011, *Wide Band Gap Compound Semiconductor Detectors for X-ray Spectroscopy in Harsh Environments*, PhD Thesis, Department of Physics and Astronomy, University of Leicester, Leicester, UK.

Barnett, A.M., Lees, J.E., Bassford, D.J., Ng, J.S., Tan, C.H., Babazadeh, N., and Gomes, R.B., 2011, *The Spectral Resolution of High Temperature GaAs Photon Counting Soft X-ray Photodiodes*, Nuclear Instruments and Methods in Physics Research A, Vol. 654, pp. 336-339.

Barnett, A.M., Lees, J.E., Bassford, D.J., and Ng, J.S., 2012a, *A Varied Shaping Time Noise Analysis of $Al_{0.8}Ga_{0.2}As$ and GaAs soft X-ray Photodiodes Coupled to a Low-Noise Charge Sensitive Preamplifier*, Nuclear Instruments and Methods in Physics Research A, Vol. 673, pp. 10-15.

Barnett, A.M., Lees, J.E., and Bassford, D.J, 2012b, *Direct Detection of Tritium and Carbon-14 Beta Particles with GaAs Photodiodes*, Journal of Instrumentation, Vol. 7, Art. No. P09012.

Barnett, A.M., Lees, J.E., and Bassford, D.J., 2013, *First Spectroscopic X-ray and Beta Results from a 400 μm diameter $Al_{0.8}Ga_{0.2}As$ Photodiode*, Journal of Instrumentation, Vol 8, Art. No. P10014.

Barnett, A.M., 2014, *Characterisation of GaAs Mesa Photodiodes with X-ray and γ-ray Photons*, Nuclear Instruments and Methods in Physics Research A, Vol. 756, pp. 39-44.

Nuclear Instruments and Methods in Physics Research A, Vol. 673, pp. 10-15.

Barnett, A.M., Lioliou, G., and Ng, J.S., 2015, *Characterisation of Room Temperature AlGaAs soft X-ray Mesa Photodiodes*, Nuclear Instruments and Methods in Physics Research A, Vol. 774, pp. 29-33.

Barret, D., Lam Trong, T., den Herder, J.-W., Piro, L., Barcons, X., Huovelin, J., Kelley, R., Mas-Hesse, J.M., Mitsuda, K., Paltani, S., Rauw, G., Rożanska, A., Wilms, J., Barbera, M., Bozzo, E., Ceballos, M.T., Charles, I., Decourchelle, A., den Hartog, R., Duval, J.-M., Fiore, F., Gatti, F., Goldwurm, A., Jackson, B., Jonker, P., Kilbourne, C., Macculi, C., Mendez, M., Molendi, S., Orleanski, P., Pajot, F., Pointecouteau, E., Porter, F., Pratt, G.W., Prêle, D., Ravera, L., Renotte, E., Schaye, J., Shinozaki, K., Valenziano, L., Vink, J., Webb, N., Yamasaki, N., Delcelier-Douchin, F., Le Du, M., Mesnager, J.-M., Pradines A., Branduardi-Raymont, G., Dadina, M., Finoguenov, A., Fukazawa, Y., Janiuk, A., Miller, J., Nazé, Y.,

Nicastro, F., Sciortino, S., Torrejon, J.M., Geoffray, H., Hernandez, I., Luno, L., Peille, P., André, J., Daniel, C., Etcheverry, C., Gloaguen, E., Hassin, J., Hervet, G., Maussang, I., Moueza, J., Paillet, A., Vella, B., Campos Garrido, G., Damery, J.-C., Panem, C., Panh, J., Bandler, S., Biffi, J.-M., Boyce, K., Clénet, A., DiPirro, M., Jamotton, P., Lotti, S., Schwander, D., Smith, S., van Leeuwen, B.-J., van Weers, H., Brand, T., Cobo, B., Dauser, T., de Plaa, J., and Cucchetti, E., 2016, *The Athena X-ray Integral Field Unit (X-IFU)*, SPIE proceedings, Space Telescopes and Instrumentation: Ultraviolet to Gamma Ray, Vol. 9905, Art. No. 99052F.

Barret, D., Nandra, K., Barcons, X., Fabian, A., den Herder, J.W., Piro, L., Watson, M., Aird, J., Branduardi-Raymont, G., and Cappi, M., 2013, *Athena+: The first Deep Universe X-ray Observatory*. *ArXiv*, Available from: https://arxiv.org/abs/1310.3814. [Last retrieved: 9th January 2017].

Barthelmy, S.D., Barbier, L.M., Cummings, J.R., Fenimore, E.E., Gehrels, N., Hullinger, D., Krimm, H.A., Markwardt, C.B., Palmer, D.M., Parsons, A., Sato, G., Suzuki, M., Takahashi, T., Tashiro, M., and Tueller, J., 2005, *The Burst Alert Telescope (BAT) on the SWIFT Midex Mission*, Space Science Reviews, Vol. 120, pp. 143-164.

Bavdaz, M., Peacock, A., and Owens, A., 2001, *Future space applications of compound semiconductor X-ray detectors*, Nuclear Instruments and Methods in Physics Research A, Vol. 458, pp. 123-131.

Bedington, R., Kataria, D., and Walton, D., 2012, *Using a CCD for the Direct Detection of Electrons in a Low Energy Space Plasma Spectrometer*, Journal of Instrumentation, Vol. 7, Art. No. C01079.

Benz, A.O., Krucker, S., Hurford, G.J., Arnold, N.G., Orleanski, P., Gröbelbauer, H.P., Klober, S., Iseli, L., Wiehl H.J., Csillaghy, A., Etesi, L., Hochmuth, N., Battaglia, M., Bednarzik, M., Resanovic, R., Grimm, O., Viertel, G., Commichau, V., Meuris, A., Limousin, O., Brun, S., Vilmer, N., Skup, K.R., Graczyk, R., Stolarski, M., Michalska, M., Nowosielski, W., Cichocki, A., Mosdorf, M., Seweryn, K., Przepiórka, A., Sylwester, J., Kowalinski, M., Mrozek, T., Podgorski, P., Mann, G., Aurass, H., Popow, E., Önel, H., Dionies, F., Bauer, S., Rendtel, J., Warmuth, A., Woche, M., Plüschke, D., Bittner, W., Paschke, J., Wolker, D., Van Beek, H.F., Farnik, F., Kasparova, J., Veronig, A.M., Kienreich, I.W., Gallagher, P.T., Bloomfield, D.S., Piana, M., Massone, A.M., Dennis, B.R., Schwarz, R.A., and Lin, R.P., 2012, *The Spectrometer Telescope for Imaging X-rays on Board the Solar Orbiter Mission*, SPIE proceedings, Space Telescopes and Instrumentation: Ultraviolet to Gamma Ray, Vol. 8443, Art. No. 84433L.

Berdugo, J., 2016, *Space Based Cosmic Ray Experiments: Highlights of Recent Results*, Nuclear and Particle Physics Proceedings, Vol. 273-275, pp. 110-116.

Bergonzo, P., Brambilla, A., Tromson, D., Mer, C., Guizard, B., Marshall, R.D., and Foulon, F., 2002, *CVD Diamond for Nuclear Detection Applications*, Nuclear Instruments and Methods in Physics Research A, Vol. 476, pp. 694-700.

Bertolucci, E., Conti, M., Grossi, G., Mancini, E., Russo, P., Campbell, M., Chesi, E., Heijne, E., Middelkamp, P., Scharfetter, L., Randaccio, P., Beccherle, R., Del Guerra, A., Gambaccini, M., Marchesini, R., Da Via, C., D' Auria, S., O' Shea, V., Smith, K., Snoeys, W., Amedolia, S.R., Bisogni, M.G., Bottigli, U., Ciocci, M.A., Fantacci, M.E., Romeo, N., Rosso, V., and Stefanini, O.A., 1996, *Use of Silicon and GaAs Pixel Detectors for Gigital Autoradiography*, IEEE Nuclear Science Symposium, 2-9 Nov., California, pp. 835-839.

Bertuccio, G., and Pullia, A., 1993, *A Method for the Determination of the Noise Parameters in Preamplifying Systems for Semiconductor Radiation Detectors*, Review of Scientific Instruments, Vol. 64, pp. 3294-3298.

Bertuccio, G., Rehak, P., and Xi, D., 1993, *A Novel Charge Sensitive Preamplifier without the Feedback Resistor*, Nuclear Instruments and Methods in Physics Research A, Vol. 326, pp. 71-76.

Bertuccio, G., Rehak, P., and Xi, D., Associated Universities Inc., 1994, *Low Noise Charge Sensitive Preamplifier DC Stabilized Without a Physical Resistor*, USA, US 5347231 A.

Bertuccio, G., Fasoli, L., Fiorini, C., and Sampietro, M., 1995, *Spectroscopy Charge Amplifier for Detectors with Integrated Front-End FET*, IEEE Transactions on Nuclear Science, Vol. 42, pp. 1399-1405.

Bertuccio, G., Pullia, A., and De Geronimo, G., 1996, *Criteria of Choice of the Front-End Transistor for Low-Noise Preamplification of Detector Signals at Sub-Microsecond Shaping Times for X- and γ-ray Spectroscopy*, Nuclear Instruments and Methods in Physics Research A, Vol. 380, pp. 301-307.

Bertuccio, G., Pullia, A., Lauter, J., Forster, A., and Luth, H., 1997, *Pixel X-ray Detectors in Epitaxial Gallium Arsenide with High-Energy Resolution Capabilities (Fano Factor Experimental Determination)*, IEEE Transactions on Nuclear Science, Vol. 44, pp. 1-5

Bertuccio, G., Casiraghi, R., and Nava, F., 2001, *Epitaxial Silicon Carbide for X-ray Detection*, IEEE Transactions on Nuclear Science, Vol. 48, pp. 232-233.

Bertuccio, G., and Maiocchi, D., 2002, *Electron-Hole Pair Generation Energy in Gallium Arsenide by x and γ Photons*, Journal of Applied Physics, Vol. 92, pp. 1248-1255.

Bertuccio, G., and Casiraghi, R., 2003, *Study of Silicon Carbide for X-ray Detection and Spectroscopy*, IEEE Transactions on Nuclear Science, Vol. 50, pp. 175-185.

Bertuccio, G., Casiraghi, R., Maiocchi, D., Owens, A., Bavdaz, M., Peacock, A., Andersson, H., and Nenonen, S., 2003, *Noise Analysis of Gallium Arsenide Pixel X-ray Detectors Coupled to Ultra-Low Noise Electronics*, IEEE Transactions on Nuclear Science, Vol. 50, pp. 723-728.

Bertuccio, G., Casiraghi, R., Cetronio, A., Lanzieri, C., and Nava, F., 2004, *Silicon Carbide for High Resolution X-ray Detectors Operating up to 100°C*, Nuclear Instruments and Methods in Physics Research A, Vol. 522, pp. 413-419.

Bertuccio, G., and Caccia, S., 2007, *Progress in Ultra-Low-Noise ASICs for Radiation Detectors*, Nuclear Instruments and Methods in Physics Research A, Vol. 579, pp. 243-246.

Bertuccio, G., Caccia, S., Puglisi, D., and Macera, D., 2011, *Advances in Silicon Carbide X-ray Detectors*, Nuclear Instruments and Methods in Physics Research A, Vol. 652, pp. 193-196.

Bertuccio, G., 2012, *The Silence of the Amps: Integrated Circuits for Very-Low-Noise Processing of Random Signals from Radiation Detectors*, IEEE Solid-State Circuits Magazine, Vol. 4, pp. 36-45.

Bertuccio, G., Puglisi, D., Pullia, A., and Lanzieri, C., 2013, *X and gamma Ray Spectroscopy With Semi-Insulating 4H-Silicon Carbide*, IEEE Transactions on Nuclear Science, Vol. 60, pp. 1436-1441.

Bertuccio, G., Puglisi, D., Macera, D., Di Liberto, R., Lamborizio, M., and Mantovani, L., 2014, *Silicon Carbide Detectors for in vivo Dosimetry*, IEEE Transactions on Nuclear Science, Vol. 61, pp. 961-966.

Bertuccio, G., Ahangarianabhari, M., Graziani, C., Macera, D., Shi, Y., Gandola, M., Rachevski, A., Rashevskaya, I., Vacchi, A., Zampa, G., Zampa, N., Bellutti, P., Giacomini, G., Picciotto, A., Piemonte,

C., and Zorzi, N., 2016, *X-Ray Silicon Drift Detector-CMOS Front-End System with High Energy Resolution at Room Temperature*, IEEE Transactions on Nuclear Science, Vol. 63, pp. 400-406.

Birtalan, D., and Nunley, W., 2009, *Optoelectronics: Infrared-Visible-Ultraviolet Devices and Applications*, 2nd ed., CRC Press, Florida, USA.

Bish, D., Blake, D., Vaniman, D., Sarrazin, P., Bristow, T., Achilles, C., Dera, P., Chipera, S., Crisp, J., Downs, R.T., Farmer, J., Gailhanou, M., Min, D., Morookian, J.M., Morris, R., Morrison, S., Rampe, E., Treiman, A., and Yen, A., 2014, *The First X-ray Diffraction Measurements on Mars*, International Union of Crystallography Journal, Vol. 1, pp. 514-522.

Blake, D., Vaniman, D., Achilles, C., Anderson, R., Bish, D., Bristow, T., Chen, C., Chipera, S., Crisp, J., Des Marais, D., Downs, R.T., Farmer, J., Feldman, S., Fonda, M., Gailhanou, M., Ma, H., Ming, D.W., Morris, R.V., Sarrazin, P., Stolper, E., Treiman, A., and Yen, A. 2012, *Characterisation and Calibration of the CheMin Mineralogical Instrument on Mars Science Laboratory*, Space Science Reviews, Vol. 170, pp. 341-399.

Blank, T.V., Goldberg, Yu A., Kalinina, E.V., Konstantinov, O.V., Konstantinov, A.O., and Hallén, A., 2005, *Temperature Dependence of the Photoelectric Conversion Quantum Efficiency of 4H–SiC Schottky UV Photodetectors*, Semiconductor Science and Technology, Vol. 20, pp. 710-715.

Bludau, W., Onton, A., and Heinke, W., 1974, *Temperature Dependence of the Band Gap of Silicon*, Journal of Applied Physics, Vol. 45, pp. 1846-1848.

Boyle, W.S., and Smith, G.E., 1970, *Charge Coupled Semiconductor Devices*, Bell System Technical Journal, Vol. 49, pp. 587-593.

Boylestad, R., and Nashelsky, L., 2006, *Electronic Devices and Circuit Theory*, 9th ed. Pearson Education, New Jersey.

Brown, W.L., Higinbotham, W.A., Miller, G.L., and Chase, R.L., 1969, *Semiconductor Nuclear-particle Detectors and Circuits: Proceedings of a Conference Conducted by the Subcommittee on Instruments and Techniques, Committee on Nuclear Science*, National Academy of Sciences, Washington, USA, pp. 283-330.

Bruckner, J., Dreibus, G., Rieder, R., and Wänke, H., 2003, *Refined data of Alpha Proton X-ray Spectrometer analyses of soils and rocks at the Mars Pathfinder site: Implications for surface chemistry*, Journal of Geophysical Research: Planets, Vol. 108.

Burrows, D.N., Hill, J.E., Nousek, J.A., Kennea, J.A., Wells, A., Osborne, J.P., Abbey, A.F., Beardmore, A., Mukerjee, K., Short, A.D.T., Chincarini, G., Campana, S., Citterio, O., Moretti, A., Pagani, C., Tagliaferri, G., Giommi, P., Capalbi, M., Tamburelli, F., Angelini, L., Cusumano, G., Bräuninger, H.W., Burkert W., and Hartner G.D., 2005, *The SWIFT X-ray Telescope*, Space Science Reviews, Vol. 120, pp. 165-195.

Butera, S., Lioliou, G., Krysa, A.B., and Barnett, A.M., 2016, *Characterisation of $Al_{0.52}In_{0.48}P$ Mesa p-i-n Photodiodes for X-ray Photon Counting Spectroscopy*, Journal of Applied Physics, Vol. 120, Art. No. 024502.

Buttay, C., Raynaud, C., Morel, H., Civrac, G., Locatelli, M.L., and Morel, F., 2012, *Thermal Stability of Silicon Carbide Power Diodes*, IEEE Transactions on Electron Devices, Vol. 59, pp. 761-769.

Cai, J., Chen, X., Hong, R., Yang, W., and Wu, Z., 2014, *High-Performance 4H-SiC-Based p-i-n Ultraviolet Photodiode and Investigation of its Capacitance Characteristics*, Optics Communications, Vol. 333, pp. 182-186.

Çakıcı, T., Güzeldir, B., and Sağlam, M., 2015, *Temperature Dependent of Electrical Characteristics of Au/n-GaAs/In Schottky Diode with In2S3 Interfacial Layer Obtained by Using Spray Pyrolysis Method*, Journal of Alloys and Compounds, Vol. 646, pp. 954-965.

Carpenter, M.S., Melloch, M.R., Lundstrom, M.S., and Tobin S.P., 1988a, *Effects of Na_2S and $(NH_4)_2S$ Edge Passivation Treatments on the Dark Current-Voltage Characteristics of GaAs pn Diodes*, Applied Physics Letters, Vol. 52, pp. 2157-2159.

Carpenter, M.S., Melloch, M.R., and Dungan, T.E., 1988b, *Schottky Barrier Formation on $(NH_4)_2S$-Treated n- and p-type (100) GaAs*, Applied Physics Letters, Vol. 53, pp. 66-68.

Catura, R.C., and Smithson, R.C., 1979, *Single Photon X-Ray Detection With a CCD Image Sensor*, Review of Scientific Instruments, Vol. 50, pp. 219-220.

Cazaux, J., 2016, *Understanding Solid State Physics: Problems and Solutions*, Taylor & Francis, Florida, USA, p. 370.

Celiktas, C., 2012, *A Method to Obtain a Noiseless Beta Spectrum*, Journal of Radioanalytical and Nuclear Chemistry, Vol. 292, pp. 1317-1323.

Chen, X., Yang, W., and Wu, Z., 2006, V*isible Blind p–i–n Ultraviolet Photodetector Fabricated on 4H-SiC*, Microelectronic Engineering, Vol. 83, pp. 104-106.

Chen, X., Zhu, H., Cai, J., and Wu, Z., 2007, *High-Performance 4H-SiC-based Ultraviolet p-i-n Photodetector*, Journal of Applied Physics, Vol. 102, Art. No. 024505.

Cheung, S.K., and Cheung, N.W., 1986, *Extraction of Schottky Diode Parameters from Forward Current-Voltage Characteristics*, Applied Physics Letters, Vol. 49, pp. 85-87.

Chicarro, A., Martin, P., and Trautner, R., 2004, *The Mars Express Mission: An Overview, in Mars Express: The Scientific Payload*, ESA Publications Division, The Netherlands, pp. 3-13.

Claeys, C., and Simoen, E., 2002, *Radiation Effects in Advanced Semiconductor Materials and Devices*, Springer-Verlag, Berlin, Germany.

Courtney, W.E., 1977, *Complex Permittivity of GaAs and CdTe at Microwave Frequencies*, IEEE Transactions on Microwave Theory and Techniques, Vol. 25, pp. 697-701.

Dahlkamp, F.J., 1993, *Uranium Ore Deposits*, Springer-Verlag, Berlin, Germany.

Dakin, J.P., and Brown, R.G.W., 2010, *Handbook of Optoelectronics*, Taylor & Francis, Florida, USA, pp. 79-80.

Damerell, C.J.S., 1998, *Charge-Coupled Devices as Particle Tracking Detectors*, Review of Scientific Instruments, Vol. 69, pp. 1549-1573.

Daud, T., Janesick, J.R., Evans, K., and Elliott, T., 1987, *Charge-Coupled-Device Response To Electron Beam Energies Of Less Than 1 keV up to 20 keV*, Optical Engineering, Vol. 26, Art. No. 268686.

Davydov, S.Yu., 2007, *On the Electron Affinity of Silicon Carbide Polytypes*, Semiconductors, Vol. 41, pp. 696-698.

De Pontieu, B., Title, A.M., Lemen, J.R., Kushner, G.D., Akin, D.J., Allard, B., Berger, T., Boerner, P., Cheung, M., Chou, C., Drake, J.F., Duncan, D.W., Freeland, S., Heyman, G.F., Hoffman, C., Hurlburt,

N.E., Lindgren, R.W., Mathur, D., Rehse, R., Sabolish, D., Seguin, R., Schrijver, C.J., Tarbell, T.D., Wülser, J.-P., Wolfson, C.J., Yanari, C., Mudge, J., Nguyen-Phuc, N., Timmons, R., van Bezooijen, R., Weingrod, I., Brookner, R., Butcher, G., Dougherty, B., Eder, J., Knagenhjelm, V., Larsen, S., Mansir, D., Phan, L., Boyle, P., Cheimets, P.N., DeLuca, E.E., Golub, L., Gates, R., Hertz, E., McKillop, S., Park, S., Perry, T., Podgorski, W.A., Reeves, K., Saar, S., Testa, P., Tian, H., Weber, M., Dunn, C., Eccles, S., Jaeggli, S.A., Kankelborg, C.C., Mashburn, K., Pust, N., Springer, L., Carvalho, R., Kleint, L., Marmie, J., Mazmanian, E., Pereira, T.M.D., Sawyer, S., Strong, J., Worden, S.P., Carlsson, M., Hansteen, V.H., Leenaarts, J., Wiesmann, M., Aloise, J., Chu, K.-C., Bush, R.I., Scherrer, P.H., Brekke, P., Martinez-Sykora, J., Lites, B.W., McIntosh, S.W., Uitenbroek, H., Okamoto, T.J., Gummin, M.A., Auker, G., Jerram, P., Pool, P., and Waltham, N., 2014, *The Interface Region Imaging Spectrograph (IRIS)*, Solar Physics, Vol. 289, pp. 2733-2779.

Defives, D., Noblanc, O., Dua, C., Brylinski, C., Barthula, M., Aubry-Fortuna, V., and Meyer, F., 1999, *Barrier Inhomogeneities and Electrical Characteristics of Ti/4H-SiC Schottky Rectifiers*, IEEE Transactions on Electron Devices, Vol. 46, pp. 449-455.

Deptuch, G., 2005, *Tritium Autoradiography with Thinned and Back-Side Illuminated Monolithic Active Pixel Sensor Device*, Nuclear Instruments and Methods in Physics Research A, Vol. 543, pp. 537-548.

Desai, P.N., and Knocke, P.C., 2004, *Mars Exploration Rovers Entry, Descent, and Landing Trajectory Analysis*, American Institute of Aeronautics and Astronautics Astrodynamics Specialist Conference and Exhibit, 16-19 August, Rhode Island, USA.

Di Bari, D., Antinori, F., Barberis, D., Becks, K.H., Beker, H., Beusch, W., Burger, P., Campbell, M., Cantatore, E., Catanesi, M.G., Chesi, E., Darbo, G., D'Auria, S., DaVia, C., Di Liberto, S., Elia, D., Gys, T., Heijne, E.H.M., Helstrup, H., Jacholkowski, A., Jæger, J.J., Jakubek, J., Jarron, P., Klempt, W., Krummenacher, F., Knudson, K., Kralik, I., Kubasta, J., Lassalle, J.C., Leitner, R., Lemeilleur, F., Lenti, V., Letheren, M., Lopez, L., Loukas, D., Luptak, M., Manzari, V., Martinengo, P., Meddeler, G., Meddi, F., Morando, M., Munns, A., Pellegrini, F., Pengg, F., Pospisil, S., Quercigh, E., Ridky, J., Rossi, L., Šafařík, K., Saladino, S., Scharfetter, L., Segato, G., Simone, S., Smith, K., Snoeys, W., Tomasicchio, G., and Vrba, V., 1997, *Performance of 0.5 × 106 Sensitive Elements Pixel Telescope in the WA97 Heavy Ion Experiment at CERN*, Nuclear Instruments and Methods in Physics Research A, Vol. 395, pp. 391-397.

Divine, N., and Garrett, H.B., 1983, *Charged Particle Distributions in Jupiter's Magnetosphere*, Journal of Geophysical Research, Vol. 88, pp. 6889-6903.

Dixit, V.K., Khamari, S.K., Manwani, S., Porwal, S., Alexander, K., Sharma, T.K., Kher, S., and Oak, S.M., 2015, *Effect of High Dose γ-ray Irradiation on GaAs p-i-n Photodetectors*, Nuclear Instruments and Methods in Physics Research A, Vol. 785, pp. 93-98.

Dressel, L., 2016, *Wide Field Camera 3 Instrument Handbook, Version 8.0*, Space Telescope Science Institute, Baltimore, USA, p. 30.

Drouin, D., Hovington, P., and Gauvin, R., 1997, *CASINO: A new Monte Carlo Code in C language for Electron Beam Interactions—part II: Tabulated Values of the Mott Cross Section*, Scanning, Vol. 19, pp. 20-28.

Dunne, J.A., and Burgess, E., 1978, *The Voyage of Mariner 10: Mission to Venus and Mercury*, Scientific and Technical Information Division, National Aeronautics and Space Administration.

Ellilä, M., and Pollari, K., 1990, *A Room-Temperature CCD Imaging System for the Detection of Beta-Emitting Tracers*, Nuclear Instruments and Methods in Physics Research A, Vol. 288, pp. 267-271.

Erd, C., Owens, A., Brammertz, G., Bavdaz, M., Peacock, A., Lämsä, V., Nenonen, S., Andersson, H., and Haack, N., 2002, *Hard X-ray Test and Evaluation of a Prototype 32×32 Pixel Gallium–Arsenide Array*, Nuclear Instruments and Methods in Physics Research A, Vol. 487, pp. 78-89.

Evans, A.D., 1981, *Designing with Field-Effect Transistors*, McGraw-Hill.

Fazzi, A., Pignatel, G.U., Dalla Betta, G.F., Boscardin, M., Varoli, V., Verzellesi, G., 2002, *Charge Preamplifier for Hole Collecting PIN Diode and Integrated Tetrode N-JFET*, IEEE Transactions on Nuclear Science, Vol. 47, pp. 829-833.

Fernandez, R.P., and Sanchez-Torres, A., 2015, *Underwater Exploration Mission on Europa Jovian Moon*, International Journal of Engineering Research & Science, Vol. 1, pp. 41-50.

Foing, B.H., Racca, G.D., Marini, A., Heather, D.J., Koschny, D., Grande, M., Huovelin, J., Keller, H.U., Nathues, A., Josset, J.L., Malkki, A., Schmidt, W., Noci, G., Birkl, R., Iess, L., Sodnik, Z., and McManamon, P., 2003, *SMART-1 Mission to the Moon: Technology and Science Goals*, Advances in Space Research, Vol. 31, pp. 2323-2333.

Fraser, G.W., Pearson, J.F., and Lees, J.E., 1987, *Dark Noise in Microchannel Plate X-ray Detectors*, Nuclear Instruments and Methods in Physics Research A, Vol. 254, pp. 447-462.

Fraser, G.W., 1989, *X-ray Detectors in Astronomy*, Cambridge University Press, Cambridge, UK.

Fraser, G.W., Abbey, A.F., Holland, A., McCarthy, K., Owens, A., and Wells, A., 1994, *The X-ray Energy Response of Silicon Part A. Theory*, Nuclear Instruments and Methods in Physics Research A, Vol. 350, pp. 368-378.

Fraser, G.W., 2008, *Extraterrestrial Analysis: Planetary X-Ray Fluorescence from Orbiting Spacecraft and Landers, in Portable X-ray Fluorescence Spectroscopy: Capabilities for in-situ Analysis*, RSC Publishing, Cambridge, UK.

Fraser, G.W., Carpenter, J.D., Rothery, D.A., Pearson, J.F., Martindale, A., Huovelin, J., Treis, J., Anand, M., Anttila, M., Ashcroft, M., Benkoff, J., Bland, P., Bowyer, A., Bradley, A., Bridges, J., Brown, C., Bulloch, C., Bunce, E.J., Christensen, U., Evans, M., Fairbend, R., Feasey, M., Giannini, F., Hermann, S., Hesse, M., Hilchenbach, M., Jorden, T., Joy, K., Kaipiainen, M., Kitchingman, I., Lechner, P., Lutz, G., Malkki, A., Muinonen, K., Näränen, J., Portin, P., Prydderch, M., Juan, J.S., Sclater, E., Schyns, E., Stevenson, T.J., Strüder, L., Syrjasuo, M., Talboys, D., Thomas, P., Whitford, C., and Whitehead, S., 2010, *The Mercury Imaging X-ray Spectrometer (MIXS) on Bepicolombo*, Planetary and Space Science, Vol. 58, pp. 79-95.

Fu, Q. 2003, *Radiation (Solar)*, *in Encyclopedia of Atmospheric Sciences*, Academic Press, Oxford, pp. 1859-1863.

Gargaud, M., Amils, R., Quintanilla, J.C., Cleaves, H.J., Irvine, W.M., Pinti, D.L., and Viso, M., 2011, Encyclopedia of Astrobiology, Springer-Verlag, Berlin, Germany.

Gatti, E., and Rehak, P., 1983, *Concept of a Solid-State Drift Chamber*, Proceedings of DPF Workshop on Collider Detectors: Present Capabilities and Future Possibilities, BNL 32718, Lawrence Berkeley Lab, California.

Gatti, E., Manfredi, P.F., Sampietro, M., and Speziali, V., 1990, *Suboptimal Filtering of 1/ƒ-Noise in Detector Charge Measurements*, Nuclear Instruments and Methods in Physics Research A, Vol. 297, pp. 467-478.

Gauglitz, G., and Vo-Dinh, T., 2006, *Handbook of Spectroscopy*, John Wiley & Sons, Weinheim, Germany, p. 389.

Gellert, R., Campbell, J.L., King, P.L., Leshin, L.A., Lugmair, G.W., Spray, J.G., Squyres, S.W., and Yen, A.S., 2009, *The Alpha-Particle-X-ray-Spectrometer (APXS) for the Mars Science Laboratory (MSL) Rover Mission*, 40th Lunar and Planetary Science Conference, The Woodlands, Texas.

Gianoncelli, A., Bufon, J., Ahangarianabhari, M., Altissimo, M., Bellutti, P., Bertuccio, G., Borghes, R., Carrato, S., Cautero, G., Fabiani, S., Giacomini, G., Giuressi, D., Kourousias, G., Menk, R.H., Picciotto, A., Piemonte, C., Rachevski, A., Rashevskaya, I., Stolfa, A., Vacchi, A., Zampa, G., Zampa, N., and Zorzi, N., 2016, *A New Detector System for Low Energy X-ray Fluorescence Coupled with Soft X-ray Microscopy: First Tests and Characterisation*, Nuclear Instruments and Methods in Physics Research A, Vol. 816, pp. 113-118.

Gilmore, G., 2008, *Practical Gamma-ray Spectrometry*, 2nd ed., John Wiley & Sons, Chichester, UK.

Glasby, G.P., 2006, *Manganese: Predominant Role of Nodules and Crusts, in Marine Geochemistry*, Springer, Berlin, Heidelberg, pp. 371-427.

Glassmeier, K.-H., Boehnhardt, H., Koschny, D., Kührt, E., and Richter I., 2007, *The Rosetta Mission: Flying Towards the Origin of the Solar System*, Space Science Reviews, Vol. 128, pp. 1-21.

Glisson, T.H., 2011, *Introduction to Circuit Analysis and Design*, Springer Science and Business Media B.V., Netherlands, p. 255.

Gohil, T., Whale, J., Lioliou, G., Novikov, S.V., Foxon, C.T., Kent, A.J., and Barnett, A.M., 2016, *X-ray Detection with Zinc-Blende (Cubic) GaN Schottky Diodes*, Scientific Reports, Vol. 6, Art. No. 29535.

Goldstein, J., Newbury, D.E., Joy, D.C., Lyman, C.E., Echlin, P., Lifshin, E., Sawyer, L., and Michael, J.R., 2003, *The SEM and Its Modes of Operation, in Scanning Electron Microscopy and X-ray Microanalysis*, 3rd ed., Kluwer Academic/Plenum Publishers, New York, USA, pp. 21-60.

Golombek, M.P., Anderson, R.C., Barnes, J.R., Bell III, J.R., Bridges, N.T., Britt, D.T., Brückner, J., Cook, R.A., Crisp, J.A., Economou, T., Folkner, W.M., Greely, R., Haberle, R.M., Hargraves, R.B., Harris, J.A., Haldemann, A.F.C., Herkenhoff, K.E., Hviid, S.F., Jaumann, R. Johnson, J.R., Kallemeyn, P.H. Keller, H. U., Kirk, R.L., Knudsen, J.M., Larsen, S., Lemmon, M.T., Madsen, M.B., Magalhães, J.A., Maki, J.N., Malin, M.C., Manning, R.M., Matijevic, J., McSween, H.Y., Moore, H.J., Murchie, S.L., Murphy, J.R., Parker, T.J., Reider, R., Rivellini, T.P., Schofield, J.T., Seiff, A., Singer, R.B., Smith, P.H., Soderblom, L. A., Spencer, D.A., Stoker, C.R., Sullivan, R., Thomas, N., Thurman, S.W., Tomasko, M.G., Vaughn, R. M., Wänke, H., and Wilson, G.R., 1999, *Overview of the Mars Pathfinder Mission: Launch through Landing*, Surface Operations, Data Sheets, and Science Results, Journal of Geophysical Research, Vol. 104, pp. 8523-8553.

Gramberg, G., 1971, *Temperature Dependence of Space Charge Capacitance of Silicon Carbide Diodes*, Solid-State Electronics, Vol. 14, pp. 1067-1070.

Grande, M., Browning, R., Waltham, N., Parker, D., Dunkin, S.K., Kent, B., Kellett, B., Perry, C.H., Swinyard, B., Perry, A., Feraday, J., Howe, C., McBride, G., Phillips, K., Huovelin, J., Muhli, P., Hakala,

P.J., Vilhu, O., Laukkanen, J., Thomas, N., Hughes, D., Alleyne, H., Grady, M., Lundin, R., Barabash, S., Baker, D., Clark, P.E., Murray, C.D., Guest, J., Casanova, I., d'Uston, L.C., Maurice, S., Foing, B., Heather, D.J., Fernandes, V., Muinonen, K., Russell, S.S., Christou, A., Owen, C., Charles, P., Koskinen, H., Kato, M., Sipila, K., Nenonen, S., Holmstrom, M., Bhandari, N., Elphic, R., and Lawrence, D., 2003, *The D-CIXS X-ray Mapping Spectrometer on SMART-1*, Planetary and Space Science, Vol. 51, pp. 427-433.

Grande, M., Kellett B., Howe, C., Perry, C.H., Swinyard, B., Dunkin, S., Huovenin, J., Thomas, N., Mall, U., Hughes, D., Alleyne, H., Russell, S., Grady, M., Lundin, R., Barabash, S., Baker, D., Murray, C.D., Guest, J.E., Crawford, I., Casanova, I., Maurice, S., Gasnault, O., Foing, B., Lawrence, D., and Fernandez, V., 2005, *First Results — Lunar X-ray Mapping Spectrometer on Smart-1*, Space Research Today, Vol. 163, pp. 18-22.

Grande, M., Maddison, B.J., Howe, C.J., Kellett, B.J., Sreekumar, P., Huovelin, J., Crawford, I.A., Duston, C.L., Smith, D., Anand, M., Bhandari, N., Cook, A., Fernandes, V., Foing, B., Gasnaut, O., Goswami, J.N., Holland, A., Joy, K.H., Kochney, D., Lawrence, D., Maurice, S., Okada, T., Narendranath, S., Pieters, C., Rothery, D., Russell, S.S., Shrivastava, A., Swinyard, B., Wilding, M., and Wieczorek, M., 2009, The C1XS X-ray Spectrometer on Chandrayaan-1, Planetary and Space Science, Vol. 57, pp. 717-724.

Green, J.C., Froning, C.S., Osterman, S., Ebbets, D., Heap, S.H., Leitherer, C., Linsky, J.L., Savage, B.D., Sembach, K., Shull, J.M., Siegmund, O.H.W., Snow, T.P., Spencer, J., Stern, S.A., Stocke, J., Welsh, B., Béland, S., Burgh, E.B., Danforth, C., France, K., Keeney, B., McPhate, J., Penton, S.V., Andrews, J., Brownsberger, K., Morse, J., and Wilkinson, E., 2012, *The Cosmic Origins Spectrograph*, The Astrophysical Journal, Vol. 744, Art. No. 60.

Grekov, A., Zhang, Q., Fatima, H., Agarwal, A. and Sudarshan, T., 2008, *Effect of Crystallographic Defects on the Reverse Performance of 4H–SiC JBS Diodes*, Microelectronics Reliability, Vol. 48, pp. 1664-1668.

Grotzinger, J.P., Crisp, J., Vasavada, A.R., Anderson, R.C., Baker, C.J., Barry, R., Blake, D.F., Conrad, P., Edgett, K.S., Ferdowski, B., Gellert, R., Gilbert, J.B., Golombek, M., Gómez-Elvira, J., Hassler, D.M., Jandura, L., Litvak, M., Mahaffy, P., Maki, J., Meyer, M., Malin, M.C., Mitrofanov, I., Simmonds, J.J., Vaniman, D., Welch, R.V., and Wiens, R.C., 2012, *Mars Science Laboratory Mission and Science Investigation*, Space Science Reviews, Vol. 170, pp. 5-56.

Gruenwald, J., Tskhakaya, D., Kovačič, J., Čerček, M., Gyergyek, T., Ionita, C., and Schrittwieser, R., 2013, *Comparison of Measured and Simulated Electron Energy Distribution Functions in Low-Pressure Helium Plasmas*, Plasma Sources Science and Technology, Vol. 22, Art. No. 015023.

Grundmann, M., 2006, *The Physics of Semiconductors: An Introduction Including Devices and Nanophysics*, Springer-Verlag, Berlin, Germany.

Grupen, C., and Buvat, I., 2012, *Handbook of Particle Detection and Imaging*, Springer-Verlag, Berlin, Germany, pp. 377-410.

Hansson, C.T.C., Owens, A., and van den Biezen, J., 2014, *X-ray, γ-ray and Neutron Detector Development for Future Space Instrumentation*, Acta Astronautica, Vol. 93, pp. 121-128.

Harris, G.L., 1995, *Properties of Silicon Carbide*, Institution of Electrical Engineers, London, UK.

Harris, R.J., and Shuler, W.B., 1967, *500-volt Resolution with a Si(Li) Detector Using a Cooled FET Preamplifier*, Nuclear Instruments and Methods, Vol. 51, pp. 341-344.

Hartnett, J.G., Mouneyrac, D., Krupka, J., le Floch, J.-M., Tobar, M.E., and Cros, D., 2011, *Microwave Properties of Semi-Insulating Silicon Carbide Between 10 and 40 GHz and at Cryogenic Temperatures*, Journal of Applied Physics, Vol. 109, Art. No. 064107.

Hein, J.R., Mizell, K., Koschinsky, A., and Conrad, T.A., 2013, *Deep-Ocean Mineral Deposits as a Source of Critical Metals for High- and Green-Technology Applications: Comparison with Land-Based Resources*, Ore Geology Reviews, Vol. 51, pp. 1-14.

Henck, R., Gutknecht, D., Siffert, P. De Laet, L., and Schoenmaekers, W., 1970, *Trapping Effects in Ge(Li) Detectors and Search for a Correlation with Characteristics Measured on the P-Type Crystals*, IEEE Transactions on Nuclear Science, Vol. 17, pp. 149-159.

Henke, B.L., Gullikson, E.M., and Davis, J.C., 1993, *X-Ray Interactions: Photoabsorption, Scattering, Transmission, and Reflection at E = 50-30,000 eV, Z = 1-92*, Atomic Data and Nuclear Data Tables, Vol. 54, pp. 181-342.

Hewlett Packard, 1979, *Model HP 4275A Multi-Frequency LCR Meter Operating Manual*, 04275-90004, Tokyo, Japan.

Hochedez, J.F., Bergonzo, P., Castex, M.C., Dhez, P., Hainaut, O., Sacchi, M., Alvarez, J., Boyer, H., Deneuville, A., Gibart, P., Guizard, B., Kleider, J.P., Lemaire, P., Mer, C., Monroy, E., Muñoz, E., Muret, P., Omnes, F., Pau, J.L., Ralchenko, V., Tromson, D., Verwichte, E., and Vial, J.C., 2001, *Diamond UV Detectors for Future Solar Physics Missions*, Diamond and Related Materials, Vol. 10, pp. 673-680.

Holt, D.B., and Yacobi, B.G., 2007, *Extended Defects in Semiconductors: Electronic Properties, Device Effects and Structures*, Cambridge University Press, Cambridge, UK.

Hong, M., Kwo, J., Kortan, A.R., Mannaerts, J.P., and Sergent, A.M., 1999, *Epitaxial Cubic Gadolinium Oxide as a Dielectric for Gallium Arsenide Passivation*, Science, Vol. 283, pp. 1897-1900.

Hovington, P., Drouin, D., and Gauvin, R., 1997, *CASINO: A new Monte Carlo Code in C Language for Electron Beam Interaction —part I: Description of the Program*, Scanning, Vol. 19, pp. 1-14.

Howard, R.M., 2002, *Principles of Random Signal Analysis and Low Noise Design: The power Spectral Density and Its Applications*, John Wiley & Sons, Canada, p. 60.

Howe, C.J., Drummond, D., Edeson, R., Maddison, B., Parker, D.J., Parker, R., Shrivastava, A., Spencer, J., Kellett, B.J., Grande, M., Sreekumar, P., Huovelin, J., Smith, D.R., Gow, J., Narendranath, S.K.C., and d'Uston, L., 2009, *Chandrayaan-1 X-ray Spectrometer (C1XS)—Instrument Design and Technical Details*, Planetary and Space Science, Vol. 57, pp. 735-743.

Hu, J., Xin, X., Zhao, J.H., Yan, F., Guan, B., Seely, J., and Kjornrattanawanich, B., 2006, *Highly Sensitive Visible-Blind Extreme Ultraviolet Ni/4H-SiC Schottky Photodiodes with Large Detection Area*, Optics Letters, Vol. 31, pp. 1591-1593.

Huovelin, J., Vainio, R., Andersson, H., Valtonen, E., Alha, L., Mälkki, A., Grande, M., Fraser, G.W., Kato, M., Koskinen, H., Muinonen, K., Näränen, J., Schmidt, W., Syrjäsuo, M., Anttila, M., Vihavainen, T., Kiuru, E., Roos, M., Peltonen, J., Lehti, J., Talvioja, M., Portin, P., and Prydderch, M., 2010, *Solar Intensity X-ray and particle Spectrometer (SIXS)*, Planetary and Space Science, Vol. 58, pp. 96-107.

Hwang, C.J., 1969, *Optical Properties of n-Type GaAs. I. Determination of Hole Diffusion Length from Optical Absorption and Photoluminescence Measurements*, Journal of Applied Physics, Vol. 40, pp. 3731-3739.

Hwang, K.C., and Li, S.S., 1990, *A Study of New Surface Passivation Using $P_2S_5/(NH_4)_2S$ on GaAs Schottky Barrier Diodes*, Journal of Applied Physics, Vol. 67, pp. 2162-2165

Ishikawa, T., Aoyagi, H., Asaka, T., Asano, Y., Azumi, N., Bizen, T., Ego, H., Fukami, K., Fukui, T., Furukawa, Y., Goto, S., Hanaki, H., Hara, T., Hasegawa, T., Hatsui, T., Higashiya, A., Hirono, T., Hosoda, N., Ishii, M., Inagaki, T., Inubushi, Y., Itoga, T., Joti, Y., Kago, M., Kameshima, T., Kimura, H., Kirihara, Y., Kiyomichi, A., Kobayashi, T., Kondo, C., Kudo, T., Maesaka, H., Marechal, X.M., Masuda, T., Matsubara, S., Matsumoto, T., Matsushita, T., Matsui, S., Nagasono, M., Nariyama, N., Ohashi, H., Ohata, T., Ohshima, T., Ono, S., Otake, Y., Saji, C., Sakurai, T., Sato, T., Sawada, K., Seike, T., Shirasawa, K., Sugimoto, T., Suzuki, S., Takahashi, S., Takebe, H., Takeshita, K., Tamasaku, K., Tanaka, H., Tanaka, R., Tanaka, T., Togashi, T., Togawa, K., Tokuhisa, A., Tomizawa, H., Tono, K., Wu, S., Yabashi, M., Yamaga, M., Yamashita, A., Yanagida, K., Zhang, C., Shintake, T., Kitamura, H., and Kumagai, N., 2012, *A Compact X-ray Free-Electron Laser Emitting in the Sub-Angstrom Region*, Nature Photonics, Vol. 6, pp. 540-544.

Jafari, H., and Feghhi, S.A.H., 2016, *Analytical Modeling for Gamma Radiation Damage on Silicon Photodiodes*, Nuclear Instruments and Methods in Physics Research A, Vol. 816, pp. 62-69.

Jethwa, P., Saxton, R., Guainazzi, M., Rodriguez-Pascual, P., and Stuhlinger, M., 2015, *When is Pile-Up iImportant in the XMM-Newton EPIC Cameras?*, Astronomy and Astrophysics, Vol. 581, Art. No. A104.

Jung, H.S., Yang, W.I., Cho, M.S., Joo, K.N., and Lee, S.Y., 2014, *Microwave Losses of Undoped n-type Silicon and Undoped 4H-SiC Single Crystals at Cryogenic Temperatures*, Electronic Materials Letters, Vol. 10, pp. 541-549.

Kahn, S.M., Behar, E., Kinkhabwala, A., and Savin, D.W., 2002, *X–ray spectroscopy of astrophysical plasmas*, Philosophical Transactions of the Royal Society of London A: Mathematical, Physical and Engineering Sciences, Vol. 360, pp. 1923-1933.

Kaiser, K.L., 2006, *Electromagnetic Shielding*, Taylor & Francis, Florida, USA, p. 32.

Kamal, A., 2014, *Particle physics*, Springer-Verlag, Berlin, Germany.

Kania, D.R., Landstrass, M.I., Plano, M.A., Pan, L.S., and Han, S., 1993, *Diamond Radiation Detectors*, Diamond and Related Materials, Vol. 2, pp. 1012-1019.

Keithley Instruments, 2011, *Model 6487 Picoammeter/Voltage Source Reference Manual*, 6487-901-01 Rev C, Ohio, USA.

Keithley Instruments, 2013, *Low Level Measurements Handbook*, 7th ed., Ohio, USA.

Kemmer, J., Lutz, G., Prechtel, U., Schuster, K., Sterzik, M., Strüder, L., and Ziemann, T., 1990, *Experimental Confirmation of a New Semiconductor Detector Principle*, Nuclear Instruments and Methods in Physics Research A, Vol. 288, pp. 92-98.

Kern, W., and Puotinen, D.A., 1970, *Cleaning Solutions Based on Hydrogen Peroxide for Use in Silicon Semiconductor Technology*, RCA Review, Vol. 31, pp. 187-206.

Khan, A.A., and Dey, K.K., 2006, *A First Course in Electronics*, Prentice Hall of India, New Delhi, India, pp. 440-441.

Kimble, R.A., Woodgate, B.E., Bowers, C.W., Kraemer, S.B., Kaiser, M.E., Gull, T.R., Heap, S.R., Danks, A.C., Boggess, A., Green, R.F., Hutchings, J.B., Jenkins, E.B., Joseph, C.L., Linsky, J.L., Maran, S.P., Moos, H.W., Roesler, F.L., Timothy, J.G., Weistrop, D.E., Grady, J.F., Loiacono, J.J., Brumfield, M.D.,

Feinberg, L.D., Krebs, C.A., Meyer, W.W., Hood, D.F., Argabright, V.S., Hetlinger, J.C., Stocker, R.B., Woodruff, R.A., Baum, S.A., Hartig, G.F., Bohlin, R.C., Clampin, M., Ferguson, H.C., Goudfrooij, P., McGrath, M., Lindler, D.J., Beck, T.L., Feggans, K., Plait, P.C., Sandoval, J.L., Hill, R.S., Collins, N.R., Cornett, R.H., Fowler, W.B., Hill, R.J., Landsman, W., Malumuth, E.M., Crenshaw, D.M., Robinson, R.D., and Valenti, J.A., 1998, *On-Orbit Performance of the Space Telescope Imaging Spectrograph*, SPIE proceedings, Space Telescopes and Instrumentation V, Vol. 3356, pp. 188-202.

Kitsinelis, S., 2015, *Light Sources: Basics of Lighting Technologies and Applications*, 2nd ed., CRC Press, Florida, USA.

Kittl, J.A., Pawlak, M.A., Lauwers, A., Demeurisse, C., Opsomer, K., Anil, K.G., Vrancken, C., van Dal, M.J.H., Veloso, A., Kubicek, S., Absil, P., Maex, K., and Biesemans, S., 2006, *Work function of Ni Silicide Phases on HfSiON and SiO_2: NiSi, Ni_2Si, $Ni_{31}Si_{12}$, and Ni_3Si fully Silicided Gates*, IEEE Electron Device Letters, Vol. 27, pp. 34-36.

Klaassen, F.M., 1971, *Comments on Hot Carrier Noise in Filed-Effect Transistors*, IEEE Transactions on Nuclear Devices, Vol. 18, pp. 74-75.

Klingelhöfer, G., Brückner, J., D'uston, C., Gellert, R., and Rieder, R., 2007, *The Rosetta Alpha Particle X-ray Spectrometer (APXS)*, Space Science Reviews, Vol. 128, pp. 383-396.

Knoll, G.F., 2010, *Radiation Detection and Measurements*, 4th ed., John Wiley & Sons.

Kohler, B., Singer, A., and Stoffers, P., 1994, *Biogenic Nontronite from Marine White Smoker Chimneys*, Clays and Clay Minerals, Vol. 42, pp. 689-701.

Kokubun, M., Watanabe, S., Nakazawa, K., Tajima, H., Fukazawa, Y., Takahashi, T., Kataoka, J., Kamae, T., Katagiri, H., Madejski, G.M., Makishima, K., Mizuno, T., Ohno, M., Sato, R., Takahashi, H., Tanaka, T., Tashiro, M., Terada, Y., and Yamaoka, K., 2010, *Hard X-ray and gamma-ray detector for ASTRO-H based on Si and CdTe imaging sensors*, Nuclear Instruments and Methods in Physics Research A, Vol. 623, pp. 425-427.

Kolawa, E., Balint, T., Birur, G., Bolotin, G., Brandon, E., Del Castillo, L., Garrett, H., Hall, J., Johnson, M., Jones, J., Jun, I., Manvi, R., Mojarradi, M., Moussessian, A., Patel, J., Pauken, M., Peterson, C., Surampudi, R., Schone, H., Whitacre, J., Martinez, E., Laub, B., Venkapathy, R., and Neudeck, P., 2007, *Extreme Environment Technologies for Future Space Science Missions*, Technical Reports, JPL D-32832.

Konczakowska, A, and Wilamowski, B.M., 2011, *Noise in Semiconductor Devices, in Fundamentals of Industrial ELectronics*, 2nd ed., Taylor & Francis, Florida, USA.

Kozlov, V., Andersson, H., Gostilo, V., Leskelä, M., Owens, A., Shorohov, M., and Sipilä, H., 2008, *Improved Process for the TlBr Single-Crystal Detector*, Nuclear Instruments and Methods in Physics Research A, Vol. 591, pp. 209-212.

Kozorezov, A.G., Wigmore, J.K., Owens, A., den Hartog, R., Peacock, A., and A Al-Jawhari, H., 2005, *Resolution Degradation of Semiconductor Detectors due to Carrier Trapping*, Nuclear Instruments and Methods in Physics Research A, Vol. 546, pp. 209-212.

Kriss, A.A., and Hamby, D.M., 2004, *Beta Spectroscopy with a Large-Area Avalanche Photodiode Module and a Plastic Scintillator*, Nuclear Instruments and Methods in Physics Research A, Vol. 525, pp. 553-559.

Krupka, J., Breeze, J., Centeno, A., Alford, N., Claussen, T., and Jensen, L., 2006, *Measurements of Permittivity, Dielectric Loss Tangent, and Resistivity of Float-Zone Silicon at Microwave Frequencies*, IEEE Transactions on Microwave Theory and Techniques, Vol. 54, pp. 3995-4001.

Krupka, J., Mouneyrac, D., Hartnett, J.G., and Tobar, M.E., 2008, *Use of Whispering-Gallery Modes and Quasi- TE_{0np} Modes for Broadband Characterization of Bulk Gallium Arsenide and Gallium Phosphide Samples*, IEEE Transactions on Microwave Theory and Techniques, Vol. 56, pp. 1201-1206.

La Via, F., Galvagno, G., Roccaforte, F., Ruggiero, A., and Calcagno, L., 2005, *Drift Mobility in 4H-SiC Schottky Diodes*, Applied Physics Letters, Vol. 87, Art. No. 142105.

Ladzianský, M., Šagátová, A., Nečas, V., Dubecký, F., and Linhart, V., 2009, *Deep Traps Study of Radiation-Damaged Semi-Insulating GaAs Detectors Introduced by Neutrons*, Nuclear Instruments and Methods in Physics Research A, Vol. 607, pp. 135-137.

Lebedev, A.A., 1999, *Deep Level Centers in Silicon Carbide: A Review*, Semiconductors, Vol. 33, pp. 107-130.

Lee, H.H., Racicot, R.J., and Lee, S.H., 1989, *Surface Passivation of GaAs*, Applied Physics Letters, Vol. 54, pp. 724-726.

Lees, J.E., Bassford, D.J., Fraser, G.W., Horsfall, A.B., Vassilevski, K.V., Wright, N.G., and Owens, A., 2007, *Semi-Transparent SiC Schottky Diodes for X-ray Spectroscopy*, Nuclear Instruments and Methods in Physics Research A, Vol. 578, pp. 226-234.

Lees, J.E., Barnett, A.M., Bassford, D.J., Stevens, R.C., and Horsfall, A.B., 2011, *SiC X-ray Detectors for Harsh Environments*, Journal of Instrumentation, Vol. 6, Art. No. C01032.

Lehtolainen, A., Huovelin, J., Alha, L., and Tikkanen, T., 2011, *Estimates of in-Flight Calibration Source Activities for the SIXS X-Ray Detectors on Board BepiColombo*, Nuclear Instruments and Methods in Physics Research A, Vol. 636, pp. 48-60.

Lehtolainen, A., Alha, L., Huovelin, J., Moissl, R., Korpela, S., Andersson, H., and Kuparinen, K., 2014, *Ground Calibrations of the Solar Intensity X-ray Spectrometer (SIXS) on Board BepiColombo*, Nuclear Instruments and Methods in Physics Research A, Vol. 735, pp. 496-511.

Leo, W.R., 1994, *Techniques for Nuclear and Particle Physics Experiments: A How-to Approach*, 2nd ed., Springer-Verlag, Berlin, Germany.

Leroy, C., and Rancoita, P.G., 2007, *Particle Interaction and Displacement Damage in Silicon Devices Operated in Radiation Environments*, Reports on Progress in Physics, Vol. 70, pp. 493-625.

Leroy, C., and Rancoita, P.G., 2009, *Principles of Radiation Interaction in Matter and Detection*, Word Scientific, Singapore.

Levinshtein, M.E., Rumyantsev, S.L., and Shur, M.S., 2001, *Properties of Advanced Semiconductor Materials: GaN, AIN, InN, BN, SiC, SiGe*, John Wiley & Sons, Chichester, UK.

Levinshtein, M.E., Rumyantsev, S.L., Shur, M.S., Gaska, R., and Khan, M.A., 2002, *Low Frequency and 1/f Noise in Wide-Gap Semiconductors: Silicon Carbide and Gallium Nitride*, IEEE Proceedings of Circuits, Devices and Systems, Vol. 149, pp. 32-39.

Levinzon, F., and Vandamme, L., 2011, *Comparison of 1/f Noise in JFETs and MOSFETs with Several Figures of Merit*, Fluctuation and Noise Letters, Vol. 10, pp. 447-465.

Lifshin, E., 1999, *X-ray Characterization of Materials*, John Wiley & Sons, Weinheim, Germany.

Linder, D.R., Coates, A.J., Woodliffe, R.D., Alsop, C., Johnstone, A.D., Grande, M., Preece, A., Narheim, B., and Young, D.T., 1998, *The Cassini CAPS Electron Spectrometer, in Measurement Techniques in Space Plasmas: Particles*, American Geophysical Union, Washington, pp. 257-262.

Lindström, G., 2003, *Radiation Damage in Silicon Detectors*, Nuclear Instruments and Methods in Physics Research A, Vol. 512, pp. 30-43.

Lioliou, G., Mazzillo, M.C., Sciuto, A., and Barnett, A.M., 2015, *Electrical and Ultraviolet Characterisation of 4H-SiC Schottky Photodiodes*, Optics Express, Vol. 23, pp. 21657-21670.

Lioliou, G., Meng, X., Ng, J.S., and Barnett, A.M., 2016, *Characterisation of Gallium Arsenide X-ray Mesa p-i-n Photodiodes at Room Temperature*, Nuclear Instruments and Methods in Physics Research A, Vol. 813, pp. 1-9.

Liu, X., Fowler, B.A., Onishi, S.K., Vu, P., Wen, D.D., Do, H., and Horn, S., 2005, *CCD/CMOS Hybrid FPA for Low Light Level Imaging*, SPIE proceedings, Infrared and Photoelectronic Imagers and Detector Devices, Vol. 5881, Art. No. 58810C.

Livi, S.A., McNutt, R., Andrews, G.B., Keath, E., Mitchell, D., and Ho, G., 2003, *The Energetic Particles Spectrometers (EPS) on MESSENGER and New Horizons*, Solar Wind Ten: Proceedings of the Tenth International Solar Wind Conference, American Institute of Physics, Vol. 679, pp. 838-841.

Llopart, X., Campbell, M., San Segundo, D., Pernigotti, E., and Dinapoli, R., 2001, *Medipix2, a 64k Pixel Read Out Chip With 55 μm Square Elements Working in Single Photon Counting Mode*, IEEE Nuclear Science Symposium Conference Record, Vol. 3, pp. 1484-1488.

Llopart, X., Ballabriga, R., Campbell, M., Tlustos, L., and Wong, W., 2007, *Timepix, a 65k Programmable Pixel Readout Chip for Arrival Time, Energy and/or Photon Counting measurements*, Nuclear Instruments and Methods in Physics Research A, Vol. 581, pp. 485-494.

Lottermoser, B., 2010, *Mine Wastes: Characterisation, Treatment and Environmental Impacts*, 3rd ed., Springer-Verlag, Berlin, Heidelberg, pp. 270-272.

Lowe, B.G., 1997, *Measurements of Fano Factors in Silicon and Germanium in the Low-Energy X-ray Region*, Nuclear Instruments and Methods in Physics Research A, Vol. 399, pp. 354-364.

Lowe, B.G., and Sareen, R.A., 2014, *Semiconductor X-ray Detectors*, Taylor & Francis Group, Florida.

Ly Anh, T., Perd'ochová, A., Nečas, V., and Pavlicová, V., 2006, *Radiation Resistance Study of Semi-Insulating GaAs-Based Radiation Detectors to Extremely High Gamma Doses*, Nuclear Physics B - Proceedings Supplements, Vol. 150, pp. 402-406.

Ma, X., Sadagopan, P., and Sudarshan, T.S., 2006, *Investigation on Barrier Inhomogeneities in 4H-SiC Schottky Rectifiers*, Physica Status Solidi A, Vol. 203, pp. 643-650.

Magill, J., and Galy, J., 2005, *Radioactivity Radionuclides Radiation*, Springer-Verlag, Berlin, Germany.

Mandal, K.C., Krishna, R.M., Muzykov, P.G., Das, S., and Sudarshan, T.S., 2011, *Characterization of Semi-Insulating 4H Silicon Carbide for Radiation Detectors*, IEEE Transactions on Nuclear Science, Vol. 58, pp. 1992-1999.

Mann, H.M., Haslett, J.W., and Janarek, F.J., 1962, *Lithium-Drifted p-i-n Junction Detectors*, IRE Transactions on Nuclear Science, Vol. 9, pp. 43-54.

Massey, D.J., David, J.P.R., and Rees, G.J., 2006, *Temperature Dependence of Impact Ionization in Submicrometer Silicon Devices*, IEEE Transactions on Electron Devices, Vol. 53, pp. 2328-2334.

Mauk, B.H., Haggerty, D.K., Jaskulek, S.E., Schlemm, C.E., Brown, L.E., Cooper, S.A., Gurnee, R.S., Hammock, C.M., Hayes, J.R., Ho, G.C., Hutcheson, J.C., Jacques, A.D., Kerem, S., Kim, C.K., Mitchell, D.G., Nelson, K.S., Paranicas, C.P., Paschalidis, N., Rossano, E., and Stokes, M.R., 2013, *The Jupiter Energetic Particle Detector Instrument (JEDI) Investigation for the Juno Mission*, Space Science Reviews, pp. 1-58.

Mazzillo, M., Condorelli, G., Castagna, M.E., Catania, G., Sciuto, A., Roccaforte, F., and Raineri, V., 2009, *Highly Efficient Low Reverse Biased 4H-SiC Schottky Photodiodes for UV-Light Detection*, IEEE Photonics Technology Letters, Vol. 21, pp. 1782-1784.

Mazzillo, M., Sciuto, A., Catania, G., Roccaforte, F., and Raineri, V., 2012, *Temperature and Light Induced Effects on the Capacitance of 4H-SiC Schottky Photodiodes*, IEEE Sensors Journal, Vol. 12, pp. 1127-1130.

McCluney, W.R., 2014, *Black Bodies and Other Sources, in Introduction to Radiometry and Photometry*, 2nd ed., Artech House, Massachusetts, USA.

McNutt, R.L., Livi, S.A., Gurnee, R.S., Hill, M.E., Cooper, K.A., Andrews, G.B., Keath, E.P., Krimigis, S.M., Mitchell, D.G., Tossman, B., Bagenal, F., Boldt, J.D., Bradley, W., Devereux, W.S., Ho, G.C., Jaskulek, S.E., LeFevere, T.W., Malcom, H., Marcus, G.A., Hayes, J.R., Moore, G.Ty, Perry, M.E., Williams, B.D., Wilson, P., Brown, L.E., Kusterer, M.B., and Vandegriff, J.D., 2008, *The Pluto Energetic Particle Spectrometer Science Investigation (PEPSSI) on the New Horizons Mission*, Space Science Reviews, Vol. 140, pp. 315-385.

McNutt, R.L., Solomon, S.C., Bedini, P.D., Anderson, B.J., Blewett, D.T., Evans, L.G., Gold, R.E., Krimigis, S.M., Murchie, S.L., Nittler, L.R., Phillips, R.J., Prockter, L.M., Slavin, J.A., Zuber, M.T., Finnegan, E.J., and Grant, D.G., 2014, *MESSENGER at Mercury: Early Orbital Operations*, Acta Astronautica, Vol. 93, pp. 509-515.

Meidinger, N., Strüder, L., Soltau, H., and von Zanthier, C., 1995, *Radiation Hardness of pn-CCDs for X-ray Astronomy*, IEEE Transactions on Nuclear Science, Vol. 42, pp. 2066-2073.

Meidinger, N., Andritschke, R., Dennerl, K., Haelker, O., Hasinger, G., Hartmann, R., Hartner, G., Herrmann, S., Holl, P., Kimmel, N., Soltau, H., and Strüder, L., 2005, *First Measurements With DUO/ROSITA PNCCDs*, SPIE proceedings, UV, X-Ray, and Gamma-Ray Space Instrumentation for Astronomy, Vol. 5898, Art. No. 58980W.

Meidinger, N., Eder, J., Eraerds, T., Nandra, K., Pietschner, D., Plattner, M., Rau, A., and Strecker, R., 2016, *The Wide Field Imager Instrument for Athena*, SPIE proceedings, Space Telescopes and Instrumentation 2016: Ultraviolet to Gamma Ray, Vol. 9905, Art. No. 99052A.

Mettivier, G., Montesi, M.C., and Russo, P., 2004, *Tritium Digital Autoradiography with a Medipix2 Hybrid Silicon Pixel Detector*, Nuclear Instruments and Methods in Physics Research A, Vol. 516, pp. 554-563.

Michaelson, H.B., 1978, *Relation between an Atomic Electronegativity Scale and the Work Function*, IBM Journal of Research and Development, Vol. 22, pp. 72-80.

Mitchell, D.L., Mazelle, C., Sauvaud, J.-A., Thocaven, J.-J., Rouzaud, J., Fedorov, A., Rouger, P., Toublanc, D., Taylor, E., Gordon, D., Robinson, M., Heavner, S., Turin, P., Diaz-Aguado, M., Curtis, D.W.,

Lin, R.P., and Jakosky, B.M., 2016, *The MAVEN Solar Wind Electron Analyzer*, Space Science Reviews, Vol. 200, pp. 495-528.

Mitsuda, K., Bautz, M., Inoue, H., Kelley, R.L., Koyama, K., Kunieda, H., Makishima, K., Ogawara, Y., Petre, R., Takahashi, T., Tsunemi, H., White, N.E., Anabuki, N., Angelini, L., Arnaud, K., Awaki, H., Bamba, A., Boyce, K., Brown, G.V., Chan, K-W., Cottam, J., Dotani, T., Doty, J., Ebisawa, K., Ezoe, Y., Fabian, A.C., Figueroa, E., Fujimoto, R., Fukazawa, Y., Furusho, T., Furuzawa, A., Gendreau, K., Griffiths, R.E., Haba, Y., Hamaguchi, K., Harrus, I., Hasinger, G., Hatsukade, I., Hayashida, K., Henry, P.J., Hiraga, J.S., Holt, S.S., Hornschemeier, A., Hughes, J.P., Hwang, U., Ishida, M., Ishisaki, Y., Isobe, N., Itoh, M., Iyomoto, N., Kahn, S.M., Kamae, T., Katagiri, H., Kataoka, J., Katayama, H., Kawai, N., Kilbourne, C., Kinugasa, K., Kissel, S., Kitamoto, S., Kohama, M., Kohmura, T., Kokubun, M., Kotani, T., Kotoku, J., Kubota, A., Madejski, G.M., Maeda, Y., Makino, F., Markowitz, A., Matsumoto, C., Matsumoto, H., Matsuoka, M., Matsushita, K., McCammon, D., Mihara, T., Misaki, K., Miyata, E., Mizuno, T., Mori, K., Mori, H., Morii, M., Moseley, H., Mukai, K., Murakami, H., Murakami, T., Mushotzky, R., Nagase, F., Namiki, M., Negoro, H., Nakazawa, K., Nousek, J.A., Okajima, T., Ogasaka, Y., Ohashi, T., Oshima, T., Ota, N., Ozaki, M., Ozawa, H., Parmar, A.N., Pence, W.D., Porter, F.S., Reeves, J.N., Ricker, G.R., Sakurai, I., Sanders, W.T., Senda, A., Serlemitsos, P., Shibata, R., Soong, Y., Smith, R., Suzuki, M., Szymkowiak, A.E., Takahashi, H., Tamagawa, T., Tamura, K., Tamura, T., Tanaka, Y., Tashiro, M., Tawara, Y., Terada, Y., Terashima, Y., Tomida, H., Torii, K., Tsuboi, Y., Tsujimoto, M., Tsuru, T.G., Turner, M.J.L., Ueda, Y., Ueno, S., Ueno, M., Uno, S., Urata, Y., Watanabe, S., Yamamoto, N., Yamaoka, K., Yamasaki, N.Y., Yamashita, K., Yamauchi, M., Yamauchi, S., Yaqoob, T., Yonetoku, D., and Yoshida, A., 2007, *The X-Ray Observatory Suzaku*, Publications of the Astronomical Society of Japan, Vol. 59, pp. S1-S7.

Miyaguchi, K., Suzuki, H., Dezaki, J. and Yamamoto, K., 1999, *CCD developed for scientific application by Hamamatsu*, Nuclear Instruments and Methods in Physics Research A, Vol. 436, pp. 24-31.

Moldovan, G., Sikharulidze, I., Matheson, J., Derbyshire, G., Kirkland, A.I., and Abrahams, J.P., 2012, *Characterisation of a Counting Imaging Detector for Electron Detection in the Energy Range 10–20 keV*, Nuclear Instruments and Methods in Physics Research A, Vol. 681, pp. 21-24.

Molokovsky, S.I., and Sushkov, A.D., 2005, *Electron and Ion Sources with Field and Plasma Emitters, in Intense Electron and Ion Beams*, Springer, Berlin, Germany, pp. 157-167.

Monroy, E., Omnès, F., and Calle, F., 2003, *Wide-Bandgap Semiconductor Ultraviolet Photodetectors*, Semiconductor Science and Technology, Vol. 18, pp. R33-R51.

Müller, D., Marsden, R.G., St. Cyr, O.C., and Gilbert, H.R., 2013, *Solar Orbiter*, Solar Physics, Vol. 285, pp. 25-70.

Münch, U., Blum, N., and Halbach, P., 1999, *Mineralogical and Geochemical Features of Sulfide Chimneys from the MESO Zone, Central Indian Ridge*, Chemical Geology, Vol. 155, pp. 29-44.

Nakamura, T., Noguchi, T., Tanaka, M., Zolensky, M.E., Kimura, M., Tsuchiyama, A., Nakato, A., Ogami, T., Ishida, H., Uesugi, M., Yada, T., Shirai, K., Fujimura, A., Okazaki, R., Sandford, S.A., Ishibashi, Y., Abe, M., Okada, T., Ueno, M., Mukai, T., Yoshikawa, M., and Kawaguchi, J., 2011, *Itokawa Dust Particles: A Direct Link Between S-Type Asteroids and Ordinary Chondrites*, Science, Vol. 333, pp. 1113-1116.

Nava, F., Vittone, E., Vanni, P., Verzellesi, G., Fuochi, P.G., Lanzieri, C., and Glaser, M., 2003, *Radiation Tolerance of Epitaxial Silicon Carbide Detectors for Electrons, Protons and Gamma-Rays*, Nuclear Instruments and Methods in Physics Research A, Vol. 505, pp. 645-655.

Nava, F., Bertuccio, G., Cavallini, A., and Vittone, E., 2008, *Silicon Carbide and its Use as a Radiation Detector Material*, Measurement Science and Technology, Vol. 19, Art. No. 102001.

Neudeck, P.G., Okojie, R.S., and Chen, L.-Y., 2002, *High-Temperature Electronics - a Role for Wide Bandgap Semiconductors?*, Proceedings of the IEEE, Vol. 90, pp. 1065-1076.

Neudeck, P.G., Garverick, S.L., Spry, D.J., Chen, L-Y., Beheim, G.M., Krasowski, M.J., and Mehregany, M., 2009, *Extreme Temperature 6H-SiC JFET Integrated Circuit Technology*, Physica Status Solidi (a), Vol. 206, pp. 2329-2345.

Ng, J.S., Meng, X., Lees, J.E., Barnett, A.M., and Tan, C.H., 2014, *Fabrication Study of GaAs Mesa Diodes for X-ray Detection*, Journal of Instrumentation, Vol. 9, Art. No. T08005

Nikjoo, H., Uehara, S., and Emfietzoglou, D., 2012, *Interaction of Radiation with Matter*, CRC Press, Florida, USA.

Norton, M.P., and Karczub, D.G., 2003, *Fundamental of Noise and Vibration Analysis for Engineers*, 2nd ed., Cambridge University Press, UK, p. 352.

O'Flynn, D., Desai, H., Reid, C.B., Christodoulou, C., Wilson, M.D., Veale, M.C., Seller, P., Hills, D., Wong, B., and Speller, R.D., 2013, *Identification of Simulants for Explosives Using Pixellated X-ray Diffraction*, Crime Science, Vol. 2, pp. 1-6.

Okada, T., Shirai, K., Yamamoto, Y., Arai, T., Ogawa, K., Hosono, K., and Kato, M., 2006, *X-ray Fluorescence Spectrometry of Asteroid Itokawa by Hayabusa*, Science, Vol. 312, pp. 1338-1341.

Owens, A., 1985, *Spectral Degradation Effects in an 86 cm3 Ge(HP) Detector*, Nuclear Instruments and Methods in Physics Research A, Vol. 238, pp. 473-478.

Owens, A., Bavdaz, M., Peacock, A., Poelaert, A., Andersson, H., Nenonen, S., Sipila, H., Tröger, L., and Bertuccio, G., 2001, *High Resolution X-Ray Spectroscopy Using GaAs Arrays*, Journal of Applied Physics, Vol. 90, pp. 5376-5381.

Owens, A., Bavdaz, M., Andersson, H., Gagliardi, T., Krumrey, M., Nenonen, S., Peacock, A., Taylor, I., and Tröger, L., 2002a, *The X-ray Response of CdZnTe*, Nuclear Instruments and Methods in Physics Research A, Vol. 484, pp. 242-250.

Owens, A., Andersson, H., Bavdaz, M., van den Berg, L., Peacock, A., and Puig, A., 2002b, *The Hard X-ray Response of a Large Area HgI_2 Detector*, Nuclear Instruments and Methods in Physics Research A, Vol. 487, pp. 90-95.

Owens, A., Peacock, A.J., and Bavdaz, M., 2003, *Progress in Compound Semiconductors*, SPIE proceedings, X-ray and Gamma-Ray Telescopes and Instruments for Astronomy, Vol. 4851, pp. 1059-1070.

Owens, A., 2012a, *Compound Semiconductor Radiation Detectors*, CRC Press, Florida, USA.

Owens, A., Barnes, A., Farley, R.A., Germain, M., and Sellin, P.J., 2012b, *GaN Detector Development for Particle and X-ray Detection*, Nuclear Instruments and Methods in Physics Research A, Vol. 695, pp. 303-305.

Oxner, E.S., 1989, *FET Technology and Application. An Introduction*, Marcel Dekker, New York, USA, p. 76.

Özer, M., Yıldız, D.E., Altındal, Ş., and Bülbül, M.M., 2007, *Temperature Dependence of Characteristic Parameters of the Au/SnO2/n-Si (MIS) Schottky Diodes*, Solid-State Electronics, Vol. 51, pp. 941-949.

Page, M.J., Yershov, V., Breeveld, A., Kuin, P., Mignani, R., Smith, P.J., Rawlings, J., Oates, S., Siegel, M., and Roming, P., 2014, *The Swift UVOT Serendipitous Source Catalogue*, Proceedings of Swift: 10 Years of Discovery (SWIFT 10), 2-5 Decembr 2014, Rome, Italy.

Palik, E.D., 1997, *Gallium Arsenide (GaAs), in Handbook of Optical Constants of Solids*, Academic Press, Burlington, pp. 429-443.

Palmour, J.W., Levinshtein, M.E., Rumyantsev, S.L., and Simin, G.S., 1996, *Low-Frequency Noise in 4H-Silicon Carbide Junction Field Effect Transistors*, Applied Physics Letters, Vol. 68, pp. 2669-2671.

Pantazis, T., Pantazis, J., Huber, A., and Redus, R., 2010, *The Historical Development of the Thermoelectrically Cooled X-ray Detector and its Impact on the Portable and Hand-Held XRF Industries*, X-ray Spectrometry, Vol. 39, pp. 90-97.

Paranicas, C., Cooper, J.F., Garrett, H.B., Johnson, R.E., and Sturner, S.J., 2009, *Europa's radiation environment and its effects on the surface, in Europa*, University of Arizona Press, Tucson, pp. 529-545.

Park, K.S., 1997, *High Quantum-Efficiency 4H-SiC UV Photodiode*, Journal of the Korean Physical Society, Vol. 30, pp. 123-130.

Park, S.W., 2012, *Key Issues on the Commercial Development of Deep Seabed Mineral Resources*, in LOSI Conference on Securing the Ocean for the Next Generation, 21-24 May, Korea.

Patrick, L., and Choyke, W.J., 1970, *Static Dielectric Constant of SiC*, Physical Review B, Vol. 2, pp. 2255-2256.

Pell, E.M., 1960, *Ion Drift in an n-p Junction*, Journal of Applied Physics, Vol. 31, pp. 291-302.

Potts, P.J., and West, M., 2008, *Portable X-ray Fluorescence Spectroscopy: Capabilities for in-situ Analysis*, RSC Publishing, Cambridge, UK.

Powell, J., Powell, J., Maise, G., and Paniagua, J., 2005, *NEMO: A Mission to Search for and Return to Earth Possible Life Forms on Europa*, Acta Astronautica, Vol. 57, pp. 579-593.

Prasai, D., John, W., Weixelbaum, L., Krüger, O., Wagner, G., Sperfeld, P., Nowy, S., Friedrich, D., Winter, S., and Weiss, T., 2012, *Highly Reliable Silicon Carbide Photodiodes for Visible-Blind Ultraviolet Detector Applications*, Journal of Materials Research, Vol. 28, pp. 33-37.

Preiss, I.L., Fink, R.W., and Robinson, B.L., 1957, *The Beta Spectrum of Carrier-Free Ni63*, Journal of Inorganic and Nuclear Chemistry, Vol. 4, pp. 233-236.

Prettyman, T.H., Feldman, W.C., McSween, H.Y., Dingler, R.D., Enemark, D.C., Patrick, D.E., Storms, S.A., Hendricks, J.S., Morgenthaler, J.P., Pitman, K.M., and Reedy, R.C., 2012, *Dawn's Gamma Ray and Neutron Detector, in The Dawn Mission to Minor Planets 4 Vesta and 1 Ceres*, Springer, New York, USA, pp. 371-459.

Pullia, A., and Bertuccio, G., 1996, *Resolution Limits of Silicon Detectors and Electronics for Soft X-ray Spectroscopy at Non Cryogenic Temperatures*, Nuclear Instruments and Methods in Physics Research A, Vol. 380, pp. 1-5.

Puri, S., Shahi, J.S., Chand, B., Garg, M.L., Singh, N., Trehan, P.N., and Nath, N., 1998, *Elemental Analysis of Polymetallic Nodules from the Central Indian Basin: a Study Using EDXRF*, X-ray Spectrometry, Vol. 27, pp. 105-110.

Radeka, V., 1973, *Field Effect Transistors for Charge Amplifiers*, IEEE Transactions on Nuclear Science, Vol. 20, pp. 182-189.

Raghunathan, R., and Baliga, B.J., 1999, *Temperature Dependence of Hole Impact Ionization Coefficients in 4H and 6H-SiC*, Solid State Electronics, Vol. 43, pp. 199-211.

Ramo, S., 1939, *Currents induced by electron motion*, Proceedings of the IRE, Vol. 27, pp. 584-585.

Redus, R., Huber, A., Pantazis, J., and Pantazis, T., 2011, *Enhanced Energy Range Thermoelectrically Cooled Silicon X-ray Detectors*, Proceedings of the IEEE Nuclear Science Symposium and Medical Imaging Conference, pp. 580-585.

Renker, D., and Lorenz, E., 2009, *Advances in Solid State Photon Detectors*, Journal of Instrumentation, Vol. 4, Art. No. P04004.

Rieder, R., Economou, T., Wänke, H., Turkevich, A., Crisp, J., Brückner, J., Dreibus, G., and McSween, H.Y., 1997, *The Chemical Composition of Martian Soil and Rocks Returned by the Mobile Alpha Proton X-ray Spectrometer: Preliminary Results from the X-ray Mode*, Science, Vol. 278, pp. 1771-1774.

Rieder, R., Gellert, R., Brückner, J., Klingelhöfer, G., Dreibus, G., Yen, A., and Squyres, S.W., 2003, *The new Athena alpha particle X-ray spectrometer for the Mars Exploration Rovers*, Journal of Geophysical Research: Planets, Vol. 108.

Roccaforte, F., La Via, F., Raineri, V., Pierobon, R., and Zanoni, E., 2003a, *Richardson's Constant in Inhomogeneous Silicon Carbide Schottky Contacts*, Journal of Applied Physics, Vol. 93, pp. 9137-9144.

Roccaforte, F., La Via, F., La Manga, A., Di Franco, S., and Raineri, V., 2003b, *Silicon Carbide Pinch Rectifiers Using a Dual-Metal Ti-Ni_2Si Schottky Barrier*, IEEE Transactions on Electron Devices, Vol. 50, pp. 1741-1747.

Roccaforte, F., La Via, F., Raineri, V., Musumeci, P., Calcagno, L., and Condorelli, G.G., 2003c, *Highly Reproducible Ideal SiC Schottky Rectifiers: Effects of Surface Preparation and Thermal Annealing on the Ni/6H-SiC Barrier Height*, Applied Physics A, Vol. 77, pp. 827-833.

Roming, P.W.A., Kennedy, T.E., Mason, K.O., Nousek, J.A., Ahr, L., Bingham, R.E., Broos, P.S., Carter, M.J., Hancock, B.K., Huckle, H.E., Hunsberger, S.D., Kawakami, H., Killough, R., Koch, T.S., Mclelland, M.K., Smith K., Smith P.J., Soto J.C., Boyd P.T., Breeveld A.A., Holland S.T., Ivanushkina M., Pryzby M.S., Still, M.D., and Stock, J., 2005, *The Swift Ultra-Violet/Optical Telescope*, Space Science Reviews, Vol. 120, pp. 95-142.

Rossi, L., Fischer, P., Rohe, T., and Wermes, N., 2006, *Pixel Detectors: From Fundamentals to Applications*, Springer-Verlag, Berlin, Germany, pp. 123.

Roth, L., Saur, J., Retherford, K.D., Strobel, D.F., Feldman, P.D., McGrath, M.A., and Nimmo, F., 2014, *Transient Water Vapor at Europa's South Pole*, Science, Vol. 343, pp. 171-174.

Šagátová, A., Zat'ko, B., Pavlovič, M., Sedlačková, K., Hybler, P., Dubecký, F., and Nečas, V., 2014, *GaAs Detectors Irradiated by Low Doses of Electrons*, Journal of Instrumentation, Vol. 9, Art. No. C04036.

Saleh, B.E.A., and Teich, M.C., 1991, *Semiconductor Photon Detectors, in Fundamentals of Photonics*, John Wiley & Sons, New York, USA, pp. 644-695.

Sánchez del Rio, M., Brunetti, A., Golosio, B., Somogyi, A., and Simionovici, A., 2003, *XRAYLIB Tables (X-ray Fluorescence Cross-Section)*, European Synchrotron Radiation Facility and University of Sassari.

Schieber, M., James, R.B., Lund, J.C., McGregor, D.S., Gilbert, T.S., Van Scyoc, J.M., Olsen, R.W., Pontau, A.E., Schlesinger, T.S., and Toney, J., 1996, *State of the Art of Wide-Bandgap Semiconductor Nuclear Radiation Detectors*, in II International Conference on Large-Scale Applications and Radiation Hardness of Semiconductor Detectors, 28-30 June 1995, Florence, Italy.

Schindler, K., 2007, *Physics of Space Plasma Activity*, Cambridge University Press, Cambridge, UK, p. 22.

Schlemm, C.E., Starr, R.D., Ho, G.C., Bechtold, K.E., Hamilton, S.A., Boldt, J.D., Boynton, W.V., Bradley, W., Fraeman, M.E., Gold, R.E., Goldsten, J.O., Hayes, J.R., Jaskulek, S.E., Rossano, E., Rumpf, R.A., Schaefer, E.D., Strohbehn, K., Shelton, R.G., Thompson, R.E., Trombka, J.I., and Williams, B.D., 2007, *The X-ray Spectrometer on the MESSENGER Spacecraft*, Space Science Reviews, Vol. 131, pp. 393-415.

Schmidt-Ott, W.D., Bosch, U., and Möhlenkamp, Th., 1989, *PIN-Diodes for Electron Detection*, Nuclear Instruments and Methods in Physics Research A, Vol. 285, pp. 459-463.

Schötzig, U., 2000, *Half-Life and X-ray Emission Probabilities of ^{55}Fe*, Applied Radiation and Isotopes, Vol. 53, pp. 469-472.

Schroder, D., 2006, *Semiconductor Material and Device Characterisation*, 3rd ed., John Wiley & Sons, New Jersey.

Sciuto, A., Roccaforte F., Di Franco S., Raineri V., and Bonanno G., 2006, *High Responsivity 4H-SiC Schottky UV Photodiodes Based on the Pinch-off Surface Effect*, Applied Physics Letters, Vol. 89, Art. No. 081111.

Sciuto, A., Mazzillo M., Badala P., Scuderi M., Carbone B., and Coffa S., 2014, *Thin Metal Film Ni2Si/4H-SiC Vertical Schottky Photodiodes*, IEEE Photonics Technology Letters, Vol. 26, pp. 1782-1785.

Scott, S.D., 2001, *Deep Ocean Mining*, Geoscience Canada, Vol. 28, pp. 87-96.

Sellai, A., 2008, *Temperature Dependence of Dark Current in a Si-pin Photodiode*, in Proceedings of the IEEE International Conference on Semiconductor Electronics, Johor, Malaysia, 25 November – 27 November 2008, pp. 267-270.

Sellin, P.J., and Vaitkus, J., 2006, *New Materials for Radiation Hard Semiconductor Detectors*, Nuclear Instruments and Methods in Physics Research A, Vol. 557, pp. 479-489.

Seward, F.D., and Charles, P.A., 2010, *Exploring the X-ray Universe*, 2nd ed., Cambridge University Press, New York, USA.

Sheldon, M.T., Eisler, C.N., and Atwater, H.A., 2012, *GaAs Passivation with Trioctylphosphine Sulfide for Enhanced Solar Cell Efficiency and Durability*, Advanced Energy Materials, Vol. 2, pp. 339-344.

Sherer, M.A.S., Visconti, P.J., Ritenour, E.R., and Haynes, K., 2014, *Radiation Protection in Medical Radiography*, 7th ed., Elsevier Health Sciences, Missouri, USA, pp. 48.

Shirai, K., Okada, T., Yamamoto, Y., Arai, T., Ogawa, K., Shiraishi, H., Iwasaki, M., Arakawa, M., Grande, M., and Kato, M., 2008, *Instrumentation and Performance Evaluation of the XRS on SELENE Orbiter*, Earth, Planets and Space, Vol. 60, pp. 277-281.

Shockley, W., 1938, *Currents to conductors induced by a moving point charge*, Journal of Applied Physics, Vol. 9, pp. 635-636.

Shur, M., Rumyantsev, S., and Levinshtein, M., 2006, *SiC Materials and Devices*, Word Scientific, Singapore.

Siegmund, O.H.W., Vallerga, J., and Wargelin, B., 1988, *Background Events in Microchannel Plates*, IEEE Transactions on Nuclear Science, Vol. 35, pp. 524-528.

Siliconix, 2001, *2N4416/2N4416A/SST4416 N-Channel JFETs*, Data Sheet, 70242 S-04028, Rev. F, 04-Jun-01, Vishay Electronic GmbH, Selb, Germany.

Sinclair, C.K., 2003, V*ery High Voltage Photoemmision Electron Guns*, Proceedings of the Particle Accelerator Conference, Vol. 1, pp. 76-80.

Singh, K.P., Tandon, S.N., Agrawal, P.C., Antia, H.M., Manchanda, R.K., Yadav, J.S., Seetha, S., Ramadevi, M.C., Rao, A.R., Bhattacharya, D., Paul, B., Sreekumar, P., Bhattacharyya, S., Stewart, G.C., Hutchings, J., Annapurni, S.A., Ghosh, S.K., Murthy, J., Pati, A., Rao, N.K., Stalin, C.S., Girish, V., Sankarasubramanian, K., Vadawale, S., Bhalerao, V.B., Dewangan, G.C., Dedhia, D.K., Hingar, M.K., Katoch, T.B., Kothare, A.T., Mirza, I., Mukerjee, K., Shah, H., Shah, P., Mohan, R., Sangal, A.K., Nagabhusana, S., Sriram, S., Malkar, J.P., Sreekumar, S., Abbey, A.F., Hansford, G.M., Beardmore, A.P., Sharma, M.R., Murthy, S., Kulkarni, R., Meena, G., Babu, V.C., and Postma, J., 2014, *ASTROSAT mission*, SPIE proceedings, Space Telescopes and Instrumentation: Ultraviolet to Gamma Ray, Vol. 9144, Art. No. 91441S.

Smith, G., and Leach, S., Nautilus Minerals Pacific Pty Ltd, 2014, *A Method of Subsea Testing Using a Remotely Operated Vehicle*, Australia, WO 2014/015363 A1.

Solomon, S.C., McNutt Jr, R.L., Gold, R.E., Acuña, M.H., Baker, D.N., Boynton, W.V., Chapman, C.R., Cheng, A.F., Gloeckler, G., Head III, J.W., Krimigis, S.M., McClintock, W.E., Murchie, S.L., Peale, S.J., Phillips, R.J., Robinson, M.S., Slavin, J.A., Smith, D.E., Strom, R.G., Trombka, J.I., and Zuber, M.T., 2001, *The MESSENGER Mission to Mercury: Scientific Objectives and Implementation*, Planetary and Space Science, Vol. 49, pp. 1445-1465.

Son, N.T., Chen, W.M., Kordina, O., Konstantinov, A.O., Monemar, B., Janzén, E., Hofman, D.M., Volm, D., Drechsler, M., and Meyer, B.K., 1995, *Electron Effective Masses in 4H-SiC*, Applied Physics Letters, Vol. 66, pp. 1074-1076.

Sparks, W.B., Hand, K.P., McGrath, M.A., Bergeron, E., Cracraft, M., and Deustua, S.E., 2016, *Probing for Evidence of Plumes on Europa with HST/STIS*, The Astrophysical Journal, Vol. 829, Art. No. 121.

Spieler, H., 2005, *Semiconductor Detector Systems*, Oxford University Press, New York, USA.

Sridhara, S.G., Devaty, R.P., and Choyke, W.J., 1998, *Absorption Coefficient of 4H Silicon Carbide from 3900 to 3250 Å*, Journal of Applied Physics, Vol. 84, pp. 2963-2964.

Stearns, D.G., and Wiedwald, J.D., 1989, *Response of Charge-Coupled Devices to Direct Electron Bombardment*, Review of Scientific Instrument, Vol. 60, pp. 1095-1103.

Stein, H.J., 1969, *Electrical Studies of Low-Temperature Neutron- and Electron-Irradiated Epitaxial n-Type GaAs*, Journal of Applied Physics, Vol. 40, pp. 5300-5307.

Stevens, R.C., Vassilevski, K., Lees, J.E., Wright, N.G., and Horsfall, A.B., 2011, *Effect of Proton Irradiation Induced Defects on 4H-SiC Schottky Diode X-Ray Detectors*, Materials Science Forum, Vols. 679-680, pp. 547-550.

Street, R.A., 2000, *Technology and Applications of Amorphous Silicon*, Springer-Verlag, Berlin, Germany.

Strüder, L., Meidinger, N., Stotter, D., Kemmer, J., Lechner, P., Leutenegger, P., Soltau, H., Eggert, F., Rohde, M., and Schulein, T., 1999, *High-Resolution X-ray Spectroscopy Close to Room Temperature*, Microscopy and Microanalysis, Cambridge University Press, Vol. 4, pp. 622-631.

Strüder, L., Briel, U., Dennerl, K., Hartmann, R., Kendziorra, E., Meidinger, N., Pfeffermann, E., Reppin, C., Aschenbach, B., Bornemann, W., Bräuninger, H., Burkert, W., Elender, M., Freyberg, M., Haberl, F., Hartner, G., Heuschmann, F., Hippmann, H., Kastelic, E., Kemmer, S., Kettenring, G., Kink, W., Krause, N., Müller, S., Oppitz, A., Pietsch, W., Popp, M., Predehl, P., Read, A., Stephan, K.H., Stötter, D., Trümper, J., Holl, P., Kemmer, J., Soltau, H., Stötter, R., Weber, U., Weichert, U., von Zanthier, C., Lutz, G., Richter, R.H., Solc, P., Böttcher, H., Kuster, M., Staubert, R., Abbey, A., Holland, A., Turner, M., Balasini, M., Bignami, G.F., La Palombara, N., Villa, G., Buttler, W., Gianini, F., Lainé, R., Lumb, D., and Dhez, P., 2001, *The European Photon Imaging Camera on XMM-Newton: The pn-CCD Camera*, Astronomy and Astrophysics, Vol. 365, pp. L18-L26.

Sussmann, R.S., 2009, *CVD Diamond for Electronic Devices and Sensors*, John Wiley & Sons, Chichester, UK.

Swinyard, B.M., Joy, K.H., Kellett, B.J., Crawford, I.A., Grande, M., Howe, C.J., Fernandes, V.A., Gasnault, O., Lawrence, D.J., Russell, S.S., Wieczorek, M.A., and Foing, B.H., 2009, *X-ray Fluorescence Observations of the Moon by SMART-1/D-CIXS and the First Detection of Ti Kα from the Lunar Surface*, Planetary and Space Science, Vol. 57, pp. 744-750.

Sze, S.M., 1981, *Physics of Semiconductor Devices*, 2nd ed., John Wiley & Sons, New Jersey.

Sze, S.M., and Ng, K.K., 2007, *Physics of Semiconductor Devices*, 3rd ed., John Wiley & Sons, New Jersey.

Szűcs, B., Hajnal, Z., Frauenheim Th. González, C., Ortega, J., Pérez, R., and Flores, F., 2003, *Chalcogen Passivation of GaAs (1 0 0) Surfaces: A Theoretical Study*, Applied Surface Science, Vol. 212-213, pp. 861-865.

Takahashi, T., Kokubun, M., Mitsuda, K., Kelley, R., Ohashi, T., Aharonian, F., Akamatsu, H., Akimoto, F., Allen, S., Anabuki, N., Angelini, L., Arnaud, K., Asai, M., Audard, M., Awaki, H., Axelsson, M., Azzarello, P., Baluta, C., Bamba, A., Bando, N., Bautz, M., Bialas, T., Blandford, R., Boyce, K., Brenneman, L., Brown, G., Bulbul, E., Cackett, E., Canavan, E., Chernyakova, M., Chiao, M., Coppi, P., Costantini, E., de Plaa, J., den Herder, J.-W., DiPirro, M., Done, C., Dotani, T., Doty, J., Ebisawa, K., Eckart, M., Enoto, T., Ezoe, Y., Fabian, A., Ferrigno, C., Foster, A., Fujimoto, R., Fukazawa, Y., Furuzawa, A., Galeazzi, M., Gallo, L., Gandhi, P., Gilmore, K., Giustini, M., Goldwurm, A., Gu, L., Guainazzi, M., Haas, D., Haba, Y., Hagino, K., Hamaguchi, K., Harayama, A., Harrus, I., Hatsukade, I., Hayashi, T., Hayashi, K., Hayashida, K., Hiraga, J., Hirose, K., Hornschemeier, A., Hoshino, A., Hughes, J., Ichinohe, Y., Iizuka, R., Inoue, Y., Inoue, H., Ishibashi, K., Ishida, M., Ishikawa, K., Ishimura, K., Ishisaki, Y., Itoh, M., Iwata, N., Iyomoto, N., Jewell, C., Kaastra, J., Kallman, T., Kamae, T., Kara, E., Kataoka, J., Katsuda, S., Katsuta, J., Kawaharada, M., Kawai, N., Kawano, T., Kawasaki, S., Khangulyan, D., Kilbourne, C., Kimball, M., King, A., Kitaguchi, T., Kitamoto, S., Kitayama, T., Kohmura, T., Kosaka, T., Koujelev, A., Koyama, K., Koyama, S., Kretschmar, P., Krimm, H., Kubota, A., Kunieda, H., Laurent, P., Lebrun, F., Lee, S.-H., Leutenegger, M., Limousin, O., Loewenstein, M., Long, K., Lumb, D., Madejski, G., Maeda, Y., Maier, D., Makishima, K., Markevitch, M., Masters, C., Matsumoto, H., Matsushita, K., McCammon, D., McGuinness, D., McNamara, B., Mehdipour, M., Miko, J., Miller, J., Miller, E., Mineshige, S.,

Minesugi, K., Mitsuishi, I., Miyazawa, T., Mizuno, T., Mori, K., Mori, H., Moroso, F., Moseley, H., Muench, T., Mukai, K., Murakami, H., Murakami, T., Mushotzky, R., Nagano, H., Nagino, R., Nakagawa, T., Nakajima, H., Nakamori, T., Nakano, T., Nakashima, S., Nakazawa, K., Namba, Y., Natsukari, C., Nishioka, Y., Nobukawa, M., Nobukawa, K., Noda, H., Nomachi, M., O'Dell, S., Odaka, H., Ogawa, H., Ogawa, M., Ogi, K., Ohno, M., Ohta, M., Okajima, T., Okamoto, A., Okazaki, T., Ota, N., Ozaki, M., Paerels, F., Paltani, S., Parmar, A., Petre, R., Pinto, C., Pohl, M., Pontius, J., Porter, F.S., Pottschmidt, K., Ramsey, B., Reynolds, C., Russell, H., Safi-Harb, S., Saito, S., Sakai, S., Sakai, K., Sameshima, H., Sasaki, T., Sato, G., Sato, Y., Sato, K., Sato, R., Sawada, M., Schartel, N., Serlemitsos, P., Seta, H., Shibano, Y., Shida, M., Shidatsu, M., Shimada, T., Shinozaki, K., Shirron, P., Simionescu, A., Simmons, C., Smith, R., Sneiderman, G., Soong, Y., Stawarz, Ł., Sugawara, Y., Sugita, H., Sugita, S., Szymkowiak, A., Tajima, H., Takahashi, H., Takeda, S., Takei, Y., Tamagawa, T., Tamura, T., Tamura, K., Tanaka, T., Tanaka, Y., Tanaka, Y., Tashiro, M., Tawara, Y., Terada, Y., Terashima, Y., Tombesi, F., Tomida, H., Tsuboi, Y., Tsujimoto, M., Tsunemi, H., Tsuru, T., Uchida, H., Uchiyama, Y., Uchiyama, H., Ueda, Y., Ueda, S., Ueno, S., Uno, S., Urry, M., Ursino, E., de Vries, C., Wada, A., Watanabe, S., Watanabe, T., Werner, N., Wik, D., Wilkins, D., Williams, B., Yamada, T., Yamada, S., Yamaguchi, H., Yamaoka, K., Yamasaki, N., Yamauchi, M., Yamauchi, S., Yaqoob, T., Yatsu, Y., Yonetoku, D., Yoshida, A., Yuasa, T., Zhuravleva, I., and Zoghbi, A., 2016, *The ASTRO-H (Hitomi) X-Ray Astronomy Satellite*, SPIE proceedings, Space Telescopes and Instrumentation: Ultraviolet to Gamma Ray, Vol. 9905, Art. No. 99050U.

Takenaka, M., Morii, K., Sugiyama, M., Nakano, Y., and Takagi, S., 2012, *Dark Current Reduction of Ge Photodetector by GeO2 Surface Passivation and Gas-Phase Doping*, Optics Express, Vol. 20, pp. 8718-8725.

Talboys, D.L., Potts, P.J., Fraser, G.W., Butcher, G., and Wegrzynek, D., 2009, *The comparative analytical performance of the Beagle 2 X-ray Spectrometer for in-situ geochemical analysis on Mars*, X-ray Spectrometry, Vol. 38, pp. 417-428.

Tatsuhiko, U., Takao, K., Masahiro, T., Satoshi, T., Takeshi, I., and Katsuyoshi, T., 2010, *Detection Efficiency of Plastic Scintillator for Gaseous Tritium Sampling and Measurement System*, Fusion Engineering and Design, Vol. 85, pp. 1474-1478.

Thompson, A., Attwood, D., Gullikson, E., Howells, M., Kim, K.J., Kirz, J., Kortright, J., Lindau, I., Liu, Y., Pianetta, P., Robinson, A., Scofield, J., Underwood, J., Williams, G., and Winick, H., 2009, *X-Ray Data Booklet (Center for X-Ray Optics and Advanced Light Source)*, Lawrence Berkeley National Laboratory, Berkeley, California.

Tivey, M., 1998, *How to Build a Black Smoker Chimney. The Formation of Mineral Deposits at Mid-Ocean Ridges*, Oceanus Magazine, Vol. 41.

Torvik, J.T., Pankove, J.I., and Van Zeghbroeck, B.J., 1999, *Comparison of GaN and 6H-SiC p-i-n Photodetectors with Excellent Ultraviolet Sensitivity and Selectivity*, IEEE Transactions on Electron Devices, Vol. 46, pp. 1326-1331.

Trofimenkoff, F.N., 1965, *Field-Dependent Mobility Analysis of the Field-Effect Transistor*, Proceedings of the IEEE, Vol. 53, pp. 1765-1766.

Trümper, J.E., and Hasinger, G., 2008, *The Universe in X-rays*, Springer-Verlag, Berlin, Germany.

Tsoulfanidis, N., 1995, *Measurement and Detection of Radiation*, 2nd ed., Taylor & Francis, Washington, USA.

Tsuji, K., Injuk, J., and Van Grieken, R., 2004, *X-Ray Spectrometry: Recent Technological Advances*, John Wiley & Sons, Chichester, UK.

Tsunemi, H., Hayashida, K., Tsuru, T.G., Dotani, T., Hiraga, J.S., Anabuki, N., Bamba, A., Hatsukade, I., Kohmura, T., Mori, K., Murakami, H., Nakajima, H., Ozaki, M., Uchida, H., and Yamauchi, M., 2010, *Soft X-ray Imager (SXI) Onboard ASTRO-H*, SPIE proceedings, Space Telescopes and Instrumentation: Ultraviolet to Gamma Ray, Vol. 7732, Art. No. 77321O.

Tumakha, S., Ewing, D.J., Porter, L.M., Wahab, Q., Ma, X., Sudharshan, T.S., and Brillson, L.J., 2005, *Defect-Driven Inhomogeneities in Ni/4H–SiC Schottky Barriers*, Applied Physics Letters, Vol. 87, Art. No. 242106.

Tung, R.T., 1991, *Electron Transport of Inhomogeneous Schottky Barriers*, Applied Physics Letters, Vol. 58, pp. 2821-2823.

Tyagi, M.S., and Van Overstraeten, R., 1983, *Minority Carrier Recombination in Heavily-Doped Silicon*, Solid-State Electronics, Vol. 26, pp. 577-597.

Ulrici, J., Fischer, P., Klein, P., Lutz, G., Neeser, W., Richter, R., Strüder, L., Trimpl, M., and Wermes, N., 2005, *Imaging Performance of a DEPFET Pixel Bioscope System in Tritium Autoradiography*, Nuclear Instruments and Methods in Physics Research A, Vol. 547, pp. 424-436.

Unicam, 2000, *Unicam UV Series User Manual*, 9499-230-43311 Issue 2a, ThermoSpectronic, Cambridge, UK.

Ung, J.W., and Karacolak, T., 2013, *Silicon Carbide (SiC) Antennas for Extreme Environment Sensing Applications*, Radio Science Meeting, USNC-URSI, 7-13 July, Orlando, Florida, USA.

Vallerga, J., Zaninovich, J., Welsh, B., Siegmund, O., McPhate, J., Hull, J., Gaines, G., and Buzasi, D., 2002, *The FUV detector for the cosmic origins spectrograph on the Hubble Space Telescope*, Nuclear Instruments and Methods in Physics Research A, Vol. 477, pp. 551-555.

Van der Ziel, A., 1963, *Gate Noise in Field Effect Transistors at Moderately High Frequencies*, Proceedings of the IEEE, Vol. 51, pp. 461-467.

Van Grieken, R., and Markowicz, A., 2002, *Handbook of X-ray Spectrometry*, 2nd ed., CRC Press.

Vapirev, E.I., Sueva, D., Spassov, V., Chikov, N., and Ivanov, I., 1994, *Detection of β-particles, Conversion Electrons and γ-rays with Silicon Planar Detectors*, Applied Radiation and Isotopes, Vol. 45, pp. 453-459.

Vasilescu, G., 2005, *Electronic Noise and Interfering Signals. Principles and Applications*, Springer-Verlag, Berlin, Germany.

Vavilov, V.S., 1965, *Effects of Radiation on Semiconductors*, Springer Science and Business Media, New York, USA.

Von Damm, K.L., 1990, *Seafloor Hydrothermal Activity: Black Smoker Chemistry and Chimneys*, Annual Review of Earth and Planetary Sciences, Vol. 18, pp. 173-204.

Wang, W., Lee, G., Huang, M., Wallace, R.M., and Cho, K., 2010, *First-Principles Study of GaAs(001)-β2(2×4) Surface Oxidation and Passivation with H, Cl, S, F, and GaO*, Journal of Applied Physics, Vol. 107, Art. No. 103720.

Watanabe, N., Kimoto, T., and Suda, J., 2012, *4H-SiC pn Photodiodes with Temperature-Independent Photoresponse up to 300 °C*, Applied Physics Express, Vol. 5, Art. No. 094101.

Weisskopf, M.C., Brinkman, B., Canizares, C., Garmire, G., Murray, S., and Van Speybroeck, L.P., 2002, *An Overview of the Performance and Scientific Results from the Chandra X-Ray Observatory*, Publications of the Astronomical Society of the Pacific, Vol. 114, pp. 1-24.

Wermes, N., 2003, *Pixel detectors for particle physics and imaging applications*, Nuclear Instruments and Methods in Physics Research A, Vol. 512, pp. 277-288.

Wermes, N., Andricek, L., Fischer, P., Harter, M., Herrmann, S., Karagounis, M., Kohrs, R., Kruger, H., Lutz, G., Lechner, P., Peric, I., Porro, M., Richter, R., Soltau, H., Struder, L., Trimpl, M., Ulrici, J., and Treis, J., 2003, *New Results on DEPFET Pixel Detectors for Radiation Imaging and High Energy Particle Detection*, Proceedings of the IEEE Nuclear Science Symposium, Vol. 1, pp. 325-330.

Whitaker, M.D.C., Lioliou, G., Butera, S., and Barnett, A.M., 2016, *$Al_{0.2}Ga_{0.8}As$ X-ray Photodiodes for X-ray Spectroscopy*, Nuclear Instruments and Methods in Physics Research A, Vol. 840, pp. 168-173.

White, J.F., 1982, *Practical PIN Diodes, in Microwave Semiconductor Engineering*, Springer, Dordrecht, Netherlands, pp. 91-115.

Wight, D.R., Oliver, P.E., Prentice, T., and Steward, V.W., 1981, *Diffusion Lengths in p-type MOCVD GaAs*, Journal of Crystal Growth, Vol. 55, pp. 183-191.

Woods, N.J., and Hall, S., 1994, *On the Contribution of Recombination Currents in Schottky Barrier Diodes*, Semiconductor Science and Technology, Vol. 9, pp. 2295-2297.

Xin, X., Yan, F., Koeth, T.W., Joseph, C., Hu, J., Wu, J., and Zhao, J.H., 2005, *Demonstration of 4H-SiC Visible-Blind EUV and UV Detector with Large Detection Area*, Electronics Letters, Vol. 41, pp. 1192-1193.

Yan, F., Xin, X., Aslam, S., Zhao, Y., Franz, D., Zhao, J.H., and Weiner, M., 2004, *4H-SiC UV Photo Detectors with Large Area and Very High Specific Detectivity*, IEEE Journal of Quantum Electronics, Vol. 40, pp. 1315-1320.

Zhang, C., Lechner, P., Lutz, G., Porro, M., Richter, R., Treis, J., Strüder, L., and Nan Zhang, S., 2006, *Development of DEPFET Macropixel Detectors*, Nuclear Instruments and Methods in Physics Research A, Vol. 568, pp. 207-216.

Zhao, S., Gohil, T., Lioliou, G., and Barnett, A.M., 2016, *Soft X-ray Detection and Photon Counting Spectroscopy with Commercial 4H-SiC Schottky Photodiodes*, Nuclear Instruments and Methods in Physics Research A, Vol. 830, pp. 1-5.